Nanoscale Probing of Interlayer Interactions in 2D Materials and vdW Heterostructures

by

Hossein Rokni Damavandi Taher

A dissertation submitted in partial fulfillment
of the requirements for the degree of
Doctor of Philosophy
(Mechanical Engineering)
in The University of Michigan
2019

Doctoral Committee:

Professor Wei Lu, Chair
Associate Professor Jianping Fu
Associate Professor Xiaogan Liang
Associate Professor Zhaohui Zhong

Hossein Rokni Damavandi Taher

rokni@umich.edu

ORCID iD: 0000-0003-1422-9546

© Hossein Rokni Damavandi Taher 2019

DEDICATION

To someone who will fill the world with love, justice and fairness

ACKNOWLEDGMENTS

First and foremost, I would like to thank the Almighty Allah for providing me with everything I needed to successfully complete my thesis.

I would also like to take this opportunity to acknowledge many people without whom this work would not have been possible. First, I would like to express my sincere gratitude to my advisor, Prof. Wei Lu, for his technical/financial support and valuable guidance. He taught me to be an independent thinker and gave me the freedom to choose problems that I found interesting. I have been very fortunate to work in his highly well-equipped NanoStructures lab with the state-of-the-art nano/microfabrication instruments. This, coupled with his continued encouragement, patience and invaluable suggestions, made this work successful.

I would also like to extend special thanks to other members of my committee, Prof. Xiaogan Liang, Prof. Jianping Fu and Prof. Zhaohui Zhong. I learnt a lot from each of my committee member, whether this was through direct one-on-one discussions, research collaborations, class instruction, or even through their graduate students.

In particular, I am extremely grateful to Prof. Liang for the opportunity to be involved in a number of collaborative projects in his Nanoengineering and Nanodevice lab. I learnt a lot from him about novel nanofabrication techniques for the future scalable manufacturing of nanoscale (bio)electronics. I would also like to thank his graduate students, Mikai Chen, Hongsuk Nam, Sungjin Wi, Byunghoon Ryu and Da Li to share their great experiences on device nanofabrication, exfoliation, manipulation and characterization of 2D layered materials with me. Also, I would like to thank Prof. Fu for his useful comments and suggestions during my research fundamental examination (RFE) about using an atomic force microcopy (AFM)-assisted experimental setup (rather than a combined AFM-electrostatic microactuator setup) to measure the interlayer interaction of thin layered materials.

I would especially like to thank each and every one of my labmates for all their help with my research and more importantly for making our lab a comfortable and joyful place to work.

Thank you Dandan Wang and Jianyu Zhang for your help with Scanning Electron Microscopy, and thank you Guangyu Liu and Hosop Shin for all your help with molecular dynamics simulations, sputtering, spin coating, etc. I would also like to thank Zi Li from Department of Chemistry for her help with Raman Spectroscopy measurements.

I would like to thank Prof. Liang Qi, an assistant professor in Department of Materials Science and Engineering, for the discussion regarding the interlayer bonding in heterostructures and Prof. John Hart, an associate professor at MIT, for his helpful suggestions on growth and characterization of one-dimensional graphitic systems (i.e., carbon nanotubes).

I would like to thank the National Science Foundation (NSF) and Rackham Predoctoral Fellowship for supporting the project I was involved in during the last seven years. I would like to thank our collaborators at the Lurie Nanofabrication Facility (LNF) and the Michigan Center for Materials Characterization (MC^2), whose contributions were essential to the completion of this work. In particular, I would like to thank Dr. Azadeh Ansari, currently an assistant professor at Georgia Tech, and Dr. Ali Darvishian, currently a postdoctoral scholar at UC Berkeley, for being not only resourceful mentors in microfabrication techniques but also great friends. I cannot thank you enough for all the help and guidance you have given me both at the LNF as well as outside.

Coming to my family, I would like to first thank my parents-in-law for their patience and support all along my studies. I am deeply and forever indebted to my parents and family for their unconditional love, support and encouragement throughout my life, especially during the more challenging times.

Finally, words are unable to express my heartfelt gratitude to my wife, Saeedeh, who has been and will be the love of my life forever. Thanks for your love, support, patience and understanding over my years of graduate studies. Finally, I would like to thank the newest addition to my family, my son, Ali Hami. I did my best to complete this dissertation before he was born, but he beat me to it by coming 12 days before his due date.

TABLE OF CONTENTS

DEDICATION ..... **ii**
ACKNOWLEDGMENTS ..... **iii**
LIST OF FIGURES ..... **viii**
LIST OF TABLES ..... **xxv**
LIST OF APPENDICES ..... **xxvi**
ABSTRACT ..... **xxviii**

CHAPTER 1 ..... **1**
Introduction **1**
1.1 2D Layered Materials and vdW Heterostructures 1
1.2 Large-Scale Production of 2DLMs-Based Devices 3
1.3 Significance of Interlayer vdW Interactions in 2DLMs and vdW Heterostructures 4
1.4 Summary of Dissertation 6

CHAPTER 2 ..... **9**
Nanofabrication of 2DLMs Device Arrays Using Mechanical Exfoliation Techniques **9**
2.1 Introduction 9
2.2 Plasma-Assisted Exfoliation of MoS_2 Flakes into Large-Area Arrays 10
2.3 Nanoimprint-Assisted Shear Exfoliation of MoS_2 Flakes into Large-Area Arrays 15
2.4 Fabrication of FET and Biosensor Arrays Using Mechanical Exfoliation Techniques 24
2.5 Atomic Force Microscopy-Assisted Exfoliation of G Flakes 31
2.5.1 Nano-sized HOPG mesas 33
2.5.2 In-situ preparation of flat AFM tips 34
2.5.3 Probe tip characterization 34
2.5.4 Adhesive and conductive polymer 35
2.5.5 High precision attachment of FLG to the AFM tips 36
2.5.6 Layer number identification 37

2.5.7 Results and discussion 37
2.6 Summary 39

CHAPTER 3 41
Interfacial Electrostatic Behavior of 2D Layered Materials: Few-Layer Graphene 41
3.1 Introduction 41
3.2 Dielectric Constant Measurements of FLG 44
3.3 Layer-by-Layer Insight into Electrostatic Charge Distribution of FLG 48
3.3.1 Comparison studies 53
3.3.2 Layer–by–layer charge density profiles in 5–LG system 55
3.3.3 Layer–dependent charge screening in *N*–LG systems 57
3.3.4 Temperature–dependent charge screening model 59
3.4 Summary 60

CHAPTER 4 62
Atomistic Simulations of Electrostatic Exfoliation in 2DLMs: Few-Layer Graphene 62
4.1 Introduction 62
4.2 Atomistic Simulation Setup 62
4.3 Three-Dimensional Spatial Charge Distribution of FLG 64
4.3.1 Electric charge on each carbon atom in FLG 65
4.3.2 Attractive and repulsive electrostatic forces on each atom 66
4.4 Results and Discussion 67
4.5 Summary 72

CHAPTER 5 73
In Situ Measurements of Interfacial Adhesion in 2D Materials and vdW Heterostructures 73
5.1 Introduction 73
5.2 *In Situ* AFM-Assisted Experimental Setup 74
5.2.1 Sample preparation 77
5.2.2 Fabrication of nano-sized 2D crystal mesas 78
5.2.3 Attachment of 2D crystal nanomesas to *in situ* flattened AFM tip 79
5.2.4 Fabrication and characterization of microheaters 80

5.2.5 Cooling stage setup 84
5.3 Interfacial Adhesion Energy Measurements 85
5.4 Cohesion Energy in 2D Crystals 86
5.4.1 Force-displacement measurements of nanobubbles and G/copper 88
5.5 Adhesion Between Similar vdW Heterostructures 89
5.5.1 Interaction of 2D crystals with airborne contaminants using water contact angle measurements 91
5.6 Adhesion Between Dissimilar vdW Heterostructures 94
5.7 Adhesion Between 2D Crystals and SiO_x 96
5.8 Tabulated Experimental Data 98
5.9 Adhesion at G/SiO_x Interface: Beyond vdW Interaction 99
5.8.1 Origin of distinctive interfacial behavior in G/SiO_x heterostructures: surface roughness measurements 104
5.9 Summary 107

CHAPTER 6 109
Conclusions and Suggestions for Future Work 109
6.1 Summary 109
6.2 Future Outlook 111

APPENDICES 113

BIBLIOGRAPHY 148

LIST OF FIGURES

Figure 1.1. Side-view high-resolution TEM images of (a) G, (b) hBN and (c) MoS_2 crystals, showing interlayer vdW interactions with an interlayer separation of 0.335 nm, 0.333 nm and 0.655 nm, respectively. (d)-(f) illustrate the corresponding ball-and-stick representation of G, hBN and MoS_2 crystals where carbon, boron, nitrogen, molybdenum, and sulfur atoms are shown in gray, green, pink, cyan, and yellow, respectively. Top-view high-resolution TEM images of (g) G and (h) MoS_2 crystals, showing strong in-plane covalent bonds. Lattice structure in G is similar to hBN with only slightly shorter (~1.8%) lattice constant. (i) Ball-and-stick representation of hBN/G/MoS_2 heterostructures. 1

Figure 1.2. Top-down exfoliation approach: (a) Scotch tape, (b) liquid phase and (c) ion/compound intercalations. (d) External normal and shear forces for the exfoliation. Bottom-up approach: (e) CVD and (f) epitaxial growth. 3

Figure 2.1. (a) Schematic flowchart of transfer printing of prepatterned few-layer MoS_2 flakes, which includes (1) initial bulk MoS_2 with a pristine surface; (2) photolithography for patterning device features; (3) formation of Ti masks by metal deposition followed by lift-off; (4) plasma etching of underlying MoS_2; (5) removal of Ti masks and finalization of a bulk MoS_2 stamp bearing relief features; (6) plasma treatment of the SiO_2 substrate; (7) direct transfer printing of prepatterned few-layer MoS_2 flakes onto the substrate. (b) SEM images of a bulk MoS_2 stamp prestructured with 5 μm size periodic pillars. 11

Figure 2.2. (a) SEM image of arrays of 10 μm size MoS_2 flake pixels printed onto a pristine SiO_2 substrate. (b) Stacked column chart of the average thickness data collected from 100 as-printed MoS_2 pixels. The thickness data were obtained from MoS_2 pixels printed over a ~1cm^2 area by using an AFM. (c) Secondary-electron SEM images of MoS_2 pixel arrays printed onto an O_2 plasma-charged substrate, which exhibit clear, well-

defined edge profiles faithfully correlated to the edge profiles of pillar features on the bulk MoS_2 stamps. (d) Backscattered SEM images of MoS_2 pixel arrays, which show the presence of thin inner MoS_2 flakes within each printed pixel. (e) Backscattered image of MoS_2 pixels with broken inner films. 12

Figure 2.3. (a) AFM image of a 10 μm size MoS_2 pixel printed on a plasma-charged SiO_2 substrate. The solid line indicates a scanning trace across the pixel, which is explicitly plotted in (b). (c) Stacked column chart of the average thickness data collected from 100 as-printed MoS_2 pixels. Here, the thickness data acquired from the inner flakes (solid columns) and the outer edge ribbons (hatched columns) of these MoS_2 pixels are separately plotted. 13

Figure 2.4. (a) Illustration of the 2-D model for Maxwell stress tensor calculation of surface charge-induced electrostatic attractive stress between the bulk MoS_2 stamp and the dielectric substrate. (b) Calculated attractive stress plotted as a function of positions. (c) Zoomed view of attractive stress distribution within a single MoS_2 mesa in contact with a SiO_2 surface. It is found that the attractive stress acting on a microscale MoS_2 mesa is uniform in the central region of the MoS_2 mesa but is significantly increased along the mesa edges due to the fringe effect. 14

Figure 2.5. SEM images of (a) a HOPG stamp prepatterned with 100 nm half-pitch relief gratings by using nanoimprint lithography followed with plasma etching and (b) graphene nanoribbons printed onto a plasma-charged SiO_2 substrate. 15

Figure 2.6. Illustration of nanoimprint-assisted shear exfoliation (NASE) for producing few-layer/multilayer MoS_2 device structure arrays: (a) fabrication of a bulk MoS_2stamp bearing protrusive device features; (b) nanoimprint process for pressing the protrusive features on the bulk MoS_2 stamp into a polymeric fixing layer coated on a substrate; (c) exfoliation of imprinted MoS_2 features along a shear direction, which is actuated by a motorized roller tool; (d) multilayer MoS_2 flakes imprinted/exfoliated by NASE, which are expected to exhibit a high uniformity in thickness as well as electronic properties; (e) post-NASE processes for further adjusting the final thicknesses of exfoliated MoS_2 flakes to meet various device application requirements. 16

Figure 2.7. Photographs of (a) the motorized roller tool for performing NASE processes and (b) an exemplary 1 cm-size MoS_2 stamp. (c) shows the SEM image of this stamp, which bears 40 nm-high, 15 µm-size protrusive mesa (or pillar) arrays. 18

Figure 2.8. NASE results: (a) four optical micrographs of MoS_2 flake arrays imprinted/exfoliated into a PS fixing layer coated on a SiO_2/Si substrate by using NASE, which were captured from different locations over the whole NASE-processed area (~1 cm^2), as mapped in the inset photograph of the whole NASE sample; (b) Raman spectrum of an exemplary multilayer MoS_2 flake; (c) optical micrographs of typical imperfections that occur in NASE. (d–f) SEM images of a set of NASE-produced arrays of multilayer MoS_2 flakes with various flake diameters (D) and flake-to-flake spacings (L). For all of these samples, the imprint depth (d_{NIL}) is ~50 nm. 19

Figure 2.9. AFM characterization of NASE-produced MoS_2 flakes exfoliated into a PS fixing layer: (a) schematic of a multilayer MoS2 flake with thickness of $tMoS_2$ exfoliated into an imprinted PS well with imprint depth of d_{NIL}, resulting in an effective well depth of d_W; (b) an exemplary 3-D AFM image of a multilayer MoS_2 flake exfoliated into an imprinted PS well; (c) an AFM scanline extracted from the AFM image shown in (b) (i.e., the dashed line shown in (b)), from which the d_W value of this MoS_2-embeded well can be measured from the topographic difference between locations denoted with arrows; (d) statistics of d_W/d_{NIL} data measured from 100 MoS_2-embeded wells, which shows that the standard deviation of d_W/d_{NIL} data (or the relative thickness error of NASE-produced multilayer MoS_2 flakes) is estimated to ~12%. 21

Figure 2.10. Molecular dynamics (MD) simulation of the NASE process for exfoliating atomically layered nanostructures: (a) a selected part of the 3-D simulation region, showing the cross-sectional view of the initial configuration of the NASE process, involving a graphite stamp bearing 5 nm size, 4-layer mesas and a PS fixing layer; (b–d) cross-sectional snapshots of the MD simulation result of a postnanoimprint shear exfoliation course at t = 0, 50, 90 ns; (e) a 3-D snapshot of the simulated system at t = 90 ns; (f) a zoom-in view of the imprinted PS well bearing graphene

layers, especially displaying the interface between the edges of exfoliated layers and the sidewall of the imprinted PS well. 22

Figure 2.11. Molecular dynamics (MD) simulation of the NASE process for exfoliating relatively low-aspect-ratio layered structures: (a) a cross-sectional snapshot of the NASE stage, in which a graphite stamp bearing 50 nm size, bilayer mesas has been imprinted into a PS fixing layer (i.e., t = 0); (b) a cross-sectional snapshot of the postnanoimprint shear exfoliation course taken at t = 1 ns; (c) and (d) are tilted and side views, respectively, of a 3-D snapshot of the simulated system at t = 1 ns, which exhibits wrinkle features induced by the shear dislocation process............. 23

Figure 2.12. (a) BSE image of an exemplary back-gated FET made from the inner flake of a printed MoS_2 pixel with flake. (b) I_{DS}-V_{DS} characteristics under different gate voltages (V_G) ranging from -75 to 100 V. (c) Semi-logarithmic plot of an I_{DS}-V_G characteristic curve under a fixed drain-source voltage V_{DS} = 10 V. The inset graph shows the linear plot of the same I_{DS}-V_G curve, and the transconductance (dI_{DS}/dV_G) is obtained by fitting the linear region of the I_{DS}-V_G curve, as indicated by the red line... 24

Figure 2.13. (a) SEM image of an exemplary back-gated FET made from the outer edge ribbon of a printed MoS_2 pixel. (b) I_{DS}-V_{DS} and (c) I_{DS}-V_G characteristics of the edge ribbon-based FET.. 25

Figure 2.14. Back-gated FET arrays made from NASE-produced MoS_2 flakes: (a) Schematic illustration of a back-gated MoS_2 FET. (b) SEM images of a representative FET array made from the multilayer MoS_2 flakes (thickness ~20 nm) produced in a NASE process. For all FETs, the channel width (W) and length (L) are 15 and 10 μm, respectively; the back gate dielectric is 300 nm SiO_2 + residual PS (estimated to be thinner than 5 nm). The following graphs display the statistics of (c) mobility (μ), (d) On/Off currents (I_{ON} and I_{OFF}), (e) subthreshold swing (SS), and (f) threshold voltage (V_T) data measured from 45 MoS_2 FETs fabricated by a NASE process... 27

Figure 2.15. Optical micrograph of two representative back-gated FETs made from selected NASE-produced multilayer MoS_2 flakes. These NASE-produced MoS_2 flakes (~30 nm thick) were soaked in toluene for 1-2 hours in order to remove the residual PS

layers under them. This toluene etching process shifted most MoS_2 flakes away from their original locations in the array. Therefore, to make working FETs, special finger contacts (5 nm Ti/50 nm Au) were fabricated to access to individual selected MoS_2 flakes. 28

Figure 2.16. (a) Transfer characteristics of 4 back-gated FETs, made from NASE-produced multilayer MoS_2 flakes. For these FETs, the residual PS layers under MoS_2 channel flakes were completely removed by toluene. This toluene cleaning process shifted MoS_2 flakes away from their original locations in the array. Therefore, these devices had to be fabricated using repetitive lithography and metallization processes. Statistics of (b) mobility (μ), (c) On/Off currents (I_{ON} and I_{OFF}), (d) subthreshold swing (SS), and (e) threshold voltage (V_T) data measured from 11 FETs made from NASE-produced MoS2 flakes. These selected MoS_2 flakes were cleaned with toluene. 29

Figure 2.17. MoS_2 transistor biosensors made from NASE-produced multilayer MoS_2 flakes: (a) illustration of a MoS_2 transistor biosensor, in which anti-human TNF-α antibodies are directly functionalized on the MoS_2 transistor channel; (b) sensor responses (i.e., transfer characteristics) to various TNF-α concentrations (i.e., n = 0, 60 fM, 600 fM, 6 pM, and 60 pM) measured from eight different sensors; (c) calibrated responses (i.e., relative change of ON-state I_{DS} measured at a fixed V_G=98 V) with respect to n, measured from difference sensors, which exhibit a high degree of device-to-device consistency and can be well fitted with Langmuir isotherm. 30

Figure 2.18. Schematics of mechanical exfoliation of 2DLMs features using (a,c) bias voltage, (b) plasma-charged surface and (d) polymeric fixing layer, followed by applying (a,b) pull-off and (c,d) shear forces. 32

Figure 2.19. (a) Schematic of a typical macro-scale exfoliation setup and (b) the corresponding nano-scale AFM-based exfoliation setup. (c) Schematic of the CAFM experimental setup used to perform shear and normal electrostatic exfoliation of FLG from nanosized HOPG mesa onto the SiO_2/Si substrate. 33

Figure 2.20. (a) AFM image (top) and height profile (bottom) of 75-nm-deep cylindrical mesas with a diameter of 60 nm from HOPG. Inset: SEM image of the nano-sized HOPG mesa arrays. (b) Pt/Ir_5-coated AFM probe tilted at an angle of 12° due to the mount

of Park XE-70 AFM head. (c) SEM image of AFM tip after the fattening procedure. Inset: Flat surface of AFM tip. 34

Figure 2.21. (a) SEM image of the flattened tip. (b) Tapping-mode AFM topography image of nanoindentation of the flattened tip apex into the 50-nm-thick PEDOT/PSS thin film on the SiO_2/Si substrate. The indented profile, taken along the red arrow, shows a very flat and smooth surface. AFM topography image (top) and height profile (bottom) of (c) a 25-nm-thick PEDOT:PSS(D-sorbitol) film and (d) raised letters 100 nm width and 12 nm height, formed at -5 V with a tip speed of 0.5 um/s. 35

Figure 2.22. (a) SEM image of the probe tip with (b) the corresponding zoom-in image, showing a firm attachment of a cylindrical mesa onto flat tip surface. (c) Side-view of the tip with an attached HOPG nanomesa. In (b) and (c), scale bars indicate 50 and 100 nm, respectively. 36

Figure 2.23. (a) Raman spectra of *N*-LG flakes. The four most intense peaks are first-order (Si) and second-order (2Si) optical phonon peaks of the silicon substrate, and G and 2D peaks of graphene. Raman spectra are scaled and upshifted for clarity. The scaling factors of 1/5 and 1 are used for $\omega<1200cm^{-1}$ and $\omega>1200cm^{-1}$, respectively. (b) The ratios of the integrated intensity of the G and Si peaks, I(G)/I(Si), versus layer number *N*. Blue circles are present data, red triangles and green squares are data measured for mechanically exfoliated *N*-LG on 280-nm-thick-SiO_2/Si at λ=488 nm and on 89-nm-thick-SiO_2/Si at λ=532 nm, respectively. 37

Figure 2.24. (a) Shear exfoliation and (b) normal exfoliation histograms of the number of printed flakes collected from 110 and 50 samples, respectively, under different bias voltages. (c) SEM image of mono-, bi-, and trilayer graphene flakes printed by the shear exfoliation method in the form of the letter "M" at V = 10 V. (d) SEM image of monolayer and 15-layer graphene flakes printed by the normal exfoliation method at V = 9.5 V. (e) SEM image of an incompletely sheared HOPG nanopillar at an incommensurate basal plane 18 nm above the substrate at the bias voltage of 10 V. 39

Figure 3.1. (a) AFM topography image of 1-8LG onto a 10-nm-thick SiO_2/Si substrate with the corresponding layer numbers labeled; (b) Height profile (blue line) and contact

potential difference V_{CPD} profile (red line) corresponding to the green line in (a); (c) SEM images of the conductive SCM-PIT tip used for the measurements. (d) Total force-voltage curves taken on the 4LG/SiO_2/Si substrate at each tip-surface distance. Circles are experimental data and the lines are parabolic fits using Eq. (3.1) at a constant lift height. Three fitting parameters $\partial C \partial z$(aF/nm), VCPD(V) and FvdW(nN) are given for each curve 44

Figure 3.2. (a) Geometric representation of the tip-FLG/SiO_2 system along with the parameters used in electrostatic 3D finite element calculations. (b) Cross-section of 3D finite element calculation of the electrostatic field distribution between the tip and the 28LG/SiO_2 sample at a tip-surface distance of 10nm. The applied potential between tip and substrate is V=10V. 46

Figure 3.3. (a) Measured electrostatic force versus tip-Si distance taken on the bare Si surface (gray circles), on the 10-nm-thick SiO_2 film (blue triangles), and on the 28LG (red squares) at V = 10 V. The lines are theoretical fittings to Eq. (1). Top inset shows that as the tip moves across the sample surface in constant height, the tip experiences a larger electrostatic force on 28LG than that on Si and SiO_2. Bottom inset shows the cross-section of 3D finite element calculation of the electrostatic potential distribution between the tip and the 28LG/SiO_2 sample (see **Figure 3.2(b)** for the corresponding electric field distribution); (e) Relative dielectric constant as a function of the layer number under relatively low and high bias voltages. The application of the bias voltage $\leq$ 3V makes the dielectric response extremely weak in our setup. The dashed line is a guide to the eyes and represents the dielectric constant of the bulk HOPG; (f) Dependence of the relative dielectric constant of 1-3LG and bulk HOPG on oxygen reaction at V=10 V. 47

Figure 3.4. Schematic illustration of an eight-layer graphene/SiO_2 system. The Si substrate beneath the SiO_2 film is not shown for simplicity. The arrows correspond to the electric field lines focusing near the edges of FLG. Left inset: density of states in the four innermost graphene flakes versus the electronic band energy, where the transparent area represents the average induced charge density Qi and the average value of the Fermi energy profile is denoted by $\mathbb{E}Fi$. 49

Figure 3.5. (a-h) Low–energy band structures of Bernal–stacked *N*–LG near the K–point of the Brillouin zone. There exist $N2$ pairs of split-off hyperbolic bands, where denotes the integer part of the quantity. The excitation energy from the ground state to the first excited state ($\mathbb{E}N$ex) is shown with arrows. Blue lines in (a)-(d) correspond to the electronic dispersion of the effective monolayer graphene ($\theta = 0$) which only appears in systems with an odd number of graphene layers, whereas red, green, pink and brown in (e)-(h) correspond to the electronic dispersion of the bilayer-like graphene ($\theta \neq 0$). Negative and positive $\mathbb{E}$ refer to the valence(hole)/conduction(electron) bands, respectively. **(i)** Density of states in *N*–LG showing discontinuous jumps at the excited states. **(j)** Zoom-in view of discontinuous jumps at the first excited state ($\mathbb{E}N$ex). 50
Figure 3.6. (a) Our work functions in the 1-8-LG systems relative to that of 8LG, Φ8, for $Q0 = 7.9 \times 1012\text{cm} - 2$; **(b)** work functions across a 4-LG system which are given relative to that of the outermost layer Φ4 as the zero-reference level for $Q0 = 2.2 \times 1013\text{cm} - 2$ [41]; **(c)** work functions in the 1-6-LG systems relative to that of bulk graphite Φ∞ for $Q0 = 4.85 \times 1012\text{cm} - 2$ [43]; and **(d)** difference between the work function of the uppermost layer in the *N*-LG system and that in the (*N*-1)-LG system for *N*=1 to 8 when $Q0 = 1.7 \times 1013\text{cm} - 2$ [44]. 54
Figure 3.7. Normalized charge distribution profiles of an 8-LG system for three different values of $Q0$. Dashed curves with open symbols represent the results obtained by the linear energy dispersion ($mj *= 0$), whereas solid curves with filled symbols denote the results obtained by the actual energy dispersion of an 8-LG system ($mj * \neq 0$)...... 55
Figure 3.8. (a) Charge density profiles of a 5-LG system for $Q0 = 1013\text{cm} - 2$, where each dashed line represents the average charge density $qi = Qi$ in the layer i. **(b)** Charge density at the edge qie and the center qic of the layer i. **(c)** Fermi level profile of the innermost layer. Inset: low-energy band structure of 5-LG system. Solid green curve in the Fermi level profile and dashed green curve in the band structure represent the first (0.4 eV) excitation energy. **(d)** Blue curves: normalized average charge profiles across the layers of a 5-LG system for different gate charge densities of 1012 (circles), 1013 (rectangles) and $1014\text{cm} - 2$ (diamonds). Red curves: corresponding changes in the local charge screening $\lambda i, i + 1$............................... 56

Figure 3.9. **(a)** Normalized average charge distribution profiles across the layers of 1-8-LG systems for $Q0 = 1013\mathrm{cm} - 2$. Insets: Normalized charge density of the first (lower inset) and second (upper inset) layer in 2-8-LG. **(b)** Circles with blue borders: global charge screening length in 1-8-LG systems for $Q0 = 1013\mathrm{cm} - 2$. A decay length (d/λ) of 1.04 is found by fitting the data with a function $e^{-(i-1)d/\lambda}$, indicated by a dashed curve. Rectangles with red borders: local charge screening length in 1-8-LG systems for $Q0 = 1013\mathrm{cm} - 2$. **(c)** Edge-to-center charge density ratio as a function of the layer position in 1-8-LG systems when $Q0 = 1013\mathrm{cm} - 2$. Inset: Edge-to-center charge density ratio for the innermost (red circles) and outermost (blue squares) layers of 1-8-LG systems. 57

Figure 3.10. Local screening length between the first and second layers of an 8-LG system as a function of $Q0$. Dashed curves with open circles (squares) represent the results obtained by the linear energy dispersion model ($mj *= 0$) at *T*=0 K (*T*=300 K), whereas solid curves with filled circles (squares) denote the results obtained by the actual energy dispersion of the 8-LG system ($mj * \neq 0$) at *T*=0 K (*T*=300 K)........ 59

Figure 4.1. Atomic structure of the 8–LG/SiO_2 system. The background color and the arrows in the figure correspond to the local electric fields (color can be read from the scale bar and the length of arrows is proportional to the field intensity). Left inset: density of states in the four innermost graphene flakes versus the electronic band energy, in which the transparent area represents the average induced charge density. Right inset: top view of AB-stacked circular flakes cut out of the rectangular sheet with a mixture of armchair and zigzag edges. 63

Figure 4.2. (a) Charge density profiles of an 8–LG system for $Q = 1013\mathrm{cm} - 2$, where each dashed line represents the average charge density $qi = Qi$ in the layer i; (c) 3D discrete charge density profile of the innermost flake ($i = 1$) in the 8–LG system for $Q = 1013\mathrm{cm} - 2$ where $q1j$ is the charge density on atom *j* belonging to the innermost flake. (b) Normalized average charge density across the layers of an 8–LG system for different gate charge densities. Inset: normalized average charge density in the two innermost layers to show the electrostatic charge screening effect. Zoom-in of a region in which the charge screening between the first and second layers is shown by a dashed black square. 64

Figure 4.3. (a) Uniform charge distribution over a triangular area ($Ac = 33a24$, where $a =$ 1.42 Å is the C–C bond length) surrounding the associated atom. (b) 3D discrete charge density profile of the innermost flake ($i = 1$) in the 8–LG system for $Q = 1013\text{cm} - 2$ where $q1j$ is the charge density on atom j belonging to the innermost flake.. 65

Figure 4.4. (a) Number of printed layers as a function of the induced charge density for both normal and shear exfoliation techniques. Snapshots from MD simulation of (b) the normal exfoliation for $Q = 8.5 \times 1012\text{cm} - 2$ at $t = 1$ ns and (c) the shear exfoliation for $Q = 9.5 \times 1012\text{cm} - 2$ at $t = 3$ ns;.. 69

Figure 4.5. (a) A portion of the MD trajectory for the normal exfoliation of the 8-LG system when $Q = 10.5 \times 1012\text{cm} - 2$. Variation of the interlayer rotation/distance between layers, labeled 5 and 6, and between 6 and 7 as a function of simulation time. The separation of the layer 7 from 6 is initiated at $t \approx 0.45$ ns (highlighted by magenta dashed line); (b) Corresponding snapshot of the MD simulation for such exfoliation taken at $t = 0.6$ ns. Local delamination is marked in transparent red circles. 71

Figure 4.6. 2D and corresponding 3D contours of the potential corrugation of (a) the bilayer system in equilibrium ($\Delta d = 3.35$Å) and (b) the compressed bilayer ($\Delta d = 3.00$Å). In (a) and (b), the maximum energy difference $\Delta V = VAA - VAB$ is reported. (c) Three stacking configurations AA, AB and saddle corresponding to the Max, Min and Saddle points on the contour plots, respectively. 72

Figure 5.1. (a) Schematic of the AFM setup used to perform interfacial adhesion measurements under different annealing temperatures. Left inset: SEM image of the microheater with an MoS_2 flake exfoliated on the heating line whose corresponding AFM image was taken by the G crystal tip. Right Inset: SEM images of the tip-attached G circular nanomesa (top image) and hBN square nanomesa (bottom image). Scale bars indicate 100 nm. (b) Normal and (c) shear interfacial adhesion measurements at the intact homointerfaces. Interfacial adhesion measurements at the (d) untreated and (e) precooling-treated homointerfaces. 75

Figure 5.2. (a) SEM images of MoS_2 square and G circular nanomesa arrays. (b) 3D AFM image of MoS_2 square nanomesas. (c) Corresponding height profiles of 60-nm-deep MoS_2 square mesas with an average width of 60 nm. 78

Figure 5.3. (a) SEM image of an in situ flattened tip apex. (b) AFM topography image of nanoindentation of the tip apex into the 50-nm-thick PEDOT/PSS film on the SiO_x/Si substrate. (c) Indented profile of the tip shows a very flat and smooth surface. (d) Typical SEM images of the tip with an attached square or circular nanomesa... 79

Figure 5.4. (a) SEM images of the probe exposed to a temperature of 95°C using a 1cm×1cm Kapton heater (i.e., global heating) and a micron-sized heater (i.e., local heating). (b) SEM image of a representative microheater surrounded by the exfoliated MoS_2 flakes. (c) AFM noncontact-mode image of the region marked by the square in (b), taken by the G crystal tip. 80

Figure 5.5. (a) Calibration of the microheater devices using the hot chuck/Joule heating (red dots) and IR camera (blue dots), both showing a linear relationship between the temperature and the input power. The dashed red line is linearly fitted to the combined hot chuck/Joule heating results. (b, c) IR results for the temperature distribution of the microheaters with the thermally-disconnected (b) and connected (c) G flakes.. 81

Figure 5.6. (a) 3D model of the AFM setup developed in COMSOL. (b) Steady state thermal simulation of the G flakes and microheater over the SiO_x/Si substrate at an input power of 5 mW. (c) Temperature distribution of the AFM probe. (d) Temperature distribution profile along the probe length... 83

Figure 5.7. (a) Schematic of Peltier-based cooling stage setup. (b) Infrared image for the temperature distribution of the SiO_x/Si pieces on the multistage Peltier element, showing a very uniform temperature of -15.2°C. 84

Figure 5.8. Wetting behavior during condensation and evaporation of water microdroplets on the surface of the mechanically exfoliated G/SiO_x/Si substrate when the Peltier cooling element is (a) turned ON at 0 sec, (b) then turned back OFF right after 5 sec and (c) kept in the OFF state for another 5 sec. 84

Figure 5.9. (a) Typical retraction *F–d* curves recorded at the intact homointerface of G(in red), hBN(in blue) and MoS_2 (in brown) crystals and also the approach *F–d* curve (in gray) recorded at the hBN tip/substrate homointerface. The light blue-shaded area between the approach and retraction curves at the hBN homointerface represents the cohesion energy in units of Joules. Each raw data set was given an offset to provide the same equilibrium position for all *F–d* curves. Right Inset: SEM images of lower section of the nanomesas on their corresponding bulk substrate after the full tip retraction. Left inset: Perspective AFM image corresponding to the SEM image of the MoS_2 nanomesa shown in the right inset. Scale bars indicate 50 nm. **(b)** Typical shear force–lateral piezo displacement curves recorded at the intact homointerface of G(in red), hBN(in blue) and MoS_2(in brown) crystals. Schematic inset shows that the 2D crystal substrate moves along the long axis of the cantilever tip at zero contact force. Inset: Corresponding SEM images of the sheared G, hBN and MoS_2 nanomesas. **(c)** Cohesion energy of G, hBN and MoS_2 crystals obtained by normal force measurements (circles with cyan borders) and shear force measurements (circles with orange borders) at room temperature. Data are presented as average ± standard deviation. 87

Figure 5.10. Typical retraction *F–d* curves recorded at the interface of tip-attached G nanomesa/G substrate (in blue), bare Si tip-attached nanobubble/SiO_x substrate (in blue) and tip-attached G mesa/Cu substrate (in brown) at the relative humidity of 15%, 70% and 15%, respectively. The light blue-shaded area represents the interfacial adhesion energy in units of Joules. Each raw data set was given an offset to provide the same equilibrium position for all *F–d* curves. Schematic inset shows the bridging bubble rupture between the in-situ flattened Si tip and the SiO_x/Si substrate, where the energy required to rupture the nanobubble is roughly obtained by dividing the area under the *F–d* curve over the area of the flat tip. 89

Figure 5.11. IAE values as a function of annealing temperatures at the G, hBN and MoS_2 homointerfaces using normal force microscopy technique. Filled gray circles denote the intrinsic IAE values at the intact G, hBN and MoS_2 homointerfaces whereas filled blue (red) circles denote the IAE values between 2D crystal tips and precooling-treated (untreated) substrates. Each open transparent gray circle

represents a single IAE measurement at the intact homointerfaces, whereas each data point shown in open transparent blue and red circles represents the IAE of the tips on an individual 2D crystal flake averaged over 10 measurements from different locations of the flake surface. Each filled circle is presented as average of all corresponding open circles ± standard deviation. Insets illustrate ball-and-stick representation of various tip/substrate interfaces where carbon, boron, nitrogen, molybdenum, and sulfur atoms are shown in gray, green, pink, cyan and yellow, respectively. 91

Figure 5.12. SEM images of (a), (b) hBN, (c), (d) G and (e), (f) MoS_2 flakes which are exfoliated on the heating line of the microheaters and exposed to the ambient air for several months. 92

Figure 5.13. Temporal evolution of the adhesion energy (left axis in blue) and contamination thickness (right axis in red) measured on the mechanically exfoliated HOPG surface during the first 60 min of air exposure. Adhesion energy is extracted from WCA measurements of refs. [90], [91], [93], [94], [95] and [86] denoted by black, cyan, brown, orange, magenta, green circles, respectively. Adsorbed contamination layers linearly grow within the first 60 min of air exposure, reaching a thickness of ~0.55nm, and then the growth rate considerably decreases and plateaus at ~0.60nm after several hours [86]. 94

Figure 5.14. IAE values as a function of annealing temperatures at the G/hBN, G/MoS_2 and MoS_2/hBN heterointerfaces using normal force microscopy technique. Filled blue (red) circles denote the IAE values between 2D crystal tips and precooling-treated (untreated) substrates. Each data point shown in open transparent blue and red circles represents the IAE of the tips on an individual 2D crystal flake averaged over 10 measurements from different locations of the flake surface. Each filled circle is presented as average of all corresponding open circles ± standard deviation. Insets illustrate ball-and-stick representation of various tip/substrate interfaces where carbon, boron, nitrogen, molybdenum, and sulfur atoms are shown in gray, green, pink, cyan and yellow, respectively. 96

Figure 5.15. IAE values as a function of annealing temperatures at the G/SiO_x, hBN/SiO_x and MoS_2/SiO_x heterointerfaces using normal force microscopy technique. Filled blue

(red) circles denote the IAE values between 2D crystal tips and precooling-treated (untreated) substrates. Each data point shown in open transparent blue and red circles represents the average IAE value obtained from 10 measurements within an individual small region ($1\mu m \times 1\mu m$) of SiO_x substrate. Each filled circle is presented as average of all corresponding open circles ± standard deviation. Insets illustrate ball-and-stick representation of various tip/substrate interfaces where carbon, boron, nitrogen, molybdenum, sulfur, silicon and oxygen atoms are shown in gray, green, pink, cyan, yellow, white and orange, respectively. 97

Figure 5.16. **(a)** Typical retraction *F–d* curves of the G/SiO_x interface recorded at no contact pressure (in purple) and 5MPa (in brown, magenta and orange) and also a typical approach *F–d* curve (in gray). **(b)** IAE values as a function of contact pressure at the intact G homointerfaces (filled blue squares in top panel), G/SiO_x interfaces (filled red circles in top panel) and aged G homointerfaces (filled blue circles in bottom panel). Each open transparent symbol represents a single IAE measurement at the given contact pressure. Each filled symbol is presented as average of all corresponding open symbols ± standard deviation. From 110 IAE measurements shown in the top panel, 33 and 77 contacts result in the separation of G crystal tip across the thickness of the nanomesa (open blue squares) and from the SiO_x surface (open red circles), respectively. In the top panel, cyan and orange shaded regions indicate the vdW-only and vdW+non-vdW interactions of G/SiO_x, respectively, where the liftoff in the vdW-only region is relatively gradual in comparison to the vdW+non-vdW region. Dashed blue lines denote an overall average IAE value of 0.328 ± 0.022 Jm^{-2} and 0.263 ± 0.032 Jm^{-2} at the intact G homointerface (top panel) and aged G homointerface (bottom panel), respectively. Dashed red line in the top panel represents the best fit to the data, indicating the pressure dependence of IAE at the interface with an average value of 0.284 ± 0.046 Jm^{-2} taken within the pressure-independent region (i.e., ≥3MPa). Inset of bottom panel: SEM image showing $2\mu m \times 2\mu m$ square regions of G (in turquoise) and SiO_x (in rose) substrates on which all measurements are performed in close proximity to the microheater. 100

Figure 5.17. MD-calculated force versus relative displacement curves for the interaction of G/G (in black), the vdW-only interaction of G/SiO_x (in purple) and vdW+non-vdW

interaction of G/SiO_x (in magenta) with three covalent C–O–Si bonds at the interface. Each force jump labeled by 1, 2 and 3 represents the break of the corresponding covalent bond, as illustrated by the MD pull-off simulation in the inset. 102

Figure 5.18. **(a)** High resolution AFM images of the surface roughness of bare SiO_x, monolayer graphene (1LG), monolayer hBN (1LhBN) and monolayer MoS_2 (1LMoS_2) on SiO_x substrate; **(b)** PSD profiles corresponding to the images in (a); and **(c)** surface roughness measurements of different heterostructures. Error bars show the spread of data over several independent measurements of different flakes. Left inset: Histogram of the height distribution (surface roughness) for bare SiO_x, 1LG/SiO_x, 1LhBN/SiO_x, 1LMoS_2/SiO_x, 1LG/hBN and 1LG/MoS_2 substrates. Solid lines are Gaussian fits to the distribution. Right inset: Representative SEM images of 2D crystal square mesas exfoliated onto the substrate. Scale bar in each is 5μm. (b), (c) and the insets of (c) share the same color legend.. 106

Figure A.1. (a) Geometric representation of the tip-SWCNT/SiO_2 system along with the parameters used in electrostatic 3D finite element calculations. (b) Cross-section of 3D finite element calculation of the electrostatic field distribution between the tip and the SWCNT/SiO_2 sample at z=8nm and V=5V. 114

Figure B.1. Induced charge density profile of the sheet for different thickness-to-radius ratios. 116

Figure B.2. **(a)** Fermi level profiles of a 5-LG system for $Q0 = 1013\text{cm} - 2$. **(b)** Fermi level profile of the innermost layer in an 8-LG system for $Q0 = 1013\text{cm} - 2$. Inset: low- and high-energy band structure of the 8-LG system. Brown, orange and green solid curves in the Fermi level profile and brown, orange and green dashed curves in the band structure represent the first (0.14 eV), second (0.40 eV) and third (0.61 eV) excitation energies, respectively. 119

Figure B.3. Normalized average charge profiles across the layers of **(a)** a 5-LG system and **(b)** an 8-LG system for different values of $Q0$. A decay length (d/λ) of 1.0, 1.2 and 1.6 is found by fitting the data with a function $e^{-(i-1)d/\lambda}$. 120

Figure C.1. (a) Graphene–SiO_2 adhesion energy as a function of the scaling factor. (b) Number of printed layers as a function of the scaling factor obtained by the normal exfoliation technique in the absence of the electrostatic forces. 127

Figure C.2. Fermi level profiles of the 8–LG system for $Q = 1013\text{cm} - 2$. 128

Figure C.3. (a) Fermi level profile of the innermost layer for $Q = 1013\text{cm} - 2$. Inset: low–energy band structure of 8-LG. Brown, orange and green colors in the Fermi level profile and the band structure represent the first (0.14 eV), second (0.40 eV) and third (0.61 eV) excitation energies. (b) Corresponding charge density profile and the average charge density of the innermost layer. 128

Figure C.4. (a) Charge density at the edge qie and at the center qic of the layer i. (b) Normalized average charge density across the layers of an 8–LG system for different gate charge densities. Inset: normalized average charge density in the two innermost layers to show the electrostatic charge screening effect. Zoom-in of a region in which the charge screening between the first and second layers is shown by a dashed black square. 129

Figure C.5. (a) Local and (b) global charge screening lengths for different values of $Q0$. A decay length (d/λ) of 1.0, 1.2 and 1.6 is found by fitting the data with a function $e^{-d/\lambda}$... 130

Figure C.6. (a) Comparison of the normalized charge profile along the zigzag edge of the graphene flake between the present spatial discrete model and the charge-dipole model. (b) Corresponding 3D charge distribution of the rectangular graphene sheet. 130

Figure C.7. (a) Shear stress-strain curves and (b) normal stress-strain curves for the graphene flake in the commensurate ($\theta = 0°$) and incommensurate ($\theta = 2.5°$) stacking.... 134

Figure D.1. (a) Typical optical microscope image of the AFM tip with an effective length and width of L and b, respectively. (b) Schematic drawing of probe dimensions and a lateral load applied to the apex. (c) Dimensions of the probes used. (a)-(c) are directly used from [124]. (d) Corresponding 3D model of the AFM probe. (e) Rotation of the probe A about its long axis x when a lateral force of 10 nN is applied to the tip apex in the positive y direction, yielding a torsional stiffness value of c_φ=222.74 N/m. (e) Lateral deflection of the probe A when a force of 10 nN in the positive y direction is applied to a point on the cantilever shank with the same x

distance from the cantilever root as the *x* distance of the tip apex, yielding a lateral bending stiffness value of k_l=344.59 N/m. 137

Figure D.2. **(a)** Interfacial adhesion energy measurements of G/G as a function of tilt angle. **(b)** MD calculations of normalized pull-off force versus the tilt angle of the SiO_x substrate at the interface of SiO_x and the small (2nm×2nm) and large (10nm×10nm) graphene flakes. 140

Figure D.3. Schematic drawing of a cantilever tilted by an angle θ with respect to a horizontal surface subjected to a normal force along the positive *z* axis. 142

Figure D.4. (a) Mean square fluctuations in amplitude as a function of frequency for the probe with the protruded tip in air. The blue curve is the original data while the dash curve is the fit to the data using Eq. (12). (b) Deflection of the probe when a contact force of 30 nN is applied to the apex in the positive *z* direction, yielding a spring constant of 2.99 N/m. 144

Figure D.5. (a) Schematic drawing of a cantilever tilted by an angle θ with respect to a horizontal surface subjected to a axial force directed to the long axis of the cantilever along the positive *x* axis. (b) Deflection of the probe when a contact force of 30 nN is applied to the apex in the positive *x* direction, yielding a spring constant of 8.20 N/m. 146

LIST OF TABLES

Table 1.1. Comparison of Young's modulus (*E*) and fracture strength (σ_f) of monolayer and few-layer G, hBN and MoS_2 using AFM nanoindentation of suspended 2D crystal membranes. 2

Table 3.1. Dielectric constant measurements of different graphitic systems. 42

Table 3.2. Charge screening depth measurements in FLG systems. 42

Table 5.1. Summary of water contact angle measurements and corresponding IAE values of G crystal. 93

Table 5.2. Summary of cohesion energy Γ (Jm^{-2}) at intact G, hBN and MoS_2 homointerfaces. . 98

Table 5.3. Interfacial adhesion energy Γ (Jm^{-2}) in similar/dissimilar heterostructures using normal force microscopy. 99

Table C1. Interlayer elastic properties of FLG and graphite using experimental methods. 132

Table D1. Cohesion energy of carbon nanotubes, few-layer graphene, and graphite.......... 136

Table D2. Comparisons between calibrated stiffness of probes reported by Koren et al. [124] and the present work. 137

Table D3. Interlayer adhesion energy of carbon nanotubes, few-layer graphene, and graphite on SiO_x. 138

Table D4. Interlayer adhesion energy of MoS_2 on SiO_x. 138

LIST OF APPENDICES

APPENDIX A **114**
Dielectric Constant of a Single-Walled Carbon Nanotube **114**

APPENDIX B **115**
Electrostatic Charge Distribution in FLG Systems **115**
B1 Electrostatic Fringe Field Effects in Graphene Flake 115
B1.1 Circular graphene flake 115
B1.2 Graphene nanoribbon 117
B1.3 Rectangular/square graphene flakes 117
B2 Non-Uniform Fermi Energy Profile 118
B3 Fermi Level Profiles in *N*-Layer Graphene 119
B4 Local and Global Interlayer Charge Screening 119
B5 Temperature-Dependent Discrete Model 121

APPENDIX C **122**
Atomistic Simulations in FLG Systems **122**
C1 Atomistic Simulation Setup 122
C1.1 Description of intralayer carbon–carbon interactions 122
C1.2 Description of interlayer carbon-carbon interactions 122
C1.3 LJ potential vs. RD potential for vdW interaction of FLG 123
C1.4 Description of SiO_2 substrate 125
C1.5 Description of graphene/SiO_2 interface 125
C2 Charge Distribution and Fermi Profiles in a 8-LG System 127
C2.1 Charge density/Fermi level profiles of 8-LG 127
C2.2 Layer-by-layer charge distribution in 8-LG 129
C2.3 Effective interlayer screening: 129
C2.4 Charge distribution in rectangular graphene flakes 130

C3 Configuration-Dependent Interlay Mechanical Properties of FLG 131
C3.1 MD simulations of interlayer mechanical properties of FLG 132

APPENDIX D 135
Interfacial Adhesion Energy of 2D Materials and vdW Heterostructures 135
D1 Comparative Studies of Interfacial Adhesion Energy 135
D1.1 Comparison study on cohesion energy of 2D crystal homostructures 135
D1.2 Comparison study on interfacial adhesion energy of 2D crystal/SiO_x 138
D2 Effect of Tilt Angle on Interfacial Adhesion Energy Measurements 138
D3 Static Spring Constant Calibration 140
D3.1 Spring constant calibration under a normal load at the apex 141
D3.2 Spring constant calibration under an axial load at the apex 145
D4 Calculation of Bending Stiffness in 2D Crystals 146
D5 Molecular Dynamics Simulations of G/SiOx Heterostructure 146

ABSTRACT

Two-dimensional layered materials (2DLMs), such as ultrathin graphite (G), hexagonal boron nitride (hBN), transition metal dichalcogenides (e.g., molybdenum disulfide MoS_2), and their newly-emerged van der Waals (vdW) heterostructures with strong in-plane covalent bonding but weak interlayer vdW bonding exhibit a unique combination of high elasticity, extreme mechanical flexibility, visual transparency, and superior (opto)electronic performance, making them ideally suited to modern (bio/opto)electronic devices. Since intrinsic ultrahigh surface to volume ratio in 2DLMs dictates an extremely strong and dominant vdW force in many processes related to not only synthesis, transfer and manipulation of 2DLMs but also fabrication, integration and performance of 2DLMs-based devices, precise nanoscale quantification of their weak interlayer vdW bonding is of fundamental, theoretical and technological importance for the large-scale production of such promising materials and continued development of flexible and transparent electronics incorporating these materials. Although physical and chemical properties of similar and dissimilar 2DLMs associated with in-plane covalent bonds are well studied both experimentally and theoretically, an extensive atomic and nanoscale characterization of their interlayer vdW-dependent properties (e.g., interfacial charge transfer/distribution, interfacial adhesion energy, etc.) is still a great challenge due to the highly anisotropic nature of weak interlayer vdW interactions, the lack of precise experimental techniques to quantify such complex interlayer behavior and difficult mechanical manipulation of ultrathin and highly transparent 2DLMs.

This dissertation aims to address these inherent challenges by developing a novel atomic force microscopy (AFM)-assisted manipulation setup with ultrahigh force-displacement resolution combined with multiscale modeling at atomistic and continuum levels to advance our fundamental understanding of nanoscale interlayer electrostatic and vdW behavior of 2DLMs and their heterostructures. We first develop, in a collaborative project, highly–efficient and clean plasma–assisted exfoliation and nanoimprint–assisted shear exfoliation techniques to

produce large–scale, ordered graphene and MoS_2 device arrays at micro and nanoscale. Then, in order to gain a deeper insight into the interlayer vdW interactions of 2DLMs during the exfoliation process, I qualitatively study the mechanical response of interlayer vdW interactions to external shear or normal forces by gently moving an *in situ* flattened, conductive AFM tip with an attached 2D crystal nanomesa away from the substrate in a direction parallel or normal to the basal plane of 2D crystals, followed by shear and normal exfoliation of high-quality mono- and few-layer 2D crystal features onto the substrate. My experimental observations show that in contrast to the shear exfoliation technique, the normal exfoliation technique exhibits a very stochastic exfoliation process. This unique nanoscale manipulation setup with ultrahigh force-displacement resolution allows producing The University of Michigan's thinnest possible logo by only mono-, bi- and trilayer G flakes.

To investigate the atomistic details underlying my AFM-assisted shear/normal electrostatic exfoliation mechanisms, I first study the electrostatic response of interlayer vdW interactions of few-layer graphene (FLG) to the external electric field using DC electrostatic force microscopy (DC-EFM). A series of dielectric measurements on one-to-eight layers of graphene under ambient conditions show that although dielectric screening ability of monolayer graphene is about 20% weaker than that of bulk graphite, the overall dielectric response of FLG samples is almost independent of the number of layers and external electric field. Next, I exploit the layered nature of FLG to develop a novel spatial discrete model that successfully accounts for both electrostatic screening and fringe field effects on the charge distribution of FLG systems. My spatial charge distribution model shows that the overall dielectric response of FLG samples is almost independent of the number of layers and the external electric field, which is well consistent with my DC-EFM results.

Next I implement, for the first time, 3D spatial charge distribution of FLG (obtained from the proposed spatial discrete model) into molecular dynamics (MD) simulations to further gain an atomistic insight into the electrostatic shear/normal exfoliation mechanisms. My MD analysis of the simulation trajectories suggests that the coexistence of local delamination and interlayer twist in FLG is the main barrier to the accurate control of the number of exfoliated layers using the normal exfoliation technique. Instead, the ability of the shear exfoliation method to eliminate the interlayer spacing variations and simultaneously suppress the interlayer twist angles (due to

the larger interlayer potential corrugation) provides much better control over the desired number of the exfoliated flakes, making it superior to the normal exfoliation method.

As the last piece in the puzzle of understanding the interlayer behavior of 2DLMs, I report the first direct quantitative characterization of interfacial adhesion behavior of both fresh and aged vdW homointerfaces (G/G, hBN/hBN and MoS_2/MoS_2) and heterointerfaces (G/hBN, hBN/MoS_2, G/MoS_2, G/SiO_x, hBN/SiO_x and MoS_2/SiO_x) under different temperatures and humidity conditions through very well-defined interactions between AFM tip-attached 2D crystal nanomesas and different 2D crystal and SiO_x substrates. I precisely control the temperature of nanocontact interfaces in the range of -15–300°C by microheaters on the top and a cooling stage underneath the substrate. I also quantify how different levels of short-range dispersive (vdW) and long-range electrostatic (Coulombic) interactions of similar and dissimilar 2D crystals will respond to airborne contaminants and humidity upon thermal annealing. My measurements reveal highly stronger interactions in transition metal dichalcogenides than predicted by well-established first-principles calculations. Moreover, my combined experimental and MD computational analysis show the formation of short-range chemical bonds only in G/SiO_x heterostructures, which explains mechanistic origin of their distinctive ultrastrong adhesion behavior beyond the widely accepted vdW interaction.

CHAPTER 1

Introduction

1.1 2D Layered Materials and vdW Heterostructures

Two-dimensional layered materials (2DLMs), such as conducting graphene (G), insulating hexagonal boron nitride (hBN), transition metal dichalcogenides (TMDCs: e.g., semiconducting molybdenum disulfide (MoS_2) and so many others) and their newly emerged vdW heterostructures (stacks of individual monolayer flakes of different 2DLMs assembled layer by layer) possess strong in-plane covalent bonds but very weak out-of-plane van der Waals (vdW) interactions (**Figure 1.1**). Such a distinct class of anisotropic solids exhibit a unique combination of high elasticity, extreme mechanical flexibility, visual transparency, and superior (opto)electronic performance, making them ideally suited to modern devices, such as photovoltaic devices, hybrid electrochemical capacitors, lithium– and sodium–ion batteries, hydrogen evolution catalysis, transistors, photodetectors, DNA detection, memory devices and flexible and transparent devices [1].

Mechanical properties of 2DLMs associated with their in-plane covalent bonds are well studied both experimentally and theoretically and there is a broad consensus on the reported in-plane stiffness, breaking strength and elastic deformation of 2DLMs. A direct measurement of

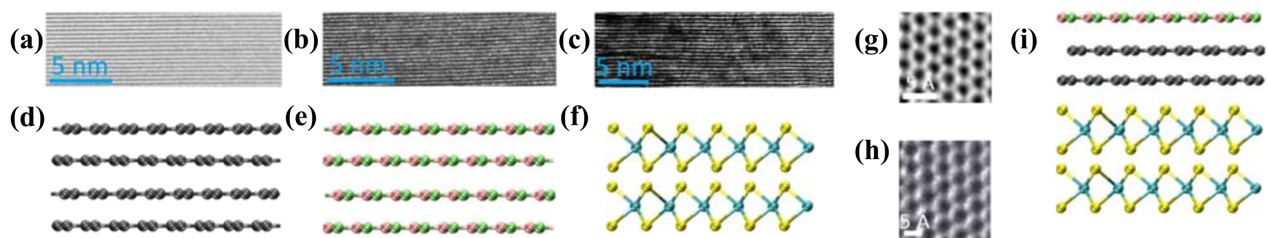

Figure 1.1. Side-view high-resolution TEM images of (a) G, (b) hBN and (c) MoS_2 crystals, showing interlayer vdW interactions with an interlayer separation of 0.335 nm, 0.333 nm and 0.655 nm, respectively. (d)-(f) illustrate the corresponding ball-and-stick representation of G, hBN and MoS_2 crystals where carbon, boron, nitrogen, molybdenum, and sulfur atoms are shown in gray, green, pink, cyan, and yellow, respectively. Top-view high-resolution TEM images of (g) G and (h) MoS_2 crystals, showing strong in-plane covalent bonds. Lattice structure in G is similar to hBN with only slightly shorter (~1.8%) lattice constant. (i) Ball-and-stick representation of hBN/G/MoS_2 heterostructures.

Young's modulus and fracture strength of monolayer and few-layer G [2], hBN [2] and MoS_2 [3] is reported by AFM nanoindentation of suspended 2D crystal membranes (**Table 1.1**), indicating that G is the strongest 2DLMs, followed by hBN and MoS_2. This table also suggests that the Young's modulus and fracture strength of MoS_2 (as the weakest 2D crystal in **Table 1.1**) are still larger than those of stainless steel (i.e., 210 GPa and 0.9 GPa, respectively), making G, hBN and MoS_2 promising materials for novel flexible and wearable electronic and photonic applications. Monolayers of G, hBN and MoS_2 can sustain elastic deformation up to 20%, 17%, and 11%, respectively, without any fracture [2], thanks to the strong in-plane covalent bonds in 2DLMs.

2DLMs also offer a wide range of electronic properties. For instance, monolayer and few layers of G exhibit a unique band structure featuring massless Dirac Fermions. The transport of such Dirac Fermions is partially immune to the scattering induced by the defects in G layers. This transport property could be exploited for making new-generation low-power dissipation electronic devices. While the lack of band gap has limited some of the applications of G, transition metal dichalcogenides such as MoS_2 and WSe_2 offer new alternatives to designing semiconducting materials. The bandgap of MoS_2 can be modulated from the direct to indirect bandgap through changing the MoS_2 flake thickness (or the number of stacked layers). In particular, monolayer MoS_2 has a direct bandgap of ~1.8 eV, whereas multilayer MoS_2 has an indirect bandgap of ~0.9 eV [4]. Such a transition behavior from the indirect to direct bandgap and other layer-thickness-dependent optoelectronic properties has motivated a series of research efforts, seeking to create new optoelectronic devices with tunable transport and photoresponse characteristics. The isoelectric equivalent of graphene, hBN (so called white graphene), is an insulator with an indirect bandgap of 5.955 eV. It also exhibits unique electronic properties such as low dielectric constant (~2–4), high thermal conductivity, and chemical inertness. With a honeycomb structure based on sp^2 covalent bonds similar to G, bulk hBN has first gained tremendous attention as an exceptional substrate for other 2DLMs with an atomically smooth surface. hBN in the form of few-layer crystals or monolayers of hBN, has then appeared as a fundamental building block of vdW heterostructures.

Table 1.1. Comparison of Young's modulus (E) and fracture strength (σ_f) of monolayer and few-layer G, hBN and MoS_2 using AFM nanoindentation of suspended 2D crystal membranes.

# of layers	G [2]		hBN [2]		MoS_2 [3]	
	E (GPa)	σ_f (GPa)	E (GPa)	σ_f (GPa)	E (GPa)	σ_f (GPa)
Monolayer	1026±22	125±0.0	865±73	70.5±5.5	270±100	22±4
Few layers	942.0±3	85.3±5.4	856±3	72.3±2.5	260±70	21±6

1.2 Large-Scale Production of 2DLMs-Based Devices

In general, fabrication of 2D systems involves transferring 2DLMs from their growth substrate or bulk stamp onto a target substrate using different transfer–printing techniques. An intrinsic weak vdW interaction between neighboring layers allows 2DLMs to be easily sheared parallel and/or expanded normal to the layer surface, leading to the generation of so-called atomically thin layered materials (ATLMs) with few-layer down to monolayer thickness. ATLMs display unique electrical, mechanical, electrochemical, and optical properties that are not essentially observed in their bulk layered counterparts. Therefore, over the past decade, two distinct strategies have been pursued for the production of ATLMs: a top-down and a bottom-up approach. The former generally aims at overcoming the vdW forces between the adjacent layers for the exfoliation of ATLMs from their bulk crystals through mechanical (e.g., Scotch tape exfoliation), chemical (e.g., liquid phase exfoliation), and electrochemical (e.g., ion/compound intercalations) processes (**Figure 1.2**) [5]. On the other hand, the bottom-up method depends on the chemical reaction of molecular building blocks to form covalently linked 2D networks by means of catalytic (e.g., chemical vapor deposition, CVD), thermal (e.g., epitaxial growth), or chemical (organic synthesis) processes [5]. Since ATLM samples with transfer-induced residues and randomly distributed nanoflakes (mainly due to the formation of defects and grain boundaries during the growth process) are inevitable in the bottom–up method, it can be expected that the highest quality samples are still produced by the top-down methods. Despite rapidly growing demands for mass production of high-quality 2DLMs–based electronic device arrays at micro and nanoscales, appropriate mechanical exfoliation techniques to meet such demands are still lacking.

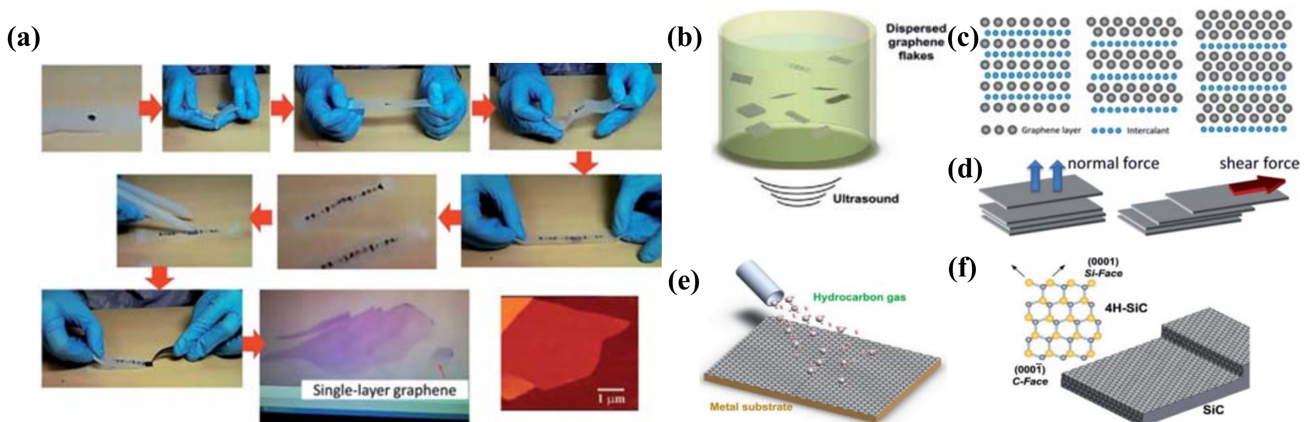

Figure 1.2. Top-down exfoliation approach: (a) Scotch tape, (b) liquid phase and (c) ion/compound intercalations. (d) External normal and shear forces for the exfoliation. Bottom-up approach: (e) CVD and (f) epitaxial growth.

1.3 Significance of Interlayer vdW Interactions in 2DLMs and vdW Heterostructures

Since intrinsic ultrahigh surface to volume ratio in 2DLMs dictates an extremely strong and dominant vdW force in many processes related to not only synthesis, transfer and manipulation of 2DLMs but also fabrication, integration and performance of 2DLMs-based devices, a deep insight into their weak interlayer vdW interactions is of fundamental, theoretical and technological importance for the large-scale production of such promising materials and continued development of flexible and transparent electronics incorporating these materials.

Recent studies have shown that monolayer and few layers of 2DLMs reveal unique friction, interfacial charge screening, lithium ion intercalation, quantum capacitance and electrical conductivity properties that are not essentially observed in their bulk crystals [5]. However, turning the bulk crystals into monolayer and few layers with an accurate control over the number and quality of exfoliated layers requires precise quantitative characterization of interlayer vdW behavior of 2DLMs and vdW heterostructures at the nanoscale. As also discussed in **Section 1.2**, in order to fabricate 2DLM systems, individual or combined external normal and lateral shear forces in a direction, respectively, perpendicular or parallel to the basal plane of 2DLMs are required to overcome the internal vdW forces between the adjacent layers or between 2DLMs and their supporting substrates. As a result, a better understanding of weak interlayer vdW interactions of 2DLMs and also their interactions with various substrates is highly desired as an essential step toward enhancing the transfer efficiency and thickness uniformity of printed flakes and thus producing high–quality, large–scale 2DLMs–based electronic device arrays at micro and nanoscales. Moreover, the vdW interaction between 2DLMs and their neighbors is also an important parameter for the mechanical integrity of the device whose operation is highly influenced by slippage and delamination of 2DLMs during thermal and mechanical loadings. As such, a 2DLM needs to make secure contact not only with supporting substrates and metallic interconnects in 2DLMs–based devices but also with other 2DLMs and encapsulation layers in vdW heterostructure devices [6, 7].

Newly emerged vdW heterostructures – stacks of individual monolayer flakes of different 2DLMs assembled layer by layer, conceptualized from 2D Lego pieces – offer a variety of new physical properties that may not exist in nature, thanks to the full spectrum of electronic properties in 2DLMs, from conducting G, to semiconducting MoS_2, to insulating hBN. An essential feature of such heterostructures is atomically clean interfaces to achieve the best device

performance – any interfacial contamination (e.g., blisters) results in deterioration of transport properties [8]. Wet transfer and dry pick-and-lift transfer techniques for assembly of vdW heterostructures rely strongly on vdW interactions between the 2D crystals where the polymer membrane with an attached 2D crystal is brought into contact with another 2D crystal on a substrate. If the second 2D crystal has strong adhesion to the substrate, the first crystal is released by the carrier membrane and deposited on top of the second crystal, otherwise the second crystal is picked up by the first crystal attached to the membrane, followed by the deposition of the fully attached stack onto a final substrate by dissolving the carrying membrane [9]. In both direct mechanical assembly techniques, an accurate quantification of vdW interactions between different 2DLMs is crucial for the mass production of blister–free vdW hetersostructures. One example of the importance of clean interlayer vdW interactions in vdW hetersostructures is the field-effect tunneling transistor (FETTs). In this type of transistors, G electrodes are separated by few-layer MoS_2 or hBN. Because of the clean and weak interlayer interactions, the insulating 2DLMs behaves purely as a tunneling barrier with length equivalent to the thickness of the flake. Hence, FETTs possess fast transfer kinetics due to tunneling, nanometer scale morphology appropriate for advanced technological applications and an on/off ratio of 10^6 at room temperature [10, 11].

Fascinating interlayer vdW-dependent properties of 2DLMs and their vdW heterostructures provide a unique opportunity to study the nature of electronic structure and band alignment, interfacial thermal and electrical resistance, ion intercalation and deintercalation process, interfacial nanofluidic transport and drug delivery behavior, photon absorption and photocurrent/photovoltaic production, interfacial charge polarization and redistribution, spin–orbit coupling and many others in 2DLMs-based devices [12, 13, 14, 15, 16]. Notably, interfacial electrical, mechanical, optoelectronic, magnetic and thermal properties of layered materials can also interact in a rather complex way. For instance, formation of any delamination-motivated surface corrugations (e.g., wrinkles, ripples, folds, and crumples) in 2DLMs can give rise to local strain distribution and curvature-induced rehybridization, which modify the electronic structure and local charge distribution, create polarized carrier puddles and dipole moment, induce pseudomagnetic fields and thus alter magnetic, optical and electrical properties and chemical surface reactivity [17]. Moreover, the vdW interaction as a key medium for the stress transfer both within and across the interface of 2DLMs can highly impact their thermal and electrical

properties in such a way that a 2D layered system can act as a heat conductor or insulator and/or a semimetal or electrical insulator through strain engineering [18, 19, 20]. The interfacial physical and chemical behavior of layered materials becomes even more complicated when we consider that airborne contaminants are an inevitable part of any vdW heterostructures and therefore addressing quantitatively to what degree their interlayer vdW interaction is influenced by interfacial contaminants and nanoblisters and how to effectively remove them is of fundamental importance for the continued development of such promising materials.

Despite the significance of such a fundamental property for any 2DLMs, an extensive atomic and nanoscale characterization of their interlayer vdW-dependent physical properties has still remained to be elucidated. The main difficulties in exploring the interlayer electrostatic and mechanical properties of layered materials are related to (1) the highly anisotropic nature of the vdW interactions which makes their modeling more challenging; (2) the lack of precise experimental techniques to quantify such complex interlayer behavior; and (3) the sub to few–nanometer thickness and high transparency of mono and few layers of 2D materials which make them much more difficult to be detected for the mechanical manipulation and subsequent physical measurements.

1.4 Summary of Dissertation

As a means to address the inherent challenges discussed in **Sections 1.2** and **1.3**, this thesis aims at developing a novel atomic force microscopy (AFM)-assisted experimental technique with an exceptionally high force-displacement resolution combined with atomistic- and continuum-based simulations to directly and precisely measure the interlayer electrostatic and vdW properties of 2DLMs and their vdW heterostructures, which have remained elusive for decades. **Chapter 2** and **Chapters 3-5** aim to provide a reliable basis to fill the apparent gap discussed in **Section 1.2** and **Section 1.3**, respectively.

To fill the apparent gap discussed in **Section 1.2**, we first develop, in a collaborative project, two economic, highly–efficient and clean exfoliation techniques (termed plasma–assisted exfoliation and nanoimprint–assisted shear exfoliation) to produce large–scale, ordered G and MoS_2 device arrays at micro and nanoscale. Then, in order to gain a deeper insight into the interlayer vdW interactions of 2DLMs during the exfoliation process, I qualitatively study the mechanical response of interlayer vdW interactions to external shear or

normal forces by gently moving an in-situ flattened, conductive AFM tip with an attached 2D crystal nanomesa away from the substrate in a direction parallel or normal to the basal plane of 2D crystals, followed by shear and normal exfoliation of high-quality mono- and few-layer 2D crystal features onto the substrate. I reliably produce high-quality mono- and few-layer crystal features of different shapes and sizes at significant yields by shear exfoliation method. My experimental observations show that in contrast to the shear exfoliation technique, the normal exfoliation technique exhibits a very stochastic exfoliation process. This unique nanoscale manipulation setup with ultrahigh force-displacement resolution allowed me to successfully produce The University of Michigan's thinnest possible logo by only mono-, bi- and trilayer graphene flakes (**Chapter 2**).

To investigate the atomistic details underlying my AFM-assisted shear/normal electrostatic exfoliation mechanisms, I first study the electrostatic response of the interlayer vdW interactions of few-layer graphene (FLG) to the external electric field. To do so, I quantify, for the first time, the effect of layer number and external electric field (up to my experimental limit of 0.1 V/Å) on the relative dielectric constant of FLG using a DC electrostatic force microscopy (DC-EFM) technique. I perform a series of dielectric measurements on the one-to-eight layers of G under ambient conditions and successfully show that although the dielectric screening ability of monolayer graphene is about 20% weaker than that of bulk graphite, the overall dielectric response of few-layer graphene samples is almost independent of the number of layers and the external electric field. Next, I exploit the layered nature of FLG to develop a novel spatial discrete model that successfully accounts for both electrostatic screening and fringe field effects on the charge distribution of the finite-size FLG system. An effective bilayer model based on two tight-binding parameters is utilized to accurately describe electronic band structures and thus density of states (DOS) of one to eight Bernal-stacked graphene layers. I then explore the unclear relationship between the gate-induced charge densities and layer-by-layer Fermi level and charge density profiles in FLG systems using a global energy minimization, where its total energy is calculated based on electrostatic interaction between graphene layers and band-filling energy in each layer. My spatial charge distribution model shows that the overall dielectric response of FLG samples is almost independent of the number of layers and the external electric field, which is well consistent with my DC-EFM results (**Chapter 3**).

Next I implement, for the first time, 3D spatial charge distribution of FLG (obtained from the proposed spatial discrete model) into molecular dynamics (MD) simulations to further gain an atomistic insight into the electrostatic shear/normal exfoliation mechanisms. My MD analysis of the simulation trajectories suggests that the coexistence of local delamination and interlayer twist in FLG is the main barrier to the accurate control of the number of exfoliated layers using the normal exfoliation technique. Instead, the ability of the shear exfoliation method to eliminate the interlayer spacing variations and simultaneously suppress the interlayer twist angles (due to the larger interlayer potential corrugation) provides much better control over the desired number of the exfoliated flakes, making it superior to the normal exfoliation method (**Chapter 4**).

As the last and most important piece in the puzzle of understanding the interlayer vdW interactions of 2DLMs, I provide an accurate nanoscale quantitative (rather than qualitative) description of interlayer mechanical behavior of 2DLMs and their vdW heterostructures. I use the AFM-assisted nanomanipulation setup to report precise *in situ* measurements of interfacial adhesion energy through well-defined interactions between AFM tip-attached 2D crystal nanomesas (G, hBN and MoS_2) and mechanically exfoliated 2D crystal flakes and also the bare SiO_x substrate (as the most widely used substrate in modern electronics). Moreover, since airborne contaminants are an inevitable part of any vdW heterostructures, addressing quantitatively to what degree their interfacial adhesion energy is influenced by the interfacial contaminants and how to effectively remove them is of fundamental and technological importance for the continued development of such promising materials. As such, I report the first direct quantitative characterization of interfacial adhesion behavior of both fresh and aged vdW homointerfaces (G/G, hBN/hBN and MoS_2/MoS_2) and heterointerfaces (G/hBN, hBN/MoS_2, G/MoS_2, G/SiO_x, hBN/SiO_x and MoS_2/SiO_x) under different annealing temperatures (up to 300°C). I precisely control the temperature of nanocontact interfaces using microheaters. I quantify how different levels of short-range dispersive (vdW) and long-range electrostatic (Coulombic) interactions of similar and dissimilar 2DLMs will respond to airborne contaminants and humidity upon thermal annealing. My measurements reveal highly stronger interactions in transition metal dichalcogenides than predicted by well-established first-principles calculations. Similarly, my combined experimental and computational analysis shows a distinctive interfacial behavior in G/SiO_x heterostructures beyond the widely accepted vdW interaction (**Chapter 5**).
I conclude with a summary and outlook for the future of this and related work (**Chapter 6**).

CHAPTER 2

Nanofabrication of 2DLMs Device Arrays Using Mechanical Exfoliation Techniques

2.1 Introduction

Owing to their excellent electronic, photonic and mechanical properties, large natural abundance on the earth, as well as good compatibility to planar nanofabrication processes, the atomically layered transition metal dichalcogenides (TMDCs) (e.g., WSe_2 and MoS_2) have recently emerged as attractive material candidates to potentially enable a variety of novel functional devices with high cost efficiency [4]. A series of new prototype devices based on TMDC layers have been demonstrated in the research laboratories, such as high-performance thin-film transistors (TFTs) [21], highly sensitive chemical/biological sensors [22], phototransistors [23], multibit non-volatile transistor memories [24], and photovoltaic (PV) devices with high quantum efficiencies [25], etc. To leverage the superior electronic/photonic characteristics of such devices for practical scale-up applications, the research community currently needs new nanomanufacturing methods capable of producing TMDC device arrays with deterministic and uniform properties. A great deal of recent research effort focuses on the attractive properties associated with monolayer TMDC structures, such as direct bandgaps, which are suitable for lightemitting applications [26], strong valley-selective circular dichroism, which can potentially enable future low-energy-dissipation valleytronic devices [27], as well as atomic scale thicknesses that represent the ultimate scaling of material dimension in the vertical direction and can potentially enable miniaturization of electronic devices beyond Moore's Law. Therefore, there have been many material-synthesis-oriented works seeking to product TMDC monolayers over large areas. In spite of such intensive effort related to monolayers, many important nanoelectronic/optoelectronic applications, such as transistor-based memories/sensors [28], photovoltaics [29], and power switching TFTs [30], indeed demand high-quality multilayer TMDC structures, because multilayer structures can provide excellent transport properties (e.g., relatively high mobility) and sizable densities/amounts of electronic/photonic states, enabling

device applications that need to drive large current/voltage signals or absorb a large amount of photons [31]. However, currently there are very few research efforts dedicated to fabricate high-quality multilayer TMDC structures with a high uniformity of thickness and electronic/photonic properties over large areas. Especially, the research society needs the upscalable production technology of multilayer TMDC device arrays or large-scale circuits.

In this chapter, we first present two top-down nanofabrication approaches (termed plasma–assisted exfoliation and nanoimprint–assisted shear exfoliation) capable of producing pristine multilayer MoS_2 and G fake arrays with a high uniformity of flake thicknesses over cm^2-scale areas. Using the as-produced MoS_2 flakes, we also demonstrate multiple working transistors and electronic biosensors which exhibit very consistent performance. Then, in order to gain a deeper insight into the interlayer vdW interactions of 2DLMs during the exfoliation process, I qualitatively study the mechanical response of interlayer vdW interactions to the external shear or normal forces by gently moving an in-situ flattened, conductive AFM tip with an attached 2D crystal nanomesa away from the substrate in a direction parallel or normal to the basal plane of 2D crystals, followed by shear and normal exfoliation of high-quality mono- and few-layer 2D crystal features onto the substrate.

2.2 Plasma-Assisted Exfoliation of MoS_2 Flakes into Large-Area Arrays

Figure 2.1(a) schematically illustrates our approach for transfer printing prepatterned MoS_2 flakes. The fabrication process consists of the following steps. (1) The process starts with a piece of pristine bulk MoS_2. (2) Photolithography is performed to pattern a photoresist layer spin-coated on top of the MoS_2 surface. (3) Arrays of metal masks are created by depositing 100nm Ti followed with lift-off in acetone. (4) SF_6-based reactive ion etching (RIE) is performed to transfer the Ti mask pattern onto underlying MoS_2 [29-31]. (5) Ti masks are completely removed in hydrofluoric (HF) acid, and a bulk MoS_2 stamp is created. (6) A SiO_2 substrate is treated with O_2 plasma to generate electric charges on the surface [32]. (7) Finally, the bulk MoS_2 stamp is used for printing out MoS_2 flake arrays onto the SiO_2 substrate. This process can generate MoS_2 device patterns directly from pristine geographic MoS_2 materials that have the largest crystalline domains (typically, 1 to 100's μm size) and the best electronic properties to date [24-26]. Further, this approach can be generalized for manufacturing other emerging

atomically layered nanomaterials such as graphene, boron nitride, and topological insulator thin films.

Figure 2.1(b) shows SEM of an exemplary MoS_2 stamp prepatterned with 5 μm size, 600nm high pillars. The zoomed view in **Figure 1(b)** shows that the SF_6 plasma etched area exhibits a relatively high roughness, which is attributed to plasma etching or ion bombardment. However, the raised pillar mesas protected by the Ti masks are still as smooth as a pristine MoS_2 surface. This should yield a conformal contact with the flat substrate during a mechanical printing process and therefore a high transfer-printing efficiency of MoS_2 flakes.

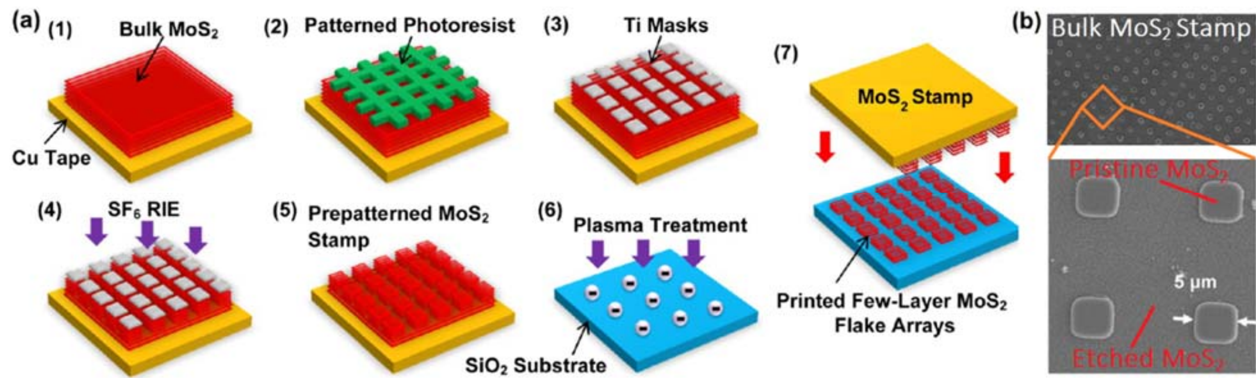

Figure 2.1. (a) Schematic flowchart of transfer printing of prepatterned few-layer MoS_2 flakes, which includes (1) initial bulk MoS_2 with a pristine surface; (2) photolithography for patterning device features; (3) formation of Ti masks by metal deposition followed by lift-off; (4) plasma etching of underlying MoS_2; (5) removal of Ti masks and finalization of a bulk MoS_2 stamp bearing relief features; (6) plasma treatment of the SiO_2 substrate; (7) direct transfer printing of prepatterned few-layer MoS_2 flakes onto the substrate. (b) SEM images of a bulk MoS_2 stamp prestructured with 5 μm size periodic pillars.

Figure 2.2(a) displays SEM images of MoS_2 flakes printed on a pristine SiO_2 surface. These images, captured over a large printed area (~1 cm^2), show that the mechanical printing process can produce large-area, orderly paved arrays of MoS_2 pixel features. However, most of the printed pixels have relatively irregular edge profiles that are not faithfully correlated to the edge profiles of pillars prestructured on the bulk stamp. For each of the printed MoS_2 pixels, the average flake thickness was extracted from AFM topographic data. **Figure 2.2(b)** plots the statistical distribution of the average thickness data of 100 MoS_2 flake pixels of 10 μm size produced in a single transfer-printing cycle. **Figure 2.2(b)** shows that the overall average flake thickness is measured to be 4.1 nm (~6 monolayers), and the standard deviation is 2.2 nm (~3 monolayers) over a ~1 cm^2 area. About 95% and 80% of printed MoS_2 flakes are thinner than 10 and 5 nm, respectively.

Figure 2.2(c) shows an SEM image of MoS_2 patterns printed onto an O_2 plasma-charged SiO_2 substrate, indicating that the printing process on plasma-charged substrates can produce large-area, orderly arranged arrays of MoS_2 flake pixels with a higher uniformity of pixel profiles in comparison with the printing result on a pristine substrate. In particular, MoS_2 pixel patterns feature clear, well defined edge profiles that are faithfully correlated to the edge profiles of pillars prestructured on the bulk stamp. The zoomed image in **Figure 2.2(c)** reveals that the clear edge profile of a MoS_2 pixel is indeed made up of a ring-shaped MoS_2 ribbon. Such outer edge ribbons of MoS_2 pixels have widths ranging from 200 to 400 nm. Besides these edge ribbon features, there are indeed thinner MoS_2 films or flakes located in the inner regions of printed pixels enclosed by the edge ribbons. These inner MoS_2 flakes typically exhibit a poor feature contrast in secondary-electron images. To enhance the SEM contrast, printed MoS_2 pixels were also imaged by detecting backscattered electrons (BSEs), as shown in **Figures 2.2(d)** and **(e)**, which are often used to detect contrast between areas with different chemical compositions. The BSE image contrast in **Figures 2.2(d)** and **(e)** suggests the presence of thin MoS_2 flakes within each of the pixels. To obtain the inner flake thickness data, MoS_2 pixels with partially broken inner films (e.g., the pixels shown in **Figure 2.2(e)**) were imaged by using AFM, and the thickness of an inner MoS_2 flake was measured from its broken edges.

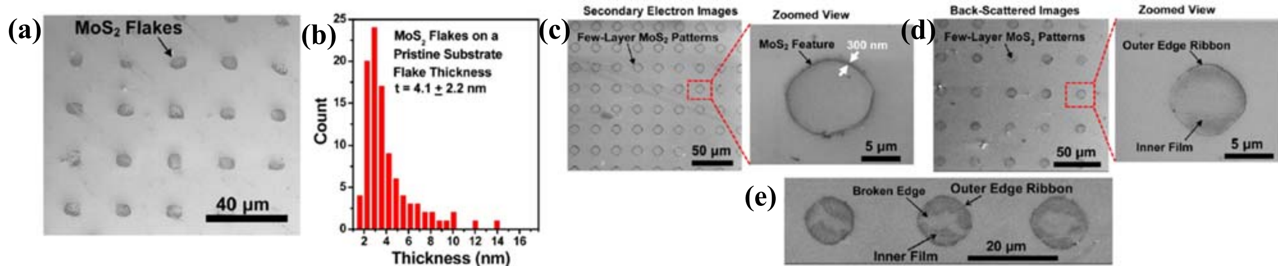

Figure 2.2. (a) SEM image of arrays of 10 μm size MoS_2 flake pixels printed onto a pristine SiO_2 substrate. (b) Stacked column chart of the average thickness data collected from 100 as-printed MoS_2 pixels. The thickness data were obtained from MoS_2 pixels printed over a $\sim$1cm^2 area by using an AFM. (c) Secondary-electron SEM images of MoS_2 pixel arrays printed onto an O_2 plasma-charged substrate, which exhibit clear, well-defined edge profiles faithfully correlated to the edge profiles of pillar features on the bulk MoS_2 stamps. (d) Backscattered SEM images of MoS_2 pixel arrays, which show the presence of thin inner MoS_2 flakes within each printed pixel. (e) Backscattered image of MoS_2 pixels with broken inner films.

Figure 2.3(a) displays an AFM image of an exemplary MoS_2 pixel consisting of a relatively thick edge ribbon and broken inner flakes. The scan line denoted by the solid line and accordingly plotted in **Figure 2.3(b)** explicitly displays that the thickness values measured at the

left and the right sides of this outer edge ribbon are 7 nm (~11 monolayers) and 8 nm (~12 monolayers), respectively; the thickness of the broken inner flakes is measured to be 2.4 nm(~4 monolayers). The thickness data acquired from 10 scan lines are used to calculate the average thickness of the inner film and the outer edge ribbon of an individual MoS_2 pixel. **Figure 2.3(c)** plots the statistical distribution of the average thickness data of 100 MoS_2 pixels printed on a plasma-charged substrate. Here, the thickness data of inner films (solid columns) and outer edge ribbons (blue hatched columns) of MoS_2 pixels are separately plotted. **Figure 2.3(c)** shows that the overall average thickness of outer edge ribbons is 17 nm (~26 monolayers) with a standard deviation of 3 nm (~5 monolayers), whereas the overall average thickness of inner films is 3.0 nm (~5 monolayers) with a standard deviation of 1.9 nm (~3 monolayers). About 90% of inner flakes of MoS_2 pixels printed on a plasma-charged SiO_2 substrate are thinner than 5 nm (~8 monolayers). On the basis of such SEM and AFM characterizations, it is concluded that microscale MoS_2 pixels printed on a plasma-charged SiO_2 surface feature relatively thinner inner films or flakes enclosed by relatively thicker ring-shaped edge ribbons and a higher percentage yield of few-layer MoS_2 flakes thinner than 5 nm in comparison with pixels printed on a pristine SiO_2 substrate.

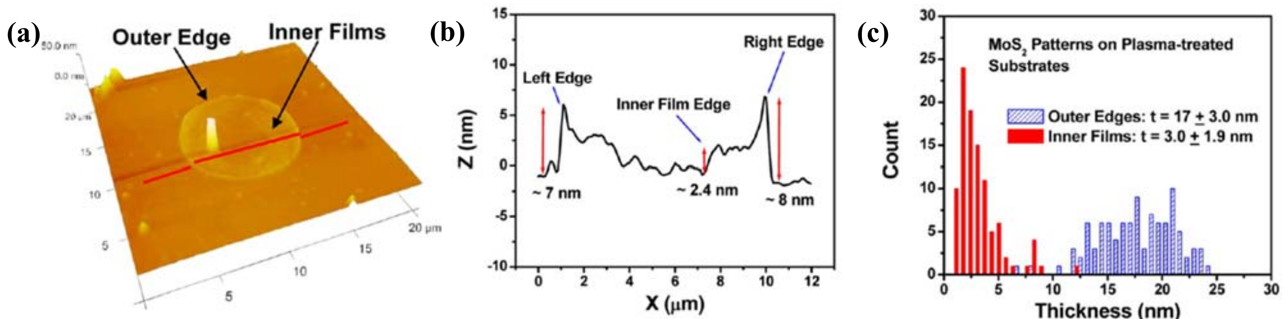

Figure 2.3. (a) AFM image of a 10 μm size MoS_2 pixel printed on a plasma-charged SiO_2 substrate. The solid line indicates a scanning trace across the pixel, which is explicitly plotted in (b). (c) Stacked column chart of the average thickness data collected from 100 as-printed MoS_2 pixels. Here, the thickness data acquired from the inner flakes (solid columns) and the outer edge ribbons (hatched columns) of these MoS_2 pixels are separately plotted.

To obtain a preliminary understanding of plasma-assisted printing mechanisms responsible for the resultant morphology of MoS_2 pixels, Maxwell stress tensor calculation was performed and used for evaluating the distribution of surface charge-induced electrostatic attractive stress between the bulk MoS_2 stamp and the dielectric substrate. **Figure 2.4(a)** illustrates the 2-D model for the calculation, in which a plasma-charged SiO_2 substrate is in

contact with a bulk MoS_2 stamp and the surface charge density is arbitrarily set to 0.05 C/m^2. **Figure 2.4(b)** plots the calculated attractive stress exerted by the plasma-charged SiO_2 substrate on the bulk MoS_2 stamp as a function of positions. **Figure 2.4(c)** shows the zoomed view of the attractive stress distribution within a single MoS_2 mesa in contact with a SiO_2 surface. It is found that the attractive stress acting on a microscale MoS_2 mesa is uniform in the central region of the mesa but is significantly increased along the mesa edges due to the fringe effect. During a transfer-printing process, such high attractive stress at the mesa edges is expected to result in the exfoliation of MoS_2 flake pixels with well-defined edges, as experimentally demonstrated. In addition, the strong electric field at the MoS_2/SiO_2 interface is expected to influence dispersion and dipole interactions of atoms there and therefore change the cohesive energy of MoS_2 layers close to the SiO_2 surface. This could lead to a dependence of the number of printed MoS_2 monolayers on the field magnitude, which could qualitatively explain our experimental result that for MoS_2 pixels printed on plasma-charged substrates the edge portions are statistically thicker than the inner flakes, as shown in **Figure 2.3(c)**.

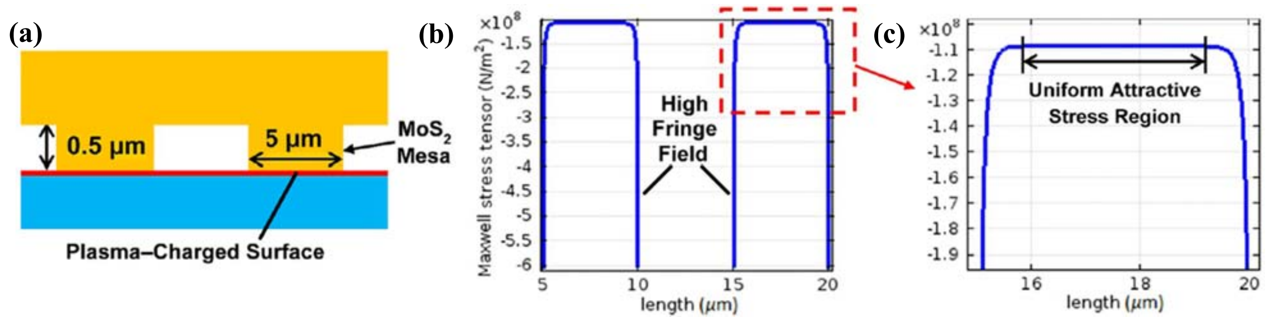

Figure 2.4. (a) Illustration of the 2-D model for Maxwell stress tensor calculation of surface charge-induced electrostatic attractive stress between the bulk MoS_2 stamp and the dielectric substrate. (b) Calculated attractive stress plotted as a function of positions. (c) Zoomed view of attractive stress distribution within a single MoS_2 mesa in contact with a SiO_2 surface. It is found that the attractive stress acting on a microscale MoS_2 mesa is uniform in the central region of the MoS_2 mesa but is significantly increased along the mesa edges due to the fringe effect.

Although plasma-assisted printing can produce large-area arrays of microscale MoS_2 pixels with regular edge profiles, many pixels have broken areas in their central regions, as shown in **Figure 2.2(e)**. This can be attributed to several possible reasons, including the limited size of crystalline domains in bulk MoS_2, non-uniformity of attractive stress within a microscale MoS_2 pixel mesa, as discussed in the simulation analysis, and the paradigm rule that the direct exfoliation of a large-area atomic layer (e.g., a complete microscale MoS_2 pixel film free of

defects) is thermodynamically unfavorable. Such an analysis suggests that it is indeed desirable to prepattern bulk MoS_2 stamps with densely arranged nanostructures that can improve the printing fidelity and eliminate the defects in the middle of printed patterns. In addition, such relief nanostructures are expected to generate a higher fringe field during printing processes because of the higher density of sharp feature edges and result in the higher transfer-printing efficiency of MoS_2 features. Thus far we have not developed a scalable process for patterning nanostructures on bulk MoS_2 because of its overly rough surface. However, we have successfully realized the nanopatterning of highly oriented pyrolytic graphite (HOPG) stamps with 100 nm half-pitch gratings using nanoimprint lithography, as shown in **Figure 2.5(a)**. SEM images of 100 nm half-pitch graphene nanoribbons (GNRs) produced by using plasma-assisted transfer printing are shown in **Figure 2.5(b)**. The printed GNRs exhibit a high degree of uniformity in ribbon widths over large areas and do not exhibit any visible defects in the middle of individual ribbons. The thickness of GNRs was measured to be 2.0±1.0 nm by using an AFM. This work demonstrates that (1) nanoscale defect-free atomic layer patterns can be more easily produced by using plasma-assisted printing in comparison with microscale ones; (2) plasma-assisted printing can be generalized for producing high-quality nanostructures of other atomically layered materials.

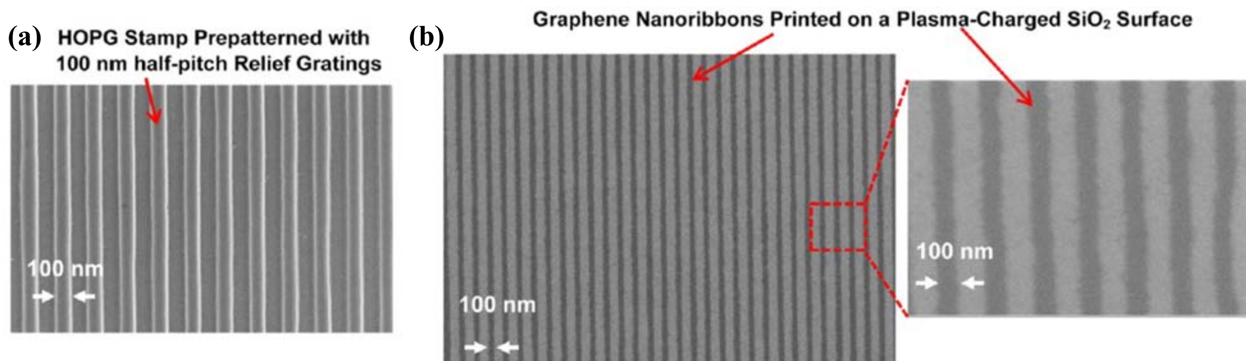

Figure 2.5. SEM images of (a) a HOPG stamp prepatterned with 100 nm half-pitch relief gratings by using nanoimprint lithography followed with plasma etching and (b) graphene nanoribbons printed onto a plasma-charged SiO_2 substrate.

2.3 Nanoimprint-Assisted Shear Exfoliation of MoS_2 Flakes into Large-Area Arrays

Toward ultimately realizing upscalable production of highly uniform multilayer MoS_2 device arrays or large-scale circuits, in this section we propose a top-down nanofabrication approach capable of producing pristine multilayer MoS_2 flake arrays with high uniformity of flake thicknesses (*i.e.*, relative thickness error ∼12%) over cm^2-scale areas. **Figure 2.6** illustrates

our nanoimprint-assisted shear exfoliation (NASE) method for producing multilayer MoS_2 flake arrays with uniform thicknesses. In a NASE process, first a bulk MoS_2 ingot is prestructured with protrusive multilayer mesa arrays by using photolithography followed with plasma etching (**Figure 2.6(a)**). After this process, this ingot becomes a bulk MoS_2 stamp. Here, the height of protrusive mesas can be well controlled by adjusting the plasma etching duration. This mesa height will determine the imprint depth (d_{NIL}) resulted by the stamp. When the stamp is ready, a substrate (*e.g.*, glass, Si, or SiO_2) is spin-coated with a polymeric fixing layer (*e.g.*, thermoplastics or cross-linkable polymers), and the MoS_2 stamp is subsequently pressed into the fixing layer on the substrate through a nanoimprint lithography (NIL) process (**Figure 2.6(b)**). Afterward, a lab-made motorized roller tool is used to displace the MoS_2 stamp along the substrate surface (*i.e.*, a shear direction). Due to the shear displacement, the multilayer MoS_2 mesas already imprinted into the fixing layer can be exfoliated away from the bulk stamp (**Figure 2.6(c)**). The thicknesses of exfoliated multilayer flakes are anticipated to be mainly determined by the imprint depth (d_{NIL}) (**Figure 2.6(d)**).

In comparison with previously reported exfoliation methods for generating layered materials, such as electrostatic exfoliation, plasma-assisted nanoprinting and mechanical cutting/

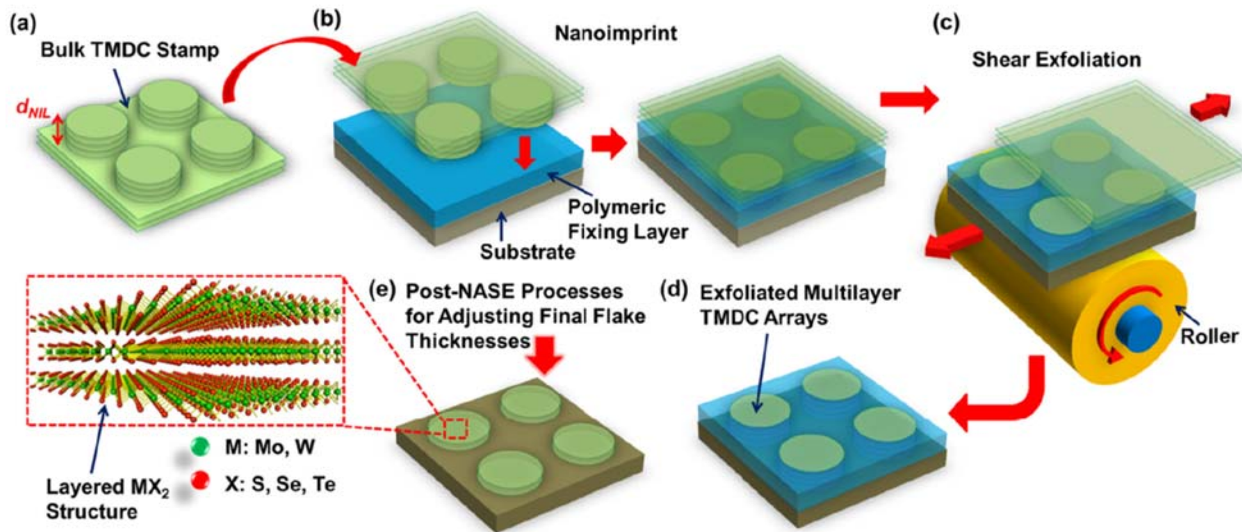

Figure 2.6. Illustration of nanoimprint-assisted shear exfoliation (NASE) for producing few-layer/multilayer MoS_2 device structure arrays: (a) fabrication of a bulk MoS_2stamp bearing protrusive device features; (b) nanoimprint process for pressing the protrusive features on the bulk MoS_2 stamp into a polymeric fixing layer coated on a substrate; (c) exfoliation of imprinted MoS_2 features along a shear direction, which is actuated by a motorized roller tool; (d) multilayer MoS_2 flakes imprinted/exfoliated by NASE, which are expected to exhibit a high uniformity in thickness as well as electronic properties; (e) post-NASE processes for further adjusting the final thicknesses of exfoliated MoS_2 flakes to meet various device application requirements.

transfer-printing, the unique shear exfoliation mechanism involved in NASE can result in significantly improved transfer-printing efficiency of prestructured MoS_2 features as well as higher uniformity of exfoliated MoS_2 feature thicknesses. In comparison with chemical synthesis approaches for generating multilayer MoS_2, NASE is expected to be able to produce MoS_2 structures with larger average crystal domain size (10s–100s μm), higher ordering of interlayer stacking configurations and therefore better transport properties. Furthermore, NASE could be further generalized for producing high-quality multilayer structures of other atomically layered materials, such as highly ordered pyrolytic graphite (HOPG) and emerging topological insulators (*e.g.*, Bi_2Se_3 and Bi_2Te_3). After a NASE process, additional etching/ablation processes could be subsequently used for further adjusting the thicknesses of NASE-produced MoS_2 flakes to meet the requirements of various device applications (**Figure 2.6(e)**), such as monolayers for light-emitting devices, 10–50 nm thick flakes for making high-mobility transistors and 50–200 nm flakes for photovoltaic/photodetection devices.

Figure 2.7(a) shows a photograph of our lab-made motorized roller tool for performing the shear exfoliation of multilayer MoS_2 structures. This tool consists of an AC brushless motor with an electric speed controller, a flat sample holder for immobilizing either the stamp or the substrate, a motor-driven roller for generating the relative shear displacement between the stamp and the substrate, and a vertical stage for applying a gauge pressure to maintain the stamp flat during the shear exfoliation. In particular, the web speed of the roller surface can be adjusted in the range of 0–3 cm/s. The vertical stage bearing a set of coil springs can generate an adjustable gauge pressure (0–0.5 MPa) for firmly pressing the MoS_2 stamp against the substrate, therefore effectively avoiding the formation of wrinkles in exfoliated MoS_2 layers. In this work, we chose MoS_2 as the test-bed material for investigating NASE processes, because (i) MoS_2 is the most widely studied TMDC material; (ii) MoS_2 and other TMDCs share very similar mechanical properties, which makes the nanofabrication processes developed in this work generally applicable to all other TMDCs and layered materials. **Figure 2.7(b)** and **(c)** display an optical micrograph (OM) and a scanning electron micrograph (SEM) of an exemplary MoS_2 stamp prestructured with 40 nm high, 15 μm size pillar arrays, respectively. The size of the whole stamp is ∼1 cm.

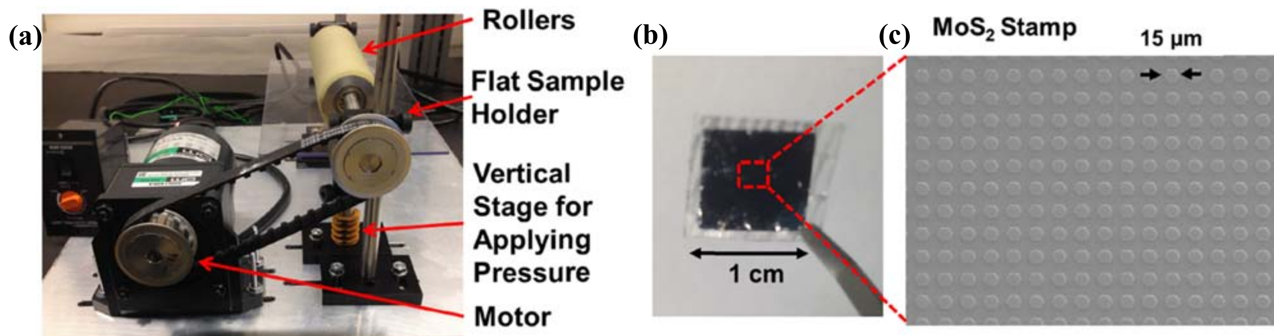

Figure 2.7. Photographs of (a) the motorized roller tool for performing NASE processes and (b) an exemplary 1 cm-size MoS_2 stamp. (c) shows the SEM image of this stamp, which bears 40 nm-high, 15 μm-size protrusive mesa (or pillar) arrays.

Figure 2.8(a) shows four optical micrographs of NASE-produced MoS_2 flakes, which were exfoliated into a 55 nm thick polystyrene (PS) fixing layer coated on a SiO_2/Si substrate (SiO_2thickness, 300 nm). These micrographs were captured from different locations over the whole NASE-processed area (~1 cm^2), as mapped in the inset photograph of the whole NASE sample. Raman spectroscopy was performed to identify the existence of exfoliated MoS_2 flakes in the imprinted PS layer. Our Raman results show that more than 80% of imprinted wells in the PS fixing layer have MoS_2 flakes. **Figure 2.8(b)** shows a typical Raman spectrum of a NASE-produced MoS_2 flake, which exhibits two characteristic peaks, A_{1g} and E_{2g}, corresponding to the out-of-plane and in-plane vibration modes of MoS_2 layers, respectively. For all NASE-produced MoS_2flakes, their A_{1g}–E_{2g} peak spacings are larger than 19 cm^{-1}. This indicates that all NASE-produced flakes are multilayer MoS_2 structures. Our OM and Raman characterizations show that NASE can produce orderly arranged multilayer MoS_2 device structures over cm^2-scale areas. Although most imprinted well pixels in PS fixing layers have high-quality MoS_2 flakes faithfully exfoliated from the bulk stamps, observable imperfection features still occur during NASE processes. **Figure 2.8(c)** displays the OM images of typical imperfection features occurring in NASE, which includes (i) imprinted PS wells without MoS_2 (*i.e.*, no exfoliation), (ii) imprinted wells with broken MoS_2 fragments (*i.e.*, incomplete exfoliation), (iii) MoS_2 dislocated away from the imprinted PS wells, and (iv) nonuniform thickness distribution within individual flakes. The occurring probabilities of these imperfection features may be relevant to mechanical properties of TMDC stamps and polymeric fixing layers, flatness/total size of TMDC stamps, geometric dimensions of prestructured TMDC structures, and NASE processing parameters (*e.g.*, roller speed and vertical pressure), *etc*. Especially, we found that the aspect ratio (*i.e.*, the ratio of the height to the lateral size of a feature) of protrusive mesas prestructured on TMDC stamps greatly affects the quality of NASE-produced flakes. In particular, given a fixed lateral size of mesas of

15 μm, our current NASE system can easily exfoliate 40–200 nm high MoS_2 mesas without resulting in significant imperfections. However, when the initial mesa thickness (or height) is thinner than 40 nm, the occurring probability of broken, wrinkled, and dislocated mesa flakes is significantly increased. Therefore, as mentioned above, the better route for producing 0.7–40 nm thick, 15 μm size MoS_2 flake arrays (*i.e.*, monolayer to 60-layer structures) is to employ NASE for producing uniform flake arrays thicker than 40 nm, and subsequently perform a post-NASE etching process to thin the NASE-produced flakes. For example, Liu *et al.* has demonstrated layer-by-layer thinning of multilayer MoS_2 structures [32]. This thinning approach in combination with NASE can potentially produce MoS_2 structure arrays with arbitrary thicknesses for meeting the requirements of various device applications. More nanomechanics-oriented works will be performed in the future to fully understand the role of other factors in generating imperfections during NASE processes and optimize the processing conditions to eliminate the imperfection features displayed in **Figure 2.8(c)**.

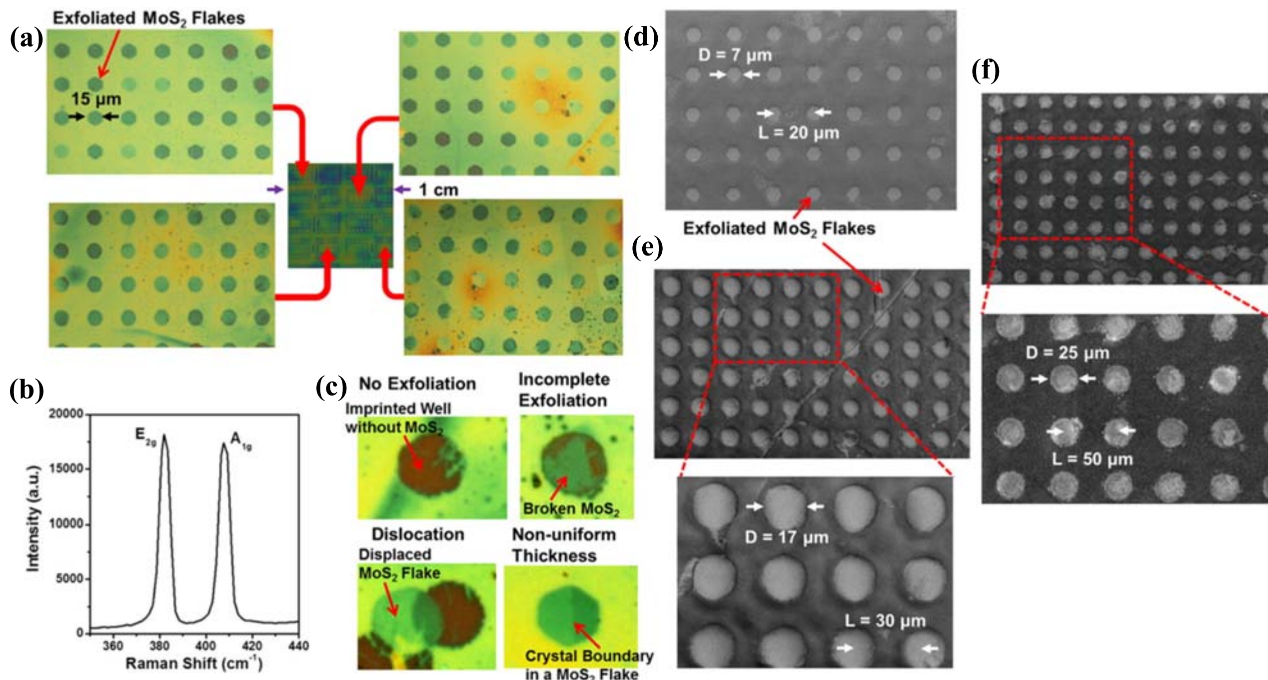

Figure 2.8. NASE results: (a) four optical micrographs of MoS_2 flake arrays imprinted/exfoliated into a PS fixing layer coated on a SiO_2/Si substrate by using NASE, which were captured from different locations over the whole NASE-processed area (~1 cm^2), as mapped in the inset photograph of the whole NASE sample; (b) Raman spectrum of an exemplary multilayer MoS_2 flake; (c) optical micrographs of typical imperfections that occur in NASE. (d–f) SEM images of a set of NASE-produced arrays of multilayer MoS_2 flakes with various flake diameters (*D*) and flake-to-flake spacings (*L*). For all of these samples, the imprint depth (d_{NIL}) is ~50 nm.

To study the effect of the lateral dimensions of MoS_2 mesas on the quality of NASE-produced flake arrays, we also produced MoS_2 flake arrays with different lateral dimensions. **Figure 2.8(d–f)** display the SEM images of a set of NASE-produced arrays of multilayer MoS_2 flakes with various flake diameters (*D*) and flake-to-flake spacings (*L*) (*i.e.*, (d) $D = 7$ μm, $L = 20$ μm; (e) $D = 17$ μm, $L = 30$ μm; (f) $D = 25$ μm, $L = 50$ μm). For all of these samples, the imprint depth (d_{NIL}) is ~50 nm. The flake arrays with $D = 7$ and 17 μm exhibit very similar quality as compared to 15 μm size ones shown in **Figure 2.8(a)**. Especially, most flakes in these arrays have relatively smooth top surfaces, as shown in **Figures 2.8(d)** and **(e)**. **Figure 2.8(f)** shows that the NASE-produced array with $D = 25$ μm also exhibits a comparable yield (~80%) of exfoliated MoS_2 flakes, but the top surfaces of these 25 μm size flakes exhibit a noticeably larger roughness in comparison with those of the flakes with the smaller *D* values. This is attributed to the relatively low aspect-ratio (*i.e.*, d_{NIL}/D) of these 25 μm size flakes, which results in relatively low flake rigidity and therefore a high occurring probability of wrinkled MoS_2 layers. In this work, we found that the quality of NASE-produced flakes is not sensitive to the flake spacing (*L*) or density. The relationship between the flake rigidity and the occurring probability of wrinkling in exfoliated layers is further discussed below based on our molecular dynamics (MD) simulations.

Because NASE-produced MoS_2 flakes are embedded into PS fixing layers, their thicknesses cannot be directly measured by using atomic force microscopy (AFM) or the color coding method. Especially, it should be noted that our MoS_2 flakes, under OM illumination, exhibit varying colors ranging from green to deep blue, as demonstrated in **Figure 2.8(a)**. Such a color variation among MoS_2 flakes are mainly attributed to the spatial variation of the PS film thickness or the residual layer thickness (RLT), which are caused by the nonflatness of our current MoS_2 stamps (or current commercially available MoS_2 ingots). Therefore, such a color variation does not correctly indicate the thickness distribution among exfoliated MoS_2 flakes. To evaluate the uniformity of NASE-produced MoS_2 flake thicknesses, we employed AFM to measure the effective well depth (d_W) of imprinted PS wells bearing exfoliated MoS_2 layers, as illustrated in **Figure 2.9(a)**. The d_W value of a MoS_2-embeded well is assumed to be the difference between the imprint depth (d_{NIL}, or the initial height of MoS_2 mesas prestructured on the stamp) and the thickness (t_{MoS2}) of the MoS_2 flake embedded inside this well. **Figure 2.9(b)** shows a 3-D AFM image of an exemplary NASE-produced MoS_2 flake exfoliated into an imprinted PS well. The dashed line indicates an AFM scanline that is replotted in **Figure 2.9(c)**. The d_W value of this MoS_2-embeded well is measured from the topographic difference between

the center of this MoS_2 flake and a location outside the well, as indicated by the red arrows in **Figure 2.9(c)**. For this specific imprinted well, d_W is measured to be ~0, indicating that t_{MoS2} ~ d_{NIL} = 40 nm. **Figure 2.9(d)** displays the statistics of d_W/d_{NIL} values measured from 100 imprinted wells bearing MoS_2 flakes. These structures were produced in a single NASE process. **Figure 2.9(d)** shows that the standard deviation of d_W/d_{NIL}data (or the relative thickness error of NASE-produced multilayer MoS_2 flakes) is estimated to ~12%. This relative thickness error is much smaller than those of multilayer structures produced by previously reported exfoliation methods [6].

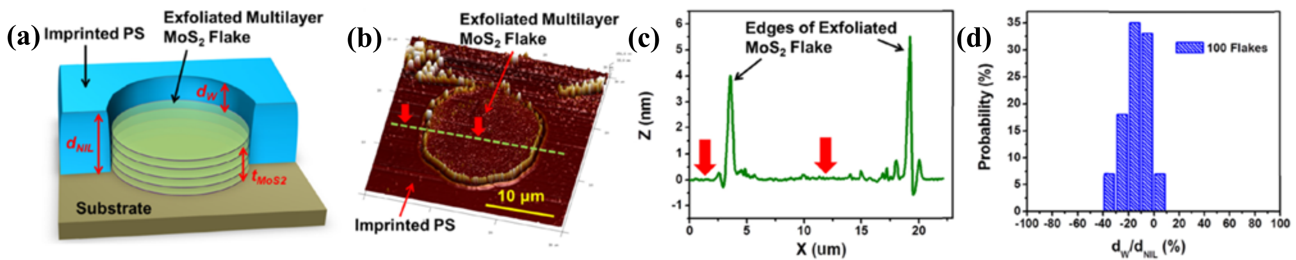

Figure 2.9. AFM characterization of NASE-produced MoS_2 flakes exfoliated into a PS fixing layer: (a) schematic of a multilayer MoS2 flake with thickness of $tMoS_2$ exfoliated into an imprinted PS well with imprint depth of d_{NIL}, resulting in an effective well depth of d_W; (b) an exemplary 3-D AFM image of a multilayer MoS_2 flake exfoliated into an imprinted PS well; (c) an AFM scanline extracted from the AFM image shown in (b) (i.e., the dashed line shown in (b)), from which the d_W value of this MoS_2-embeded well can be measured from the topographic difference between locations denoted with arrows; (d) statistics of d_W/d_{NIL} data measured from 100 MoS_2-embeded wells, which shows that the standard deviation of d_W/d_{NIL} data (or the relative thickness error of NASE-produced multilayer MoS_2 flakes) is estimated to ~12%.

To further evaluate the scalability of NASE for generating atomically layered structures with nanoscale lateral dimensions, we performed a molecular dynamics (MD) simulation of the NASE processes for exfoliating nanoscale-lateral-size layered structures. In this simulation work, we specifically simulated the shear exfoliation of few-layer-graphene nanostructures into PS fixing layers, because few-layer-graphene has the simpler crystal structure than TMDCs, which can simplify our simulation, but graphene layers exhibit mechanical properties very similar to most TMDCs. **Figure 2.10** shows the simulation results of the NASE process for exfoliating 5 nm size, 4-layer graphene mesas into a PS layer. In particular, **Figure 2.10(b–e)** display a set of snapshots of the simulated postnanoimprint shear exfoliation stages at selected times (t = 0, 50, 90 ns). These dynamic simulation results show that at least three layers from a mesa can be reliably exfoliated and trapped into the imprinted PS well, whereas the layer closest to the top edge of the PS well (*i.e.*, the green layer shown in **Figure 2.10**) exhibits a significant probability

to be dislocated out of the PS well. **Figure 2.10(f)** shows a zoom-in view of the interface between the graphene layer edges and the sidewall of the imprinted PS well. From **Figure 2.10(f)**, it can be observed that the imprinted well is deep enough to prevent the trapped graphene layers from sliding over one another. This guarantees that the imprinted/exfoliated multiple layers can retain their original AB-stacking mode after a NASE process. These MD simulation results imply that NASE could be potentially used for generating high-quality nanoscale-lateral-size layered device structures.

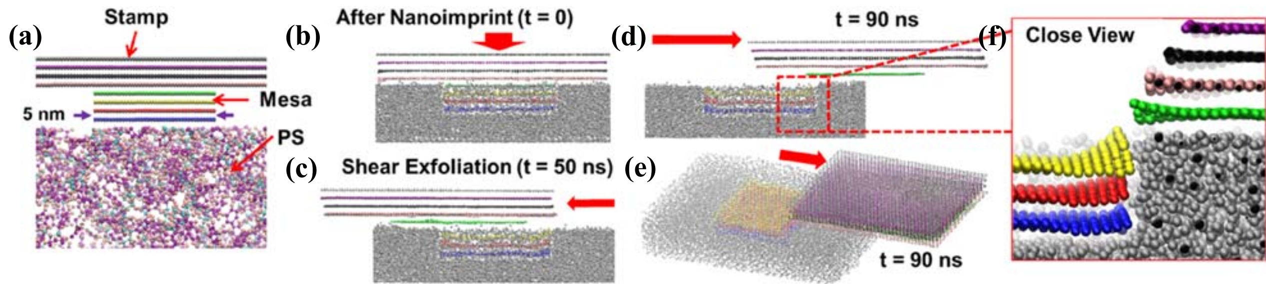

Figure 2.10. Molecular dynamics (MD) simulation of the NASE process for exfoliating atomically layered nanostructures: (a) a selected part of the 3-D simulation region, showing the cross-sectional view of the initial configuration of the NASE process, involving a graphite stamp bearing 5 nm size, 4-layer mesas and a PS fixing layer; (b–d) cross-sectional snapshots of the MD simulation result of a postnanoimprint shear exfoliation course at t = 0, 50, 90 ns; (e) a 3-D snapshot of the simulated system at t = 90 ns; (f) a zoom-in view of the imprinted PS well bearing graphene layers, especially displaying the interface between the edges of exfoliated layers and the sidewall of the imprinted PS well.

We also used MD simulations to investigate the effects of the geometric dimensions of prestructured stamping structures on the resultant morphology of NASE-produced layered nanostructures. For example, we simulated the NASE process for exfoliating relatively low-aspect-ratio graphene nanostructures (*i.e.*, 50 nm size, bilayer graphene mesas prestructured on a stamp), as shown in **Figure 2.11**. Specifically, **Figure 2.11(a)** and **(b)** display two cross-sectional snapshots of the postnanoimprint shear exfoliation course taken at $t = 0$ and 1 ns, respectively. **Figure 2.11(b)** shows that the imprinted bilayer mesa is pulled out of the imprinted PS by the bulk stamp moving along a shear direction, and the imprinted PS well fails to immobilize such low-aspect-ratio structures. This can be attributed to the fact that the layered structures with a lower aspect-ratio possess much lower bending rigidity than the ones with a higher aspect-ratio, because the bending rigidity of a solid flake can be expressed as $Eh^3/12(1 - v^2)$, where E, h, and v are the Young's modulus, thickness, and Poisson's ratio of the flake. Therefore, relatively low-aspect-ratio layered structures can easily deform under the shear stress

exerted by the bulk stamp, and therefore they can be easily pulled out of the imprinted well. Our simulation shows that the initial form of such shear-stress-induced deformation in exfoliated mesa layers is a set of nanoscale wrinkles. **Figure 2.11(c)** and **(d)** display the tilted and side views, respectively, of a 3-D snapshot of the low-aspect-ratio graphene layers at $t = 1$ ns, which exhibits a set of wrinkle features induced by the shear dislocation process. Such wrinkle features do not appear in relatively high-aspect-ratio layered nanostructures (*e.g.*, 5 nm size, 4-layer mesas shown in **Figure 2.10**) due to their large in-plane stiffness. In addition, our simulations indicate that the large deformations created in relatively low-aspect-ratio layered structures can reduce the cohesive energies of graphene/graphene as well as graphene/PS interfaces, and further enhance the occurring probability of the detachment of imprinted/exfoliated layers from the PS fixing layer. Therefore, our MD simulation results, consistent with our experimental results, also suggest that NASE is more suitable for producing uniform multilayer structures with relatively high aspect-ratios than to producing monolayer/few-layer structures with relatively low aspect-ratios. However, as mentioned above, NASE-produced multilayer structures with uniform initial thicknesses could be further trimmed to the thinner thicknesses by using established layer-thinning approaches. As discussed above, in a real NASE process, when a MoS_2 stamp is sheared horizontally, a vertical pressure is applied to the stamp to avoid the ripple formation.

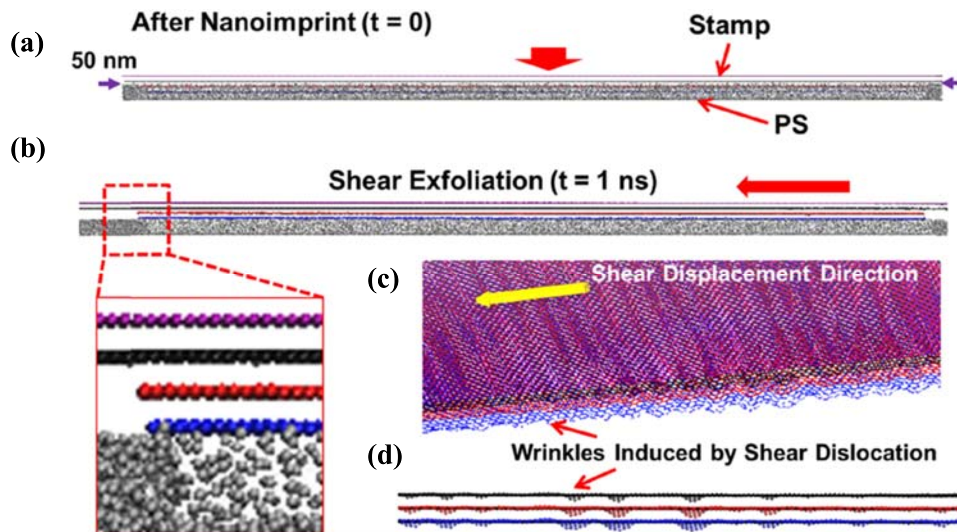

Figure 2.11. Molecular dynamics (MD) simulation of the NASE process for exfoliating relatively low-aspect-ratio layered structures: (a) a cross-sectional snapshot of the NASE stage, in which a graphite stamp bearing 50 nm size, bilayer mesas has been imprinted into a PS fixing layer (i.e., t = 0); (b) a cross-sectional snapshot of the postnanoimprint shear exfoliation course taken at t = 1 ns; (c) and (d) are tilted and side views, respectively, of a 3-D snapshot of the simulated system at t = 1 ns, which exhibits wrinkle features induced by the shear dislocation process.

2.4 Fabrication of FET and Biosensor Arrays Using Mechanical Exfoliation Techniques

We characterized the electronic properties of MoS_2 flakes exfoliated on the plasma-charged SiO_2/p^+ Si substrates by the fabrication of back-gated field-effect transistors (FETs). To do so, the metallic drain/source contact pads (5nm Ti/55nm Au) were fabricated by photolithography or electron-beam lithography (EBL) followed by metal deposition then lift-off. In particular, photolithography was used to fabricate FETs based on the inner flakes of MoS_2 pixels, and EBL was specifically used for the fabrication of FETs based on the outer edge ribbons of MoS_2 pixels. Finally, another indium metallic contact was fabricated onto the p^+-Si substrate, which serves as a back gate contact. The device characteristic curves of FETs were measured by using an Agilent-4145B semiconductor parameter analyzer.

Figure 2.12(a) presents a BSE image of an inner flake of a MoS_2 pixel that was used to fabricate a back-gated FET with flake thickness of ~5 nm, channel length of L=5.4 μm, average channel width of W~3.7 μm, and gate dielectric thickness of d=330 nm. **Figure 2.12(b)** demonstrates drain-source current (I_{DS}) – drain-source voltage (V_{DS}) characteristics of this exemplary FET under different gate voltages (V_G) in the range from -75 to 100 V. **Figure 2.12(c)** plots the I_{DS} – V_G characteristics under a fixed drain-source voltage (V_{DS} = 10 V).

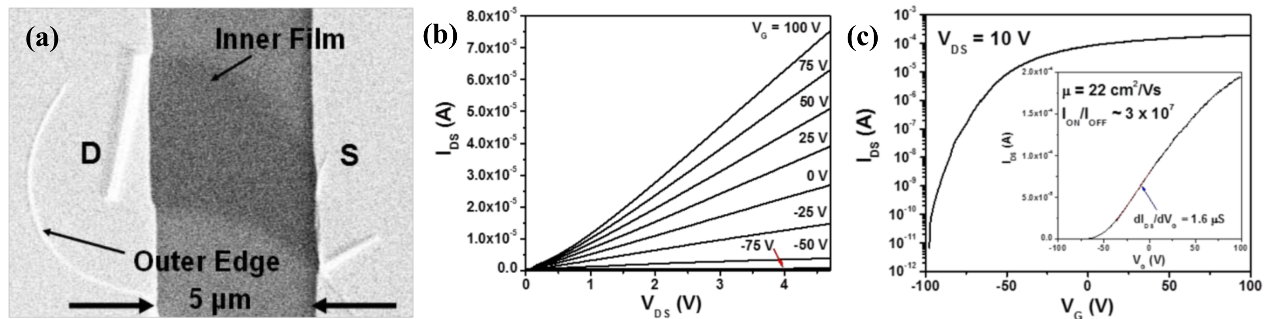

Figure 2.12. (a) BSE image of an exemplary back-gated FET made from the inner flake of a printed MoS_2 pixel with flake. (b) I_{DS}-V_{DS} characteristics under different gate voltages (V_G) ranging from -75 to 100 V. (c) Semi-logarithmic plot of an I_{DS}-V_G characteristic curve under a fixed drain-source voltage V_{DS} = 10 V. The inset graph shows the linear plot of the same I_{DS}-V_G curve, and the transconductance (dI_{DS}/dV_G) is obtained by fitting the linear region of the I_{DS}-V_G curve, as indicated by the red line.

As shown in **Figures 2.12 (b)** and **(c)**, this FET shows N-type conduction with an ON/OFF current ratio (I_{ON}/I_{OFF}) of ~107. The transconductance at the linear region of the I_{DS} – V_G characteristic curve was evaluated to be $\Delta I_{DS}/\Delta V_G$ = 1.60 μS by the linear fitting (denoted with the red solid line in the inset of **Figure 2.12 (c)**). The field-effect mobility was estimated to be μ = 22 cm^2/Vs based on below equation (2.1), where C_{ox} is the gate capacitance; ϵ_0 is the

vacuum permittivity; $\epsilon_r \sim 3.9$ is the dielectric constant of SiO_2; W/L is the width/length ratio of the MoS_2 flake channel. The mobility values evaluated from the inner flakes of printed MoS_2 pixels range from 6-44 cm^2/Vs, which are comparable to previously studied values for MoS_2 FETs using SiO_2 as the gate dielectric [33]. This confirms that our plasma-assisted transfer-printing approaches can produce high-quality MoS_2 features and are capable of practical electronic applications.

$$\mu = -\frac{\Delta I_{\mathrm{DS}}}{C_{\mathrm{ox}} \frac{W}{L} V_{\mathrm{DS}} \Delta V_{\mathrm{G}}} \quad \text{where} \quad C_{\mathrm{ox}} = \frac{\epsilon_0 \epsilon_r}{d} \tag{2.1}$$

Using a similar fabrication process, we made FETs using the ring-shaped edge ribbons of MoS_2 pixels as the semiconducting channels. In the electron beam lithography, the overlay alignment was carefully performed to prevent incorporating any inner pixel flakes into the FET channel. **Figure 2.13(a)** displays an SEM image of an exemplary edge ribbon-based FET with a channel width of $W \approx 300$ nm, channel length of $L \approx 500$ nm, and average MoS_2 thickness of ~10 nm. **Figure 2.13(b, c)** exhibits I_{DS}-V_{DS} and I_{DS}-V_G characteristics, respectively, which indicate that this edge ribbon-based FET shows p-type conduction for V_G = -100 to 100 V. The transconductance at the linear region of the I_{DS}-V_G characteristic curve was evaluated as dI_{DS}/dV_G = -1.74 nS by the linear fitting (denoted with the red solid line in the inset of **Figure 2.13(c)**). The field-effect mobility was estimated to be μ = 0.27 cm^2/Vs according to $\mu = [L/(C_g V_{DS})](dI_{DS}/dV_G)$, where C_g is the average gate capacitance associated with a single MoS_2 edge ribbon per unit channel length [unit: F/m]. Here, C_g is calculated by using a simulation model based on finite element analysis that takes into account the fringe effect at the MoS_2 nanoribbon edges. This fringe effect can significantly affect the values of C_g for MoS_2 FETs with nanoscale channel widths. The field effect mobility measured from other edge ribbon-based FETs range from 0.1 to 1.0 cm^2/Vs.

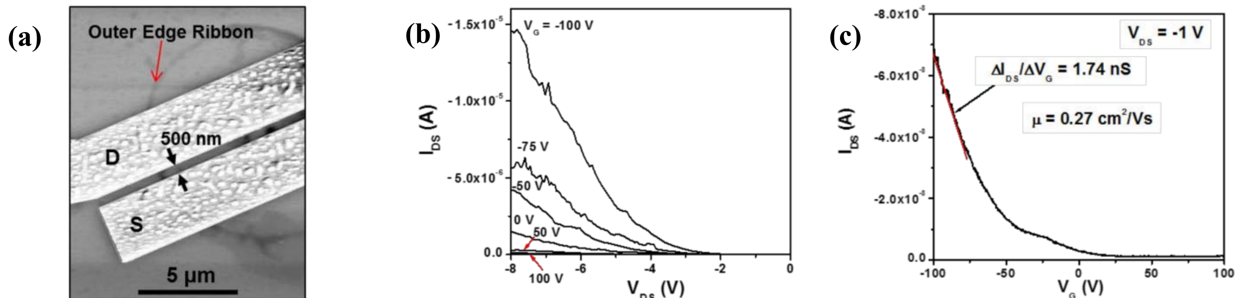

Figure 2.13. (a) SEM image of an exemplary back-gated FET made from the outer edge ribbon of a printed MoS_2 pixel. (b) I_{DS}-V_{DS} and (c) I_{DS}-V_G characteristics of the edge ribbon-based FET.

To evaluate the uniformity of the electronic properties of multilayer MoS_2 flakes produced by nanoimprint-assisted shear exfoliation (NASE), back-gated FET arrays were fabricated with NASE-produced MoS_2 channels and the statistical data of the multiple FET transfer characteristics was obtained. **Figure 2.14(a)** schematically illustrates the FET structure. **Figure 2.14(b)** shows the SEM images of a representative FET array made from the multilayer MoS_2 flakes produced in a NASE process. For all as-fabricated FETs, the channel width (W) and length (L) are 15 and 10 μm, respectively; the MoS_2 channel thickness is around 20 nm; the back-gate dielectric consists of a 300 nm thick thermally grown SiO_2 layer plus a residual PS layer. Here, the residual PS thickness ($t_{residual}$) under each MoS_2 channel is estimated to be thinner than 5 nm by using $t_{residual} = t_{PS} - d_{NIL}$, in which t_{PS} is the initial PS layer thickness before the NASE process.

It should be noted that our current post-NASE FET fabrication process sometimes results in the peeling off of the NASE-produced MoS_2 flakes and thus need to be further optimized. This is because of the poor adhesion between layered materials and most of substrate materials. This issue is not only for NASE-produced MoS_2 samples, but also generally for all 2D layered materials. Exploring the ultimate solution to this problem is underway but still beyond the scope of the present work. Fortunately, in our work, the survived MoS_2 flakes remain staying at their original locations in the array, and the yields of working FETs over cm^2 -scale areas are typically 50-60% (the yield of NASE-produced MoS_2 flakes is ~80%). Such samples are sufficiently good for providing a number of FETs to evaluate the uniformity of the electronic properties of NASE-produced MoS_2 flakes.

FETs were made from the multilayer MoS_2 flakes produced in a NASE process and distributed over a 1 cm^2 area. **Figures 2.14(c)** to **(f)** show the statistics of field-effect mobility (μ), On/Off currents (I_{ON} is the I_{DS} measured at V_G = 60 V; I_{OFF} is the minimum value of I_{DS} within the V_G range of (60 V), subthreshold swing (SS), and threshold voltage (V_T) data, which were extracted from the transfer characteristic curves of these 45 FETs. Specifically, the mean values of μ, I_{ON}, I_{OFF}, SS, and V_T were statistically measured to be $\mu = 46 \pm 10$ cm^2 / (Vs), I_{ON} = 24.0 ± 5 μA (or, 1.60 ± 0.33 μA per 1 μm channel width), I_{OFF} = 21 ± 20 pA, SS = 11.9 ± 2.7 V/dec, and V_T = 28 ± 8 V, respectively. First, it should be noted that the relatively large SS values of our FETs are attributed to the relatively thick back-gate dielectric (i.e., 300 nm SiO_2) used here, and such SS values could be significantly reduced by using much thinner dielectrics.

The I_{OFF} data of our FETs exhibit a much larger relative standard deviation (~95%) as compared to other parameters, which is mainly attributed to the measurement precision (2-10 pA) of our semiconductor analyzer. The quantity V_T could have zero or negative values, and therefore the relative standard deviation of V_T data is meaningless for evaluating the uniformity of our FETs. Therefore, we specifically use the relative standard deviations of μ, I_{ON}, and SS data for evaluating the uniformity. The relative standard deviations of these parameters range from 21 to 23%. This shows that even though our post-NASE FET fabrication process is yet to be optimized, our current FET arrays made from NASE-produced multilayer MoS_2 flakes already exhibit a good uniformity in critical FET parameters. The observed variances in the performance parameters of our FETs are mainly attributed to several possible factors, including (1) the device-to-device variance in the residual PS layer thicknesses; the NASE-introduced defects, as discussed above (**Figure 2.8(c)**); (3) the contaminants introduced during the post-NASE FET fabrication processes; (4) intrinsic nonuniformity of the material properties of initial MoS_2 ingots (e.g., crystal orientations, domain size distributions, and intrinsic defects).

To further investigate the effect of the residual polystyrene (PS) layers on the uniformity of the electronic properties of NASE-produced MoS_2 flakes, another batch of MoS_2 FETs were

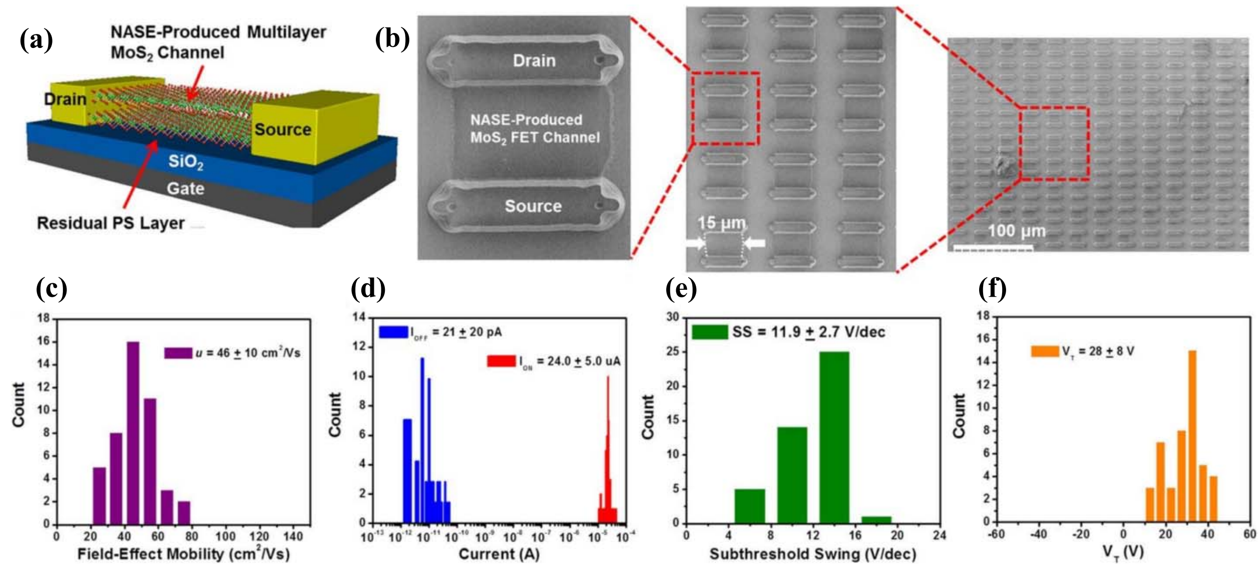

Figure 2.14. Back-gated FET arrays made from NASE-produced MoS_2 flakes: (a) Schematic illustration of a back-gated MoS_2 FET. (b) SEM images of a representative FET array made from the multilayer MoS_2 flakes (thickness ~20 nm) produced in a NASE process. For all FETs, the channel width (W) and length (L) are 15 and 10 μm, respectively; the back gate dielectric is 300 nm SiO_2 + residual PS (estimated to be thinner than 5 nm). The following graphs display the statistics of (c) mobility (μ), (d) On/Off currents (I_{ON} and I_{OFF}), (e) subthreshold swing (SS), and (f) threshold voltage (V_T) data measured from 45 MoS_2 FETs fabricated by a NASE process.

fabricated using an alternative method to eliminate residual PS. To make such FETs, a SiO_2-coated p^+-Si substrate bearing NASE-produced MoS_2 flakes was soaked in toluene for 1-2 h. Until this step, the sample had not been subjected to any plasma etching. Therefore, the imprinted PS on the substrate (including the residual PS layers under MoS_2 flakes) was able to be completely removed because there is no cross-linking in PS. However, this cleaning process displaced (and even peeled) many MoS_2 flakes and only a few survived MoS_2 flakes were chosen for making FETs. Because the selected MoS_2 flakes had been shifted away from their original array configurations, we had to perform repetitive lithography, metal deposition, and lift-off processes for making multiple FETs. In particular, special finger contacts (5 nm Ti/50 nm Au) were fabricated to access to individual selected MoS_2 flakes. This was a time-consuming task and resulted in a much lower device yield as compared to the method, discussed above, for making FET arrays with the residual PS. **Figure 2.15** displays two representative back-gated FETs made from multilayer MoS_2 flakes that were cleaned by Toluene. **Figure 2.16(a)** shows the transfer characteristics of 4 such FETs made from PS-free multilayer MoS_2 flakes, and **Figures 2.16(b)-(e)** display the statistics of (a) mobility (μ), (b) On/Off currents (I_{ON} and I_{OFF}), (c) subthreshold swing (SS), and (d) threshold voltage (V_T) data measured from these 11 FETs. For the following discussion, these FETs are referred to as PS-free FETs, and the previous array FETs as shown in **Figure 2.14** are referred to as PS-retained FETs.

First, our device characterization shows that the field-effect mobility data measured from our PS-retained FETs (i.e., μ=46±10 $cm^2/(Vs)$) have a slightly smaller mean value and a slightly larger standard deviation in comparison with those measured from our PS-free FETs (i.e., μ = 53 ± 7 $cm^2/(Vs)$). This slight difference is attributed to the roughness scattering at the MoS_2/PS

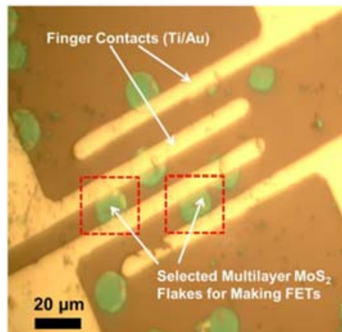

Figure 2.15. Optical micrograph of two representative back-gated FETs made from selected NASE-produced multilayer MoS_2 flakes. These NASE-produced MoS_2 flakes (~30 nm thick) were soaked in toluene for 1-2 hours in order to remove the residual PS layers under them. This toluene etching process shifted most MoS_2 flakes away from their original locations in the array. Therefore, to make working FETs, special finger contacts (5 nm Ti/50 nm Au) were fabricated to access to individual selected MoS_2 flakes.

interface, which could slightly reduce the field effect mobility of the multilayer MoS_2 FET and broaden the dispersion of the mobility values measured from different FETs. Because such a PS-induced mobility reduction is estimated to be only ~13%, we can think that the presence of residual PS between multilayer MoS_2 flakes and SiO_2 gate dielectrics does not result in a detrimental damage to the mobility property of multilayer MoS_2 FETs. In comparison with our PS-retained FETs, our PS-free FETs exhibit a smaller average SS (i.e., SS=8.4±1.1 V/dec for PS-free FETs, whereas SS =11.9±2.7 V/dec for PS-retained ones). This difference is attributed to that the residual PS layer under a MoS_2 FET channel introduces an additional capacitor connected with the SiO_2 capacitor in series, which decreases the overall gate dielectric capacitance and therefore increases the SS value of this FET. In addition, the relative standard deviation of the SS data measured from PS-retained FETs (~23%) is noticeably larger than that measured from PS-free FETs (~13%). This is attributed to the non-uniformity of the residual PS layer thicknesses under NASE-produced MoS_2 flakes, which may introduce an additional non-uniformity in back-gate capacitances and hence the SS data of PS-retained FETs. In comparison with PS-free FETs, the PS-retained FETs have statistically more positive V_T values (i.e., V_T = -27 ± 10 V for PS-free FETs, whereas V_T = 28 ± 8 V for PS-retained ones). This difference is presumably attributed to the polymer-induced surface-charge-transfer (SCT) doping (p-type doping) in MoS_2 channels.

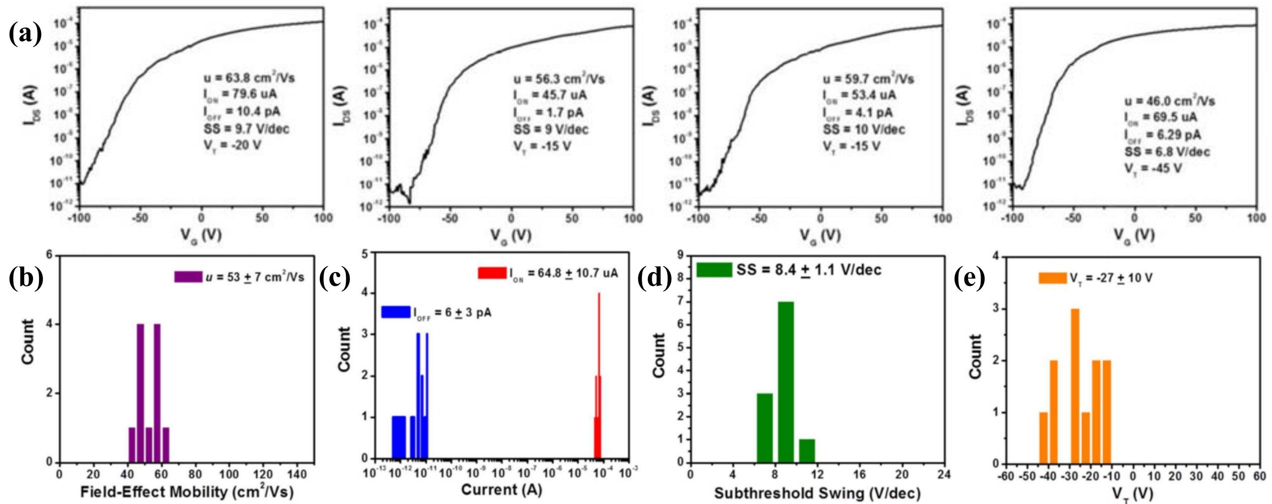

Figure 2.16. (a) Transfer characteristics of 4 back-gated FETs, made from NASE-produced multilayer MoS_2 flakes. For these FETs, the residual PS layers under MoS_2 channel flakes were completely removed by toluene. This toluene cleaning process shifted MoS_2 flakes away from their original locations in the array. Therefore, these devices had to be fabricated using repetitive lithography and metallization processes. Statistics of (b) mobility (μ), (c) On/Off currents (I_{ON} and I_{OFF}), (d) subthreshold swing (SS), and (e) threshold voltage (V_T) data measured from 11 FETs made from NASE-produced MoS2 flakes. These selected MoS_2 flakes were cleaned with toluene.

More importantly, our NASE-produced MoS_2 transistors can be directly implemented as electronic biosensors for detecting and quantifying specific illness-related biomarkers. In this work, we specifically demonstrated quantification of a standard curve for tumor necrosis factor-alpha (TNF-α) detection by using multiple MoS_2 FET biosensors. **Figure 2.17(a)** illustrates a MoS_2 FET sensor functionalized with anti-human TNF-α antibody receptors for detecting TNF-α molecules. To realize biomarker quantification, multiple sensors with consistent sensor responses to specific biomarker concentrations are needed. We choose the relative change of ON-state I_{DS} under a fixed set of V_G and V_{DS}, i.e., R = (I_{DS}(anti)- I_{DS})/I_{DS}, as the sensor response quantity. Here, I_{DS}(anti) is referred to be the ON-state I_{DS} measured from an as-functionalized sensor (i.e., TNF-α concentration n = 0). **Figure 2.17(b)** shows the transfer characteristics of eight different

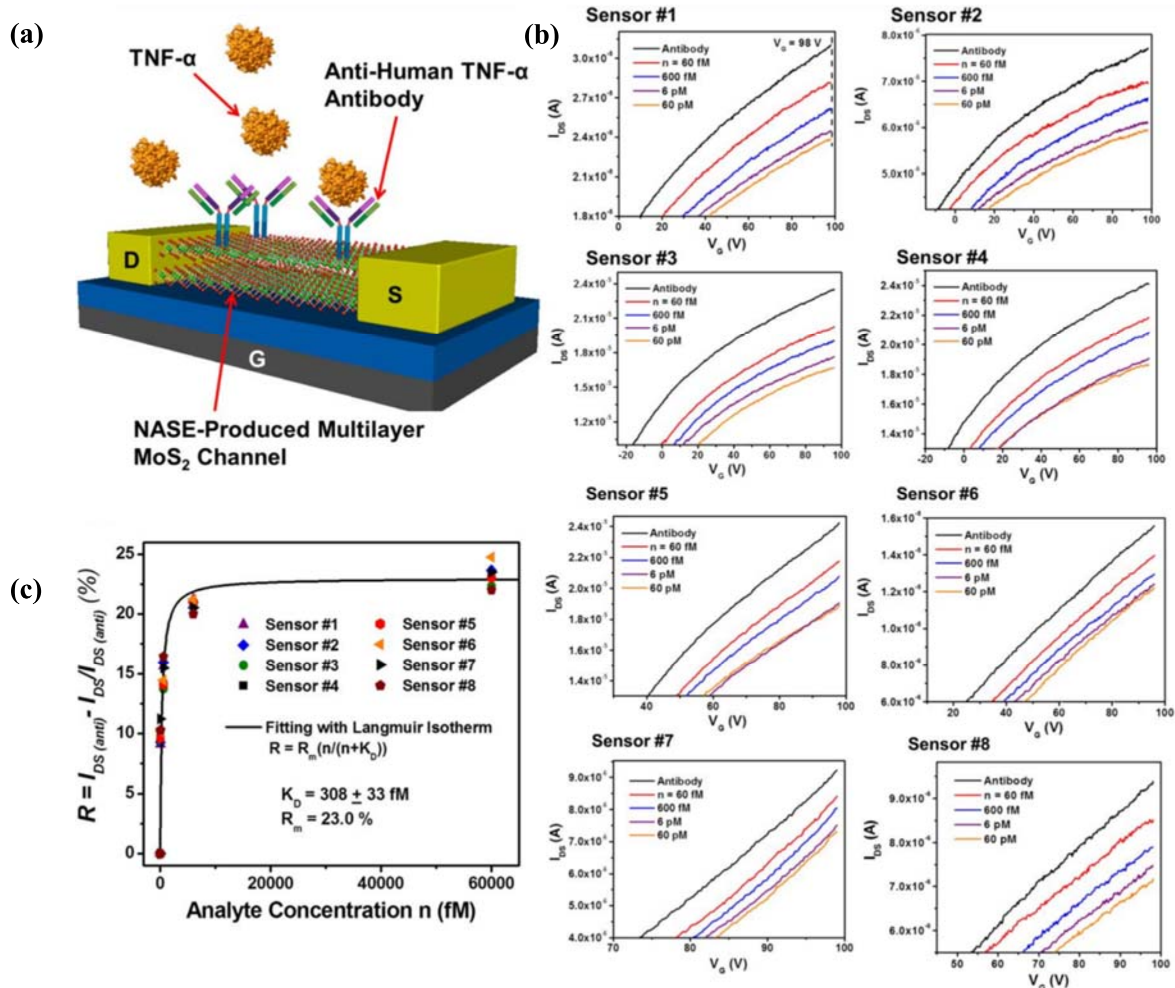

Figure 2.17. MoS_2 transistor biosensors made from NASE-produced multilayer MoS_2 flakes: (a) illustration of a MoS_2 transistor biosensor, in which anti-human TNF-α antibodies are directly functionalized on the MoS_2 transistor channel; (b) sensor responses (i.e., transfer characteristics) to various TNF-α concentrations (i.e., n = 0, 60 fM, 600 fM, 6 pM, and 60 pM) measured from eight different sensors; (c) calibrated responses (i.e., relative change of ON-state I_{DS} measured at a fixed V_G=98 V) with respect to n, measured from difference sensors, which exhibit a high degree of device-to-device consistency and can be well fitted with Langmuir isotherm.

MoS_2 FETs measured under a set of incremental TNF-α concentrations (i.e., n = 0, 60 fM, 600 fM, 6 pM, and 60 pM). The sensor responses (i.e., values of R were extracted at a fixed V_G=98 V (i.e., ON-state) and plotted with respect to TNF-α concentration (n) in **Figure 2.17(c)**.

Figure 2.17(c) shows that the R-n relationships measured from multiple NASE-produced sensors exhibit a high degree of device-to-device consistency and can serve as a standard curve for TNF-α quantification. These R-n relationships can be well fitted with Langmuir isotherm, and the equilibrium constant of the antibody-(TNF-α) pair was extracted to be K_D = 308+33 fM. These device demonstrations have preliminarily demonstrated that NASE can produce multilayer TMDC device structures with a high uniformity of electronic properties. In addition, it should be noted that our MoS_2 FET biosensors exhibit a very low limit-of-detection (LOD) (< 60 fM). Comparing to device multiplexing capability of NASE process, such an fM-level LOD potentially enables new bioassay chips offering single-molecule-level analysis capabilities.

2.5 Atomic Force Microscopy-Assisted Exfoliation of G Flakes

We noted that our 2DLMs FETs and biosensors more or less suffer from the lack of precise control over the thickness of the printed layers and thus a deeper understanding of exfoliation mechanism in 2DLMs is of fundamental and technological importance.

Generally speaking, our proposed mechanical exfoliation techniques for the fabrication of ordered 2DLMs device arrays at micro and nanoscale consist of four key steps: (1) Pattern any arbitrary micro and nano-features on the cm-sized 2D crystal stamp using standard lithography methods; (2) Press the pre-patterned stamp against the target substrate; (3) Enhance the interfacial adhesion between the stamp and the substrate using an external bias voltage (**Figure 2.18(a,c)**), built-in electric field (e.g., plasma-charged substrate surface, **Figure 2.18(b)**) or polymeric fixing layer (**Figure 2.18(d)**); and (4) Transfer the micro and nano-features from the stamp to the substrate as they are separated from each other in a direction perpendicular (**Figure 2.18(a,b)**) or parallel (**Figure 2.18(c,d)**) to the substrate surface. As such, the mechanical exfoliation of 2DLMs features could be a combined action of electrostatic attractive forces (**Figure 2.18(a)**), applied contact pressure (being used to improve the conformity of the mesa to the underlying substrate morphology), external pull-off/shear forces, surface friction forces (**Figure 2.18(c)**), and intermolecular vdW forces (associated with the 2DLMs/substrate interfacial adhesion and 2DLMs interlayer cohesion).

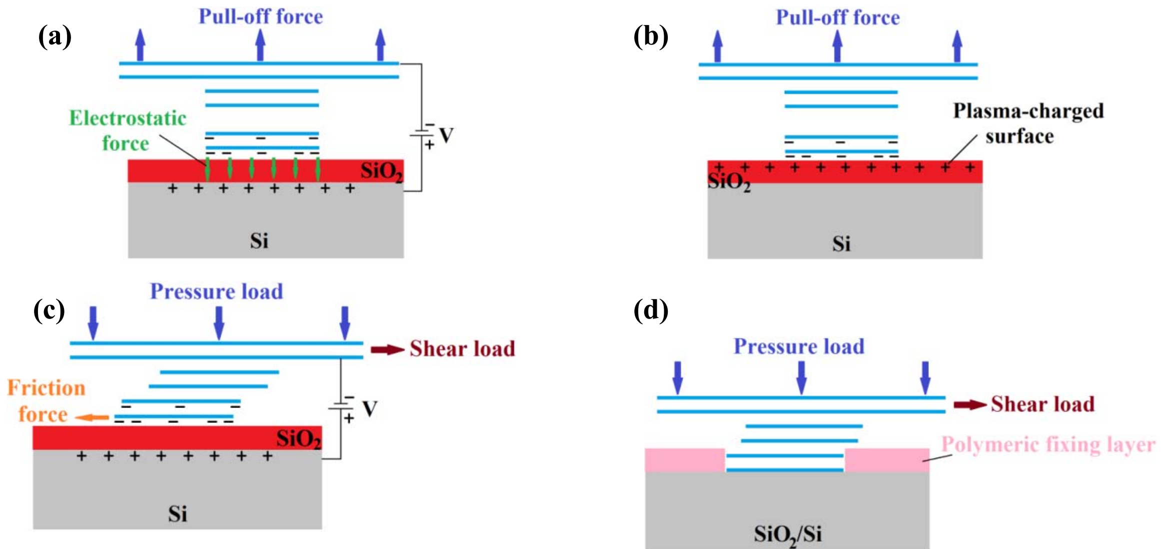

Figure 2.18. Schematics of mechanical exfoliation of 2DLMs features using (a,c) bias voltage, (b) plasma-charged surface and (d) polymeric fixing layer, followed by applying (a,b) pull-off and (c,d) shear forces.

To further gain an in-depth understanding of underlying mechanisms associated with the electrostatic exfoliation of 2DLMs, I exploit for the first time conductive atomic force microscopy (CAFM) with ultrahigh force–displacement resolution to unravel the relative contributions of electrostatic attraction/repulsion, internal layer-to-layer shear, and intermolecular vdW forces to the exfoliation of the 2DLMs in general and graphite specifically. I have drawn a simple analogy between a typical macro-scale exfoliation setup (as discussed in sections 2.3 and 2.4) (**Figure 2.19(a)**) and the present nano-scale AFM-based exfoliation setup (**Figure 2.19(b)**). **Figure 2.19(c)** presents a schematic illustration of the CAFM-assisted electrostatic manipulation setup, in which an electrically conducting Pt/Ir-coated AFM tip is used in contact mode to perform all measurements. For the scope of this section, we focus on the exfoliation and characterization of graphite (G) as a model system for other 2DLMs. After nanostructure fabrication of 75 nm deep cylindrical mesas with a diameter of 60 nm from highly oriented pyrolytic graphite (HOPG), we utilize an in situ flattened AFM tip to uniformly adhere the selected HOPG mesa to the tip apex with a conductive adhesive polymer PEDOT:PSS(D-sorbitol). The tip with an attached mesa is then brought into contact with the SiO_2/Si substrate, followed by applying a bias voltage of up to 10 V between the mesa and the highly doped Si substrate, separated by the 10 nm thick SiO_2 film. Pristine G monolayers subjected to attractive electrostatic forces are transferred from the nanomesa onto the SiO_2 film as the tip is gently moved away from the SiO_2/Si substrate in a direction normal to the basal plane (hereafter

referred to simply as normal exfoliation method) or parallel to the basal plane of graphite (referred to as shear exfoliation method). An atomically well-defined contact formed between the nanomesa and the substrate combined with piconewton force and sub-nanometer displacement resolution in our CAFM setup facilitates the precise evaluation of both the applied force and the vertical/lateral displacement of mesas with respect to the substrate during the exfoliation process. Key steps involved in the fabrication procedure and geometrical design are presented with the detailed fabrication steps in sections 2.4.1-2.4.6.

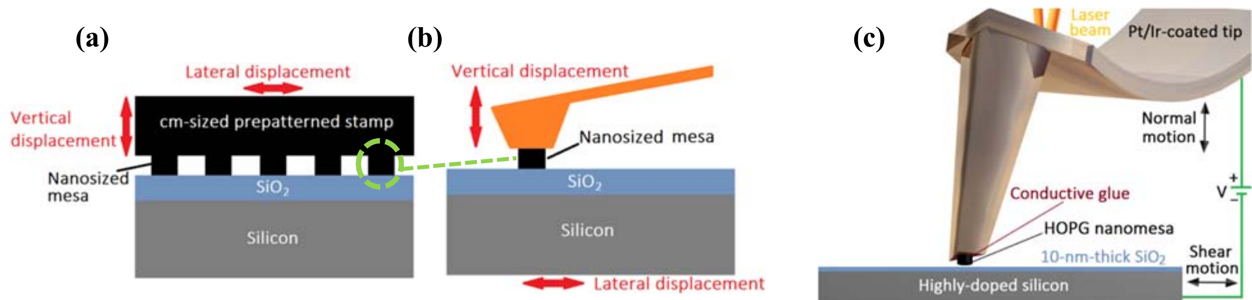

Figure 2.19. (a) Schematic of a typical macro-scale exfoliation setup and (b) the corresponding nano-scale AFM-based exfoliation setup. (c) Schematic of the CAFM experimental setup used to perform shear and normal electrostatic exfoliation of FLG from nanosized HOPG mesa onto the SiO_2/Si substrate.

2.5.1 Nano-sized HOPG mesas

A ~100-nm-thick bilayer of polymethyl methacrylate (PMMA) 495K (60 nm)/950K (40 nm) is spin coated onto the freshly cleaved surface of 1-mm-thick HOPG substrate (SPI-1 grade with a mosaic spread value of 0.4º), baked each layer for 10 min at 120 °C to evaporate the solvent and then patterned by electron beam lithography. After developing the exposed PMMA area in 1:3 MIBK/NMP, a 10-nm-thick aluminum film is deposited by thermal evaporation, followed by a lift-off step. To thin down the unprotected HOPG area, oxygen plasma etching is carried out in a reactive ion etching system using pure O_2 as the reactive gas. Cylindrical mesas with a radius of 30 nm and etch depth of 75 nm emerge from the HOPG substrate during the plasma etch. After plasma etching, the sample is soaked in 0.1 mol/l KOH water solution for ~3 min to remove the Al layer, followed by an annealing process at 600 °C under constant Ar/H_2 flow for one hour to remove any resist/metallic residues from the HOPG substrate. **Figure 2.20(a)** shows the AFM and SEM images of cylindrical mesa arrays. The sidewall profile in the AFM images is steep, indicating that a low etch rate of 15nm/min for the fabrication of the mesa structures results in a minor sidewall taper toward the substrate. Also, nanometer-sized mesas in our experiments can guarantee the presence of a single-crystalline grain across the whole mesa.

2.5.2 In-situ preparation of flat AFM tips

We used Pt/Ir_5-coated AFM probes (Nanosensors, ATEC-EFM) with a radius of curvature of less than 20nm at the apex. As can be seen in **Figure 2.20(b)**, the tip is positioned at the very end of the cantilever and pointing outwards, which allows a very exact positioning of the tip. Since our experiments require a flat plateau at the apex parallel to the SiO_2/Si surface, we scanned the tips in contact mode on the SiO_2/Si substrate for 15-30 minutes at a load of 2 μN and 65-70% relative humidity, followed by cleaning the flattened tips via a polishing over ultra-smooth monolayer graphene for 15 min at a load of 200 nN to achieve a residue-free contact surface. Once polished, the surface area of the tip was measured in a scanning electron microscope for the subsequent attachment of FLG onto the flat tip via a conductive adhesive PEDOT:PSS(D-sorbitol), as shown in **Figure 2.20(c)**. This in-situ preparation of the flattened tips can account for a tilt angle of 12º in the cantilever (which is provided by our XE-70 AFM head) such that the flattened tips are parallel to the substrate surface, as can be seen in the inset of **Figure 2.20(c)**.

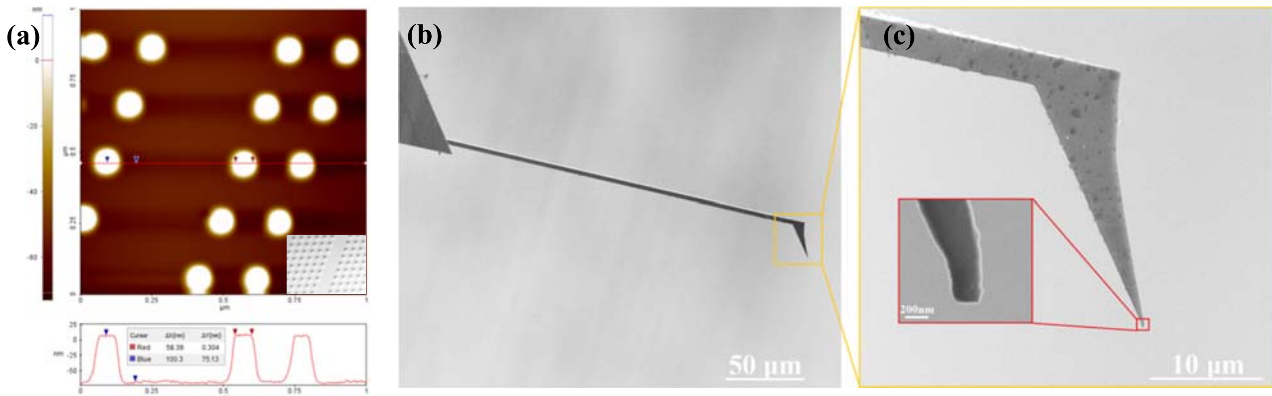

Figure 2.20. (a) AFM image (top) and height profile (bottom) of 75-nm-deep cylindrical mesas with a diameter of 60 nm from HOPG. Inset: SEM image of the nano-sized HOPG mesa arrays. (b) Pt/Ir_5-coated AFM probe tilted at an angle of 12º due to the mount of Park XE-70 AFM head. (c) SEM image of AFM tip after the fattening procedure. Inset: Flat surface of AFM tip.

2.5.3 Probe tip characterization

Our preliminary SEM observation of the tip at the apex area suggests a very flat triangular shape, as shown in **Figure 2.21(a)**. The surface roughness and the triangular contact area of the tip apex can be accurately measured through imprints on the 50-nm-thick PEDOT/PSS thin film and AFM tapping-mode imaging, as shown in **Figure 2.21(b)**. The AFM

indent profile of the tip confirms an atomically flat surface with an RMS roughness of < 0.5 nm. The contact surface area of the tip was measured to be 0.0135 μm^2.

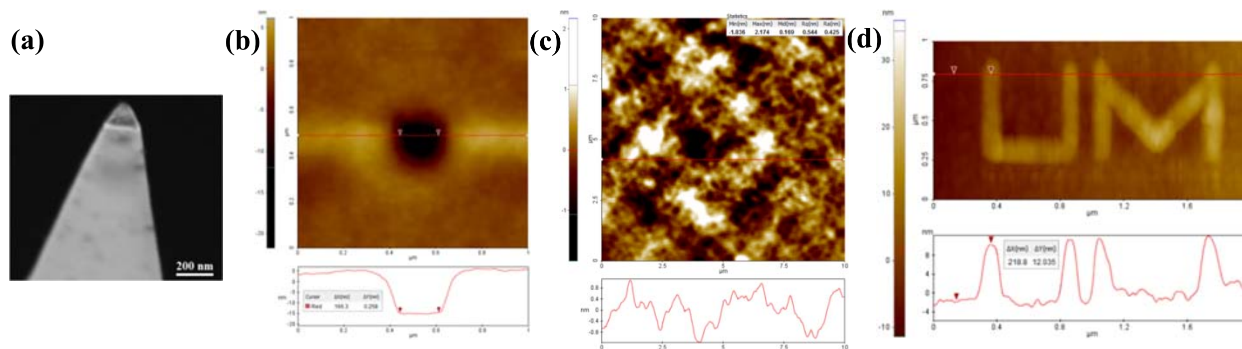

Figure 2.21. (a) SEM image of the flattened tip. (b) Tapping-mode AFM topography image of nanoindentation of the flattened tip apex into the 50-nm-thick PEDOT/PSS thin film on the SiO_2/Si substrate. The indented profile, taken along the red arrow, shows a very flat and smooth surface. AFM topography image (top) and height profile (bottom) of (c) a 25-nm-thick PEDOT:PSS(D-sorbitol) film and (d) raised letters 100 nm width and 12 nm height, formed at -5 V with a tip speed of 0.5 um/s.

2.5.4 Adhesive and conductive polymer

Poly(3,4-ethylenedioxythiophene):poly(styrenesulfonate) (PEDOT:PSS) aqueous solution (Clevios™ PH 1000) was purchased from Heraeus Company. The concentration of PEDOT:PSS was 1.3% by weight, and the weight ratio of PEDOT:PSS was 1:2.5 in the solution. 0.45µm syringe filters made from PVDF were used to remove any possible residual gel or dried particulates from the PEDOT:PSS. D-sorbitol, as an organic compound with a hydroxyl group, was added into the PEDOT:PSS aqueous solution with 10:90 ratio to make PEDOT:PSS adhesive without sacrificing its electrical conductivity. The highly adhesive and conductive PEDOT:PSS(D-sorbitol) film was formed by spin-coating this blended solution at 8000 rpm on the SiO_2/Si substrate which was pre-cleaned sequentially with DI water, acetone and isopropyl alcohol. After baking at 90 °C for 60 min to remove the water, the electrical conductivity of the PEDOT:PSS(D-sorbitol) film was measured as 690 S/cm on the SiO_2/Si substrate using the four-point probe technique. The thickness of the film (~25 nm) was measured at different positions by gently scratching the surface with a sharp needle and measuring the height difference between the film and the substrate surface using the contact-mode AFM. An AFM topography image of the PEDOT:PSS(D-sorbitol) film shown in **Figure 2.21(c)** reveals a very smooth surface with an RMS surface roughness of ~2 nm.

2.5.5 High precision attachment of FLG to the AFM tips

Using an approach-retract technique, the flattened tip is coated with a very thin layer of conductive polymer glue by putting the tip apex in gentle contact (at zero normal force) with the pre-baked 25-nm-thick PEDOT:PSS(D-sorbitol) film on an electrically grounded SiO_2/Si substrate. Applying a negative bias voltage of 5 V to the probe results in the formation of raised features in the film (**Figure 2.21(d)** displays a representative structure formed by this AFM-assisted electrostatic technique in the film), followed by the mass flow of the locally softened polymer toward the tip apex due to localized Joule heating and strong electric field gradient. The location of each mesa is then determined by switching the operational mode of the AFM to non-contact mode which allows us to avoid any contact between the glue-coated flattened tip and the mesa surface during the image scanning. Although the tip apex is flat, the non-contact mode can still provide us with desired resolution imaging for the subsequent attachment of the mesa to the tip. Switching the mode of operation back to the contact mode, the glue-coated tip apex is then moved to the center of the selected mesa at an applied normal force of 200 nN, and subsequently the mesa/apex contact area is annealed at 95 °C for 30 min using a thin film heater beneath the HOPG substrate. Since D-sorbitol must be melted at 95 °C to act as glue, this annealing step is required to uniformly adhere the HOPG mesa to the tip apex. We then move the tip laterally along a single basal plane of graphite, leading to easy shear of the upper section of the mesa (attached to the tip apex) relative to the lower one (fixed to the HOPG substrate), thanks to the extremely low friction of graphite at an incommensurate contact interface (i.e., the superlubric state). **Figure 2.22(a-c)** shows a firm attachment of a 25-nm-thick HOPG cylindrical mesa onto the flat tip surface. Comparing the height of the mesa on the HOPG substrate before and after the shear motion of the AFM tip, one can estimate the number of graphene layers attached to the tip.

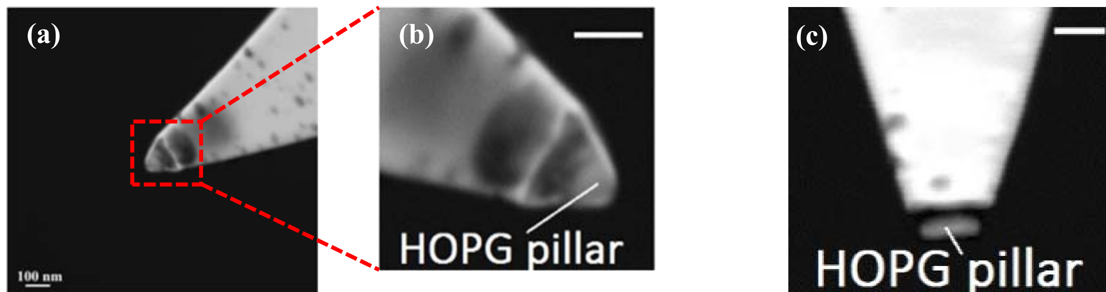

Figure 2.22. (a) SEM image of the probe tip with (b) the corresponding zoom-in image, showing a firm attachment of a cylindrical mesa onto flat tip surface. (c) Side-view of the tip with an attached HOPG nanomesa. In (b) and (c), scale bars indicate 50 and 100 nm, respectively.

2.5.6 Layer number identification

Before Raman measurements, the FLG sheets were characterized by color contrast under optical microscopy and also by AFM topographic measurements to determine the layer number. In order to identify the number of layers with monolayer accuracy, Raman measurements were performed under ambient conditions using an ultra-low noise Renishaw inVia Raman microscope with 532 nm (2.33 eV) laser excitation (**Figure 2.23**). To avoid laser-induced heating, the laser power at the sample was set to be below 1 mW. A 100× objective lens with a numerical aperture (N.A.) = 0.95 was used in the Raman experiments. Several Raman spectra of each *N*-LG sample were collected to ensure the repeatability of the results. In our Raman spectra, we did not observe the rotating modes R (~1483-1496 cm^{-1}) and R' (~1622-1626 cm^{-1}) nor any change in the integrated intensity of the G and 2D bands in the printed bilayer and multilayer graphene, which is indicative of AB stacking [5].

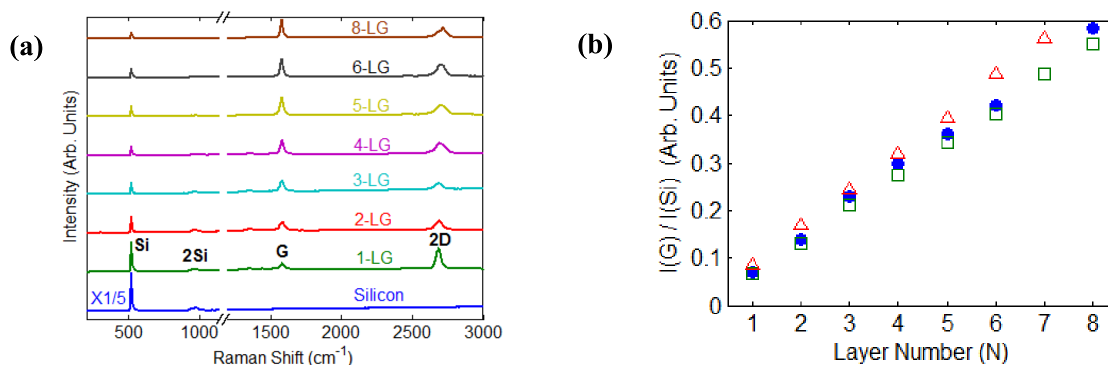

Figure 2.23. (a) Raman spectra of *N*-LG flakes. The four most intense peaks are first-order (Si) and second-order (2Si) optical phonon peaks of the silicon substrate, and G and 2D peaks of graphene. Raman spectra are scaled and upshifted for clarity. The scaling factors of 1/5 and 1 are used for $\omega<1200cm^{-1}$ and $\omega>1200cm^{-1}$, respectively. (b) The ratios of the integrated intensity of the G and Si peaks, I(G)/I(Si), versus layer number *N*. Blue circles are present data, red triangles and green squares are data measured for mechanically exfoliated *N*-LG on 280-nm-thick-SiO_2/Si at λ=488 nm and on 89-nm-thick-SiO_2/Si at λ=532 nm, respectively.

2.5.7 Results and discussion

In our proposed setup, the exfoliation of FLG features is a combined action of the electrostatic force, contact pressure, vdW force, sliding/retraction speed of the tip, surface properties of SiO_2, and ambient conditions. To narrow down the range of possible experimental parameters, we carry out all measurements on the same SiO_2 film at zero normal load with a relative tip-substrate speed of 10 nm/s under a clean and controlled environment (20% relative humidity at 21°C). Our preliminary shear and normal printing measurements in the absence of

bias voltage reveal no graphene exfoliation under the aforementioned experimental conditions, allowing us to elucidate the key role of the electrostatic and interlayer vdW forces in the subsequent electrostatic exfoliation process.

The histograms in **Figures 2.24(a)** and **(b)** show the number of printed layers as a function of the bias voltage using the shear and normal exfoliation techniques, respectively. Raman spectroscopy coupled with AFM height profile measurements are used to determine the layer number with monolayer accuracy. Ten measurements are taken for each applied bias voltage. It is evident from **Figures 2.24(a)** and **(b)** that the shear exfoliation method produces only 1–3 layers (predominantly mono and bilayer graphene) at different bias voltages (**Figure 2.24(c)**), whereas the normal exfoliation method yields graphene flakes of various thicknesses (ranging from 1 to ~20 layers) in a very stochastic manner (**Figure 2.24(d)**). We will later show in our analysis of the MD trajectories (see Chapter 4) that the weaker interlayer cohesion during the normal exfoliation process facilitates the localized delamination, thereby triggering the relative twist between the adjacent commensurate graphene flakes and thus making accurate control of the number of printed flakes almost inaccessible. In contrast, the shear exfoliation method exhibits much more robust sliding behavior with the slight change in the interlayer twist angles due to enhanced corrugation of the interlayer potential energy. **Figure 2.24(c)** also shows the SEM image of mono-,bi-, and trilayer graphene flakes printed by the shear exfoliation method in the form of letter "M" at V = 10 V, further indicating its versatility for the production of graphene flakes with high crystalline quality and uniform thickness (see the inset of **Figure 2.24(c)**). We note that regardless of the applied bias voltage, an unexpectedly thick mesa might be produced by the shear exfoliation method provided any twist grain boundaries exist along the thickness (c-axis) direction of the HOPG nanopillars (**Figure 2.24(e)**). AFM measurements and a combination of FIB/SEM and high-resolution TEM also confirm a polycrystalline structure along the c-axis direction of HOPG with a grain thickness of 11-60 nm and 5-30 nm, respectively [5]. Hence, during the attachment of the mesa to the glue-coated tip apex, we moved the AFM tip laterally rather than vertically to achieve a single crystalline HOPG nanopillar which is necessary to avoid any possible shear exfoliation of thick mesas.

To investigate the atomistic details underlying our experimental results, we first need to correctly understand the role of the number of layers and the external electric field in the interlayer electrostatic behavior of FLG flakes which will be the topic of my next chapter.

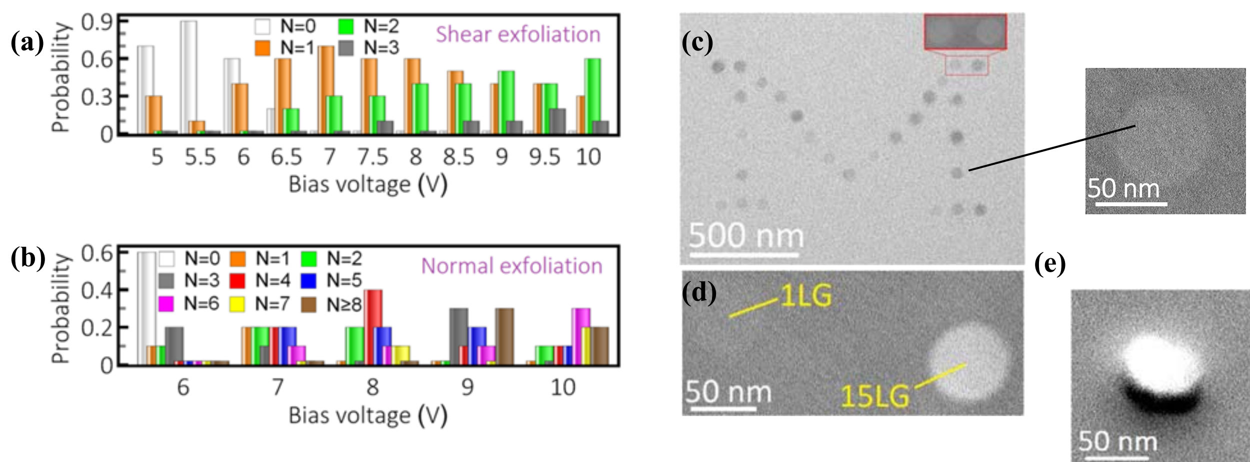

Figure 2.24. (a) Shear exfoliation and (b) normal exfoliation histograms of the number of printed flakes collected from 110 and 50 samples, respectively, under different bias voltages. (c) SEM image of mono-, bi-, and trilayer graphene flakes printed by the shear exfoliation method in the form of the letter "M" at V = 10 V. (d) SEM image of monolayer and 15-layer graphene flakes printed by the normal exfoliation method at V = 9.5 V. (e) SEM image of an incompletely sheared HOPG nanopillar at an incommensurate basal plane 18 nm above the substrate at the bias voltage of 10 V.

2.6 Summary

We first demonstrated a novel plasma–assisted exfoliation approach for producing ordered arrays of few-layer-MoS_2 device features. In this process, the relief structures were prepatterned onto a bulk MoS_2 film, which served as a stamp for printing out orderly arranged MoS_2 pixel patterns over cm^2-scale areas on both pristine and plasma-charged SiO_2 substrates. MoS_2 pixels printed on plasma-charged substrates featured a higher degree of uniformity in pattern profiles and a narrower distribution of the MoS_2 flake thickness (i.e., 3±1.9 nm) in comparison with those printed on pristine substrates. This was attributed to the strong fringe field around the feature edges that was induced by plasma-introduced electric charges. We demonstrated that such printing approaches can be generalized for producing other emerging atomically layered nanostructures (e.g., graphene nanoribbons).

We next presented a top-down nanofabrication approach, termed as nanoimprint-assisted shear exfoliation (NASE), which is capable of producing high-quality multilayer MoS_2 structures with a good uniformity of feature thicknesses as well as electronic properties. NASE uniquely combines the nanoimprinting and shear exfoliation of prestructured layered nano/microstructures into polymeric fixing layers. Our experiments demonstrated that such a NASE mechanism can result in high-quality 40–200 nm high, 10–15 µm size MoS_2 flake arrays with a high uniformity of flake thicknesses (*i.e.*, relative thickness error ∼12%) over cm^2-scale areas, which surpasses

the performance of previously reported exfoliation methods for generating layered materials, in terms of large-area ordering and thickness uniformity of exfoliated structures. Furthermore, our MD simulation results of NASE processes suggested that the presented shear-exfoliation mechanism could be further developed for generating nanoscale-lateral-size layered structures for meeting the ever-evolving demands for device miniaturization. Such a MD simulation model also provided critical information for understanding the effects of the geometric dimensions of prestructured stamping structures on the resultant morphology of NASE-produced layered nanostructures.

Finally, to gain an in-depth understanding of the interlayer vdW interactions in 2DLMs during the exfoliation/printing course, I qualitatively studied the mechanical response of interlayer vdW interactions to the external shear or normal forces by gently moving an in-situ flattened, CAFM tip with an attached nanomesa away from the substrate in a direction parallel or normal to the basal plane of 2D crystals, followed by shear and normal exfoliation of high-quality mono- and few-layer 2D crystal features onto the substrate. Our CAFM-assisted electrostatic technique showed that high-quality mono- and bilayer graphene is reliably produced at significant yields only by the shear type of bond breaking between layers, whereas the normal type of bond breaking exhibits a very stochastic process. To gain a detailed understanding of underlying mechanisms associated with the normal and shear electrostatic exfoliation of 2DLMs, a series of MD simulations will be performed in **Chapter 4**.

CHAPTER 3

Interfacial Electrostatic Behavior of 2D Layered Materials: Few-Layer Graphene

3.1 Introduction

Since its discovery in 2004, single-layer graphene (SLG) has become the most studied nanomaterial due to its exceptional mechanical, electrical and optical properties. Although several physical properties are shared between SLG and few-layer graphene (FLG), increasing layer thickness can give rise to a unique range of electronic and structural properties that has not yet been sufficiently understood. More specifically, electrical noise, charge transport and nonlinear optical properties of FLG on substrates (usually SiO_x/Si) exhibit strong dependence on the number of layers, gate-induced charge densities and underlying oxide substrates. It is therefore crucial in the design of FLG-based electronics to quantitatively understand the role of the number of layers in the charge distribution and the electric field screening of the FLG/SiO_2/Si systems and to explore the unclear relationship between the excess gate-induced charge densities and layer-by-layer Fermi level and charge density profiles in FLG systems.

In order to correctly understand the ability of FLG systems to store electrical energy in an electric field, we first need to precisely quantify the effect of layer number and electric field on the dielectric screening properties of FLG flakes. Despite the importance of such a fundamental property for any electronic material, there have been very limited studies with significant diversity in the reported values of the dielectric constant of graphitic systems, ranging from 2 to 16 [34-40] (**Table 3.1**). Surprisingly, however, there is no direct experimental evidence for the dependence of the dielectric constant of FLG on the layer number and the electric field. To fill this apparent gap, we first perform a series of dielectric measurements on the one-to-eight layers of graphene mechanically exfoliated on the SiO_2/Si substrate under ambient conditions but different electric fields using a dc electrostatic force microscopy (DC EFM) technique. We then study the effect of oxidation and thermal annealing on the dielectric constant of mono-, bi- and few layers of graphene (**Section 3.2**).

Table 3.1. Dielectric constant measurements of different graphitic systems.

Graphitic systems	Methods	ε_r
Single-walled carbon nanotube on 2-nm-thick SiO_2/Si substrate [34]	Electrostatic force microscopy	10
Mechanically-exfoliated, freestanding monolayer graphene [35]	Inelastic x-ray scattering	15.4
Mechanically-exfoliated, freestanding monolayer graphene [36]	Inelastic x-ray scattering	6.6–8.8
Mechanically-exfoliated, freestanding monolayer graphene [37]	Shubnikov-de Haas oscillation	2.2–4.9
Quasi-freestanding monolayer graphene grown on carbon face of SiC [38]	High-resolution angle-resolved photoemission spectroscopy	7.8
Quasi-freestanding monolayer graphene grown on carbon face of SiC [39]	High-resolution angle-resolved photoemission spectroscopy	6.4±0.1
CVD-grown monolayer graphene on BN/SiO_2/Si substrate [40]	Scanning tunneling microscopy	3±1

Moreover, due to the importance of the subject, the question of interlayer charge screening length λ in the FLG systems has been addressed by several experimental methods, including angle-resolved photoemission spectroscopy [41], nondegenerate ultrafast mid-infrared pump-probe spectroscopy [42], Kelvin probe force microscopy [43, 44, 45], single-gated field effect transistor [46], double-gated field effect transistor [47] and dark-field scattering spectroscopy [48]. However, a relatively wide range of experimental values for λ (from less than a single layer to seven layers) is observed, which is not yet fully understood (**Table 3.2**). Nevertheless, a part of this data scattering may be attributed to the dependence of the screening length on the device quality and experimental conditions, such as sample preparation processes, the presence of defects and impurities in graphene, the intrinsic charge density in each graphene layer and the actual doping level of the system. This diversity in the reported values of λ is also seen in theoretical approaches. Depending on whether the inter-layer electron tunneling is taken into account or not, λ between 0.54 nm [49] and 0.7 nm [50] is obtained using a random phase approximation. Kuroda and coworkers theoretically reported that both the gate charge and temperature could highly influence λ, whose value may range from ~0.2 nm to 3.1 nm [51].

Table 3.2. Charge screening depth measurements in FLG systems.

#	Methods	λ (nm)	Ref.
1	Angle-resolved photoemission spectroscopy	0.14−0.19	[41]
2	Nondegenerate ultrafast mid-infrared pump-probe spectroscopy	0.34	[42]
3	Kelvin probe force microscopy	1.36−1.70	[43]
4	Kelvin probe force microscopy	0.42	[44]
5	Kelvin probe force microscopy	2.4	[45]
6	Single-gated field effect transistor	0.6	[46]
7	Double-gated field effect transistor	1.2	[47]
8	Dark-field scattering spectroscopy	1.2±0.2	[48]

Finite-size FLG flakes and graphene nanoribbons in actual devices exhibit an intriguing dependence of the electrostatic and electrical conductivity response on their geometrical parameters (e.g., lateral sizes, thicknesses, shapes and edge types) [52]. Both experimental and theoretical studies have demonstrated that a strong charge accumulation takes place at the edges of the finite-size graphene flake due to the electrostatic fringe field effects. Scanning gate microscope measurements of a monolayer graphene device on a SiO_2/Si substrate reveal significant conductance enhancement at the edge of the graphene device due to the strong charge accumulation [53]. Similar observations of inhomogeneous charge density and capacitance profiles near the edges of both suspended and hBN-supported mono/bilayer graphene devices have been reported using quantum Hall edge channels [54]. Among different theoretical models on the charge distribution of the finite-sized graphene, we particularly note a strong charge accumulation at the edges and the corners of a positively charged rectangular graphene sheet using the charge/dipole molecular dynamics model [55] and along the edges of a graphene nanoribbon using the tight-binding model [56].

Despite recent progress, a detailed understanding of the electrostatic charge distribution in connection with the actual electronic structure of finite-size FLG is still lacking. In particular, quantification of nonlinear charge density profile, interlayer capacitance, quantum capacitance, and local surface electrostatic potential of FLG requires an accurate model that can account for both electrostatic screening and fringe field effects on the charge distribution of the finite-size FLG system. Also a general model that can not only characterize the charge density profile, interlayer screening, quantum capacitance, and local surface potential of other 2DLMs and vdW heterostructures, but also unravel the relationship between the macroscopic induced charge density and sub-nanoscopic (layer-by-layer) charge distribution in finite-size 2DLMs is still missing. As such, we exploit the layered nature of FLG to develop a novel spatial discrete model that successfully accounts for both electrostatic screening and fringe field effects on the charge distribution of the finite-size FLG system. We utilize an effective bilayer model based on two tight-binding parameters to accurately describe electronic band structures and density of states (DOS) of one to eight Bernal-stacked graphene layers. In order to verify the accuracy of the results predicted by the discrete model, we compare our local surface potentials with those measured by our DC EFM method, angle-resolved photoemission spectroscopy, and Kelvin probe force microscopy (**Section 3.3**).

3.2 Dielectric Constant Measurements of FLG

Figure 3.1(a) shows the AFM topography image of 1-8 graphene layers mechanically exfoliated from HOPG onto a 10-nm-thick SiO_2/Si substrate. A sharp needle is used to gently scratch through the thin SiO_2 film and expose the underlying Si for the dielectric constant measurement of the SiO_2 film as a validation of our subsequent experimental results. The height profile along the green line in the topography is shown in **Figure 3.1(b)**. In our setup, the contact potential difference (V_{CPD}), capacitance gradient ($\partial C/\partial z$) and the vdW force (F_{vdW}) between the tip and sample surface are first measured by acquiring the total force (sum of electrostatic force, F_{el}, and F_{vdW}) on the Pt/Ir-coated tip (SCM-PIT, Nanoworld, with the spring constant of 1.9 N/m, **Figure 3.1(c)**) while sweeping the bias voltage between -3 and 3V on the sample surface at different tip-sample distances. The total force can be given by

$$F(z,V,\epsilon_r) = -\frac{1}{2}\frac{\partial C(z,\epsilon_r)}{\partial z}[V - V_{\mathrm{CPD}}(z)]^2 + F_{\mathrm{vdW}}(z) \tag{3.1}$$

where the first term represents the electrostatic force. This parabolic equation with three fitting parameters ($\partial C/\partial z$, V_{CPD} and F_{vdW}) is used to fit F–V curves, such as the ones shown in **Figure 3.1(d)** on a 4LG/SiO_2/Si sample.

It is evident from the offset of the parabolic F–V curves along the y axis that the contribution of F_{vdW} to the total force is negligible when a bias voltage is applied, in particular,

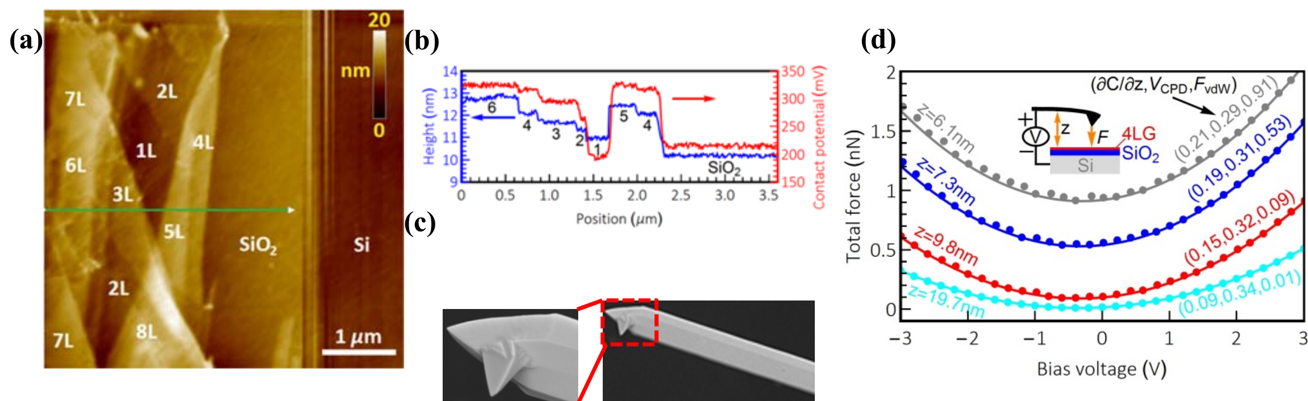

Figure 3.1. (a) AFM topography image of 1-8LG onto a 10-nm-thick SiO_2/Si substrate with the corresponding layer numbers labeled; (b) Height profile (blue line) and contact potential difference V_{CPD} profile (red line) corresponding to the green line in (a); (c) SEM images of the conductive SCM-PIT tip used for the measurements. (d) Total force-voltage curves taken on the 4LG/SiO_2/Si substrate at each tip-surface distance. Circles are experimental data and the lines are parabolic fits using Eq. (3.1) at a constant lift height. Three fitting parameters $\partial C/\partial z$(aF/nm), V_{CPD}(V) and F_{vdW}(nN) are given for each curve

at $z > 10$ nm. Hence, throughout the experiments described in the following, we scan over the sample from a distance farther than 10 nm to only measure the electrostatic force. The fitting parameter V_{CPD} also reveals a dependence on the tip-sample distance in such a way that V_{CPD} of 4LG varies from 294 mV (at $z = 6.1$ nm) to 342 mV (at $z = 19.7$ nm). Using this method, we measured in **Figure 3.1(b)** V_{CPD} between the tip and sample surface along the same green line in **Figure 3.1(a)** at $z = 10$ nm, clearly indicating the layer-dependent surface potentials in FLG up to four layers.

In order to precisely quantify the relative dielectric constant of FLG, the electrostatic force acting on the tip needs to be calculated by integrating the Maxwell stress tensor over the surface of the probe. Since an accurate analytical model that can exactly reproduce the tip-sample electrostatic interaction is not available, we carry out three-dimensional (3D) finite element electrostatic simulations using COMSOL Multiphysics (AC/DC Electrostatics module) to calculate the Maxwell stress tensor from the electrostatic potential distribution obtained by solving the following Poisson's equation in a cylindrical space:

$$\nabla.(\varepsilon_r \varepsilon_0 \mathbf{E}) = 0 \tag{3.2}$$

where ε_r is the relative permittivity of SiO_2, air or FLG (depending on the subdomain to which Eq. (3.2) is applied); ε_0 is the permittivity of vacuum ($= 8.854 \times 10^{-12}\ \mathrm{C^2N^{-1}m^{-2}}$); $\mathbf{E}$ ($= -\nabla V$) is the electric field vector (E_x, E_y, E_z); and V is the electric potential. We also set the following boundary conditions: the electrical potential (e.g., $V = 10$V) is defined on the surface of the probe while the bottom surface of the SiO_2 substrate is electrically grounded ($V = 0$). The Neumann condition ($dV/dn = 0$) is used on the lateral and upper sides of the simulation box (**Figure 3.2(a)**).

Then, we calculate the electrostatic attractive force exerted on the tip by the integration of the Maxwell stress tensor over the surface of the probe. In a given subdomain, the Maxwell stress tensor ($\boldsymbol{\sigma}$) can be expressed by

$$\boldsymbol{\sigma} = \varepsilon_r \varepsilon_0 \left[\mathbf{EE} - \frac{1}{2}(\mathbf{E}.\mathbf{E})\mathbf{I}\right] \tag{3.3}$$

where **I** is the identity tensor.

We consider a cylindrical simulation box of radius 250nm and height >300nm, as shown in **Figure 3.2(a)**. The probe is modeled as a solid truncated cone of height 250nm and the half cone angle 15° with a semi-spherical apex of radius *R* positioned in the truncated region (tangent

to the cone surface, forming continuity in the geometry) and at a distance z from the substrate. The FLG film is modeled as a solid cylinder of radius 250nm, height h, and relative dielectric constant, ε_r, over the 10-nm-thick SiO_2 substrate of $\varepsilon_r = 3.8$ (which is obtained in the absence of FLG). The air surrounding the probe is modeled as empty space of $\varepsilon_r = 1$. We adopt an extra-fine tetrahedral mesh for the entire simulation box, except for the tip apex, FLG and SiO_2 thin films where an extremely fine tetrahedral mesh is applied for better numerical accuracy. **Figure 3.2(b)** shows, as an example, the cross-section of 3D finite element calculation of the electrostatic field distribution between the tip and the 28LG/SiO_2 sample at z=10nm and V=10V (see the inset of **Figure 3.3(a)** for the corresponding potential distribution).

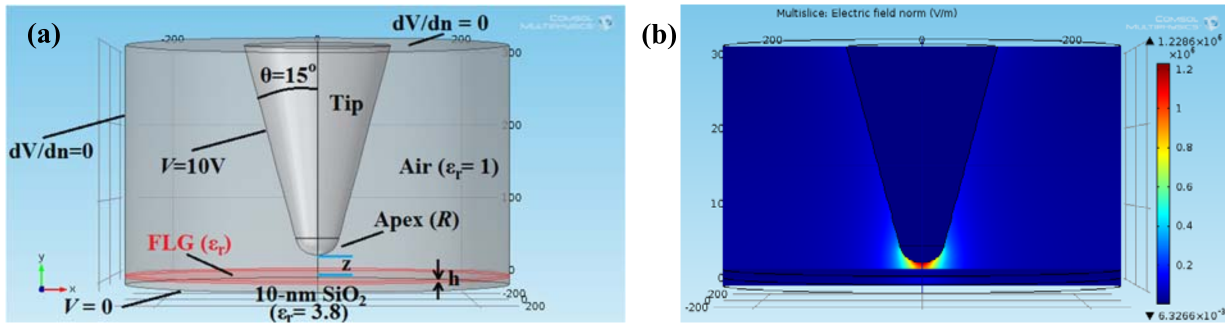

Figure 3.2. (a) Geometric representation of the tip-FLG/SiO_2 system along with the parameters used in electrostatic 3D finite element calculations. (b) Cross-section of 3D finite element calculation of the electrostatic field distribution between the tip and the 28LG/SiO_2 sample at a tip-surface distance of 10nm. The applied potential between tip and substrate is V=10V.

We first calibrate the apex geometry of the probe by taking electrostatic force-distance (F_{el}–z) curves on a conductive surface (e.g., highly-doped silicon or HOPG) close to the graphene flakes. However, we note that only local electreostatic force at the tip apex depends strongly on the tip-sample distance within the range 10-150 nm and thus the global electreostatic contribution from the cantilever shank and the cone is negligible. As such, in **Figure 3.3(a)** the electrostatic force on the tip apex is obtained by subtracting the electrostatic force of the cantilever shank/cone at $z > 200$ nm from the total force. All F_{el}–z curves were fitted with our finite-element calculations over a 10-150 nm tip-sample distance at V = 10 V, using the effective apex radius R as the only fitting parameter, while the nominal half cone angle was fixed at $\theta = 15°$. From ten F_{el}–z measurements (similar to the one shown in **Figure 3.3(a)** on the bar silicon surface), we found R to be 28 ± 0.5 nm which is consistent with the nominal value ~20 nm provided by the manufacturer.

After V_{CPD} and R were determined as a prerequisite for the accurate quantification of the dielectric constant of the FLG, we next measure the F_{el}–z curves on the graphene flake of different thicknesses, followed by matching the finite-element results to the experimental data using the only fitting parameter ϵ_r. We illustrate in **Figure 3.3(a)** the F_{el}–z curves on the bare silicon (for the sake of tip calibration), on the 10-nm-thick SiO_2 (for comparison purposes) and on the 28LG (a thicker flake was chosen for more clarity in the figure). From several measurements on different areas of the sample, we obtain $\epsilon_r = 20.1 \pm 1.9$ for the 28LG and $\epsilon_r = 3.86 \pm 0.67$ for the ultrathin SiO_2 film (in good agreement with the corresponding bulk material 3.8 [57] and ultrathin films $\sim 4.0 \pm 0.9$ [58, 59]). For further comparison, we revisited the dielectric constant of SWCNTs on 2-nm-thick SiO_2/Si substrate, reported by Lu et al. using a combination of scanning force microscopy and finite element electrostatic simulations [60]. As shown in **Figure A.1** (**Appendix A**), 3D modelling of an SWCNT of diameter 3 nm as a hollow cylinder rather than a solid cylinder leads to the dielectric constant of ~22.5, which is more than twice as large as that of a solid SWCNT of the same diameter. This modified value for the dielectric constant of SWCNTs is more consistent with that of 28LG.

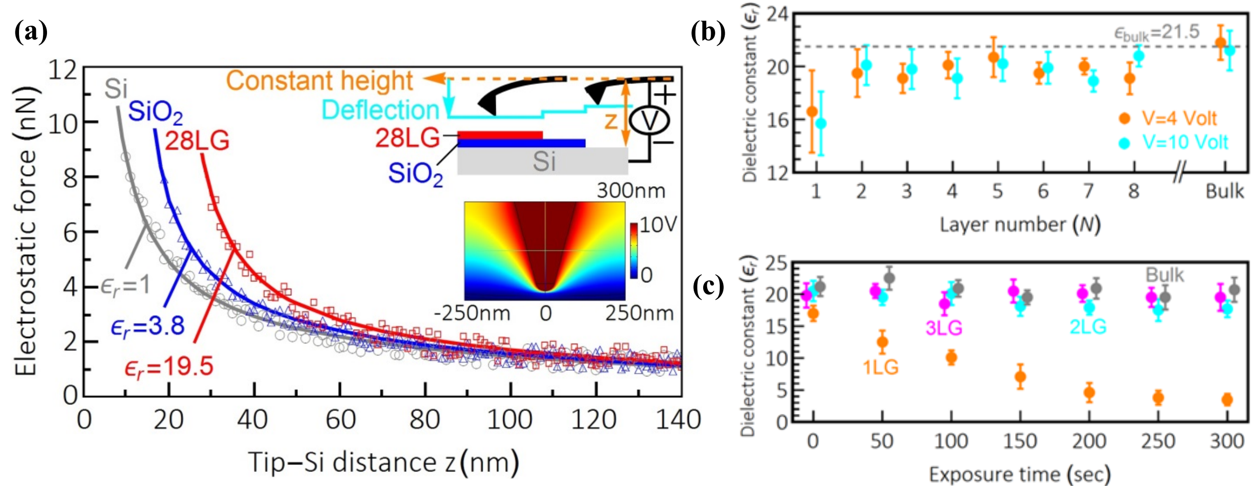

Figure 3.3. (a) Measured electrostatic force versus tip-Si distance taken on the bare Si surface (gray circles), on the 10-nm-thick SiO_2 film (blue triangles), and on the 28LG (red squares) at $V = 10$ V. The lines are theoretical fittings to Eq. (1). Top inset shows that as the tip moves across the sample surface in constant height, the tip experiences a larger electrostatic force on 28LG than that on Si and SiO_2. Bottom inset shows the cross-section of 3D finite element calculation of the electrostatic potential distribution between the tip and the 28LG/SiO_2 sample (see **Figure 3.2(b)** for the corresponding electric field distribution); (e) Relative dielectric constant as a function of the layer number under relatively low and high bias voltages. The application of the bias voltage $\leq$ 3V makes the dielectric response extremely weak in our setup. The dashed line is a guide to the eyes and represents the dielectric constant of the bulk HOPG; (f) Dependence of the relative dielectric constant of 1-3LG and bulk HOPG on oxygen reaction at V=10 V.

We now perform a series of similar dielectric measurements on the 1–8 LG of **Figure 3.1(a)** under ambient conditions and the extracted dielectric constants are shown in **Figure 3.3(b)**. Although the dielectric screening ability of 1LG is relatively weaker (~20%) than that of bulk HOPG, the overall dielectric response of FLG samples to the external electric field is almost independent of the number of layers. Interestingly, the presence of a relatively strong electric field of E=0.1V/Å (or equivalently 10V/10nm) does not show any systematic change in the dielectric response of FLG. These observations are in sharp contrast with density functional theory (DFT) calculations of effective dielectric constant of freestanding 2-10LG [27] where ϵ_r varies from ~3 (for 2LG) to ~8 (for 10LG) at E=0.1V/Å and becomes electric field-dependent for E>0.01V/Å.

A relatively large variation in the measured dielectric constant of monolayer graphene under ambient conditions (**Figure 3.3(b)**) motivates us to study the possible effect of surface reaction on the dielectric response of the FLG. To do so, we oxidized the FLG using a modified Hummer's method in which the FLG/SiO_2/Si substrate was dipped into the diluted oxidant solution (60% H_2SO_4:0.01M $KMnO_4$ = 1:1) for up to 5 min, followed by deionized water rinse and an N_2 dry. In **Figure 3.3(c)**, our measurements on the FLG under different exposure times reveal a strong dependence of the dielectric constant of monolayer graphene on the surface reaction which makes it an excellent charge screening material upon 300s oxidation, whereas bilayer graphene and FLG exhibit very high oxidation resistance. We also observed that vacuum thermal annealing of monolayer graphene at 400°C for 5 h can fully recover its charge storage capability, making it a unique material with a wide range of dielectric response upon oxidation/thermal annealing.

3.3 Layer-by-Layer Insight into Electrostatic Charge Distribution of FLG

In FLG systems on a dielectric substrate such as SiO_2, the addition of each extra layer of graphene can drastically alter their electronic and structural properties. Here, we map the charge distribution among the individual layers of finite-size FLG systems using a novel spatial discrete model and extract the interlayer charge screening length in FLG. We first examine the charge distribution of an FLG/SiO_2/Si system containing N (up to 8) layers of finite-size graphene sheet with desired shapes (i.e., square, rectangle, circle or ribbon), as schematically illustrated in **Figure 3.4**. Each graphene layer is labeled by an integer number starting from $i = 1$ for the layer

closet to the substrate (hereafter referred to as the innermost layer) to $i = N$ for the top layer (as the outermost layer). Applying a bias voltage V_0 between the highly-doped Si substrate and N-layer graphene (N-LG) induces a total excess charge density of Q_0 in N-LG, whose layer i can carry a charge density of Q_i such that the following constraint holds $Q_0 = \sum_{i=1}^{N} Q_i$.

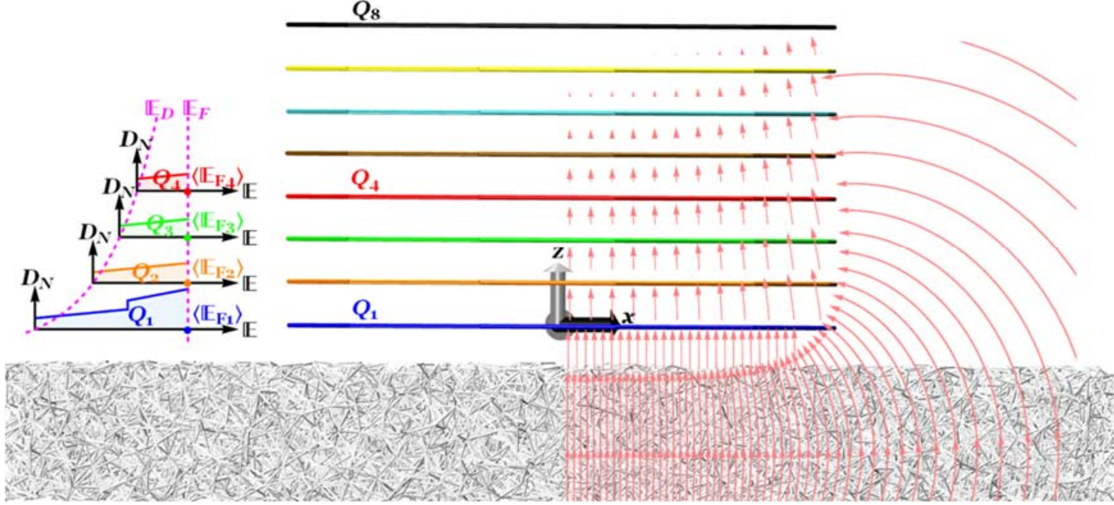

Figure 3.4. Schematic illustration of an eight-layer graphene/SiO_2 system. The Si substrate beneath the SiO_2 film is not shown for simplicity. The arrows correspond to the electric field lines focusing near the edges of FLG. Left inset: density of states in the four innermost graphene flakes versus the electronic band energy, where the transparent area represents the average induced charge density Q_i and the average value of the Fermi energy profile is denoted by $\langle \mathbb{E}_{Fi} \rangle$.

The electronic bands of N–LG can be modeled by two tight-binding parameters, namely, the nearest neighbor hopping parameter γ_0 (which defines the Fermi velocity $v_f = (3/2)\,\gamma_0 a/\hbar$, where $a = 0.142\,nm$ is the C-C bond length) and the nearest neighbor interlayer coupling constant γ_1. We take $\gamma_0 = 3.14\,eV$ and $\gamma_1 = 0.4\,eV$ as typical values of bulk graphite. The energy dispersion in Bernal-stacked N–LG, obtained from 2D cuts in the electronic dispersion of graphite, perpendicular to the graphene planes at specific values of $\theta = j\pi/2(N+1)$, can be given by $k_j^2 = \mathbb{E}^2/\gamma^2 \pm 2m_j^*\mathbb{E}/\hbar^2$, where $\gamma = v_f\hbar$ ($\hbar$ being the reduced Planck constant), $m_j^* = \left(\gamma_1/v_f^2\right)\sin\theta$ is the effective mass, j ($= 1,3,5,\dots,N-1$ for even layers and $0,2,4,\dots,N-1$ for odd layers) is the index of the energy band with kinetic energy $\mathbb{E}$. **Figures 3.5(a)** through **(h)** illustrate low–energy band structures of N–LG (near the K–point of the Brillouin zone) up to $N = 8$. It is seen that monolayer graphene (**Figure 3.5(a)**) exhibits a well-known linear dispersion which results in massless excitations, whereas bilayer graphene (**Figure 3.5(e)**) displays a set of four hyperbolic bands (with no Dirac electrons) touching at the so-called Dirac

point. Though the band structure of trilayer graphene (**Figure 3.5(b)**) comprises one pair of linear (monolayer-like) bands and two pairs of hyperbolic (bilayer–like) bands, tetralayer graphene (**Figure 3.5(f)**) interestingly shows only four pairs of hyperbolic (bilayer–like) bands. In general, based on the tight-binding model described above, both monolayer– and bilayer–like bands are present in odd multilayers ($N \geq 3$), whereas the band structure of even multilayers only consists of the bilayer–like bands.

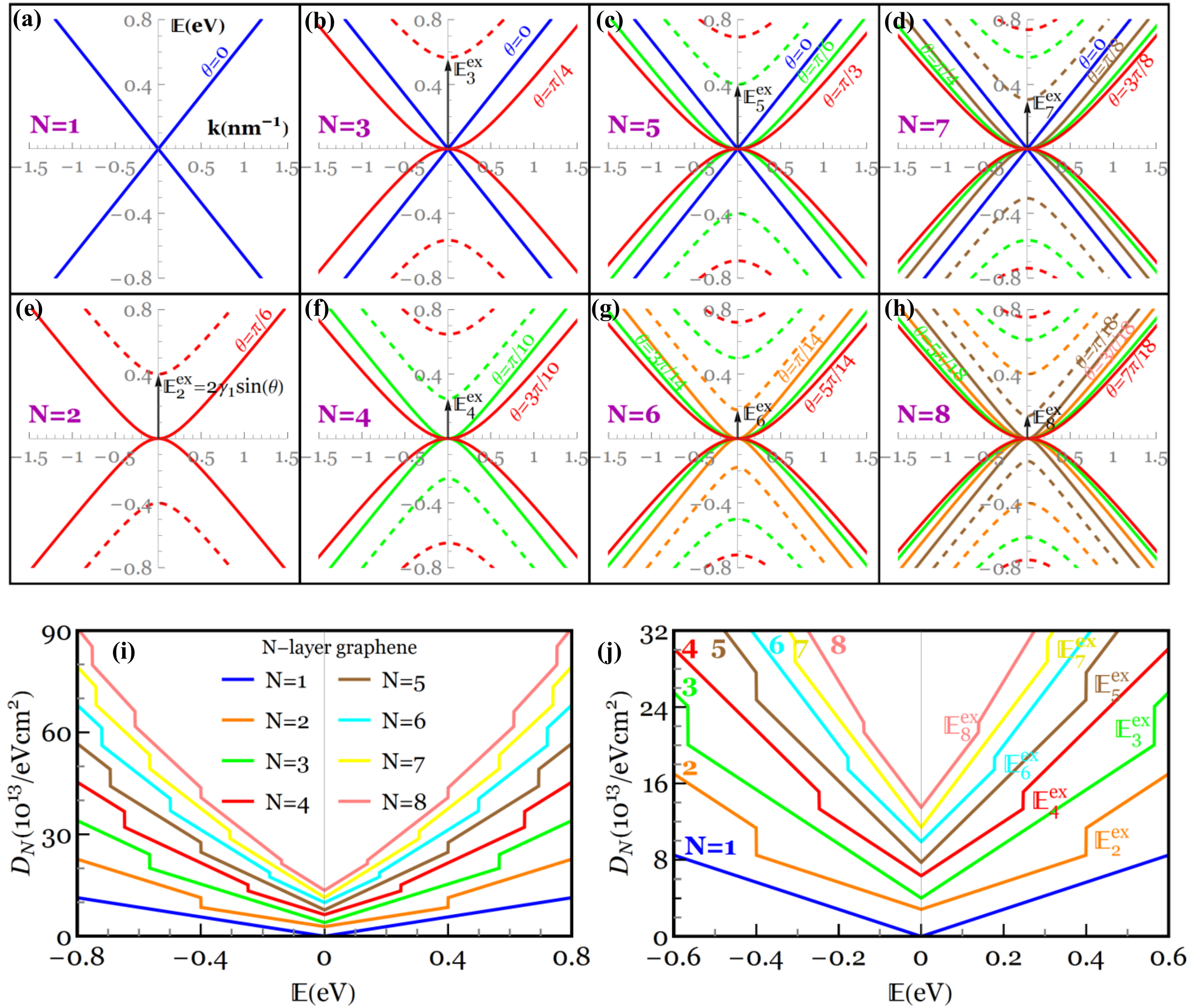

Figure 3.5. (a-h) Low–energy band structures of Bernal–stacked N–LG near the K–point of the Brillouin zone. There exist $\lfloor N/2 \rfloor$ pairs of split-off hyperbolic bands, where $\lfloor \quad \rfloor$ denotes the integer part of the quantity. The excitation energy from the ground state to the first excited state ($\mathbb{E}_N^{ex}$) is shown with arrows. Blue lines in (a)-(d) correspond to the electronic dispersion of the effective monolayer graphene ($\theta = 0$) which only appears in systems with an odd number of graphene layers, whereas red, green, pink and brown in (e)-(h) correspond to the electronic dispersion of the bilayer-like graphene ($\theta \neq 0$). Negative and positive $\mathbb{E}$ refer to the valence(hole)/conduction(electron) bands, respectively. **(i)** Density of states in N–LG showing discontinuous jumps at the excited states. **(j)** Zoom-in view of discontinuous jumps at the first excited state ($\mathbb{E}_N^{ex}$).

Figure 3.5(a)-(h) confirm that *N*–LG should be considered a single 2D system ($m_j^* \neq 0$), rather than a composite system consisting of N parallel single layers of graphene with the linear energy dispersion ($m_j^* = 0$), as experimentally confirmed by micro magneto-Raman scattering spectroscopy in 1- to 5-LG systems [61]. We will address at the end of the chapter the influence of the effective mass on the charge distributions of the *N*–LG system through comparison of our results with those obtained by a massless linear energy dispersion model.

The density of states (DOS) in *N*-LG is obtained from the summation of the DOS for each energy band with double spin and double valley degeneracies

$$D_N(\mathbb{E}) = \sum_{l=1}^{N_b}\sum_j \frac{d}{d\mathbb{E}}\left(\frac{k_j^2}{\pi}\right) = \frac{2}{\pi\gamma^2}\sum_{l=1}^{N_b}\sum_j \left[\mathbb{E} \pm \gamma_1 \sin\left(\frac{j\pi}{2(N+1)}\right)\right] \tag{3.4}$$

where N_b ($= N/2$ and $(N+1)/2$ for even and odd multilayers, respectively) is the number of bands in $\mathbb{E}$ and $j = 2l - 1$ and $2(l-1)$ for even and odd multilayers, respectively. A systematic evolution of $D_N(\mathbb{E})$ as a function of the layer number in **Figure 3.5(i)** reveals finite discontinuities at the split-off (excitation) energies $\mathbb{E}^{\text{ex}}$ ($= 2\gamma_1 \sin\theta$) which are produced by the band extrema at the K-point, followed by a linear increase with kinetic energy $\mathbb{E}$. Of particular importance for the electronic structures of N-LG at low energies is the excitation energy from the ground state (Dirac point) to the first excited state (denoted by $\mathbb{E}_N^{\text{ex}}$), as explicitly shown in **Figure 3.5(j)**.

We next determine the charge distribution profile in a finite-size N-LG stack with a circular shape of radius R, based on the method of images, followed by solving the Love equation (**Section B1.1**, **Appendix B**). The charge density profile in the circular layer i can then be expressed by

$$q_i(\mathbb{r}, \alpha_i, Q_i) = \frac{f(\mathbb{r}, \alpha_i)}{\langle f \rangle} Q_i \tag{3.5}$$

where

$$f(\mathbb{r}, \alpha_i) = \frac{g(\mathbb{r})}{\sqrt{(1+\alpha_i) - \mathbb{r}^2}} \tag{3.6}$$

is the charge distribution profile, normalized to its average value $\langle f \rangle$ for generality purposes; the index notation i varies from 1 to *N*; $\mathbb{r}$ ($= r/R$) is a dimensionless parameter; r denotes the radial coordinate of atom and $g(\mathbb{r})$ is a polynomial function of $\mathbb{r}$ which only depends on the ratio of the

graphene size to the dielectric thickness (**Figure B.1**, **Appendix B**). A new parameter α_i (> 0) is introduced by **Eq. (3.6)** in order to determine the amount of charge density at the edge of the layer i ($\mathbb{r} = 1$). Although the focus of the present work is on graphene flakes with a circular shape, we note that the charge distribution of circular graphene flakes and graphene nanoribbons is of a similar form as given by **Eq. (3.6)** and, therefore, does not qualitatively and pretty much quantitatively alter the main results of this chapter (**Section B1.2**, **Appendix B**). We also refer the interested reader to **Section B1.3** of **Appendix B** for the corresponding charge distribution profile of rectangular/square graphene flakes.

As we already discussed, in practice, the charge distribution in electrostatically doped graphene devices is inhomogeneous, yielding a non-uniform Fermi level profile. For instance, scanning gate microscope measurements of a monolayer graphene device on a SiO_2/Si substrate reveal a strong shift of the local Dirac point from the Fermi level at the graphene edge due to the contribution of both localized edge states (i.e., zigzag or armchair) and accumulated charge along the edge [23]. The Fermi energy profile $\mathbb{E}_{\mathrm{F}i}$ across the layer i can be expressed in terms of the constant Fermi energy $\mathbb{e}_{\mathrm{F}i}$ as follows (**Section B2**, **Appendix B**)

$$\mathbb{E}_{\mathrm{F}i}(\mathbb{r}, \alpha_i, \mathbb{e}_{\mathrm{F}i}) = -\frac{\gamma_1}{N_b}\sum_{l=1}^{N_b}\sum_{j}\sin\theta + \sqrt{\frac{f(\mathbb{r}, \alpha_i)}{\langle f\rangle N_b}\sum_{l=1}^{N_b}\sum_{j}\left(\mathbb{e}_{\mathrm{F}i}^2 + 2\mathbb{e}_{\mathrm{F}i}\gamma_1\sin\theta\right) + \left[\frac{\gamma_1}{N_b}\sum_{l=1}^{N_b}\sum_{j}\sin\theta\right]^2} \quad (3.7)$$

Then, the average charge density of each layer can be expressed by

$$Q_i = \frac{e}{N}\int_0^{\langle\mathbb{E}_{\mathrm{F}i}\rangle} D_N(\mathbb{E})d\mathbb{E} = \frac{e}{\pi\gamma^2 N}\sum_{l=1}^{N_b}\sum_{j}\left(\langle\mathbb{E}_{\mathrm{F}i}\rangle^2 + 2\langle\mathbb{E}_{\mathrm{F}i}\rangle\gamma_1\sin\theta\right) \quad (3.8)$$

where $\langle\mathbb{E}_{\mathrm{F}i}\rangle$ is the average value of $\mathbb{E}_{\mathrm{F}i}$ in terms of $\mathbb{e}_{\mathrm{F}i}$ and α_i. The average charge density Q_i can be obtained by minimizing the total energy of the system with respect to $\mathbb{e}_{\mathrm{F}i}$ and α_i as the variational parameters under the constraint that $Q_0 = \sum_{i=1}^{N} Q_i$. In the *N*-LG/SiO_2/Si system, the total energy can be split as, $U_t = U_r + U_e + U_b$, where the terms correspond to energy stored in SiO_2 as the dielectric medium ($= Q_0^2 h_s/(2\varepsilon_0\varepsilon_s)$ where h_s and ε_s are the SiO_2 thickness and the dielectric constant, respectively, and ε_0 is permittivity of the vacuum), electrostatic energy between the graphene layers and the band-filling energy in each layer, respectively. Charge

distribution in the *N*-LG system can be explained as a result of the competition between U_e that tends to hold the charge in the layers as close to the Si substrate as possible, and U_b that tends to spread the charge throughout the *N*-LG system. Assuming that the electronic band structures remain unchanged under an external electric field, U_e and U_b at zero temperature can be given, respectively, by

$$U_e = \frac{d_g}{2\varepsilon_0\varepsilon_g}\sum_{i=1}^{N}\left(Q_0 - \sum_{j=1}^{i} Q_j\right)^2 \tag{3.9}$$

and

$$U_b = \frac{1}{N}\sum_{i=1}^{N}\int_0^{\langle \mathbb{E}_{\mathrm{F}i}\rangle} \mathbb{E} D_N(\mathbb{E}) d\mathbb{E} = \frac{1}{\pi\gamma^2 N}\sum_{i=1}^{N}\sum_{l=1}^{N_b}\sum_{j}\left(\frac{2}{3}\langle \mathbb{E}_{\mathrm{F}i}\rangle^3 + \langle \mathbb{E}_{\mathrm{F}i}\rangle^2 \gamma_1 \sin\theta\right) \tag{3.10}$$

where d_g is the interlayer distance and ε_g is the dielectric constant in *N*-LG. One may find the equivalent bias voltage applied between the Si substrate and *N*-LG by taking the derivative of the total energy with respect to the total induced charge density (i.e., $V_0 = dU_t/dQ_0$) and local surface electrostatic potential of each layer can be obtained by $V_i = dU_e/dQ_i$.

3.3.1 Comparison studies

We first compare local work functions ($\Phi_i = -eV_i$) predicted by the present discrete model with those measured by our DC EFM technique (**Figure 3.1(b)**), angle-resolved photoemission spectroscopy (ARPS) [41] and Kelvin probe force microscopy (KPFM) [43, 44]. We note that since the accurate work function of the tip under the ambient conditions and also the accurate value of the dielectric constant for the *N*-LG/SiO_2 interface are unknown, the difference of the work function is used to achieve more accurate comparison purposes. In **Figure 3.6(a)**, we present our measured Φ_i in the 1-8-LG systems relative to that of 8LG, Φ_8, which is well consistent with that predicted by the discrete model when $Q_0 = 7.9 \times 10^{12}\mathrm{cm}^{-2}$. We also compare Φ_i in a 4-LG system with that measured by ARPS [41], as shown in **Figure 3.6(b)**. The results are given relative to the work function of the outermost layer Φ_4 as the zero-reference level and Q_0 is set to be $2.2 \times 10^{13}\mathrm{cm}^{-2}$. It is evident from **Figure 3.6(b)** that a very good agreement exists between the proposed discrete model and those measured by Ohta et al. [41]. Another comparison study is conducted in **Figure 3.6(c)** between the present discrete model and KPFM results of Ziegler et al. [43], who measured Φ_i in the 1-6-LG systems relative to that of

bulk graphite Φ_∞. **Figure 3.6(c)** clearly demonstrates that the measured work functions are generally in much better agreement with our results than those obtained by *ab initio* DFT calculations [43] when assuming a total induced charge density of $4.85 \times 10^{12}\text{cm}^{-2}$. We further perform a similar comparison in **Figure 3.6(d)** between the present work functions at the uppermost layer of N-LG (Φ_N) relative to those of $(N-1)$-LG (Φ_{N-1}) with KPFM results measured for *N*-LG with layer number ranging from 1 to 8 [44]. It is indicated that the present work functions closely match with the experimental observations for $Q_0 = 1.7 \times 10^{13}\text{cm}^{-2}$.

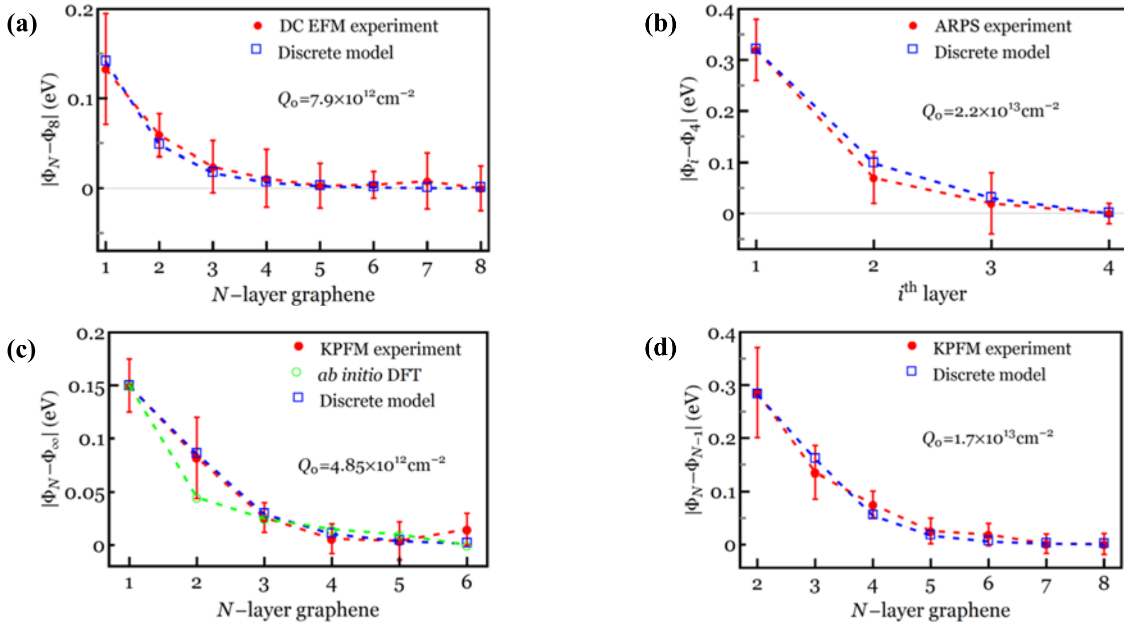

Figure 3.6. (a) Our work functions in the 1-8-LG systems relative to that of 8LG, Φ_8, for $Q_0 = 7.9 \times 10^{12}\text{cm}^{-2}$; **(b)** work functions across a 4-LG system which are given relative to that of the outermost layer Φ_4 as the zero-reference level for $Q_0 = 2.2 \times 10^{13}\text{cm}^{-2}$ [41]; **(c)** work functions in the 1-6-LG systems relative to that of bulk graphite Φ_∞ for $Q_0 = 4.85 \times 10^{12}\text{cm}^{-2}$ [43]; and **(d)** difference between the work function of the uppermost layer in the *N*-LG system and that in the (*N*-1)-LG system for *N*=1 to 8 when $Q_0 = 1.7 \times 10^{13}\text{cm}^{-2}$ [44].

Further comparison study is performed in **Figure 3.7** to investigate the influence of the effective mass m_j^* on the charge distribution of an 8-LG system. It is seen from **Figure 3.7** that the model based on the monolayer-like band structure fails to accurately predict the charge distribution of the 8-LG system, in particular at the smaller induced charge densities. This figure also shows a significant deviation in the charge densities of layers $i > 5$ for $Q_0 = 10^{13}\text{cm}^{-2}$.

Also, our energy evaluations of *N*-LG systems under a given Q_0 for three possible charge distribution scenarios– (a) optimum distribution given in **Eq. (3.6)**, (b) non-uniform distribution with the charge singularity at the very edge (i.e., $\alpha_i = 0$), and (c) fully uniform distribution (i.e.,

$q_i = Q_i$)– reveal that the minimum energy is only achieved by the present optimum charge distribution model, further indicating its merit in predicting the charge distribution of other families of atomically thin layered materials.

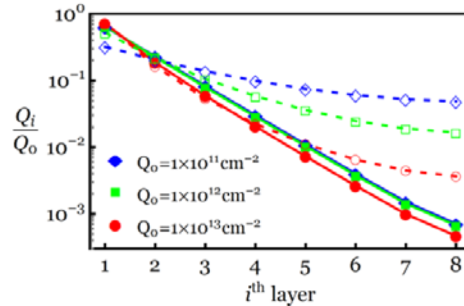

Figure 3.7. Normalized charge distribution profiles of an 8-LG system for three different values of Q_0. Dashed curves with open symbols represent the results obtained by the linear energy dispersion ($m_j^* = 0$), whereas solid curves with filled symbols denote the results obtained by the actual energy dispersion of an 8-LG system ($m_j^* \neq 0$).

3.3.2 Layer–by–layer charge density profiles in 5–LG system

We now explore the unclear relationship between the total induced charge densities and the layer-by-layer charge density and Fermi level profiles. To this end, we begin by illustrating the charge density profiles of the 5-LG system when $Q_0 = 10^{13}\text{cm}^{-2}$, as shown in **Figure 3.8(a)** (see **Figure B.2(a)**, **Appendix B** for the corresponding Fermi level profiles). Consistent with the experiments of Ohta et al. [41] and Wang et al. [44], the charge density is drastically reduced as one move away from the innermost toward the outermost layer. However, the charge density in the region very close to the edges is screened out an order of magnitude more weakly than that across the central region of the layer, as shown in **Figure 3.8(b)**, which can be explained by the presence of the strong fringe field along the edges, as schematically shown in **Figure 3.4**. Our results in **Figure 3.8(a)** also suggest that the innermost layer plays the most important role in the electrostatic charge distribution of the *N*-LG systems by hosting ~70% of the gate charge density Q_0. Hence, it is worth looking into its Fermi level profile more in detail, as illustrated in **Figure 3.8(c)**. By following the evolution of the Fermi level along the innermost layer, it is observed that a strong charge accumulation and thus sufficiently large shift in the Fermi energy at the edge can give rise to a jump in the electronic band structures of 5-LG toward the first excited state, 0.4 eV (as shown in green solid curve in **Figure 3.8(c)** and in green dashed curve in the inset, which shows the energy band structure of the 5-LG system). However, our Fermi level analyses in the innermost layer of 6-and 8-LG systems exhibit few jumps in the Fermi level of the regions both

close to and away from the edges when $Q_0 = 10^{13}\text{cm}^{-2}$ (**Figure B.2(b)**, **Appendix B** for detail). This can be attributed to the fact that the lowest energy of the first excitation band decreases for the *N*-LG system with a larger number of graphene layers, as shown in **Figure 3.8(b)**.

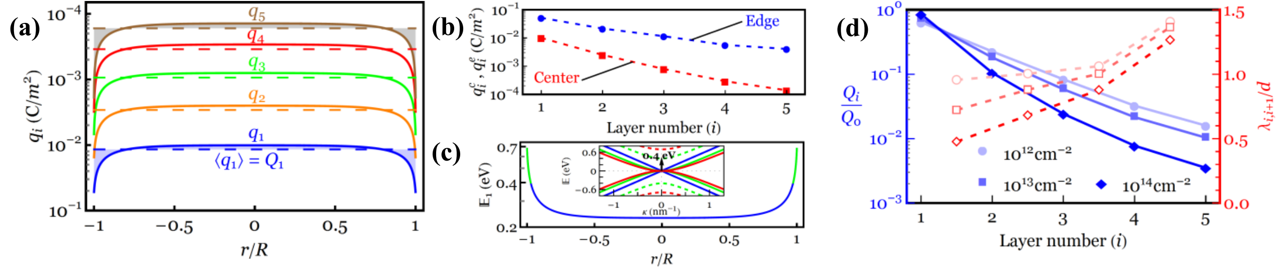

Figure 3.8. (a) Charge density profiles of a 5-LG system for $Q_0 = 10^{13}\text{cm}^{-2}$, where each dashed line represents the average charge density $\langle q_i \rangle = Q_i$ in the layer *i*. **(b)** Charge density at the edge q_i^e and the center q_i^c of the layer *i*. **(c)** Fermi level profile of the innermost layer. Inset: low-energy band structure of 5-LG system. Solid green curve in the Fermi level profile and dashed green curve in the band structure represent the first (0.4 eV) excitation energy. **(d)** Blue curves: normalized average charge profiles across the layers of a 5-LG system for different gate charge densities of 10^{12} (circles), 10^{13} (rectangles) and 10^{14}cm^{-2} (diamonds). Red curves: corresponding changes in the local charge screening $\lambda_{i,i+1}$.

To quantitatively elucidate the correlation between the magnitude of the gate charge density Q_0 and the average charge distribution Q_i through the 5-LG thickness, **Figure 3.8(d)** shows Q_i/Q_0 ratio as a function of the layer positions for three different values of Q_0 (= 10^{12}, 10^{13} and 10^{14}cm^{-2}). It is seen that a larger value of Q_0 leads to a stronger charge screening normal to the layers, however, this effect diminishes when $Q_0 < 10^{12}\text{cm}^{-2}$. This figure also demonstrates that almost 90% of the excess charge density resides in the first two layers, implying that the interlayer screening length can reliably be determined to be less than ~0.7 nm. In other words, the gate-induced electric field can be felt very weakly by layers *N*>2, which is consistent very well with our CAFM measurements in **Figure 3.3(b)** where the relative dielectric constant (which is a measure of charge storage capability and electric field screening in a material) is almost independent of electric field and layer number, in particular, for *N*>2. Having Q_i data for each layer enables us to calculate the "local" (interlayer) charge screening $\lambda_{i,i+1}$ as $Q_{i+1}/Q_i = \exp(-d/\lambda_{i,i+1})$ based on Thomas-Fermi charge screening theory (see **Section B4**, **Appendix B** for the calculation of the interlayer screening). It is deduced from **Figure 3.8(d)** that the charge screening length between the first and second layers $\lambda_{1,2}$ may reduce from $\sim 1d$ at $Q_0 = 10^{12}\text{cm}^{-2}$ to $\sim 0.5d$ at $Q_0 = 10^{14}\text{cm}^{-2}$, while a smaller variation in $\lambda_{i,i+1}$ is observed for the layers farther from the substrate due to the reduction in their DOS at the Fermi level.

3.3.3 Layer–dependent charge screening in *N*–LG systems

We now turn to a discussion of the layer-dependent charge distribution/charge screening in 1-8-LG systems for a given gate-induced charge density of 10^{13}cm^{-2}. **Figure 3.9(a)** presents a plot of Q_i/Q_0 *versus* the layer positions in 1-8-LG systems, indicating that approximately 70%, 20%, 6% and 3% (99% overall) of Q_0 sit in layers $i = 1$ to 4, respectively, and thus the gate-induced electric field is not definitely felt by $i > 4$ layers. Interestingly, we observed that the charge density of the layers located in the same position in *N*-LG systems decreases in a sawtooth-like fashion, as shown in the insets of **Figure 3.9(a)** for the normalized charge density of the innermost Q_1/Q_0 and second innermost Q_2/Q_0 layers. This saw-tooth pattern which is associated with the presence of the linear energy dispersion in *N*-LG with odd layer number has been experimentally confirmed through the measurement of the electric double-layer capacitance between an ionic liquid and 1-6-LG [33].

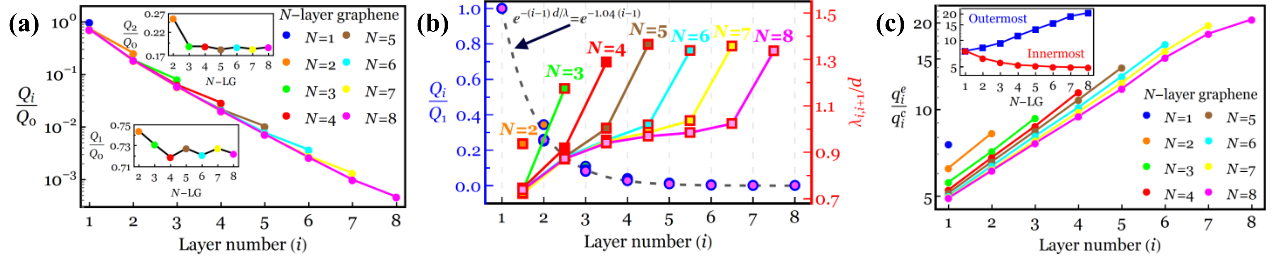

Figure 3.9. (a) Normalized average charge distribution profiles across the layers of 1-8-LG systems for $Q_0 = 10^{13}\text{cm}^{-2}$. Insets: Normalized charge density of the first (lower inset) and second (upper inset) layer in 2-8-LG. **(b)** Circles with blue borders: global charge screening length in 1-8-LG systems for $Q_0 = 10^{13}\text{cm}^{-2}$. A decay length ($d/\lambda$) of 1.04 is found by fitting the data with a function $e^{-(i-1)d/\lambda}$, indicated by a dashed curve. Rectangles with red borders: local charge screening length in 1-8-LG systems for $Q_0 = 10^{13}\text{cm}^{-2}$. **(c)** Edge-to-center charge density ratio as a function of the layer position in 1-8-LG systems when $Q_0 = 10^{13}\text{cm}^{-2}$. Inset: Edge-to-center charge density ratio for the innermost (red circles) and outermost (blue squares) layers of 1-8-LG systems.

The results in **Figure 3.9(a)** provide an important piece of information about the charge screening effect of the innermost layer on different layers of 2-8-LG. Hence, we first define a "global" (effective) charge screening λ as $Q_i/Q_1 = \exp[-d(i-1)/\lambda]$. This new definition of the "global" charge screening length allows us to explore how the innermost layer impacts the surface potential drop across the FLG thickness and also provides a single value of the screening length to predict the charge distribution of all layers relative to that of the innermost layer. Keeping both global and local screening definitions in mind, we observe from **Figure 3.9(b)** that our global charge screening can be well fitted by the simple exponential decay function (in

particular for $Q_0 \leq 10^{13}\text{cm}^{-2}$, see **Figure B.3**, **Appendix B**) when $\lambda \approx d$. **Figure 3.9(b)** also illustrates the local charge screening between the adjacent layers of 1-8-LG, showing a much lower variation in $\lambda_{i,i+1}$ of the middle layers with an average value of $\sim d$, consistent with the global charge screening length. It is also observed from **Figure 3.9(b)** that $\lambda_{i,i+1}/d$ of the innermost and outermost interlayers becomes layer-independent for $N \geq 3$ and $N \geq 4$, respectively.

We next address the problem of the charge accumulation along the graphene edge, focusing first on very limited publications that have *quantitatively* studied the charge density at the edge of graphene thus far. From prior experimental work, a nearly three-fold increase in capacitance and thus the charge density near the edge of a suspended bilayer flake (0.4 μm wide and 2.6 μm long) was observed using quantum Hall edge channels [62]. From theoretical points of view, the charge/dipole molecular dynamics model predicts a seven-fold (fifteen-fold) enhancement of the charge density at the edge (corner) over that at the center of a charged 8.5 nm × 4.8 nm rectangular graphene sheet [63] and a similar eight-fold enhancement of the charge density in a 20-nm-wide graphene nanoribbon [55]. This model also suggests that the charge enhancement is more significant in multi-layered graphene in such a way that the charge density at the edge relative to that at the center can vary from 9 in the inner layer to >14 in the outer layer of a 4-LG nanoribbon system [55]. Also, using the tight-binding Hartree model, the charge density along the edge of a 20-nm-wide graphene nanoribbon enhances up to five times over that at the center [56].

Having this quantitative description of the charge accumulation at the graphene edge in mind, we present in **Figure 3.9(c)** the charge density at the edge relative to that at the center, $q_i^{\text{e}}/q_i^{\text{c}}$, as a function of the layer position in the 1-8-LG systems for $Q_0 = 10^{13}\text{cm}^{-2}$. As is evident from the figure, our discrete model predicts the edge-to-center charge density ratio for monolayer graphene to be ~7.5 which is consistent with the theoretical results [55, 56, 63]. Surprisingly, the addition of each extra layer reduces the charge accumulation at the edge of the innermost layer from 7.5 in 1-LG down to ~5 in 8-LG, whereas an inverse trend is observed for the charge accumulation at the edge of the outermost layer, whose value varies from 7.5 in 1-LG up to ~20 in 8-LG, as shown in the inset of **Figure 3.9(c)**. While the latter can be attributed to the presence of highly weak charge screening at the edge due to the strong fringe field effect, as already shown in **Figure 3.9(b)**, the former may be accounted for by a combined effect of strong

repulsive forces at the edge and the overall charge reduction in the innermost layer. It is worth pointing out that such reduction of the charge accumulation at the edge is observed in all other layers having the same position in the *N*-LG systems (for instance, see the second innermost layer in 2-8-LG) and the edge-to-center charge density ratio eventually converges to a constant value, showing nearly layer-independent behavior for $N \geq 6$.

3.3.4 Temperature–dependent charge screening model

While the present study has focused on the charge distribution of *N*-LG at absolute zero temperature, we note that a variation in temperature from zero to room temperature has no appreciable effect on the charge screening length, more specifically at the higher gate electric field. Following a temperature-dependent model of the charge distribution detailed in **Section B5**, **Appendix B**, the local charge screening between the first and second layers of an 8-LG system is plotted in **Figure 3.10** as a function of Q_0 at $T = 0$ and 300 K. For comparison purposes, the results of Kuroda et al. [51] based on the linear energy dispersion are reproduced by setting $m_j^* = 0$, as indicated by dashed curves with open symbols in **Figure 3.10**. It is evident from **Figure 3.10** that the interlayer charge screening is insensitive to the temperature variation when $Q_0 \geq 5 \times 10^{12} \text{cm}^{-2}$ and only a slight change in $\lambda_{1,2}$ is observed at smaller gate charge densities (see lower inset) and ultimately saturates to $\lambda_{1,2} \approx d$. Consistent with our temperature-independent charge screening length, Yang and Liu reported using the first-principles calculations that the interlayer screening, static perpendicular dielectric function and density of states of bi- and tri-layer graphene slightly changes as temperature increases from 0 K to 300 K to 600 K [64].

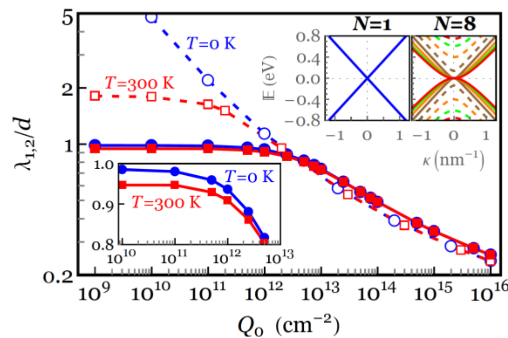

Figure 3.10. Local screening length between the first and second layers of an 8-LG system as a function of Q_0. Dashed curves with open circles (squares) represent the results obtained by the linear energy dispersion model ($m_j^* = 0$) at *T*=0 K (*T*=300 K), whereas solid curves with filled circles (squares) denote the results obtained by the actual energy dispersion of the 8-LG system ($m_j^* \neq 0$) at *T*=0 K (*T*=300 K).

It is also observed from **Figure 3.10** that the linear dispersion model fails to predict the interlayer charge screening between the two innermost layers for $Q_0 \lesssim 10^{12}\text{cm}^{-2}$ such that $\lambda_{1,2}$ goes to infinity (i.e. $Q_2 \approx Q_1$) at $T = 0$ as $Q_0 \to 0$. Interestingly, a layer-by-layer inspection of the charge density in a similar 8-LG system for different values of Q_0 reveals that the linear dispersion model not only yields inconsistent charge density profiles in almost all layers for $Q_0 \lesssim 10^{12}\text{cm}^{-2}$ but also shows a significant deviation in the charge densities of outer layers for $Q_0 > 10^{12}\text{cm}^{-2}$, as shown earlier in **Figure 3.8**. This deviation from our model can be understood in terms of the effective mass in *N*-LG with $N \geq 2$: an essential ingredient that is not captured in Kuroda's model where an *N*-LG system is considered as N parallel single layers with a massless linear energy dispersion (upper inset for $N = 1$), rather than a single 2D system with the actual energy dispersion (upper inset for $N = 8$) [65].

3.4 Summary

We quantified, for the first time, the effect of layer number and electric field on the dielectric constant of FLG. Our electrostatic force measurements on FLG/SiO_2/Si samples suggested a constant relative permittivity nearly independent of the layer number and the external electric field (up to our experimental limit of 0.1 V/Å), which is in excellent agreement with our proposed discrete model. We also demonstrated that the dielectric constant of monolayer graphene can be tuned from 17 to 3.5 upon oxidation and recovered its charge storage capacity by thermal treatment. Notably, bilayer graphene and FLG can retain their chemical inertness under oxidation and thus are well-suited for fabrication of long-term stable electronic devices with higher moisture and oxidation resistance.

We next developed a novel spatial discrete model to unravel the relationship between the macroscopic induced charge density and sub-nanoscopic (layer-by-layer) charge distribution in finite-size FLG through considering the effects of both electrostatic interlayer screening and fringe field. We showed that adding each extra layer reduces the charge accumulation at the edge relative to that at the center of the innermost layer up to 20% (from ~7.5 in 1-LG down to ~5 in 8-LG). Our model offered a simple rule of thumb regarding the charge distribution in FLG: approximately 70%, 20%, 6% and 3% (99% overall) of the total induced charge density reside within the four innermost layers (layers $i = 1$ to 4, respectively), implying that the gate-induced electric field is not definitely felt by layers $i > 4$. We finally found that a variation in

temperature from zero to 300 K has no appreciable effect on the interlayer charge screening when the gate charge density is larger than ~5×10^{12}cm^{-2}. Although our study is concerned with FLG systems, the generality of our spatial discrete model suggests that the charge density profile, interlayer screening, quantum capacitance, and local surface potential of other atomically thin layered materials (ATLMs), such as semiconducting transition metal dichalcogenides (e.g., MoS_2, WSe_2 and WS_2) and heterostructures (e.g., graphene/MoS_2 and MoS_2/WSe_2), can be characterized by feeding relevant electronic band structures of ATLMs into our model. In addition, the effect of structural defects (e.g., vacancies, adatoms, dislocations and grain boundaries) and stacking faults on the charge distribution of defective FLG systems can be studied by modifying DOS of pristine FLG.

CHAPTER 4

Atomistic Simulations of Electrostatic Exfoliation in 2DLMs: Few-Layer Graphene

4.1 Introduction

To investigate the atomistic details underlying our CAFM-assisted electrostatic shear and normal exfoliation setup (discussed in details in Chapter 2), we learnt from Chapter 3 how excess charges are distributed within FLG systems upon applying an external bias voltage between the highly-doped Si substrate and N-layer graphene (N-LG). In this chapter, we implement, for the first time, 3D spatial charge distribution of FLG (obtained from the proposed spatial discrete model in Chapter 3) into molecular dynamics (MD) simulations and perform a series of MD simulations to further gain an atomistic insight into the electrostatic shear/normal exfoliation mechanisms. In order to provide more accurate atomistic models of electrostatic exfoliation process, we chose graphene from a wide variety of 2DLMs in our simulations (and thus in our experiments) because there are well–established empirical potentials to accurately model FLG.

4.2 Atomistic Simulation Setup

Eight circular graphene layers with AB stacking and radius ~2.5 nm are placed at a distance of 3.0 Å above an amorphous SiO_2 substrate while the flattened tip is modeled by a tapered silicon (001) layer, as illustrated in **Figure 4.1**. The 8-LG stack can be printed by displacing the tip upwards (to the right) for the normal exfoliation case (shear exfoliation case) with a constant speed. In order to better mimic our exfoliation setup, the tapered silicon (001) layer was moved along the x direction with the rate of 1.5×10^{-2} Å/ps for the shear exfoliation case and was pulled away along the z direction with the rate of 1×10^{-2} Å/ps for the normal exfoliation case. To hold the system in space, 2 Å of the SiO_2 substrate from the bottom was treated as rigid. Though the contact pressure, humidity and exfoliation speed may contribute to the transfer printing of FLG, we do not investigate their possible effects in this study. Needless to say that in the case of normal exfoliation method, the contact pressure is not considered because

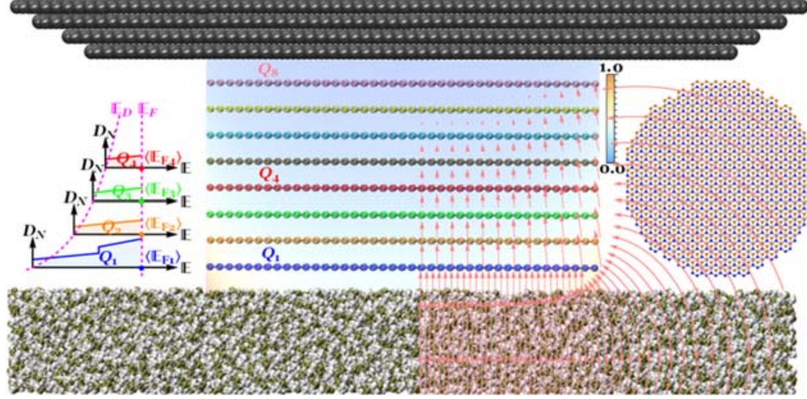

Figure 4.1. Atomic structure of the 8–LG/SiO_2 system. The background color and the arrows in the figure correspond to the local electric fields (color can be read from the scale bar and the length of arrows is proportional to the field intensity). Left inset: density of states in the four innermost graphene flakes versus the electronic band energy, in which the transparent area represents the average induced charge density. Right inset: top view of AB-stacked circular flakes cut out of the rectangular sheet with a mixture of armchair and zigzag edges.

FLG system is relaxed at room temperature for an adequate time to fully conform to the substrate surface and thus any further contact pressure will not facilitate the normal exfoliation of FLG.

We adopt reactive empirical bond order (REBO) potential function [66] to model the intralayer carbon–carbon interactions within the same graphene layer while the free graphene edges are passivated by hydrogen. A registry–dependent (RD) interlayer potential that can accurately describe the overall cohesion, corrugation, equilibrium spacing and compressibility of FLG is implemented in the LAMMPS code to model the carbon–carbon interaction between graphene flakes [67]. For the same MD simulation but different interlayer potentials (LJ or RD potential), both the number and the orientation of printed flakes were completely different, indicating that the potential corrugation (which cannot be described by the LJ potential) plays a crucial role in determining the intrinsic resistance to interlayer sliding and controlling the exfoliation behavior of the FLG under external electrostatic loads (**Section C.1, Appendix C**). Tersoff potential and Stillinger-Weber potential are utilized for the modelling of SiO_2 substrate and silicon (001) layer, respectively. Given that the graphene–SiO_2 interaction is physisorption in nature, it has been proposed that the short–range vdW interaction is the predominant mechanism at the graphene–SiO_2 interface rather than O–C and Si–C covalent bonds [68, 69, 70]. As a result, we use a standard 12–6 LJ potential for describing Si–C and O–C interactions according to the Universal Force Field (UFF) model and the Lorentz–Berthelot mixing rules. Although the extreme flexibility of graphene (which makes its interaction with SiO_2 more liquid-like than solid-like) and the surface properties of SiO_2 play a role in the exfoliation of graphene, the Si–C

and O–C interaction parameters, used in this work, alone do not lead to the graphene exfoliation, allowing us to elucidate the key role of electrostatic and interlayer vdW forces in the exfoliation process. The minimum graphene–SiO_2 interfacial adhesion strength required to print monolayer graphene onto the substrate in the absence of electrostatic forces can be obtained for $\varepsilon_{\mathrm{Si-C}} = 13.36\mathrm{meV}$ and $\varepsilon_{\mathrm{O-C}} = 5.163\mathrm{meV}$ which are 1.5 times greater than the interaction energy values we used in this Article (see **Figure C.1**, **Appendix C**). Nevertheless, we will demonstrate later that the electrostatic force can significantly facilitate the print of the graphene flakes onto the substrate with the weak surface adhesion. The glue between the tip and graphene flakes is simply modeled by applying the LJ potential between the silicon layer and the topmost graphene flake using a larger Si–C interaction energy (i.e., $\varepsilon_{\mathrm{Si-C}} = 17.8\mathrm{meV}$).

4.3 Three-Dimensional Spatial Charge Distribution of FLG

Herein, we first use our spatial discrete model to find the charge distribution within each graphene flake and through the 8–LG thickness and then assign, for the first time, the electric charge of each carbon atom by substituting their position coordinates into the relevant charge density profile. **Figure 4.2(a)** illustrates the layer-by-layer charge density profiles in the 8–LG system when a total excess charge density of $Q = 10^{13}\mathrm{cm}^{-2}$ is induced (see **Section C.2, Appendix C**, for more details about charge density/Fermi level profiles in the 8–LG system).

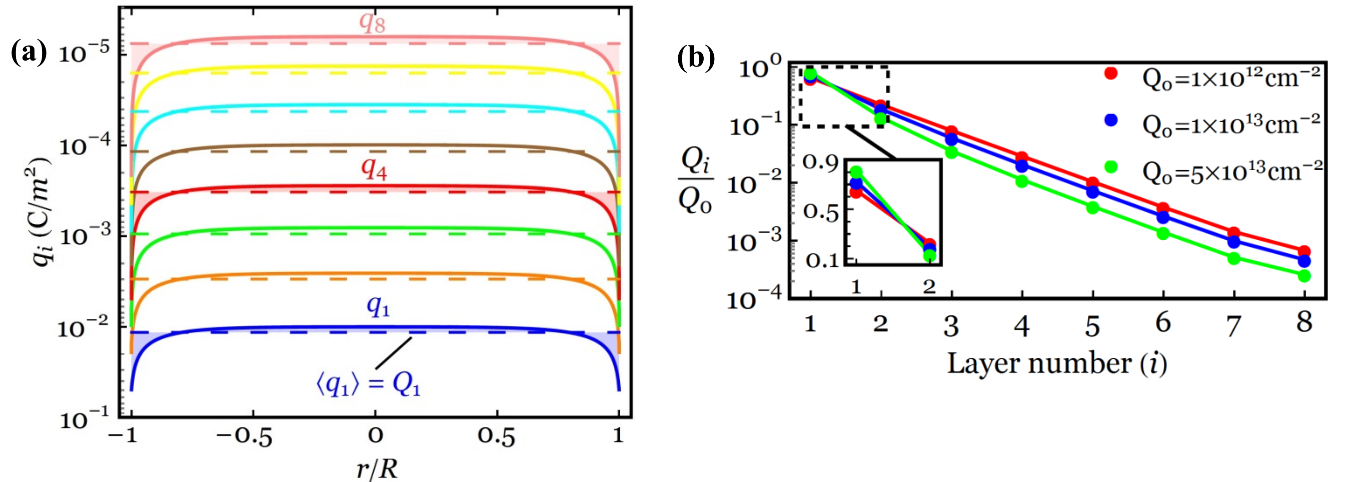

Figure 4.2. (a) Charge density profiles of an 8–LG system for $Q = 10^{13}\mathrm{cm}^{-2}$, where each dashed line represents the average charge density $\langle q_i \rangle = Q_i$ in the layer i; (c) 3D discrete charge density profile of the innermost flake ($i = 1$) in the 8–LG system for $Q = 10^{13}\mathrm{cm}^{-2}$ where q_{1j} is the charge density on atom j belonging to the innermost flake. (b) Normalized average charge density across the layers of an 8–LG system for different gate charge densities. Inset: normalized average charge density in the two innermost layers to show the electrostatic charge screening effect. Zoom-in of a region in which the charge screening between the first and second layers is shown by a dashed black square.

Our spatial discrete model in **Figure 4.2(b)** also suggests that almost 87%, 91% and 95% of the total excess charge density reside within the two innermost layers of the 8–LG system upon application of $Q = 10^{12}\text{cm}^{-2}$ (equivalent to a bias voltage of ~0.46 V), 10^{13}cm^{-2} (~ 4.6 V) and $5 \times 10^{13}\text{cm}^{-2}$ (~ 23 V), respectively, implying that the gate-induced electric field can be felt very weakly by layers *N*>2. This is consistent very well with our CAFM measurements in **Figure 3.3(b)** that the relative dielectric constant is almost independent of the electric field and the layer number, in particular, for *N*>2.

4.3.1 Electric charge on each carbon atom in FLG

To provide a quantitative determination of the charge density of an FLG system in each individual graphene flake down to a single atom, we start by dividing the surface of an *N*-atom graphene flake into *N* equilateral triangular subareas, with a carbon atom at the center of each subarea, as shown in **Figure 4.3(a)**. By doing so, a uniform charge distribution over each subarea allows us to further assume that the whole charge on such a small area is accumulated on the corresponding atom due to the strong attraction of nucleus. As a result, the graphene flake can be considered as a charge carrier with point charges at the positions of carbon atoms.

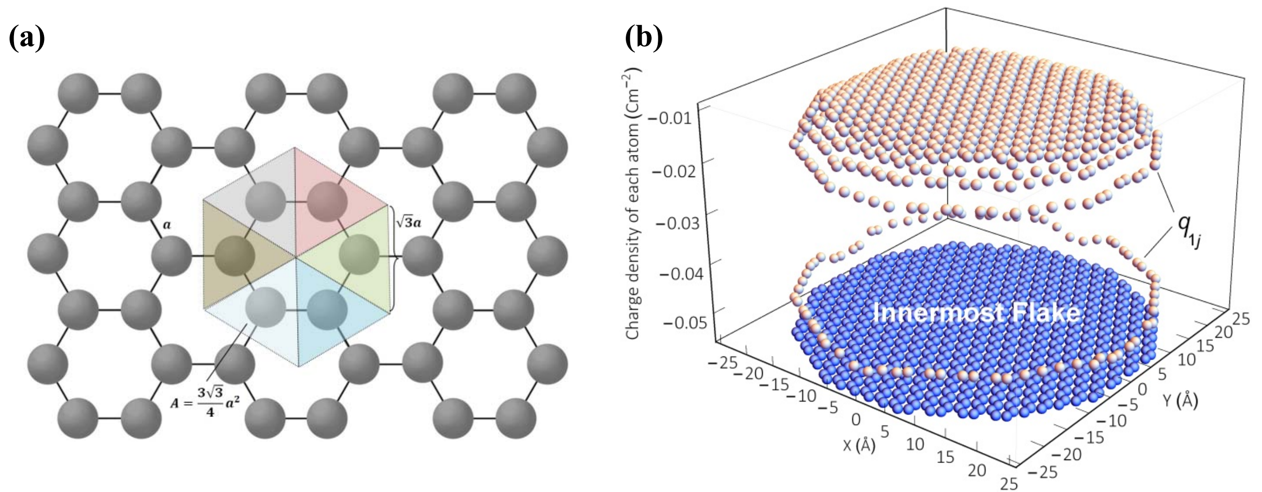

Figure 4.3. (a) Uniform charge distribution over a triangular area ($A_c = 3\sqrt{3}a^2/4$, where $a = 1.42$ Å is the C–C bond length) surrounding the associated atom. (b) 3D discrete charge density profile of the innermost flake ($i = 1$) in the 8–LG system for $Q = 10^{13}\text{cm}^{-2}$ where q_{1j} is the charge density on atom *j* belonging to the innermost flake.

The point charge on atom j belonging to the flake i can be determined by multiplying the corresponding charge density q_{ij} to the triangular area ($= 3\sqrt{3}a^2/4$), where q_{ij} can be given by:

$$q_{ij} = \frac{f(\mathbb{r}_{ij}, \alpha_i)}{\langle f(\alpha_i)\rangle} Q_i \tag{4.1}$$

where

$$f(\mathbb{r}_{ij}, \alpha_i) = \frac{g(\mathbb{r}_{ij})}{\sqrt{(1+\alpha_i) - \mathbb{r}_{ij}^2}} \tag{4.2}$$

and the charge distribution profile is normalized by

$$\langle f(\alpha_i)\rangle = \frac{1}{M}\sum_{j=1}^{M} \frac{g(\mathbb{r}_{ij})}{\sqrt{(1+\alpha_i) - \mathbb{r}_{ij}^2}} \tag{4.3}$$

with the index notations i and j varying from 1 to N (N being the total number of graphene layers) and 1 to M (M being the total carbon atoms in each layer), respectively; $\mathbb{r}_{ij}$ ($= r_{ij}/R_i$) is a dimensionless parameter; r_{ij} denotes the radial coordinate of atom j in the ith layer which carries the corresponding charge density of q_{ij}; R_i is the radial coordinate of the atom at the edge of the layer i; $g(\mathbb{r}_{ij})$ is a polynomial function of $\mathbb{r}_{ij}$ which is determined by solving the Love equation; Q_i is the average charge density in the ith layer and $Q = (1/M)\sum_{i=1}^{N}\sum_{j=1}^{M} q_{ij}$ is the total induced charge density in the FLG. The quantity α_i which determines the amount of charge density at the edge with respect to that at the center of the ith layer is obtained from the energy minimization of the system, as discussed in the main text.

We now assign the charge of each atom by substituting their radial coordinates into the charge density profile of each layer using Eq. (4.1). In **Figure 4.3(b)**, we provide 3D discrete charge density profile of the innermost flake in the 8–LG system for $Q = 10^{13}\text{cm}^{-2}$, indicating the charge variations at the zigzag and armchair edges, as previously confirmed by scanning gate microscope measurements and the charge–dipole model (**Section C.2.4**, **Appendix C**).

4.3.2 Attractive and repulsive electrostatic forces on each atom

As the last piece in the puzzle of the electrostatic MD simulations, we calculate the attractive electrostatic force of each atom using the well-established concept of the parallel plate capacitor model. Experimental studies have demonstrated that the attractive electrostatic force acting on suspended mono–, bi– and tri–layer graphene [71] and also on carbon nanotubes [72] can be approximated very well by the parallel plate capacitor model. Furthermore, implementing

the electrostatic force in MD simulations of suspended carbon nanotubes using the standard capacitance model can not only provide the results consistent with the experimental data but also significantly reduce the computational cost [73]. In this light, one may compute the total attractive force between the graphene flakes and SiO_2/Si substrate as follows:

$$F_t = \frac{Q^2 A}{2\epsilon_0 \epsilon_{\mathrm{sio}_2}} = \frac{M A_c}{2\varepsilon_0 \varepsilon_{\mathrm{sio}_2}} \sum_{i=1}^{N} \left[\frac{1}{M} \sum_{j=1}^{M} q_{ij} \right]^2 = \frac{A_c}{2M\varepsilon_0 \varepsilon_{\mathrm{sio}_2}} \sum_{i=1}^{N} \left[\sum_{j=1}^{M} q_{ij} \right]^2 \tag{4.4}$$

where $\varepsilon_{\mathrm{sio}_2}$ (=3.8) is the dielectric constant of SiO_2.

Under the assumption of uniform electric field, Eq. (4.4) reduces to

$$F_t = \frac{M A_c}{2\varepsilon_0 \varepsilon_{\mathrm{sio}_2}} \sum_{i=1}^{N} Q_i^2 = M \sum_{i=1}^{N} F_i \tag{4.5}$$

where F_i $(= A_c Q_i^2 / 2\varepsilon_0 \varepsilon_{\mathrm{sio}_2})$ denotes the attractive force *uniformly* applied to all atoms belonging to the layer number i. As a result, the force of each atom which is proportional to the square of its corresponding charge density (given by Eq. 4.1) can reliably be written as

$$F_{ij} = \frac{A_c q_{ij}^2}{2\varepsilon_0 \varepsilon_{\mathrm{sio}_2}} \tag{4.6}$$

This expression can successfully capture both the fringe field and screening effects on the attractive electrostatic force acting on each individual atom in the direction perpendicular to the substrate.

In our MD simulations, the repulsive electrostatic forces due to the like charges on all atoms are computed using the Coulomb pair potential as follows

$$\vec{F}_{ij} = \frac{A_c q_{ij}}{4\pi\varepsilon_0} \sum_{k=1}^{N} \sum_{\substack{l=1 \\ l \neq j}}^{M} \frac{\vec{r}_{ij} - \vec{r}_{kl}}{\left| \vec{r}_{ij} - \vec{r}_{kl} \right|^3} A_c q_{kl} \tag{4.7}$$

where a cut–off radius of 10 Å is taken into account for the Coulombic pairwise interaction.

4.4 Results and Discussion

After relaxation of the uncharged system at 300K for 50ps, we assign the charge of each atom and equilibrate the charged system at 300K using a Nose–Hoover thermostat for 10ps. Then, the attractive electrostatic forces are applied to each atom and the system is again equilibrated for another 10ps. For the normal (shear) exfoliation process, the tapered silicon

(001) layer is pulled in the z direction (x or y direction) with a constant speed of 1×10^{-2} Å/ps (1.5×10^{-2} Å/ps). Newton's equations of motion are integrated using the velocity Verlet algorithm with a time step of 1 fs. This time step yielded the total energy variation of $< 0.01\%$ during the whole period of simulations.

In order to provide a quantitative demonstration of the normal and shear electrostatic printing of the FLG, **Figure 4.4(a)** shows the number of printed flakes as a function of the total induced charge density in the 8-LG. As an illustration, snapshots from the MD simulations of the normal exfoliation for $Q = 8.5 \times 10^{12}\text{cm}^{-2}$ at $t = 1$ ns and the shear exfoliation for $Q = 9.5 \times 10^{12}\text{cm}^{-2}$ at $t = 3$ ns are shown in **Figures 4.4(b)** and **(c)**, respectively. From **Figure 4.4(a)**, the minimum induced charge density on 8-LG required for the normal and shear exfoliation of graphene flake is $8.5 - 9(10^{12}/\text{cm}^2)$ which is in good agreement with our experimental results for the normal exfoliation ($Q \approx 12.9 \times 10^{12}\text{cm}^{-2}$ for $h_s = 10nm$ and $V = 6\,V$) and the shear exfoliation ($Q \approx 10.8 \times 10^{12}\text{cm}^{-2}$ for $h_s = 10nm$ and $V = 5\,V$) and also with the other experimental results for the normal exfoliation of 18 nm wide FLG nanoribbons and 1.4 μm diameter pillars ($Q \approx 3.7 \times 10^{12}\text{cm}^{-2}$ for $h_s = 50nm$ and $V = 8.5\,V$) [74], the shear exfoliation of 5 µm wide square mesas and 25 μm wide ribbons ($Q \approx 12.4 \times 10^{12}\text{cm}^{-2}$ for $h_s = 52nm$ and $V = 30\,V$) [75], and also the normal exfoliation of sub-20 nm wide nanoribbons ($Q \approx 8.6 \times 10^{12}\text{cm}^{-2}$ for $h_s = 5nm$ and $V = 2\,V$) [76] where the total charge density is approximated as $Q = \varepsilon_0 \varepsilon_s V/(e h_s)$ according to the parallel plate capacitor model. It is also observed from **Figure 4.4(a)** that the overall number of printed layers in the shear exfoliation model increases by the increase of the induced charge density, reasonably consistent with our experimental results in **Figure 2.18(a)**. However, a constant number of printed layers for Q ranging, for instance, from $9.5 - 11(10^{12}\text{cm}^{-2})$ are hypothesized to primarily be the result of the electrostatic screening effect.

Unlike the case of shear exfoliation, it is observed that the number of printed flakes in the normal exfoliation technique does not necessarily increase with the increase of the bias voltage, leading to a random number of printed flakes, as already observed in **Figure 2.18(b)**. This counter–intuitive observation can be understood in terms of anisotropic nature of the vdW interactions in FLG where the interlayer shear strength τ_s within the basal plane competes with the tensile strength σ_s (i.e., interfacial cohesion strength) normal to the basal plane during the normal exfoliation/printing course, whereas in the shear exfoliation technique, the interlayer

shear strength is primarily responsible for initiating flake sliding and separation. In order to better understand how these physical parameters and their possible interplay can hinder or facilitate the FLG exfoliation, we next establish a quantitative characterization of the interlayer interactions of graphite.

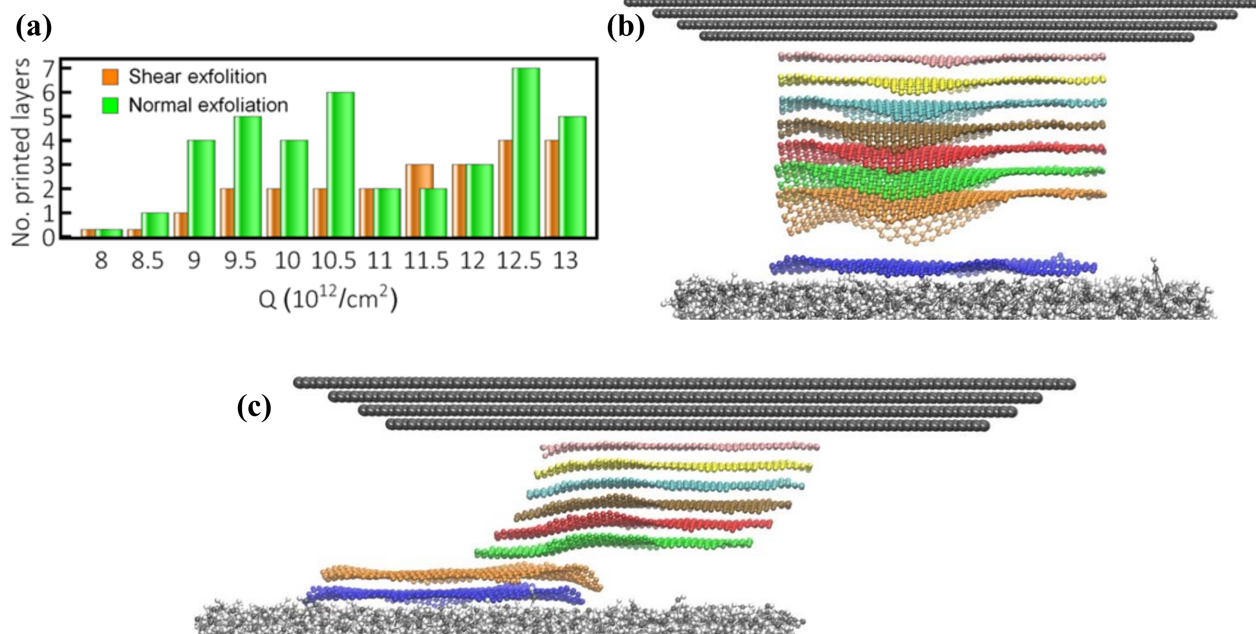

Figure 4.4. (a) Number of printed layers as a function of the induced charge density for both normal and shear exfoliation techniques. Snapshots from MD simulation of (b) the normal exfoliation for $Q = 8.5 \times 10^{12}\text{cm}^{-2}$ at $t = 1$ ns and (c) the shear exfoliation for $Q = 9.5 \times 10^{12}\text{cm}^{-2}$ at $t = 3$ ns;

Recent experimental observations on the relative sliding motion of graphite demonstrated that the interlayer shear strength of the AB–stacked (commensurate) graphite flakes ($\tau_S^c \approx 140\text{MPa}$) is drastically reduced by more than two orders of magnitude for their non–AB–stacked (incommensurate) counterparts ($\tau_S^{ic} \approx 0.25 - 2.5\text{MPa}$) due to the superlubricity phenomenon in graphite [77]. From experimental measurements [78] and atomistic results [79], a very slight interlayer rotation (~2 degrees) between two adjacent commensurate graphene flakes can cause the interlayer shear strength (i.e., interlayer friction) to suddenly decrease by over 50% (**Figure C.7, Appendix C**). This clearly indicates that the interlayer shear strength is very sensitive to the in–plane rotation. In addition, the tensile strength of polycrystalline (incommensurate) graphite normal to the basal plane was measured to be in the range $\sigma_S^{ic} \approx 10.3 - 20.7\text{MPa}$ [80], which is

one order of magnitude greater than τ_s^{ic}. To the best of our knowledge, there is no direct experimental measurement of the tensile strength for crystalline (commensurate) graphite σ_s^c. Although a slight difference in the measured interfacial adhesion energy (i.e., basal plane cleavage energy) of the incommensurate ($0.37\ \mathrm{Jm}^{-2}$) and commensurate graphite ($0.39\ \mathrm{Jm}^{-2}$) [81] implies that their corresponding out–of–basal–plane elastic modulus (C_{33}) could be relatively close to one another, their tensile strength could exhibit a remarkably different behavior (see **Table C1**, **Appendix C**, for more comprehensive data obtained from a wide range of experimental methods and a detailed discussion about the interlayer mechanical properties of FLG/graphite).

Keeping this quantitative description of the vdW interaction of graphite in mind, an evaluation of the MD trajectories and electrostatic interactions indicates that during the normal exfoliation process, the interlayer shear strength and out–of–basal–plane tensile strength are highly coupled through vdW interactions between the adjacent graphene flakes. Monitoring of the interlayer spacing ($\Delta d = d_i - d_{i-1}$) and the interlayer rotation ($\Delta\theta = \theta_i - \theta_{i-1}$) of the graphene flakes in our simulations (as an illustration, see **Figure 4.5(a)** for the normal exfoliation of the 8–LG system when $Q = 10.5 \times 10^{12}\mathrm{cm}^{-2}$ and the corresponding snapshot of the MD simulation for such a system in **Figure 4.5(b)**) reveals that as the graphene flakes are continuously being expanded during the normal exfoliation process, their attractive vdW interaction becomes progressively weaker and weaker, leading to the facile twisting and sliding of the graphene flakes. This, coupled with our MD observations that the interlayer rotation θ varies within the range $-2.5^\circ < \theta < 2.5^\circ$ before the exfoliation is initiated, indicates that adjacent graphene flakes with a larger interlayer rotation are more susceptible to sliding relative to one another under even relatively low shear stress levels. **Figure 4.5(b)** clearly shows that the interlayer shear stress, mainly induced by the local delamination of the layers during the normal exfoliation/printing course, leads to a complete separation between layers, labeled 7 and 6, rather than, for instance, between 6 and 5 due to the larger interlayer rotation between 7 and 6, as shown in **Figure 4.5(a)**. Interestingly, our MD results suggest that the normal exfoliation process is always initiated at the edges rather than the middle of the graphene flakes, which can be attributed to the greater electrostatic attractive and repulsive forces caused by the charge accumulation on the edges.

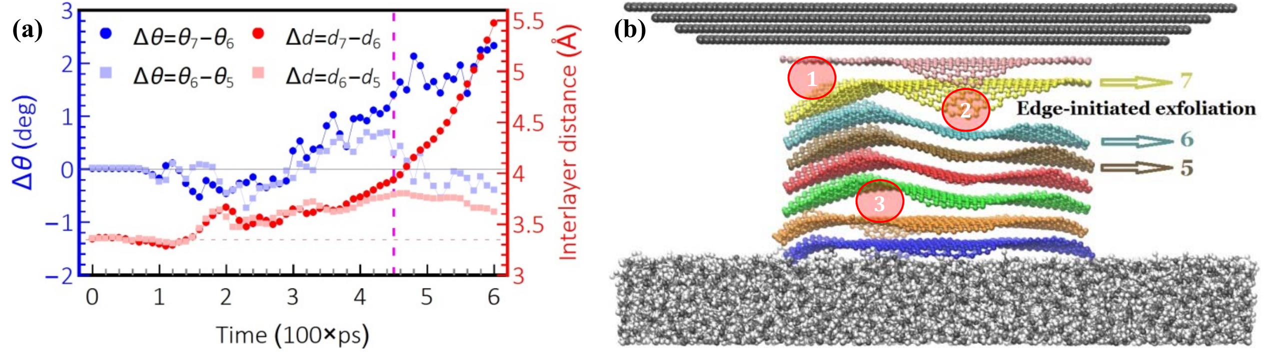

Figure 4.5. (a) A portion of the MD trajectory for the normal exfoliation of the 8-LG system when $Q = 10.5 \times 10^{12}\mathrm{cm}^{-2}$. Variation of the interlayer rotation/distance between layers, labeled 5 and 6, and between 6 and 7 as a function of simulation time. The separation of the layer 7 from 6 is initiated at $t \approx 0.45$ ns (highlighted by magenta dashed line); (b) Corresponding snapshot of the MD simulation for such exfoliation taken at $t = 0.6$ ns. Local delamination is marked in transparent red circles.

Our analysis of the simulation trajectories further reveals that the shear exfoliation method can effectively suppress the interlayer rotation whose value does not exceed $\pm 0.5^{\circ}$ before complete exfoliation is achieved. Given that the interlayer potential corrugation (i.e., the interlayer potential energy variation) is a measure of how easily adjacent layers can slide and rotate relative to one another, our MD calculations for a bilayer system will show that the potential corrugation increases when the interlayer spacing is reduced by imposing the attractive electrostatic forces. As illustrated in **Figures 4.6(a)** and **(b)**, a bilayer graphene in equilibrium ($\Delta d = 3.35$Å) exhibits a corrugation of only ~10 meV/atom, while the corrugation of a compressed bilayer ($\Delta d = 3.00$Å) is ~50 meV/atom, indicating a strong dependence of the potential corrugation on the interlayer distance and the layer stacking. This finding suggests that compared to the normal exfoliation, a larger potential corrugation and thus a smaller interlayer rotation in the shear exfoliation technique is caused by the absence of interlayer spacing variations induced by the upward pulling forces. This robust sliding/rotation behavior makes the shear exfoliation method a much more promising candidate for creating high–quality, ordered, 2DLMs–based device arrays with uniform thicknesses over large areas. **Figure 4.6(a)** also confirms that for the bilayer system in equilibrium, the AB stacking is energetically more favorable than AA stacking by ~10meV/atom, consistent with the experimental observations.

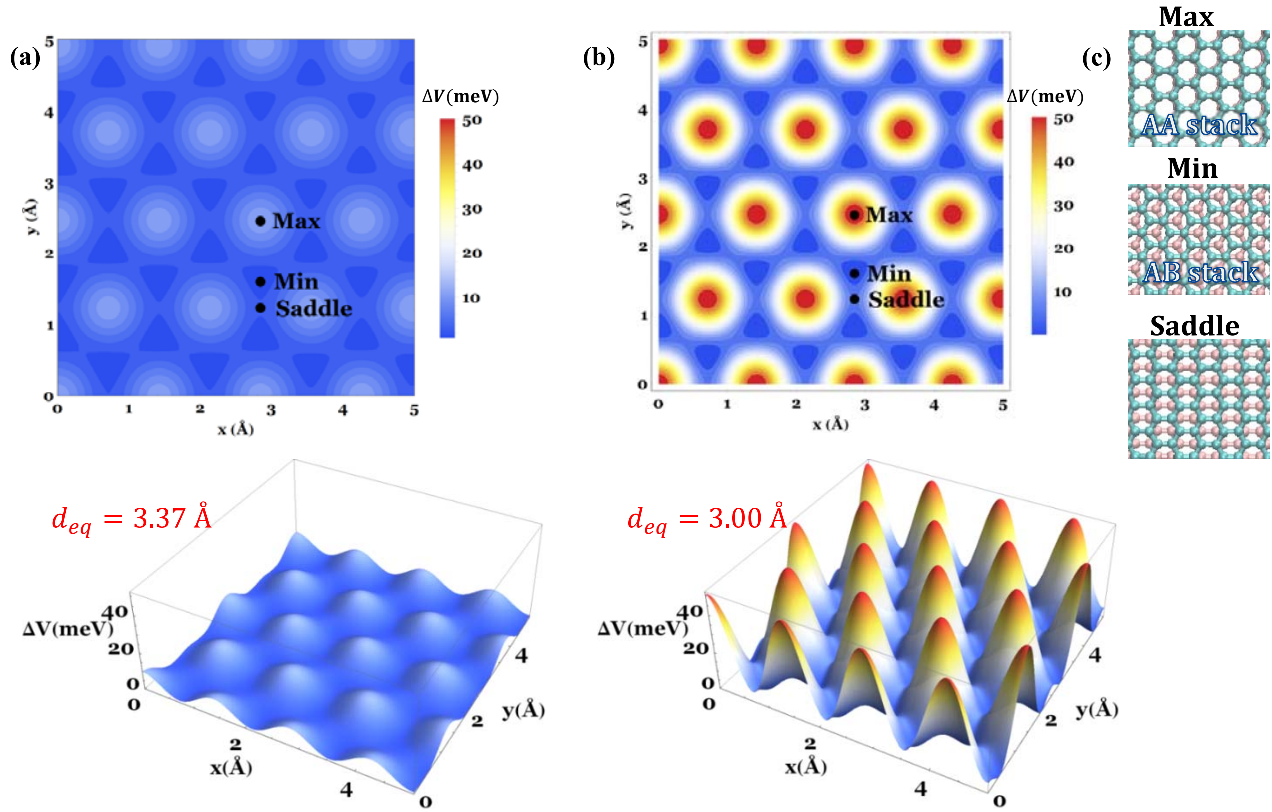

Figure 4.6. 2D and corresponding 3D contours of the potential corrugation of (a) the bilayer system in equilibrium ($\Delta d = 3.35$Å) and (b) the compressed bilayer ($\Delta d = 3.00$Å). In (a) and (b), the maximum energy difference $\Delta V = V_{AA} - V_{AB}$ is reported. (c) Three stacking configurations AA, AB and saddle corresponding to the Max, Min and Saddle points on the contour plots, respectively.

4.5 Summary

In order to gain an in-depth understanding of underlying mechanisms associated with the normal and shear electrostatic exfoliation of 2DLMs, we exploited CAFM-assisted experimental results (Chapter 2) coupled with the proposed novel spatial discrete model (Chapter 3) to conduct a series of MD simulations using the LAMMPS software package. Consistent with our experimental observations, MD simulations confirmed that the accurate control of the number of printed flakes was not feasible using the normal exfoliation method. We attributed this result to an intrinsic competition between the interlayer shear strength (which is highly influenced by the interlayer twist angle) and the out-of-plane tensile strength (which strongly depends on the interlayer spacing and local delamination) during the normal exfoliation course. Instead, the ability of the shear exfoliation method to eliminate the interlayer spacing variations and simultaneously suppress the interlayer twist angles (due to the larger interlayer potential corrugation) provides much better control over the desired number of the printed flakes, making it superior to the normal exfoliation method.

CHAPTER 5

In Situ Measurements of Interfacial Adhesion in 2D Materials and vdW Heterostructures

5.1 Introduction

As we already discussed in detail in **Section 1.3**, the interlayer vdW interaction, which can be well described by the interfacial adhesion energy (IAE), is a fundamental property of 2DLMs and vdW heterostructures due to their intrinsic ultrahigh surface to volume ratio, making vdW adhesion forces extremely strong in many processes related to fabrication, integration and performance of devices incorporating 2D crystals. Therefore, many attempts have been made over the last few decades to measure the IAE of 2D crystals using a wide range of experimental methods. While a vast majority of studies have been conducted on the interaction of G with G substrate with a wide range of reported IAE values (i.e., 0.15–0.72 Jm^{-2}, **Tables D1** and **D2, Appendix D**), no IAE measurement at the hBN/hBN interface yet exists, and also there is only one report on the interaction of MoS_2 with MoS_2. We also note that there is no direct IAE measurement on the 2D crystal vdW heterostructures. In addition, despite many experimental studies devoted to the IAE determination of 2D crystals/SiO_x heterostructures, no experimental data are available on the interaction of hBN/SiO_x, whereas the reported IAE data on the interaction of G and MoS_2 with SiO_x are very diverse, ranging from 0.09–0.90 Jm^{-2} at the G/SiO_x interface (**Table D3**) and 0.08–0.48 Jm^{-2} at the MoS_2/SiO_x interface (**Table D4**). As such, a comprehensive and accurate experimental technique that can not only directly quantify the interfacial adhesion behavior of fresh and aged 2D vdW homo/heterointerfaces at nanoscale but also successfully address the exact cause of variation in the reported IAE values is still lacking.

Herein, we use an AFM technique to report precise *in situ* adhesion measurements through well-defined interactions of AFM tip-attached 2D crystal nanomesas (G, hBN and MoS_2) with 2D crystal and SiO_x substrates. We quantify how different levels of short-range dispersive (vdW) and long-range electrostatic (Coulombic) interactions respond to airborne contaminants and humidity upon thermal annealing.

5.2 *In Situ* AFM-Assisted Experimental Setup

We record force–displacement (*F–d*) curves with piconewton–subnanometer resolution upon retraction of AFM tip-attached 2D crystal nanomesas from fresh and aged 2D crystal and SiO_x/Si substrates under controlled ambient conditions in the near–equilibrium regime (**Figure 5.1(a)**). The annealing temperature of nanocontact interfaces is precisely controlled in the range of -15–300°C by a microheater on the top (left inset of **Figure 5.1(a)**) and a cooling stage underneath the SiO_x/Si substrate. Aged substrates are prepared by two different aging conditions where the freshly exfoliated 2D crystal and bare SiO_x/Si substrates are either exposed to the ambient air directly (hereafter referred to simply as untreated substrates) or kept at subzero temperature, followed by the air exposure (referred to as precooling-treated substrates). A similar method is used to age the tip-attached nanomesas for the subsequent contact with their corresponding aged substrates.

While *F–d* curves at the fresh interfaces are recorded during the attachment of nanomesas to the glue-coated tip where the tip is gently pulled away from the substrate surface in a direction perpendicular (parallel) to the single basal plane of 2D crystal, leading to pulling (shearing) off the upper section of the nanomesa (attached to the tip apex) from the lower section (fixed to the 2D crystal substrate) (**Figures 5.1(b) and (c)**), the interfacial adhesion measurements at untreated and treated interfaces are performed upon retraction of the 2D crystal tip from the untreated and precooling treated surfaces (**Figures 5.1(d) and (e)**).

Among many different combinations of dissimilar 2DLMs, we focus on the interlayer vdW behavior of conducting G, insulating hBN and semiconducting MoS_2 crystals as a model system for a large class of 2D vdW heterostructure systems. Since direct nanoscale probing of weak vdW interactions in 2DLMs and vdW heterostructures requires a unique combination of high-resolution imaging, precise mechanical manipulation and accurate *in situ* interfacial adhesion measurements, nanosized square (circular) 2D crystal mesas with a width (diameter) of 60nm are attached to an *in situ* flattened AFM tip which is precoated with an ultrathin adhesive polymer at the apex (right inset of **Figure 5.1(a)**). Using nano-sized 2D crystal tips with a very well-defined geometric shape parallel to the substrate together with accurate determination of spring constant of the probe is an essential prerequisite for the detailed characterization of nanoscale vdW interfaces and the accurate extraction of interfacial adhesion properties of 2DLMs.

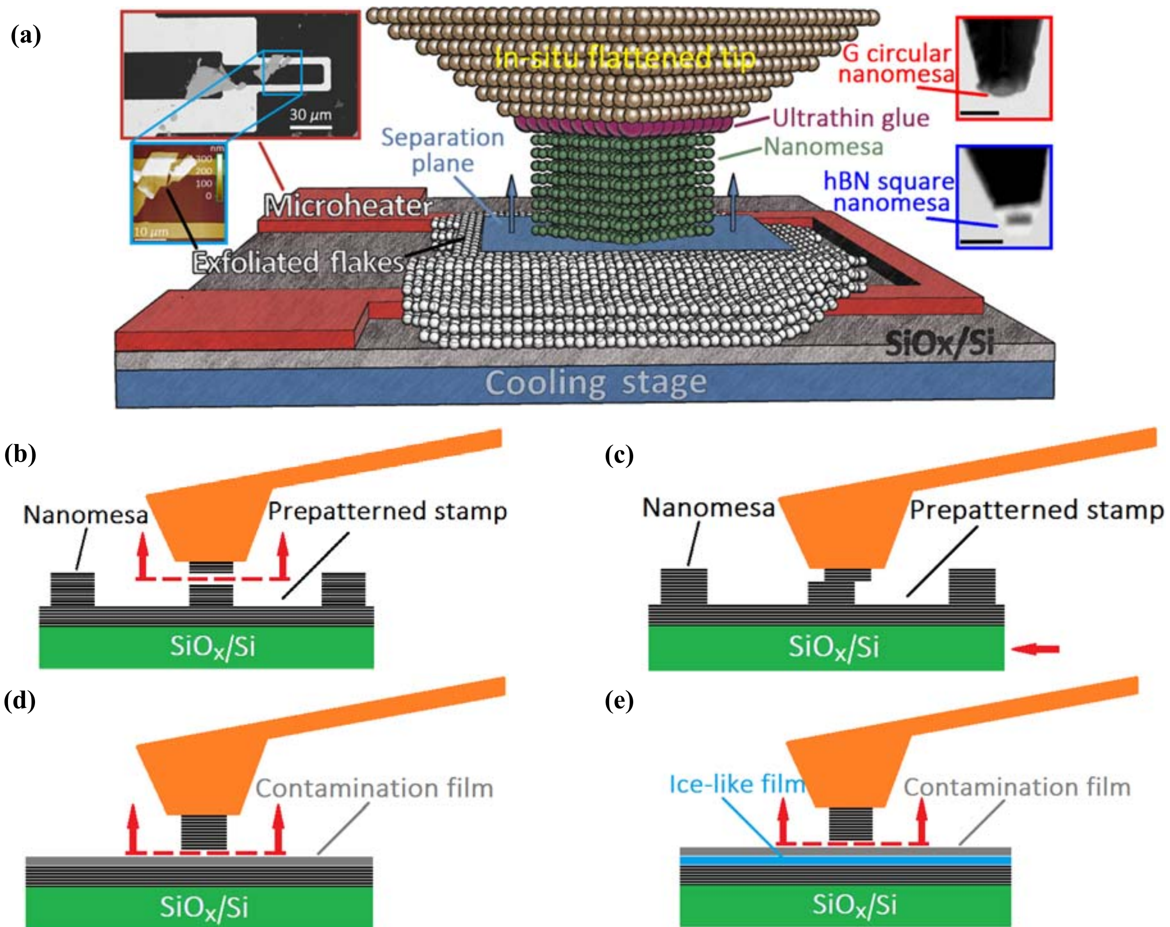

Figure 5.1. (a) Schematic of the AFM setup used to perform interfacial adhesion measurements under different annealing temperatures. Left inset: SEM image of the microheater with an MoS_2 flake exfoliated on the heating line whose corresponding AFM image was taken by the G crystal tip. Right Inset: SEM images of the tip-attached G circular nanomesa (top image) and hBN square nanomesa (bottom image). Scale bars indicate 100 nm. (b) Normal and (c) shear interfacial adhesion measurements at the intact homointerfaces. Interfacial adhesion measurements at the (d) untreated and (e) precooling-treated homointerfaces.

All AFM measurements were performed under controlled ambient conditions (T= 22°C and 15% relative humidity) by a Park XE-70 microscope which is isolated from mechanical floor vibration by a microscope vibration isolator, and also from acoustic vibration, ambient light disturbance and air flow by a closed box. The whole setup was located in an isolated place in the new Center of Excellence in Nano Mechanical Science and Engineering with the state-of-the-art ultra-low vibration chambers on the ground floor, which are tightly controlled to limit shaking, noise, temperature, humidity variations, radio frequency and magnetic interference. Having employed all these noise control facilities, we determined the noise floor of our AFM setup to be consistently less than 0.3 Å throughout the measurements.

After surface preparation of SiO_x/Si wafer (**Section 5.2.1**), three small pieces of SiO_x/Si substrate were simultaneously loaded onto the AFM stage, including (1) 2D crystal flakes mechanically exfoliated with adhesive type on microheater arrays which are prefabricated on the SiO_x/Si substrate (piece#1); (2) 25 nm thick polymer glue (PEDOT:PSS, D-sorbitol) coated on the SiO_x/Si substrate (piece#2), and (3) pre-patterned bulk 2D crystal stamps with 50-80nm–thick square and circular nanomesas of 60nm in width and diameter, respectively, (**Section 5.2.2**) which are attached to the SiO_x/Si substrate using double-sided copper tape (piece#3). To minimize the effect of the relative tilt angle, all three pieces were attached to a larger piece of SiO_x/Si substrate using the ultrathin glue film (PEDOT:PSS, D-sorbitol), followed by placing the larger piece onto a multistage Peltier cooling element equipped with a tilt control mechanism (angle resolution: ±0.5°) beneath the cooling stage. Instead of immediately removing all 2D crystal-loaded adhesive tapes from the piece#1 to complete the mechanical exfoliation onto the microheaters, we only peeled off the tape containing the 2D crystal flakes of interest for the interfacial adhesion measurements, thereby enabling much better control over the possible adsorption of airborne contaminants onto the fresh surface of 2D crystals.

For the AFM force-displacement measurements, a highly doped silicon AFM probe (NANOSENSORS™, ATEC-FM, with a nominal spring constant of 2.8 N/m and a typical tip radius of curvature better than 10 nm) was used where the tip is positioned at the very end of the cantilever and pointing outward which provides a more accurate positioning of the tip apex. Since our experiments require a flat plateau at the apex parallel the piece#1 surface on which all interfacial adhesion measurements were conducted, we scanned the tip in contact mode on its SiO_x surface to achieve an atomically flat surface with an RMS roughness of <1 nm. The in-situ flattened tip was next moved from piece#1 to piece#2 and coated with a very thin layer of polymer glue by putting the tip apex in gentle contact with the PEDOT:PSS(D-sorbitol) film. Then the tip was left at room temperature for 1 hour to remove any water from the PEDOT:PSS(D-sorbitol) aqueous solution. For the precise attachment of 2D crystal nanomesa to the glue-coated flattened apex, the tip was moved from piece#2 to piece#3, followed by locating the nanomesas by the non-contact AFM topography measurements. The glue-coated tip apex was then moved to the center of the selected 2D crystal nanomesa at an applied load of 2 nN and held in contact with the nanomesa for 10 mins. Afterwards, the X–Y piezo stage was gently moved laterally along a single basal plane of 2D crystal, leading to easy shear of the upper section of the

nanomesa (attached to the tip apex) relative to the lower section (fixed to the 2D crystal substrate) (**Section 5.2.3**). Compared to 2D crystal micro-sized mesas, the tip-attached nano-sized mesas alone offered four striking features to our setup: (1) the presence of a single-crystalline grain across the whole nanomesa is guaranteed, enabling an atomically defect-free contact interface; (2) high-resolution topographic images in noncontact mode can still be taken to locate 2D crystal flakes of interest for the subsequent IAE measurements; (3) substantially more reliable and robust IAE measurements can be achieved under any possible small relative tilting angle between the tip-attached mesa and the substrate, assuring perfect face-to-face contact during approach-retract tip manipulation; and (4) the nano-sized contact area with a significantly smaller interfacial adhesion force allows using the AFM probe with a lower spring constant and thus higher force resolution.

To study the effect of thermal annealing on the interfacial adhesion, the flakes were heated up to 300°C by applying a constant current to the microheater (**Section 5.2.4**). Using the microheater can significantly minimize the possible thermal effect on the AFM probe by locally heating the substrate. For each temperature change, enough time was given to the flakes to reach steady-state temperature (T). Then, the 2D crystal tip was engaged with the sample surface at a pressure of 5 MPa (unless otherwise noted) for 15 min to reach thermal equilibrium and then the substrate cooled back down to room temperature to perform the interfacial adhesion measurements. Similarly, we conducted a series of the interfacial adhesion measurements at subzero temperature by cooling the substrate surface down to -15°C using a multistage Peltier element (**Section 5.2.5**).

5.2.1 Sample preparation

Surface preparation of SiO_x substrates: Prior to mechanical exfoliation of 2D crystal flakes, square pieces of a 300-nm-thick SiO_x/Si wafer were ultrasonically cleaned in sequential baths of acetone, isopropanol and deionized water and dry blown with nitrogen.

2D crystal preparation: G, hBN and MoS_2 flakes were prepared by mechanical exfoliation of ultrapure single crystal of hBN, HOPG and single crystal of MoS_2 on the SiO_x/Si substrate.

5.2.2 Fabrication of nano-sized 2D crystal mesas

A ~100-nm-thick bilayer of polymethyl methacrylate (PMMA) 495K (60 nm)/950K (40 nm) is spin coated onto the freshly cleaved surface of 1-mm-thick HOPG (SPI, Grade 1, with a mosaic spread value of 0.4°), hBN (grade A, with single crystal domains over 100μm) and MoS_2 (429MS-AB, natural single crystals from Canada) substrates, baked each layer for 10 min at 120 °C to evaporate the solvent and then patterned by electron beam lithography. After developing the exposed PMMA area in 1:3 MIBK/NMP, a 10-nm-thick aluminum film is deposited by thermal evaporation, followed by lift-off process in acetone. The unprotected HOPG, hBN and MoS_2 areas are thinned down by using a reactive ion etching system with pure O_2 (precursor flow rate: 10 sccm, RF power: 40W, pressure: 10 mTorr), $CHF_3/Ar/O_2$ (10/5/2 sccm, 30W, 10 mTorr) and SF_6 (20 sccm, 100W, 20 mTorr) reactive gases, respectively. Square (circular) mesas with a width (diameter) of 60 nm and etch depth of 50-80 nm emerge from 2D crystal substrates during the plasma etch.

After plasma etching, the sample is soaked in 0.1 mol/l KOH water solution for ~3 min to remove the Al layer, followed by an annealing process at 200-600 °C under constant Ar/H_2 flow for one hour to remove any resist/metallic residues from 2D crystal substrates. **Figure 5.2(a)** shows the SEM images of MoS_2 square and G circular nanomesa arrays. The corresponding 3D AFM image of MoS_2 square nanomesas is also shown in **Figure 5.2(b)**. The sidewall profile in the AFM images is steep (as also confirmed by the height profiles in **Figure 5.2(c)**), indicating that a low etch rate of 15nm/min for the fabrication of the mesa structures results in a minor sidewall taper toward the substrate.

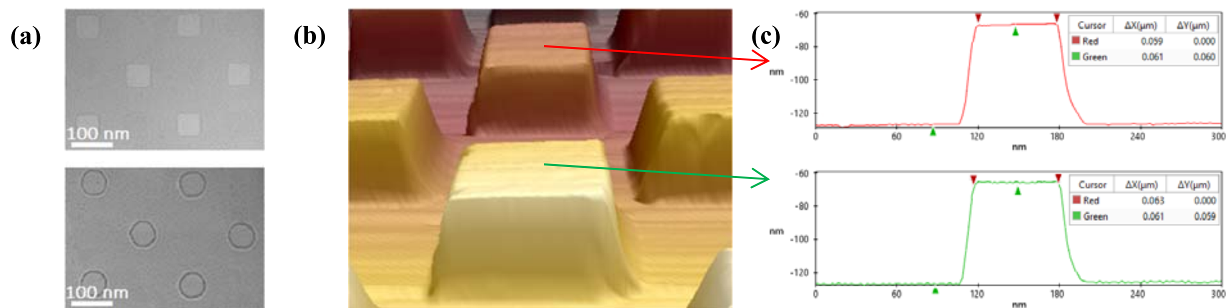

Figure 5.2. (a) SEM images of MoS_2 square and G circular nanomesa arrays. (b) 3D AFM image of MoS_2 square nanomesas. (c) Corresponding height profiles of 60-nm-deep MoS_2 square mesas with an average width of 60 nm.

5.2.3 Attachment of 2D crystal nanomesas to *in situ* flattened AFM tip

Since the attachment of 2D crystal mesas to the tip apex requires a well-defined and smooth landing area, the method described in [5] was adopted to flatten the AFM tip by scanning it in contact mode on the SiO_x/Si substrate. The morphology and area of the flat tip were first quantified through SEM and AFM images (**Figures 5.3(a) and (b)**). Next, the surface roughness and the contact area of the tip apex were determined by imprinting the tip onto the 50-nm-thick PEDOT/PSS film, followed by the AFM tapping-mode imaging. The AFM indent profile of the tip confirms a very flat triangular shape with an RMS roughness of less than 0.5 nm (**Figure 5.3(c)**). After glue coating the flattened apex by making a contact between the tip and piece#2, we moved the tip from piece#2 to piece#3 while switching the operational mode of the AFM to non-contact mode to determine the location of each nanomesa. Although the tip apex is flat, the non-contact mode can still provide us with desired resolution imaging for the subsequent attachment of the nanomesa to the tip apex. Switching the mode of operation back to the contact mode, the glue-coated tip apex was then moved to the center of the selected 2D crystal nanomesa and held in contact with the nanomesa at an applied load of 2 nN for 10 mins. Afterwards, the X–Y piezo stage was gently moved laterally along a single basal plane of 2D crystal, leading to easy shear of the upper section of the nanomesa (attached to the tip apex) relative to the lower section (fixed to the 2D crystal substrate), thanks to the extremely low friction at the contact interface of 2D crystals. **Figure 5.3(d)** shows typical SEM images of tip-attached square and circular nanomesas.

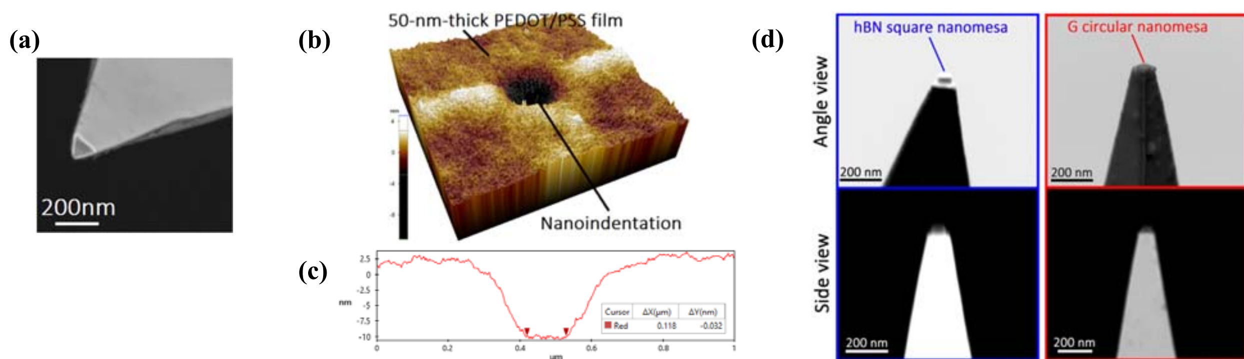

Figure 5.3. (a) SEM image of an in situ flattened tip apex. (b) AFM topography image of nanoindentation of the tip apex into the 50-nm-thick PEDOT/PSS film on the SiO_x/Si substrate. (c) Indented profile of the tip shows a very flat and smooth surface. (d) Typical SEM images of the tip with an attached square or circular nanomesa.

5.2.4 Fabrication and characterization of microheaters

In order to perform AFM measurements at elevated temperatures, an external stage heater (e.g., silicone rubber heater, Kapton heater, etc.) is widely used to heat a sample. However, microdroplets of condensed water or volatile components in the atmosphere and/or emitted from the hot sample may condense on the relatively cooler cantilever surface (being typically 10-20 μm away from the heated sample makes the probe cooler than the sample surface), as shown in **Figure 5.4(a)**. Such microdroplets can induce adverse effect on the deflection and oscillation amplitude measurements of the probe by scattering the laser beam and also on the physical properties of the probe by changing its resonance frequency and spring constant. As a remedy, we used microheaters to confine the heat to a micron-sized region on the SiO_x/Si substrate via the Joule effect with very low power consumption.

Microheater array was fabricated by the deposition of Ti(20nm)/Pt(200nm) stack on the 300-nm-thick SiO_x insulator by RF sputtering, followed by a lift-off step to pattern heating lines and contact pads. While large heating areas can be achieved by meander or spiral shaped microheaters, heating lines will be partially or fully covered by the subsequent exfoliated flakes, rendering the microheaters useless. As such, a simple U-shaped geometry was used to yield more 2D crystal flakes in direct contact with the heating lines, enabling a uniform heat distribution over the entire area of the flakes with almost the same temperature as the heating lines. **Figure 5.4(b)** shows the SEM image of the fabricated microheater device with surrounding 2D crystal flakes, indicating very smooth and uniform line width (5μm) of the heating element with 15μm spacing between the lines. Fine gold wires were used for connecting the contact pads to a programmable dc power supplier (Instek PSP-405) through package pins.

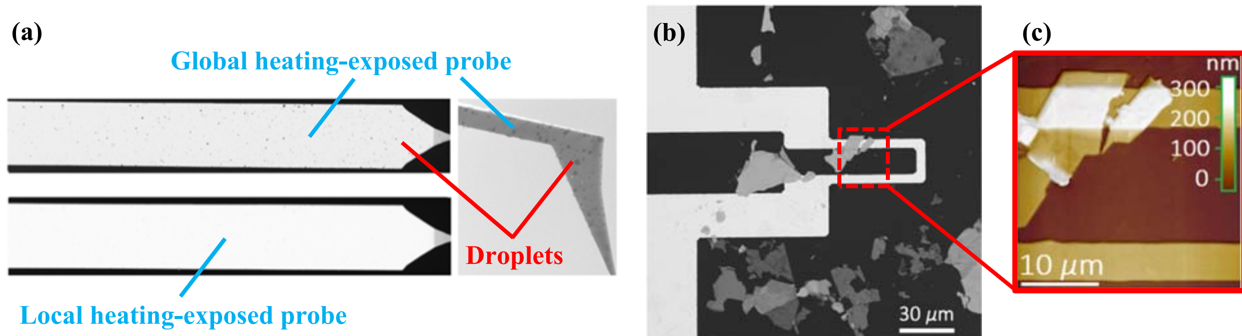

Figure 5.4. (a) SEM images of the probe exposed to a temperature of 95°C using a 1cm×1cm Kapton heater (i.e., global heating) and a micron-sized heater (i.e., local heating). (b) SEM image of a representative microheater surrounded by the exfoliated MoS_2 flakes. (c) AFM noncontact-mode image of the region marked by the square in (b), taken by the G crystal tip.

For calibration purpose, a Probe station, consisting of a microscope, a micromanipulator with a set of ultrasharp needle probes, resistance measurement unit along with an integrated hot chuck (having an accuracy of 1°C) was used to measure the electrical resistance change of the microheaters as a function of temperature ranging from RT to 300°C. The resistance measurements were repeated for ten microheaters, all showing a self-consistent linear dependence of the electrical resistance change on temperature with the best linear fit of R=0.058T+21.15 Ω, which is consistent with the following resistance-temperature expression $R=R_0+R_0\alpha_0(T-T_0)$, where R_0 and α_0 are the resistance of the microheater and the temperature coefficient of resistance of Pt, respectively, at room temperature T_0. The microheaters were subsequently characterized by Joule heating with a DC power supply of 1 to 10 mW input power, followed by measuring the electrical resistance of the microheaters using a digital multimeter. We again observed a linear dependence of the resistance on the input power P with the best linear fit of R=1.613P+22.50 Ω. Assuming that the electrical resistance of the microheaters obtained from the hot chuck measurements is equal to that obtained from the Joule heating measurements, the linear relationship between the input power and the temperature is given by T=27.81P+23.28 °C (**Figure 5.5(a)**). This equation was further verified by temperature measurements in close proximity to the microheaters by an infrared camera during Joule heating, as shown in **Figure 5.5(a)**. Slightly lower temperatures measured by the IR camera may be attributed to the aperture-limited resolution of the camera that does not allow identifying the hottest spot in the microheater devices. Our transient measurements obtained by the application of a constant voltage pulse to the microheaters for a very short time also revealed a very fast thermal response (i.e., 100 ms from RT to 300°C).

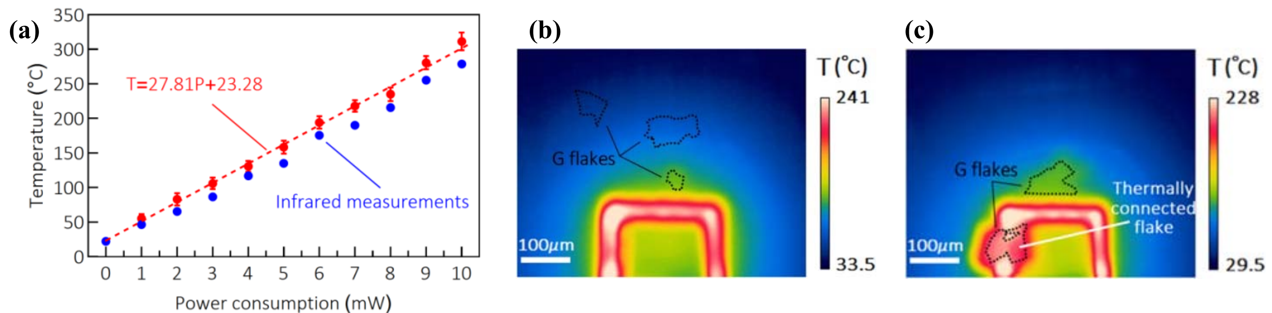

Figure 5.5. (a) Calibration of the microheater devices using the hot chuck/Joule heating (red dots) and IR camera (blue dots), both showing a linear relationship between the temperature and the input power. The dashed red line is linearly fitted to the combined hot chuck/Joule heating results. (b, c) IR results for the temperature distribution of the microheaters with the thermally-disconnected (b) and connected (c) G flakes.

It should be noted that the microheaters are mostly fabricated on a thin membrane to reduce the power consumption; however, our microheaters on the silicon substrate avoid deformation of the membrane during the approach/retraction process of the AFM tip, making adhesion measurements more accurate at a cost of higher power consumption.

After the calibration of the microheaters, we note that the temperature of 2D crystal flakes strongly depends on their distance from the heating source. This can be understood by examining the radially symmetric temperature decay of a thin silicon membrane with the heating laser spot at its center which is a logarithm function of the distance as follows

$$T(r) = T_0 - \frac{P}{2\pi dk} \ln \frac{r}{r_0} \tag{5.1}$$

where P is the input power, d is the thickness of the membrane, k is the thermal conductivity of Si and (T_0, r_0) is a reference point in the temperature field. Hence, we used IR camera to map the temperature distribution within the mechanically exfoliated 2D crystal flakes. For clarity in the IR images, we scaled up the microheaters from $25\times55\mu m^2$ to $250\times550\mu m^2$ heating area while preserving all the geometric features. We observed that the flakes exfoliated few microns away from the heating lines possess much lower temperature than the microheaters and may not be well detected under the IR camera (**Figure 5.5(b)**) while those in direct contact with the heating lines display almost the same temperature (**Figure 5.5(c)**), thanks to very high thermal conductivity of 2D crystals. As a result, only flakes exfoliated onto the heating lines were considered for the interfacial adhesion measurements at elevated temperatures.

To further evaluate the temperature of the microhetaer, 2D crystal flakes and the probe, steady state temperature distribution of our AFM setup needs to be calculated. As such, a 3D model of the setup was created using COMSOL Multiphysics (**Figure 5.6(a)**) to numerically solve the following thermal transfer equation

$$\nabla.(-k\nabla T) + \rho c \frac{\partial T}{\partial t} = q_s \tag{5.2}$$

where k, ρ and c are the thermal conductivity, material density and specific heat capacity, respectively; and T and q_s are the temperature and the density of the heat power generation, respectively. The microheater, graphite flakes, SiO_x/Si substrate and the AFM probe were surrounded by an air block of $1400\times1400\times420\mu m^3$. In the desired temperature range (<300°C), the resulting radiation losses are negligible due to the very low emissivity of the materials involved and thus heat losses caused by the thermal convection and conduction were taken into

account. Moreover, all sides of the air block were assigned a symmetry boundary condition. **Figure 5.6(b)** shows the simulated temperature distribution of the G flakes and the microheater at an input power of 5 mW. Consistent with our experimental observations, while the temperature of G flakes surrounding the microheater is highly smaller than that of the heating lines, the flake in direct contact with the microheater shows the same uniform temperature distribution as the heating line does.

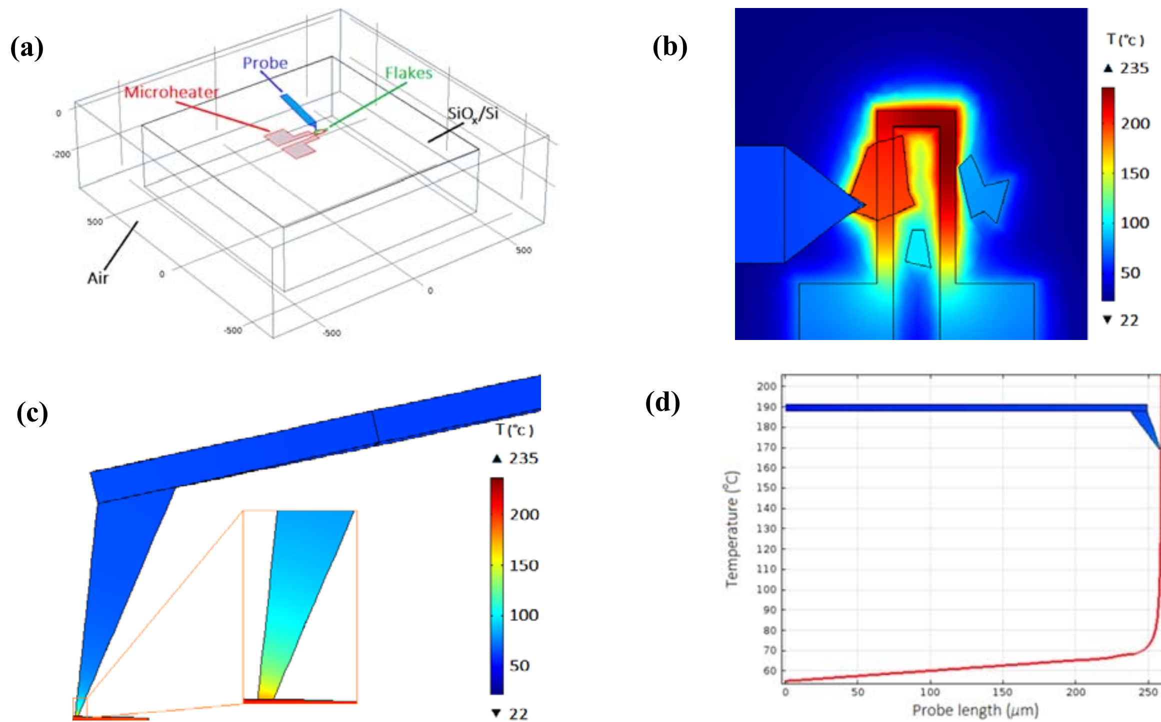

Figure 5.6. (a) 3D model of the AFM setup developed in COMSOL. (b) Steady state thermal simulation of the G flakes and microheater over the SiO_x/Si substrate at an input power of 5 mW. (c) Temperature distribution of the AFM probe. (d) Temperature distribution profile along the probe length.

We also probed temperature distribution of the AFM tip in contact with the flake at 221°C. **Figure 5.6(c)** demonstrates that the localized heating of 2D crystal flakes can effectively restrict the heat flow of the AFM tip only through the 2D crystal nanopillar with the cross-sectional area of ~0.003 μm^2, thereby maintaining the cantilever shank at temperatures consistently less than 70° C (**Figure 5.6(d)**), thanks also to the protruded (3.2 μm from the very end of the cantilever) and tall (18.5 μm) tip which also maximizes the separation between the cantilever shank and the microheater.

5.2.5 Cooling stage setup

The home-built cold stage is based on a multistage Peltier element which is attached to a machined aluminum spacer and connected to a dc power supply, where the spacer with a magnet in the Teflon base is securely fixed to the magnetic sample holder of a variable tilt mount on the X-Y piezo stage (**Figure 5.7(a)**). The Teflon base is used to further protect the piezo stage against overheating. A piece of PEDOT:PSS(D-sorbitol)-coated SiO_x/Si wafer is then attached to the cooling element using metal spring clips, where thermal compound spreads at their interface to improve the heat transfer. The aluminum spacer alone enabled to further extract the heat from the hot side of the Peltier element, thereby cooling the surface of small SiO_x/Si pieces, which are glued with PEDOT:PSS(D-sorbitol) to the SiO_x/Si substrate, down to -15.2°C (**Figure 5.7(b)**).

Figure 5.7. (a) Schematic of Peltier-based cooling stage setup. (b) Infrared image for the temperature distribution of the SiO_x/Si pieces on the multistage Peltier element, showing a very uniform temperature of -15.2°C.

Upon turning on the Peltier cooling element, microdroplets of water in the atmosphere will immediately condense on the substrate surface, increase in size and merge together to form bigger droplets and eventually cover the entire substrate surface. After turning off the Peltier, the microdroplets start to evaporate immediately at room temperature. **Figure 5.8** shows the condensation and evaporation process of microdroplets under the optical microscope within a very short time period (i.e., 10 sec).

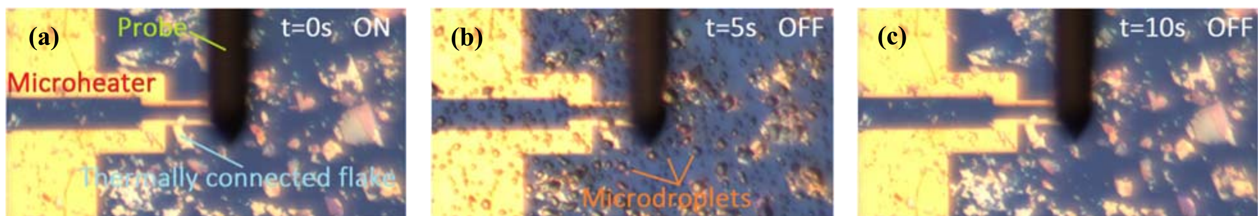

Figure 5.8. Wetting behavior during condensation and evaporation of water microdroplets on the surface of the mechanically exfoliated G/SiO_x/Si substrate when the Peltier cooling element is (a) turned ON at 0 sec, (b) then turned back OFF right after 5 sec and (c) kept in the OFF state for another 5 sec.

5.3 Interfacial Adhesion Energy Measurements

For each 2D crystal, we considered 15 thermally-connected crystal flakes on each of which 10 individual interfacial adhesion measurements at a contact pressure of 5 MPa (unless otherwise noted) were taken from different locations of the flake surface at each annealing temperature to confirm the reproducibility. The contact time (dwell time) of the 2D crystal tips with the substrate was 15 min to reach thermal equilibrium at the contact interface. The approach speed was set to be 10 nm/s while a very slow pulling rate of 1 nm/s was used so that the tip remains in thermodynamic equilibrium with the substrate upon tip retraction. Such a slow pulling rate was achieved by using a 16-bit digital-to-analog converter in low voltage mode with an ultralow noise AFM controller which significantly improved the Z scanner's vertical resolution to 0.1 Å at the expense of limiting the Z scanner's motion range. Very careful adjustment of the Z servo gain to suppress any possible oscillation of the Z scanner combined with an ultralow noise floor (<0.3 Å) in our setup could further make the retraction measurements in the near-equilibrium regime possible. In order to measure the cohesion energy, during the attachment of nanomesas to the glue-coated tip, *F–d* curves were recorded at zero normal force as the tip was gently pulled away from the substrate surface in a direction perpendicular (parallel) to the single basal plane of 2D crystal, leading to pulling (shearing) off the upper section of the nanomesa (attached to the tip apex) from the lower section (fixed to the 2D crystal substrate). The annealing temperature for the case of cohesion measurements (studied after completion of our interfacial adhesion experiments) was controlled by a Kapton heater while the probe was fully retracted (~ 4 cm) from the substrate. While the adhesion forces were calculated by the calibrated spring constant and the measured deflection signal of the AFM probe, the interfacial adhesion energy per unit area (J/m^2) was calculated by integrating the difference in force upon approach and retraction as a function of the piezo displacement, followed by dividing the resulting adhesion energy by the known contact area at the interface. To obtain the interfacial adhesion energy from the shear force-displacement curves, the maximum shear force of each nanomesa was divided by its width or diameter.

The accuracy of AFM force-displacement measurements can be limited by the uncertainty in the determination of the interfacial contact area and spring constant of the AFM probe. The first source of uncertainty in the interfacial adhesion measurements is the surface area of the tip, which must be known to determine the interfacial adhesion energy. In order to create a known contact area, we used 2D crystal tips with a very well-defined geometric shape parallel to

the substrate, enabling an atomically clean and flat contact interface. Our interfacial adhesion measurements reveal that the tilting angle between the tip and the substrate is smaller than 1°, indicating perfect face-to-face contact during measurements (**Section D.2, Appendix D**). We reduced the second main source of uncertainty in our measurements by determining the stiffness of the AFM cantilever by means of three different methods and took their mean value as the static normal (3.05±0.05 N/m) and axial (8.60±0.40 N/m) spring constants of the probe, suggesting a relative calibration error of 2% and 5%, respectively (**Section D.3, Appendix D**). Although a calibrated AFM probe was used for these experiments, the spring constant value still contains approximately ~2-5% error. Thus, the same tip was used throughout all experiments to ensure that the relative change in the interfacial adhesion energy is accurate even though the absolute value may contain some systematic error. The laser spot was also kept at the same position on the lever to avoid any changes in the force measurements. After performing all the measurements, the spring constant of the probe was again determined in ambient conditions to make sure that the cooling/annealing of the substrate has no appreciable effect on its stiffness.

5.4 Cohesion Energy in 2D Crystals

During the attachment of nanomesas to the glue-coated tip, *F–d* curves can be recorded as the tip is gently pulled away from the substrate surface in a direction perpendicular (parallel) to the single basal plane of 2D crystal, leading to pulling (shearing) off the upper section of the nanomesa (attached to the tip apex) from the lower section (fixed to the 2D crystal substrate). **Figures 5.9(a)** and **(b)** illustrate typical retraction force-displacement and shear force-displacement curves, respectively, at the intact G, hBN and MoS_2 homointerfaces. After complete retraction of the tip, our SEM and AFM inspection of the lower section of the nanomesas on the 2D crystal substrate reveals an atomically flat and defect-free surface at the separation plane (insets of **Figures 5.9(a)** and **(b)**). From retraction force measurements (**Figure 5.9(a)**), we observe a relatively gradual reduction of the adhesion force (rather than a snap-back to zero force), in particular, at the G and hBN homointerfaces, which looks at the first glance, fairly similar to the AFM rupture force curves of bridging nanobubbles. However, by closer inspection of our retraction *F–d* curves for 2D crystals and nanobubbles, we notice that not only is the effect of tip-sample capillary forces and bridging bubble ruptures on our retraction curves negligible but also there are fundamental differences in the separation mechanism of 2D crystals and bridging nanobubbles (see **Section 5.4.1**). Our shear force measurements (**Figure 5.9(b)**)

also exhibit fluctuations in plateau regions for all 2D crystals which can be attributed to the atomic stick-slip friction of the tip-attached top mesa on the mobile bottom mesa, indicating that the present axial shear force microscopy technique can provide the shear force resolution up to the atomic level compared to the conventional lateral shear force microscopy technique (**Figure D.5, Appendix D**).

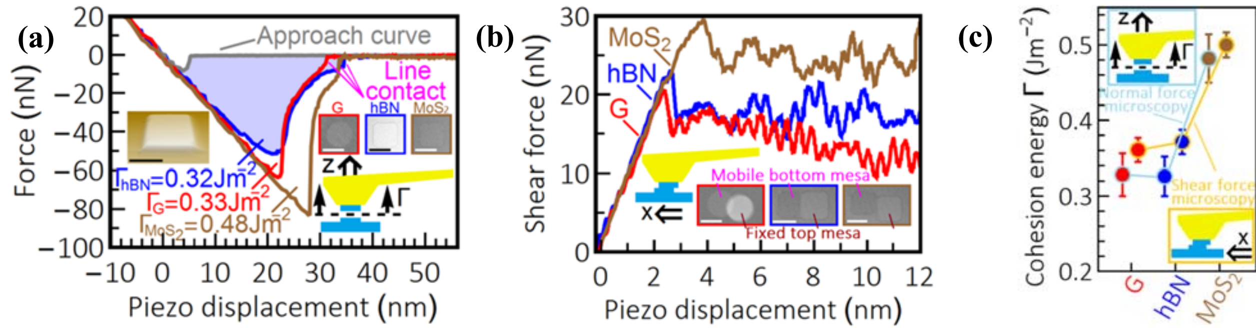

Figure 5.9. (a) Typical retraction *F–d* curves recorded at the intact homointerface of G(in red), hBN(in blue) and MoS_2 (in brown) crystals and also the approach *F–d* curve (in gray) recorded at the hBN tip/substrate homointerface. The light blue-shaded area between the approach and retraction curves at the hBN homointerface represents the cohesion energy in units of Joules. Each raw data set was given an offset to provide the same equilibrium position for all *F–d* curves. Right Inset: SEM images of lower section of the nanomesas on their corresponding bulk substrate after the full tip retraction. Left inset: Perspective AFM image corresponding to the SEM image of the MoS_2 nanomesa shown in the right inset. Scale bars indicate 50 nm. **(b)** Typical shear force–lateral piezo displacement curves recorded at the intact homointerface of G(in red), hBN(in blue) and MoS_2(in brown) crystals. Schematic inset shows that the 2D crystal substrate moves along the long axis of the cantilever tip at zero contact force. Inset: Corresponding SEM images of the sheared G, hBN and MoS_2 nanomesas. **(c)** Cohesion energy of G, hBN and MoS_2 crystals obtained by normal force measurements (circles with cyan borders) and shear force measurements (circles with orange borders) at room temperature. Data are presented as average ± standard deviation.

Figure 5.9(c) shows the intrinsic interfacial adhesion energy (i.e., cohesion energy) of G, hBN and MoS_2 crystals at room temperature with an average value of respectively 0.328±0.028, 0.326±0.026 and 0.482±0.032 Jm^{-2} using normal force microscopy, matching well with the corresponding average value of 0.361±0.014, 0.372±0.015 and 0.501±0.017 Jm^{-2} using the shear force microscopy (**Section D.1.1, Appendix D**, for a detailed comparison of cohesion energy values for 2D crystals). Slightly larger IAE values obtained by the shear measurement technique might be attributed to the small contribution of friction forces to the overall interfacial shear strength of 2D crystals. Nonetheless, both IAE measurement techniques indicate that the strongest interaction occurs between adjacent MoS_2 layers due to dipolar, partially ionic Mo–S bonds, whereas nonpolar C–C bonds and highly polar B–N bonds offer a very similar level of interaction at the G and hBN homointerfaces, respectively. In particular, our retraction *F–d* curve

for the 2D crystal/metal heterostructure is fairly similar to that for the MoS_2 homostructure, indicating more electron sharing and thus stronger interlayer bonding in MoS_2 than even predicted by first-principles calculations (see **Section 5.4.1**).

5.4.1 Force-displacement measurements of nanobubbles and G/copper

Upon retraction of the tip, we observed a relatively gradual reduction of the interfacial adhesion force (rather than a snap-back to zero force), in particular, in G and hBN crystals which is fairly similar to the AFM rupture force curves of bridging nanobubbles [82, 83]. However, our *F–d* curves upon tip approach display a small jump-to-contact force due to the hydrophobic nature of 2D crystal nanomesas (see, for instance, hBN/hBN approach curve in **Fig. 1b** in the main text), suggesting negligible effect of tip-sample capillary forces and bridging bubble ruptures on the retraction curves. In addition, similar observation in our measurements at higher annealing temperatures (up to 300°C) further confirms that the IAE in 2DLMs is mainly governed by vdW forces rather than capillary forces. For comparison purposes, we recorded rupture force curves of bridging nanobubbles formed between the *in situ* flattened Si tip and the SiO_x/Si substrate at the relative humidity of 70% (red curve in **Figure 5.10**). By closer inspection of the *F–d* curves, we notice three fundamental differences in the separation mechanism between 2DLMs (e.g., blue curve in **Figure 5.10**) and bridging nanobubbles (e.g., red curve in **Figure 5.10**). First, the separation range in the 2DLMs (typically 5-10 nm) is almost an order of magnitude shorter than that in the nanobubbles (typically 50-80 nm), further supporting the claim that the short-range vdW interaction is the major separation mechanism in 2DLMs. Second, contrary to the case of the bridging nanobubbles where the adhesion strongly depends on the retraction speed of the piezo [84], our *F–d* analysis under various tip retraction rates in the range of 1-1000nm/s reveals no appreciable effect on the IAE of 2DLMs, indicative of the absence of any dynamic (viscous) forces in the separation mechanism of 2DLMs. Third, an abrupt drop in the retraction force curves of nanobubbles just prior to the complete separation could reflect the pinch-off process of the unstable bubble neck, whereas a relatively fast transition from a surface contact to a line contact during the separation process in 2DLMs can eventually lead to the sudden break of the line contact and thereby an abrupt force drop at the very end of the separation process.

Unlike the relatively gradual reduction of the adhesion force in G and hBN crystals and bridging nanobubbles, a sudden detachment of 2D crystal tips from metal substrates (i.e., Ni, Cu, Pt and Au) is observed (see, for instance, the *F–d* curve of G tip on the Cu substrate in **Figure 5.10**). Strong interfacial adhesion energy (1.02 Jm^{-2}) between G and Cu also suggests that Cu atoms share electrons with carbon atoms. Similarly, much stronger interactions with a faster detachment at the homointerface of MoS_2 than G and hBN (Fig. 1b in the main text) suggest possible sharing electrons in the interlayer region of transition metal dichalcogenides beyond a simple vdW-only interaction. Very recent X-ray diffraction measurements on the weak interlayer interaction of 2D crystal TiS_2 also suggest more electron sharing in the S…S interaction (i.e., stronger interlayer bonding) than predicted by DFT calculations [85], implying that the presence of S…S covalent-like quasi-bonding can better account for the higher IAE value in the MoS_2 crystal of similar TMD structure.

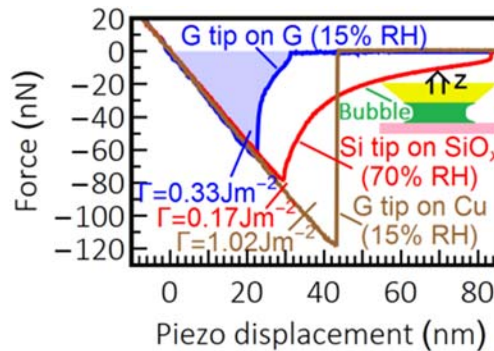

Figure 5.10. Typical retraction *F–d* curves recorded at the interface of tip-attached G nanomesa/G substrate (in blue), bare Si tip-attached nanobubble/SiO_x substrate (in blue) and tip-attached G mesa/Cu substrate (in brown) at the relative humidity of 15%, 70% and 15%, respectively. The light blue-shaded area represents the interfacial adhesion energy in units of Joules. Each raw data set was given an offset to provide the same equilibrium position for all *F–d* curves. Schematic inset shows the bridging bubble rupture between the in-situ flattened Si tip and the SiO_x/Si substrate, where the energy required to rupture the nanobubble is roughly obtained by dividing the area under the *F–d* curve over the area of the flat tip.

5.5 Adhesion Between Similar vdW Heterostructures

Figure 5.11 presents IAE values of both fresh and aged vdW homostructures at the intact, pre-cooling treated and untreated heterointerfaces as a function of annealing temperatures. We begin our discussion with IAE measurements at the intact and aged 2D crystal homointerfaces under different annealing temperatures (**Figure 5.11**). It is evident from the gray circles in **Figure 5.11** that the measured IAE at the intact homointerfaces is independent of the

annealing temperatures. However, after exposing the freshly exfoliated 2D crystal flakes to the ambient air, the IAE between similar vdW heterostructures (red circles in **Figure 5.11**) is consistently lower than their corresponding intrinsic value, mainly due to the possible adsorption of airborne contaminants (e.g., water and hydrocarbon molecules) onto the fresh surface of crystals (see **Section 5.5.1** for our detailed discussions upon water contact angle measurements). A 30% and 19% drop in the IAE of G/G and hBN/hBN, respectively, at room temperature suggests that hBN has higher chemical stability than G of very similar lattice structure (**Figure 5.12**). Although a mild annealing temperature (130°C) coupled with relatively strong vdW interactions at the interface can provide a sufficient driving force to push the trapped water molecules away from the contact interface and thus to slightly improve the IAE of the crystals (up to ~5%), a higher annealing temperature is required to build up larger pressure at the interface to drive out the majority of hydrocarbons as the main source of such IAE drop, leading to nearly full recovery of the intrinsic IAE only at the hBN homointerface upon annealing at 300°C. Interestingly, despite stronger vdW interaction of MoS_2/MoS_2 and similar level of interaction of G/G compared to hBN/hBN, the full aggregation of such contaminants into nanobubbles at the G and MoS_2 homointerfaces can only be triggered at a much elevated temperature, implying that hydrocarbons have a stronger interaction with G and MoS_2 than hBN.

We next preform a series of measurements to study the effect of pre-cooling treatment of the substrate on the IAE of the homointerfaces (blue circles in **Figure 5.11**). Surprisingly, such a precooling treatment can significantly improve the IAE of the hBN, G and MoS_2 crystals regardless of the subsequent annealing temperature. While such an IAE improvement upon 130°C and 300°C thermal annealing could be intuitively understood by hypothesizing that the formation of ice-like mono/bilayer on the freshly cleaved 2D crystals can be effectively leveraged as a self-release underlying film for the facile removal of the subsequent hydrocarbon adsorptions, this hypothesis might not be supported by our findings at room temperature and -15°C where the ice-like layer is still stable and tightly bonded to the underlying crystal surface. Notably, however, our observations can be fully supported for all range of temperatures by a recent study, showing that water adsorption on graphitic surfaces can significantly slow down the hydrocarbon adsorption rate [86], thus making the nanometer-thick ice-like water an excellent protective layer against the airborne contamination for several hours. We also note that an increase of the annealing temperature from 130°C to 300°C exhibits further improvement of the

IAE, implying that the ice-like layer which is completely removed at T≤130°C cannot fully cover the crystal surface, still leaving unprotected areas with adsorbed high boiling point hydrocarbons.

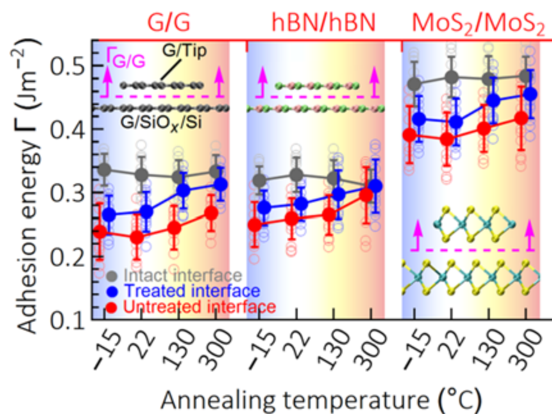

Figure 5.11. IAE values as a function of annealing temperatures at the G, hBN and MoS_2 homointerfaces using normal force microscopy technique. Filled gray circles denote the intrinsic IAE values at the intact G, hBN and MoS_2 homointerfaces whereas filled blue (red) circles denote the IAE values between 2D crystal tips and precooling-treated (untreated) substrates. Each open transparent gray circle represents a single IAE measurement at the intact homointerfaces, whereas each data point shown in open transparent blue and red circles represents the IAE of the tips on an individual 2D crystal flake averaged over 10 measurements from different locations of the flake surface. Each filled circle is presented as average of all corresponding open circles ± standard deviation. Insets illustrate ball-and-stick representation of various tip/substrate interfaces where carbon, boron, nitrogen, molybdenum, and sulfur atoms are shown in gray, green, pink, cyan and yellow, respectively.

5.5.1 Interaction of 2D crystals with airborne contaminants using water contact angle measurements

Upon the air exposure, the adsorption of airborne contaminants (e.g., water and hydrocarbon molecules) onto the fresh surface of crystals can reduce their overall free surface (Gibbs) energy, thereby the IAE between similar vdW heterostructures is consistently lower than their corresponding intrinsic value (**Figure 5.11**). A 30% and 19% drop in the IAE of G/G and hBN/hBN, respectively, at room temperature suggests that hBN has higher chemical stability than G of similar lattice structure with only slightly shorter (~1.8%) lattice constant. After exposure of mechanically exfoliated hBN, G and MoS_2 flakes to the ambient air for several months, hBN flakes exhibit much cleaner surfaces compared to G and MoS_2 flakes (**Figure 5.12**), making hBN crystals an ideal candidate for encapsulation and protection of exfoliated G and MoS_2 flakes. **Figure 5.12** also shows that the surface of G and MoS_2 flakes is readily contaminated by water, organic molecules, and other adsorbates, leading to the deterioration of their electrochemical and electronic properties.

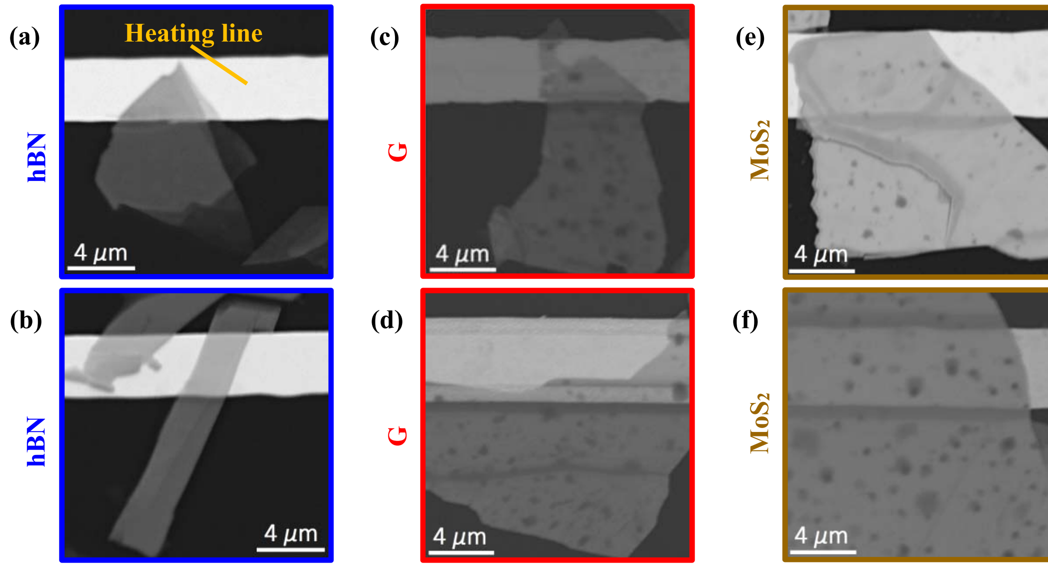

Figure 5.12. SEM images of (a), (b) hBN, (c), (d) G and (e), (f) MoS_2 flakes which are exfoliated on the heating line of the microheaters and exposed to the ambient air for several months.

Effect of airborne surface contaminations and thermal annealing on the IAE of heterostructures can be well understood in terms of intrinsic water wettability of fresh and aged surfaces of 2D crystals. Many studies on the wettability of G crystal along with very limited studies on the wettability of hBN and MoS_2 crystals all suggest that freshly cleaved crystals spontaneously adsorb airborne contamination upon the air exposure, leading to an increase in the water contact angle (WCA) of G [87], hBN [88] and MoS_2 [89] crystals, respectively, from (64°, 63°, 69°) measured within few seconds of air exposure of fresh surfaces to a saturated value of (90°, 86°, 89°) within few hours of air exposure.

We now develop an analytical model coupled with the water contact angles (WCAs) reported in literature to quantify the surface contaminations of G crystal. The total surface energy of G crystals, γ_G, which consists of contributions from both nonpolar (dispersion) interaction γ_G^d and polar (electrostatic) interaction γ_G^p of graphite (i.e., $\gamma_G = \gamma_G^d + \gamma_G^p$), can be given by the Fowkes equation:

$$2\left(\sqrt{\gamma_W^d \gamma_G^d} + \sqrt{\gamma_W^p \gamma_G^p}\right) = \gamma_W (1 + \cos\theta) \quad (5.3)$$

where γ_W^d and γ_W^p are the dispersion (21.8 mJ m^{-2}) and polar (51.0 mJ m^{-2}) components of the total surface energy of water γ_W (72.8 mJ m^{-2}), and θ is the WCA of G bulk crystal. To determine the electrostatic surface energy of G, we first measured the surface electrostatic

potential of graphite using a conductive AFM tip (SCM-PIT, Nanoworld, with the spring constant of 1.9 N/m) and found it to be ~398 mV for the tip-substrate distance of 10 nm (see **Figure 3.1**). We then calculated the electrostatic surface energy of graphite γ_G^p (0.07 mJ m^{-2}) using the well-established concept of the parallel plate capacitor model. The interfacial adhesion energy of the G crystal ($\Gamma_G = 2\gamma_G$) in **Table 5.1** and **Figure 5.13** is calculated by finding the dispersion interaction as follows

$$\gamma_G^d = \frac{1}{\gamma_W^d}\left[\frac{\gamma_W}{2}(1+\cos\theta) - \sqrt{\gamma_W^p \gamma_G^p}\right]^2 \tag{5.4}$$

The results marked by the star in **Table 5.1** are the IAE of the airborne contamination adlayer, γ_{CHO} $(= \gamma_{CHO}^d + \gamma_{CHO}^p)$, whose electrostatic interaction γ_{CHO}^p was similarly determined to be 0.32 mJ m^{-2} and therefore can be expressed by

$$\gamma_{CHO}^d = \frac{1}{\gamma_W^d}\left[\frac{\gamma_W}{2}(1+\cos\theta) - \sqrt{\gamma_W^p \gamma_{CHO}^p}\right]^2 \tag{5.5}$$

Table 5.1. Summary of water contact angle measurements and corresponding IAE values of G crystal.

Notes	Measured within	WCA	$2\gamma_G$ (J/m^2)	Ref
Ultrahigh vacuum	3 sec	42±7°	0.348±0.033	[90]
Ambient air at 24°C/48% RH	10 sec	64.4°	0.232	[87]
	2 days	91.0°	0.093*	
550°C annealing in Ar	1 min	54.1°	0.286	
Ambient air at 22-25°C/20-40% RH	10 sec	64.4±2.9°	0.232±0.015	[91]
	7 days	97.0±1.8°	0.072±0.01*	
Ultrahigh vacuum for 15 h	N.A.	59°	0.260	
Ambient air at 22-25°C/20-40% RH	10 sec	68.6±7.1°	0.210±0.034	[92]
Ambient air at 22°C/50% RH	10 sec	68.2±2°	0.212±0.010	[93]
	1 day	90±0.1°	0.096±0.002*	
Ambient air at RT/40-50% RH	1.5 min	62.9±2.2°	0.239±0.012	[94]
Ambient air at RT/40-50% RH	5 min	61.8±3.3°	0.249±0.017	
	1 day	81.9±2.9°	0.129±0.012*	
600°C annealing in He	N.A.	51.4±2.0°	0.300±0.010	
Clean room at 21°C/40% RH	5 sec	53±5°	0.292±0.027	[95]
	8 min	66±3°	0.223±0.016	
	2 days	86±4°	0.112±0.016*	
Water vapor atmosphere	N.A.	58±2°	0.266±0.010	
Ultrahigh-purity argon atmosphere	1 min	45±3°	0.333±0.016	
Evacuation/1050°C annealing/vacuum	1 min	55±1°	0.281±0.005	
Evacuation/1000°C annealing/atmosphere	1 min	73±5°	0.187±0.025	
Ambient air at 22-25°C/20-40% RH	10 sec	60±0.1°	0.255±0.002	[86]

* Interfacial adhesion energy of airborne contamination adlayer.

Our further analysis on the temporal evolution of the adhesion energy and contamination thickness measured on the mechanically exfoliated HOPG surface during the first 60 min of air exposure reveals that its intrinsic IAE of 0.341±0.025 Jm^{-2} obtained under ultrahigh vacuum or

ultrahigh-purity argon atmosphere is well consistent with our experimental value of 0.328±0.028 Jm^{-2} but drastically decreases within the first minute of air exposure and eventually approaches a saturated value of 0.15±0.02 Jm^{-2} after 10 min (**Figure 5.13**), which is much smaller than our IAE value of 0.233±0.035 Jm^{-2} upon room-temperature storage for 10 h. This could be attributed to the presence of the contact pressure and the vdW interaction between the layers in our experiments which may still play a role to squeeze away the contaminants even at room temperature, leaving cleaner interfaces with stronger interactions. We also note that a substantial decrease in the surface hydrocarbon level under vacuum, high-temperature (500–1000°C) treatment during the WCA measurements results in the IAE recovery of the G crystal (0.282±0.024 Jm^{-2}), which is in good agreement with our IAE value of 0.268±0.028 Jm^{-2} at much lower temperature (300°C), further confirming the dominant contribution of the vdW force to the IAE improvement.

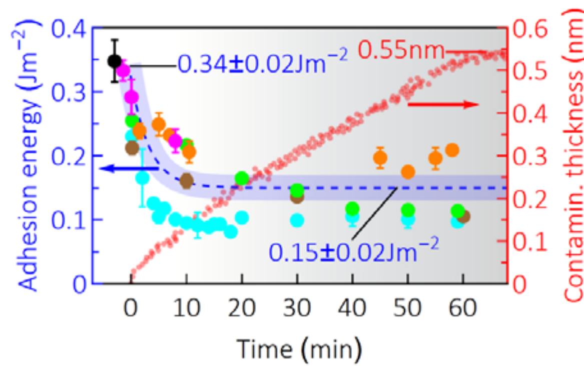

Figure 5.13. Temporal evolution of the adhesion energy (left axis in blue) and contamination thickness (right axis in red) measured on the mechanically exfoliated HOPG surface during the first 60 min of air exposure. Adhesion energy is extracted from WCA measurements of refs. [90], [91], [93], [94], [95] and [86] denoted by black, cyan, brown, orange, magenta, green circles, respectively. Adsorbed contamination layers linearly grow within the first 60 min of air exposure, reaching a thickness of ~0.55nm, and then the growth rate considerably decreases and plateaus at ~0.60nm after several hours [86].

5.6 Adhesion Between Dissimilar vdW Heterostructures

Our IAE measurements on dissimilar vdW heterostructures exposed to air at room temperature (red circles in **Figure 5.14**) reveal that the adhesion level at the untreated G/hBN interface remains roughly the same as that at the untreated G and hBN homointerfaces over the temperature range of -15–300°C, whereas the IAE value of MoS_2 on the untreated G and hBN substrates is almost two-fold smaller than that on the untreated MoS_2 substrate. During the approach-retract course, we observe a very similar adhesive response of the G nanomesa to both

G and hBN substrates within our experimental accuracy, suggesting that the IAE of G/hBN is governed primarily by the same level of dispersion energy at the interface with a negligible contribution from the electrostatic interactions of hBN, which are absent at the G/G interface. However, this is not the case at the contact interface between MoS_2 and hBN(G) where different crystal structures and different static polarizabilities of the constituent atoms dictate very different levels of short-range dispersive (vdW) and long-range electrostatic (Coulombic) interactions at the MoS_2/MoS_2 interface and MoS_2/hBN(G) interfaces. Notably, we observe that unlike very high-quality interface of untreated MoS_2/MoS_2 upon annealing at 300°C, untreated MoS_2/hBN and G/MoS_2 interfaces do not show any further improvement, implying an absent or even negative impact of such a high annealing temperature on the IAE of MoS_2/hBN(G).

This counterintuitive observation can be explained by a trade-off between interface self-cleansing mechanisms driven by the vdW forces and MoS_2 oxidation process triggered by relatively high temperatures (>130°C) in the ambient air. On one hand, two-fold weaker vdW interaction in MoS_2/hBN(G) than MoS_2/MoS_2 can still provide sufficient driving forces of similar magnitude to those of G/G, hBN/hBN and G/hBN for the segregation of the contaminants to the localized nanobubbles, leading to the enhanced IAE of MoS_2/hBN(G) at 300°C. On the other hand, the weaker interaction of MoS_2/hBN(G) can facilitate the oxygen interfacial diffusion and thereby the oxidation process which is initiated from the edges, grain boundaries and intrinsic atomic defects of MoS_2 and gradually penetrates into the MoS_2 grains at the interface. This is consistent with the gradual surface oxidation of MoS_2 in ambient conditions [96] and the low-temperature surface oxidation of MoS_2 which is initiated at ~100°C and significantly increases at 300°C [97], resulting in the negative impact of oxygen adsorption on the photocurrent and field-effect mobility of MoS_2 transistors in air [98, 99] and on the mobility and homogeneity of MoS_2/G heterostructure devices after annealing above 150°C [100].

We hypothesize two possible interfacial oxidation mechanisms responsible for the weaker interaction of MoS_2/hBN(G) at 300°C: (1) replacement of sulfur atoms with oxygen atoms results in a lower surface energy in the oxidized MoS_2 (MoO_3) than unreacted MoS_2; (2) partial protrusions (0.36±0.25nm [101]) at the interface due to formation of interfacial MoO_3 patches along with the presence of gaseous reaction products (e.g., SO_2, which cannot diffuse out of interface owing to extremely high vdW pressure on trapped molecular layer [102]) gives rise to local interlayer decoupling of unreacted MoS_2 crystal from underlying hBN and G substrates.

Similar to the precooling-treated G, hBN and MoS_2 homointerfaces, it is evident from the blue circles in **Figure 5.14** that precooling treatments can effectively protect the crystal substrates against the airborne contaminants and thus boost the adhesion level at the interface of dissimilar vdW heterostructures at much lower annealing temperature of 130°C. However, such a protective layer offers no appreciable improvement in the IAE of MoS_2/hBN(G) at 300°C, further confirming the possible destructive effect of interfacial contaminations/oxygen diffusion on the MoS_2 oxidation at higher temperatures.

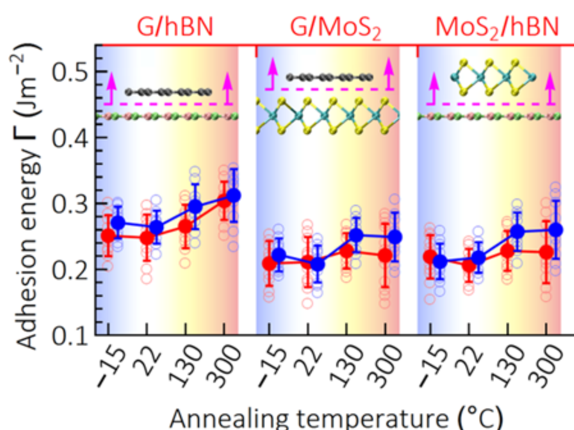

Figure 5.14. IAE values as a function of annealing temperatures at the G/hBN, G/MoS_2 and MoS_2/hBN heterointerfaces using normal force microscopy technique. Filled blue (red) circles denote the IAE values between 2D crystal tips and precooling-treated (untreated) substrates. Each data point shown in open transparent blue and red circles represents the IAE of the tips on an individual 2D crystal flake averaged over 10 measurements from different locations of the flake surface. Each filled circle is presented as average of all corresponding open circles ± standard deviation. Insets illustrate ball-and-stick representation of various tip/substrate interfaces where carbon, boron, nitrogen, molybdenum, and sulfur atoms are shown in gray, green, pink, cyan and yellow, respectively.

5.7 Adhesion Between 2D Crystals and SiO_x

Here we report in **Figure 5.15** an AFM quantitative characterization of the interlayer interactions of 2D crystals on both untreated and pre-cooling treated SiO_x substrates which provides a benchmark experimental data set for other experimental techniques (**Section D.1.2, Appendix D**). Similar to untreated 2D crystals, the thermal annealing can effectively remove the water and hydrocarbons from the untreated SiO_x surface, leading to the higher IAE at the 2D crystal/SiO_x interface. Surprisingly, however, unlike the case of 2D crystal substrates, the precooling treatment results in the weaker interaction of the 2D crystals with the SiO_x substrate at both -15°C and room temperature. This weaker interaction may be explained by the hydrophilic nature of SiO_x that can adsorb a homogeneous and flat water film of thickness 2-3nm

(~6-10 monolayers of water) on its silanol (Si–OH)-rich surface when storing at -15°C (corresponding to 100% relative humidity) [103]. As such, our IAE measurements at -15°C (i.e., 0.171±0.041, 0.177±0.042 and 0.152±0.034 Jm^{-2} for the G, hBN and MoS_2 crystals on SiO_x, respectively) essentially take place at the 2D crystal/water interface rather than 2D crystal/SiO_x interface. In addition, a larger IAE of 2D crystal/treated SiO_x at room temperature compared to that at -15°C can be attributed to the presence of a mixture of ice-like mono/bilayer structure (fully H-bonded to the silanol groups) and liquid-like few-layer structure on top of the ice-like layer at room temperature. Such trapped liquid-like film can segregate into isolated nano-sized bubbles [104] by means of the contact pressure and the interlayer vdW forces, bringing the 2D crystals into closer proximity with the SiO_x surface and thus enhancing the IAE at the 2D crystal/SiO_x interface. Similarly, the weaker interaction between the 2D crystals and the untreated SiO_x at -15°C compared to that at room temperature is presumably due to the formation of the thicker ice-like layer on the SiO_x surface at -15°C. We also note that the thermal annealing at 130°C and 300°C makes no appreciable difference in the interfacial adhesion level between 2D crystal/precooling-treated SiO_x and 2D crystal/untreated SiO_x, confirming the formation of the protective ice-like layer on the untreated SiO_x substrate due to 15% RH in the ambient air.

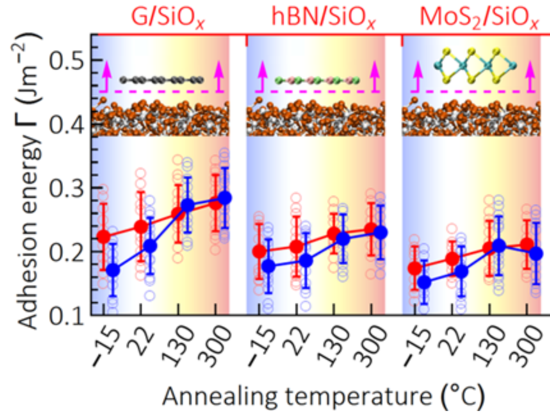

Figure 5.15. IAE values as a function of annealing temperatures at the G/SiO_x, hBN/SiO_x and MoS_2/SiO_x heterointerfaces using normal force microscopy technique. Filled blue (red) circles denote the IAE values between 2D crystal tips and precooling-treated (untreated) substrates. Each data point shown in open transparent blue and red circles represents the average IAE value obtained from 10 measurements within an individual small region (1μm×1μm) of SiO_x substrate. Each filled circle is presented as average of all corresponding open circles ± standard deviation. Insets illustrate ball-and-stick representation of various tip/substrate interfaces where carbon, boron, nitrogen, molybdenum, sulfur, silicon and oxygen atoms are shown in gray, green, pink, cyan, yellow, white and orange, respectively.

Similar to the interaction of MoS_2 crystal with the other 2D crystals, the high annealing temperature of 300°C can drastically reduce the adhesion level at the MoS_2/treated-SiO_x interface, which lends additional support to the hypothesis of MoS_2 oxidation at higher temperatures due to the chemical reaction of MoS_2 with the trapped water and the diffused oxygen. Such significantly reduced IAE of MoS_2/treated-SiO_x relative to MoS_2/hBN(G) at 300°C can be understood as a direct consequence of the strong hydrophilic property of SiO_x, where the MoS_2 crystal undergoes an additional chemical reaction with the interfacial water layer, resulting in the partial etching of the MoS_2 interface layer and needle-like protrusions due to the formation of $MoO_3.H_2O$ on the MoS_2 surface [105]. It is worth pointing out that although oxygen plasma treatment can completely remove any water and hydrocarbon molecules, leaving a contamination-free SiO_x surface terminated with more silanol groups, we observed that stronger interaction between 2D crystals and plasma-cleaned SiO_x surface leads to the exfoliation of 2D crystals across the thickness of nanomesa, making a direct IAE measurement at 2D crystals/plasma-treated SiO_x interfaces inaccessible.

5.8 Tabulated Experimental Data

In order to provide a valuable guideline for the fabrication of vdW heterostructures based on the vdW pick-up transfer techniques, we have presented a summary of the cohesion energy at the intact G, hBN and MoS_2 homointerfaces (**Table 5.2**) and the interfacial adhesion energy of untreated and precooling-treated homo/heterostructures (**Table 5.3**), corresponding to the experimental data points in **Figures 5.9(c), 5.11**, **5.14** and **5.15**.

Table 5.2. Summary of cohesion energy Γ (Jm^{-2}) at intact G, hBN and MoS_2 homointerfaces.

T(°C)	Normal force microscopy technique			Shear force microscopy technique		
	G/G	hBN/hBN	MoS_2/MoS_2	G/G	hBN/hBN	MoS_2/MoS_2
-15	0.336±0.025	0.319±0.022	0.471±0.035			
22	0.328±0.028	0.326±0.026	0.482±0.032	0.361±0.014	0.372±0.015	0.501±0.017
130	0.324±0.027	0.322±0.029	0.479±0.036			
300	0.333±0.026	0.312±0.027	0.484±0.030			

These tables show, for instance, that both G and hBN can be used to pick up all three 2D crystals from the SiO_x substrate at room temperature. However, the stronger adhesion of G to the SiO_x substrate requires careful selection of the 2D crystals for the high-yield G pick-up, making MoS_2 a relatively improper choice for such a purpose. Moreover, the simple precooling treatment of the SiO_x substrate before the mechanical exfoliation of 2D crystals can highly

facilitate the 2D crystal pick-up by reducing the interfacial adhesion energy at the 2D crystal/SiO_x interface.

Table 5.3. Interfacial adhesion energy Γ (Jm^{-2}) in similar/dissimilar heterostructures using normal force microscopy.

T(°C)	Similar vdW heterostructures			Dissimilar vdW heterostructures			2D crystal/SiO_x heterostructures		
	G/G	hBN/hBN	MoS_2/MoS_2	G/hBN	G/MoS_2	MoS_2/hBN	G/SiO_x	hBN/SiO_x	MoS_2/SiO_x
	Untreated substrates								
-15	0.239±0.044	0.250±0.035	0.391±0.045	0.251±0.031	0.209±0.034	0.219±0.033	0.223±0.052	0.200±0.043	0.174±0.034
22	0.230±0.035	0.259±0.032	0.384±0.042	0.248±0.035	0.211±0.038	0.206±0.025	0.239±0.054	0.208±0.047	0.189±0.027
130	0.245±0.034	0.265±0.031	0.401±0.037	0.265±0.033	0.228±0.027	0.228±0.030	0.259±0.045	0.228±0.031	0.205±0.043
300	0.268±0.028	0.296±0.044	0.417±0.050	0.304±0.029	0.221±0.048	0.226±0.047	0.276±0.044	0.235±0.041	0.211±0.038
	Precooling-treated substrates								
-15	0.265±0.030	0.276±0.027	0.416±0.036	0.271±0.024	0.222±0.025	0.212±0.027	0.171±0.041	0.177±0.042	0.152±0.034
22	0.270±0.031	0.282±0.026	0.411±0.037	0.264±0.025	0.208±0.028	0.218±0.023	0.209±0.044	0.186±0.043	0.169±0.039
130	0.303±0.028	0.297±0.038	0.445±0.036	0.295±0.034	0.252±0.026	0.257±0.029	0.273±0.043	0.220±0.038	0.209±0.046
300	0.313±0.026	0.310±0.042	0.455±0.038	0.312±0.040	0.249±0.037	0.260±0.044	0.284±0.047	0.230±0.042	0.197±0.048

5.9 Adhesion at G/SiO_x Interface: Beyond vdW Interaction

During interfacial adhesion measurements of G/SiO_x at the annealing temperatures of 130°C and 300°C, we unexpectedly observed abrupt detachment of G nanomesa with single/multiple force jumps in the *F–d* retraction curves, resulting in much stronger interfacial interactions in G/SiO_x than hBN(MoS_2)/SiO_x. In particular, the separation process of 2D crystal tips in our setup dictates a relatively gradual reduction of the interfacial adhesion force between two adjacent 2D crystal flakes and between hBN(MoS_2) nanomesas and SiO_x substrate. As a result, such sudden detachment with single/multiple plateau force jumps in the G/SiO_x adhesion curves cannot be interpreted as a consequence of experimental noises, thermal fluctuations and mechanical instabilities of the probe, as they are roughly equally present in all the *F–d* measurements.

From over hundred interfacial adhesion measurements for the G/SiO_x interaction, we identified three distinct *F–d* curves, each describing gradually broken contacts (i.e., weak interaction without any force jump), suddenly broken contacts (i.e., strong interaction with a single force jump), and a transition from gradually to suddenly broken contacts (i.e., mild interaction with multiple force jumps), as shown in **Figure 5.16(a)**. To provide a rational explanation of the origin of such distinctive interfacial behavior in the G/SiO_x heterostructure, we begin by addressing quantitatively to what degree the interfacial adhesion of G/SiO_x interfaces (and also intact and aged G homointerfaces for comparative purposes) is controlled by the conformity of the tip-attached G nanomesa to the underlying substrate morphology. To this

end, a series of interfacial adhesion measurements over a pressure range of 0-10 MPa was conducted at the interface of G crystal tip/pre-annealed SiO_x substrate and G crystal tip/pre-annealed G substrate, as shown in the top and bottom panel of **Figure 5.16(b)**, respectively. To further minimize experimental uncertainty, a 2μm×2μm smooth region of the SiO_x (G) substrate with an RMS surface roughness of 0.305nm (0.077nm) was first located by non-contact AFM roughness measurements and then, ten contacts with 100 nm interval spacing were formed at each pressure load under a very clean environment, allowing us to perform all measurements within a very small region in close proximity to the microheater (see the SEM image in the inset of bottom panel in **Figure 5.16(b)**). Moreover, prior to each pressure increment, SiO_x and G substrates are annealed at 300°C for 30 min to remove any possible adsorbed contaminations and then the G crystal tip/pre-annealed substrate interface is further annealed at 300°C for 15 min, followed by the new round of adhesion measurements

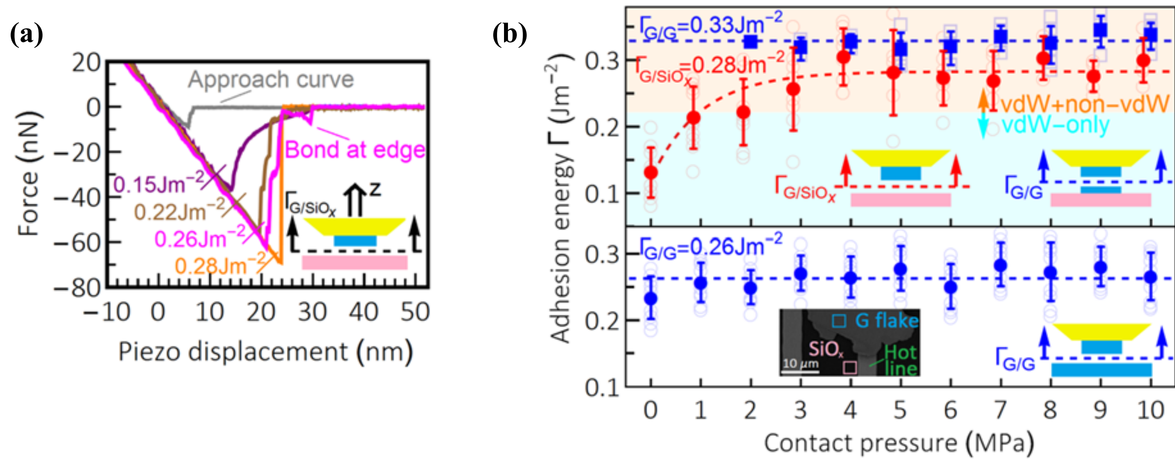

Figure 5.16. **(a)** Typical retraction *F–d* curves of the G/SiO_x interface recorded at no contact pressure (in purple) and 5MPa (in brown, magenta and orange) and also a typical approach *F–d* curve (in gray). **(b)** IAE values as a function of contact pressure at the intact G homointerfaces (filled blue squares in top panel), G/SiO_x interfaces (filled red circles in top panel) and aged G homointerfaces (filled blue circles in bottom panel). Each open transparent symbol represents a single IAE measurement at the given contact pressure. Each filled symbol is presented as average of all corresponding open symbols ± standard deviation. From 110 IAE measurements shown in the top panel, 33 and 77 contacts result in the separation of G crystal tip across the thickness of the nanomesa (open blue squares) and from the SiO_x surface (open red circles), respectively. In the top panel, cyan and orange shaded regions indicate the vdW-only and vdW+non-vdW interactions of G/SiO_x, respectively, where the liftoff in the vdW-only region is relatively gradual in comparison to the vdW+non-vdW region. Dashed blue lines denote an overall average IAE value of 0.328±0.022 Jm^{-2} and 0.263±0.032 Jm^{-2} at the intact G homointerface (top panel) and aged G homointerface (bottom panel), respectively. Dashed red line in the top panel represents the best fit to the data, indicating the pressure dependence of IAE at the interface with an average value of 0.284±0.046 Jm^{-2} taken within the pressure-independent region (i.e., ≥3MPa). Inset of bottom panel: SEM image showing 2μm×2μm square regions of G (in turquoise) and SiO_x (in rose) substrates on which all measurements are performed in close proximity to the microheater.

It is observed from **Figure 5.16(b)** (top panel) that the G crystal tip requires a contact pressure of ≥3MPa to conform closely to the SiO_x surface, thereby enhancing the IAE of the G/SiO_x interface from 0.131±0.038 Jm^{-2} at zero pressure to 0.289±0.034 Jm^{-2} at 10 MPa. In contrast, both the intact G homointerface (blue squares in the top panel of **Figure 5.16(b)**) and the aged G homointerface (bottom panel in **Figure 5.16(b)**) suggest a constant IAE value of 0.328±0.022 Jm^{-2} and 0.263±0.032 Jm^{-2}, respectively, almost entirely independent of the pressure, indicative of atomically flat and dangling bond-free G/G interfaces. It is also evident from the top panel in **Figure 5.16(b)** that graphene flakes are not exfoliated on SiO_x at very low pressure (< 2MPa) and only 10% and 20% of contacts at 2 and 3 MPa, respectively, result in the exfoliation of graphene flakes, indicating the significant contribution of the conformal adhesion to the overall interfacial adhesion strength of the G/SiO_x interface. More importantly, we observe that abrupt detachment events with single/multiple force jumps in the retraction curves of G/SiO_x take place more frequently at higher pressure in such a way that nearly all contacts are suddenly broken at the pressure load of ≥4MPa with IAE values roughly greater than 0.221 Jm^{-2}. Surprisingly, this value is very close to theoretical calculations of the intrinsic vdW interaction energy (0.230 Jm^{-2}) at the G/SiO_x interface obtained for the multilayer graphene blister tests on the SiO_x substrate under pressure loading [106]. Hence, while a continuous decrease in the retraction curves can be attributed to the long-range vdW interaction of G/SiO_x with IAE values typically smaller than 0.221 Jm^{-2}, direct observation of single/multiple force jumps at stronger G/SiO_x interfaces can be hypothesized to be the result of formation of short-range chemical bonds at the interface.

In particular, both experimental and theoretical results confirm that G flakes supported on SiO_x exhibits much higher chemical reactivity than suspended G flakes, mainly due to the combined action of inhomogeneously distributed charge puddles (induced by polar adsorbates, such as water molecules on the silanol surface and by ionized impurities, such as Na^+ ions trapped on SiO_x) and larger topographic corrugations (induced by thermal fluctuation and vdW interaction at the G/SiO_x interface) [107, 108, 109, 110]. As such, hydrogen and oxygen molecules preferentially bind to apexes of corrugated G due to the combined contribution from the enhanced elastic and electronic energies of convex regions on the G surface [111]. Notably, from **Figure 5.16(b)**, only ~22% chemical bond-induced improvement in the IAE of G/SiO_x (i.e., from 0.221±0.030 Jm^{-2} to 0.284±0.046 Jm^{-2}) under relatively low pressure (of the order of

few MPa) leads us to believe that (1) vdW interactions are still the dominant mechanism of adhesion at the G/SiO_x interface; (2) the formation of hydrogen bonds (e.g., C–H…O–Si, C–O…H–O–Si and C–O–H…O–Si in the absence of contaminants and C–H…$\underset{H}{O}$–H…O–Si and C–O…H–O–H…O–Si in the presence of water molecules) rather than covalent bonds could result in such force jumps in the retraction curves; nonetheless, the formation of any covalent bonds between G and SiO_x (e.g., C–O–Si and C–Si [112, 113, 114, 115, 116]) cannot be completely ruled out because the effect of localized tensile strain and charge transfer on the chemical activity level of the corrugated G is poorly understood, and thus exploring site-specific adsorption mechanisms of external chemical species (e.g., molecules and atoms) at the ripple apexes and edges of 2D crystal flakes is warranted. In addition, the specific chemical reactivity of the carbon atoms with accessible and highly active electrons at the edge of the G flakes can also contribute to the formation of chemical bonds, as observed in a number of our retraction curves (e.g., see the magenta curve in **Figure 5.16(a)**).

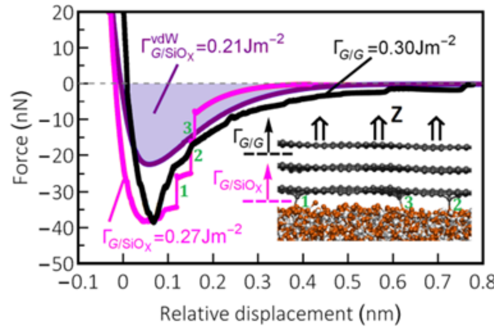

Figure 5.17. MD-calculated force versus relative displacement curves for the interaction of G/G (in black), the vdW-only interaction of G/SiO_x (in purple) and vdW+non-vdW interaction of G/SiO_x (in magenta) with three covalent C–O–Si bonds at the interface. Each force jump labeled by 1, 2 and 3 represents the break of the corresponding covalent bond, as illustrated by the MD pull-off simulation in the inset.

To gain an in-depth understanding of underlying mechanisms associated with the interaction of G crystal and the SiO_x substrate, we performed classical MD simulations using the LAMMPS simulator at room temperature. Four 98.2Å×102.1Å G layers with AB stacking were placed at a distance of 3.0 Å above an amorphous SiO_x substrate (143.3×146.5×21.3Å^3) while the flattened tip was modeled by a tapered silicon (001) layer (inset of **Figure 5.17**). The total interfacial force (i.e., vdW and non-vdW forces) and relative displacement between the innermost G layer and the SiO_x substrate were simultaneously monitored as the tapered silicon

(001) layer was pulled in the normal direction with a constant speed of 10^{-2} Å/ps. Our MD results show that force jumps in the retraction curves can only be achieved by breaking short-range chemical bonds at the G/SiO_x interface (**Figure 5.17**).

It is also to be noted that in contrast to MD-calculated retraction curves in **Figure 5.17**, the number of force jumps in **Figure 5.16(a)** does not necessarily correspond to the number of chemical bonds at the G/SiO_x interface. One may argue from an interfacial fracture standpoint that once the restoring force of the probe cantilever exceeds the strength of the G/SiO_x interaction (i.e., the pull-off force), interfacial nano-sized cracks form and propagate until complete interfacial fracture occurs. As such, the interfacial fracture of G/SiO_x heterostructure is a combined action of the external pull-off force and the internal adhesion force (i.e., vdW and/or non-vdW forces). For the case of the vdW-only interaction of G/SiO_x, both a smaller pull-off force and the smooth and slow propagation of nanocracks contribute to the relatively gradual reduction of the interfacial adhesion force (purple curve in **Figure 5.16(a)**). In contrast, faster crack propagation in the stronger vdW+non-vdW interaction of G/SiO_x which is triggered by a larger pull-off force, results in the abrupt force drop in the retraction curves immediately upon the initiation of the separation process. As the nanocracks are continuously propagating and the pull-off force becomes progressively smaller and smaller, the chemical bonds (i.e., the anchoring spots) gain the ability to pin the nanocrack tips and thus momentarily retard the crack propagation. Such unique crack arresting behavior at the G/SiO_x interface gives rise to very short signals in the retraction curves through a significant decrease in the force drop rate, making the detection of the chemical bonds possible in our setup (brown and magenta curves in **Figure 5.16(a)**). However, in the case of suddenly broken contacts with a single force jump (e.g., orange curve in **Figure 5.16(a)**), as the number of the interfacial chemical bonds increases, larger and larger pull-off forces are required to initiate the interfacial fracture of the G/SiO_x, thereby much faster nanocrack propagation at the beginning of the separation process causes all interfacial chemical bonds to suddenly break and thus no longer allows our setup to capture the crack arresting behavior during propagation. Furthermore, while both the pull-off and interfacial adhesion forces are primarily responsible for developing the interfacial nanocrack growth and separation (see step-like events in the retraction curves), when the pull-off force approaches zero, further pull-off force needs to build up to overcome possible chemical bonds at the edge of G flakes (magenta curve in **Figure 5.16(a)**).

5.8.1 Origin of distinctive interfacial behavior in G/SiO_x heterostructures: surface roughness measurements

To gain a sub-nanoscale insight into the origin of the distinctive interfacial behavior in the G/SiO_x heterostructure specifically and into the underlying interaction mechanism of 2D crystals and SiO_x in general, the interfacial contact of 2D crystal nanomesas with SiO_x substrate alone does not provide a direct access to the 2D crystal/SiO_x interface. Therefore, three-dimensional surface topography measurements of single layer 2D crystals on SiO_x with sub-nanometer resolution together with the power spectral density (PSD) analysis of the surface roughness data provides a versatile means to explore the interfacial behavior of 2D crystal/SiO_x heterostructure. To do so, 2D crystal stamps with 10 μm square mesas of thickness 10-30 nm are mechanically transferred onto a flat polydimethylsiloxane (PDMS) substrate using a combined imprint-assisted shear exfoliation and transfer printing technique [117]. The flat PDMS stamp with the uniform exfoliated multilayer mesas enables a fully conformal contact with the SiO_x substrate under a uniform pressure. A lab-made roller tool [7] was used to transfer the 2D crystal mesas from the PDMS substrate to the 90 nm thick SiO_x/Si substrate at a contact pressure of 5 MPa. Prior to the flake transfer, SiO_x samples were sonicated in acetone, isopropanol and deionized water and dry blown with nitrogen, followed by annealing at 200 °C. Raman spectroscopy coupled with AFM height profile measurements were used to determine the layer number of the exfoliated mesas with monolayer accuracy. From the

The most popular parameter characterizing the morphology of surfaces is the root mean square (RMS) roughness, which describes the RMS height of an $L \times L$ scanned surface area around its mean value as follows

$$R_q = \sqrt{\frac{1}{N^2}\sum_{m=1}^{N}\sum_{n=1}^{N} Z^2(x_m, y_n)} \tag{5.6}$$

where *N* represents the number of grid points in *x*- or *y*-direction with a pixel size of $\Delta L \times \Delta L$ ($\Delta L = L/N$), $Z(x_m, y_n)$ is the height of the surface relative to the mean line at position (x_m, y_n), and $x_m = m\Delta L$, $y_n = n\Delta L$. Despite its reliable information on the height deviation, the RMS surface roughness can neither distinguish between peaks and valleys nor describe the lateral distribution of surface features. Using a fast Fourier transform (FFT) algorithm, the power

spectral density (PSD) can however provide a more accurate and comprehensive description of the surface roughness both in vertical and lateral directions. To analyze the AFM image data, we adopt the following two-dimensional (2D) PSD function

$$\mathrm{PSD}(f_x, f_y) = \frac{1}{L^2}\left\{\sum_{m=1}^{N}\sum_{n=1}^{N} Z(x_m, y_n)\exp\left[-2\pi i\Delta L\left(mf_x + nf_y\right)\right](\Delta L)^2\right\}^2 \quad (5.7)$$

where f_x and f_y are the spatial frequency in the *x*- and *y*-directions, respectively, which take the discrete range of values $1/L$, $2/L$, . . . , $N/2L$. According to the Parseval's theorem, the square root of the area under the PSD curve is equal to the RMS roughness.

Using a 16-bit digital-to-analog converter in low voltage mode with an ultralow noise AFM controller can significantly improve the X-Y scanner's lateral resolution to subnanometer ($L/2^{16}$) and the Z scanner's vertical resolution to sub-angstrom (at the expense of limiting the X-Y and Z scanners' motion range), allowing us to image atomic-scale features. Given that the radius of the AFM tip determines the maximum spatial frequency (i.e., $N/2L$) that can be measured, 200 nm square images with 256 × 256 pixel resolution were captured for each 2D material flake at a scanning rate of 0.5 Hz, providing a pixel size of 0.8 nm smaller than the probe tip radius of <2-5 nm. To obtain a more accurate PSD of the surface, at least twenty data sets obtained from different locations of the sample were processed and then averaged for each case. A first-order regression polynomial was selected to remove any artifacts that result from the slope (consistently less than 0.1°) produced by the scanning process. Since the features smaller than 2 nm (i.e., spatial frequency > 0.5 nm^{-1}) may not be captured in our setup due to contributions from both the limited size of the tip radius and instrumental noise, we applied a low pass filter to the 2D PSD of the AFM topographic images to suppress <2nm features without any effect on the physical content of the image data [118, 119].

In order to perform accurate and repeatable surface roughness measurements, the tip sharpness and the system noise floor play a key role. We used an ultrasharp tip with 2nm nominal radius of curvature (<5nm guaranteed) and sparing constant of 39.1 N/m in the noncontact mode and in the attractive regime (with a frequency shift of -10 Hz and free amplitude of 7.5 nm) under ambient conditions and then determined the noise floor of the AFM system (being consistently less than 0.3 Å) by measuring the average surface roughness under the following conditions: contact mode with 256 × 256 pixel resolution and zero scan size (i.e., the tip apex remains in static contact with the sample surface at a single point). To ensure the tip

sharpness is preserved throughout the roughness measurements, we performed more than 50 sequential imaging with sub-angstrom precision in non-contact mode of the same area on the SiO_x surface and monitored the variation of the surface roughness measurements. We acquired an average surface roughness value of 310 pm with a standard deviation of 5 pm.

Typical high-resolution 200×200 nm^2 AFM topographic images of bare SiO_x and monolayer G, hBN and MoS_2 flakes supported on SiO_x and the PSD profiles corresponding to the images are shown in **Figures 5.18(a)** and **(b)**, respectively. It is evident that highly random corrugations with sub-nanometer vertical dimension but few-nanometer lateral dimension in monolayer 2D crystals are imposed by the underlying SiO_x substrate. In **Figure 5.18(c)**, the average surface roughness of monolayer 2D crystal/SiO_x heterostructures and histograms of the corresponding height distribution are presented, where the measurements from the bilayer of G on SiO_x and monolayer of G on the hBN and MoS_2 substrates are also shown for comparative purposes. Our roughness measurements suggest that monolayer G exhibits the highest degree of conformation to the SiO_x (roughness ratio: 0.94), followed by bilayer G (0.78), monolayer hBN (0.76) and monolayer MoS_2 (0.57).

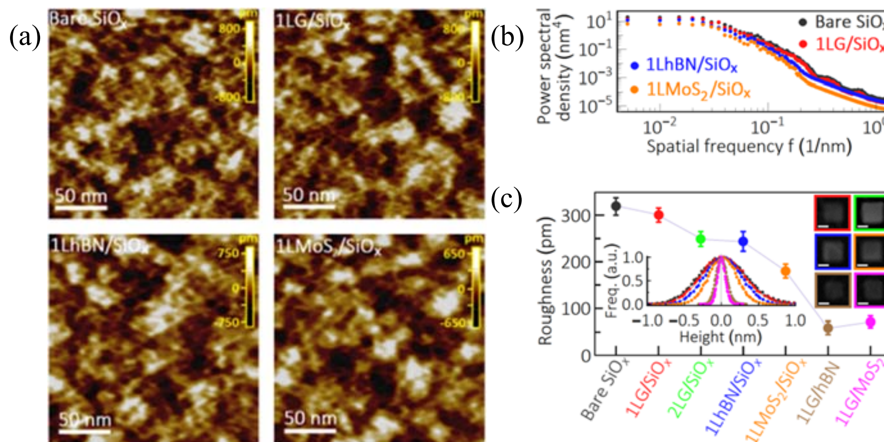

Figure 5.18. (a) High resolution AFM images of the surface roughness of bare SiO_x, monolayer graphene (1LG), monolayer hBN (1LhBN) and monolayer MoS_2 ($1LMoS_2$) on SiO_x substrate; **(b)** PSD profiles corresponding to the images in (a); and **(c)** surface roughness measurements of different heterostructures. Error bars show the spread of data over several independent measurements of different flakes. Left inset: Histogram of the height distribution (surface roughness) for bare SiO_x, 1LG/SiO_x, 1LhBN/SiO_x, $1LMoS_2$/SiO_x, 1LG/hBN and 1LG/MoS_2 substrates. Solid lines are Gaussian fits to the distribution. Right inset: Representative SEM images of 2D crystal square mesas exfoliated onto the substrate. Scale bar in each is 5μm. (b), (c) and the insets of (c) share the same color legend.

As expected, the topography of monolayer G on hBN and MoS_2 substrates is much smoother than that of monolayer G on SiO_x, suggesting an atomically flat contact at G/hBN and G/MoS_2 interfaces. Assuming that the conformation of 2D crystal flakes to the underlying SiO_x

substrate of similar corrugation pattern is proportional to their interfacial adhesion energy but inversely proportional to the bending stiffness of the flakes [118] with a value of D_{1LG}=1.49 eV, D_{2LG}=35.5 eV, D_{1LhBN}=1.34 eV and D_{1LMoS2}=11.7 eV, (see **Section D.4, Appendix D**), the smaller bending stiffness of monolayer hBN compared to mono- and bilayer G, however, results in a smoother surface morphology, further confirming the stronger IAE at the G/SiO_x interface. Moreover, our comparative study of the corrugation of bilayer G and monolayer MoS_2 with almost the same thickness (i.e., 0.670 nm in 2LG versus 0.645 nm in 1LMoS_2) also demonstrates that the adhesion of bilayer G to SiO_x is much stronger than that of monolayer MoS_2. Such intimate and strong interaction of G/SiO_x suggests that the electron scattering sites across the interface as well as the convex sites of corrugated G result in the formation of short-range chemical bonds which act as anchoring spots to locally pin G to the SiO_x surface at the location of such chemically active sites. Since monolayer G with extreme flexibility possesses more chemically active sites than multilayer G at the G/SiO_x interface, stronger adhesion energy of monolayer to SiO_x is expected, as previously confirmed by a pressurized blister test to be 0.45±0.02 Jm^{-2} for monolayer G but 0.31±0.03 Jm^{-2} for multilayer G [68].

5.9 Summary

We used an AFM-assisted nanomanipulation technique to directly and precisely measure the weak interlayer vdW bonding at the fresh and aged vdW homo/heterointerfaces under different annealing temperatures. We recorded force–displacement curves with piconewton–subnanometer resolution upon retraction of AFM tip-attached 2D crystal nanomesas from fresh and aged 2D crystal and SiO_x/Si substrates under controlled ambient conditions in the near–equilibrium regime. The annealing temperature of nanocontact interfaces was precisely controlled in the range of -15–300°C by a microheater on the top and a cooling stage underneath the SiO_x/Si substrate.

We observed highly stronger interactions at the homointerface of MoS_2 than G and hBN, suggesting possible sharing electrons in the interlayer region of transition metal dichalcogenides beyond a simple vdW-only interaction. After quantifying the effect of airborne contaminants and humidity on the interfacial adhesion level, we revealed to what degree contaminated heterointerfaces can recover their interfacial adhesion energy upon thermal annealing through precise temperature control of nanocontact interfaces. We showed that a simple but very

effective precooling treatment can significantly improve the interfacial adhesion of the hBN, G and MoS_2 crystals regardless of the subsequent annealing temperature. Our combined experimental and atomistic analysis also suggested that the formation of short-range chemical bonds only in G/SiO_x heterostructures can elucidate the mechanistic origin of the distinctive strong adhesion behavior between G and SiO_x beyond the widely accepted vdW interaction. Our precise nanoscale quantification of weak interlayer vdW bonding in 2D materials and vdW heterostructures not only provides a reliable basis for theoretical calculations but also can be of fundamental and technological importance for the mass production and continued development of such promising materials in modern electronic devices.

CHAPTER 6

Conclusions and Suggestions for Future Work

6.1 Summary

This thesis proposed a novel atomic force microscopy (AFM)-assisted experimental technique with an exceptionally high force-displacement resolution combined with atomistic- and continuum-based simulations to directly and precisely measure the interlayer electrostatic and vdW properties of 2DLMs and their vdW heterostructures, which have remained elusive for decades. **Chapter 1** included an overview of the basic concepts relevant to the experimental and theoretical results presented in **Chapters 2-5**.

In **Chapter 2**, we first developed two economic, highly–efficient and clean exfoliation techniques (termed plasma–assisted exfoliation and nanoimprint–assisted shear exfoliation) to produce large–scale, ordered G and MoS_2 device arrays at micro and nanoscale. Then, in order to gain a deeper insight into the interlayer vdW interactions of 2DLMs during the exfoliation process, I qualitatively studied the mechanical response of interlayer vdW interactions to external shear or normal forces by gently moving an in-situ flattened, conductive AFM tip with an attached 2D crystal nanomesa away from the substrate in a direction parallel or normal to the basal plane of 2D crystals, followed by shear and normal exfoliation of high-quality mono- and few-layer 2D crystal features onto the substrate. I reliably produced high-quality mono- and few-layer crystal features of different shapes and sizes at significant yields by shear exfoliation method. My experimental observations showed that in contrast to the shear exfoliation technique, the normal exfoliation technique exhibits a very stochastic exfoliation process.

Chapter 3 aimed at providing prerequisite information about the interlayer electrostatic properties of 2DLMs to investigate the atomistic details underlying my AFM-assisted shear/normal electrostatic exfoliation mechanisms. As such, I first studied the electrostatic

response of the interlayer vdW interactions of few-layer graphene (FLG) to the external electric field. To do so, I quantified, for the first time, the effect of layer number and external electric field (up to my experimental limit of 0.1 V/Å) on the relative dielectric constant of FLG using a DC electrostatic force microscopy (DC-EFM) technique. I performed a series of dielectric measurements on the one-to-eight layers of G under ambient conditions and successfully showed that although the dielectric screening ability of monolayer graphene is about 20% weaker than that of bulk graphite, the overall dielectric response of few-layer graphene samples is almost independent of the number of layers and the external electric field. Next, I exploited the layered nature of FLG to develop a novel spatial discrete model that successfully accounts for both electrostatic screening and fringe field effects on the charge distribution of the finite-size FLG system. An effective bilayer model based on two tight-binding parameters was utilized to accurately describe electronic band structures and thus density of states (DOS) of one to eight Bernal-stacked graphene layers. I then explored the unclear relationship between the gate-induced charge densities and layer-by-layer Fermi level and charge density profiles in FLG systems using a global energy minimization, where its total energy is calculated based on electrostatic interaction between graphene layers and band-filling energy in each layer. My spatial charge distribution model showed that the overall dielectric response of FLG samples is almost independent of the number of layers and the external electric field, which is well consistent with my DC-EFM results.

In **Chapter 4**, I implemented, for the first time, 3D spatial charge distribution of FLG (obtained from the proposed spatial discrete model) into molecular dynamics (MD) simulations to further gain an atomistic insight into the electrostatic shear/normal exfoliation mechanisms. My MD analysis of the simulation trajectories suggested that the coexistence of local delamination and interlayer twist in FLG is the main barrier to the accurate control of the number of exfoliated layers using the normal exfoliation technique. Instead, the ability of the shear exfoliation method to eliminate the interlayer spacing variations and simultaneously suppress the interlayer twist angles (due to the larger interlayer potential corrugation) provided much better control over the desired number of the exfoliated flakes, making it superior to the normal exfoliation method.

In **Chapter 5**, I provided an accurate nanoscale quantitative (rather than qualitative) description of interlayer mechanical behavior of 2DLMs and their vdW heterostructures. I used

the AFM-assisted nanomanipulation setup to report precise *in situ* measurements of interfacial adhesion energy through well-defined interactions between AFM tip-attached 2D crystal nanomesas (G, hBN and MoS_2) and mechanically exfoliated 2D crystal flakes and also the bare SiO_x substrate. Moreover, since airborne contaminants are an inevitable part of any vdW heterostructures, addressing quantitatively to what degree their interfacial adhesion energy is influenced by the interfacial contaminants and how to effectively remove them is of fundamental and technological importance for the continued development of such promising materials. As such, I reported the first direct quantitative characterization of interfacial adhesion behavior of both fresh and aged vdW homointerfaces (G/G, hBN/hBN and MoS_2/MoS_2) and heterointerfaces (G/hBN, hBN/MoS_2, G/MoS_2, G/SiO_x, hBN/SiO_x and MoS_2/SiO_x) under different annealing temperatures (up to 300°C). I precisely controled the temperature of nanocontact interfaces using microheaters. I quantified how different levels of short-range dispersive (vdW) and long-range electrostatic (Coulombic) interactions of similar and dissimilar 2DLMs will respond to airborne contaminants and humidity upon thermal annealing. My measurements revealed highly stronger interactions in transition metal dichalcogenides than predicted by well-established first-principles calculations. Similarly, my combined experimental and computational analysis showed a distinctive interfacial behavior in G/SiO_x heterostructures beyond the widely accepted vdW interaction.

6.2 Future Outlook

While we specifically focused on the interlayer electrostatic properties of few-layer graphene, our AFM-assisted electrostatic exfoliation technique can be used for other 2DLMs, such as semiconducting transition metal dichalcogenides (e.g., MoS_2, WSe_2 and WS_2), and their vdW heterostructures (e.g., G/MoS_2 and MoS_2/WSe_2). Also, the generality of our spatial discrete model suggests that the charge density profile, interlayer screening, quantum capacitance, and local surface potential of other 2DLMs can be characterized by feeding relevant electronic band structures of ATLMs into our model. In addition, the effect of structural defects (e.g., vacancies, adatoms, dislocations and grain boundaries) and stacking faults on the charge distribution of defective FLG systems can be studied by modifying DOS of pristine FLG.

Our interfacial adhesion measurements for 2DLMs can be extended to other 2DLMs and classical materials, such as metals, composites, ceramics, polymers, semiconductors,

biomaterials, etc. The effect of temperature, humidity and airborne contaminants on their interactions can also be quantified through precise measurements of their force-displacement curves. Although our study focuses on the interlayer electrostatic and mechanical properties of 2DLMs and their vdW heterostructures, an *in situ* flattened magnetic probe can be used to study their magnetic properties under different temperatures, humidity and airborne contaminants.

APPENDICES

APPENDIX A

Dielectric Constant of a Single-Walled Carbon Nanotube

In order to obtain the relative dielectric constant of single-walled carbon nanotube (SWCNT), we revisited the work of Lu et al. [60] who reported the first experimental measurement of dielectric polarization of individual SWCNTs on 2-nm-thick SiO_2/Si substrate using a combination of scanning force microscopy and electrostatic force microscopy and finite element electrostatic simulations. We employed a similar finite element model, as shown in **Figure A.1(a)**, except that a hollow cylinder of inner radius 1nm, outer radius 1.5nm and length 200nm was used to model an SWCNT rather than a solid cylinder of radius 1.5nm and length 200nm, as used by Lu et al. [60]. We noted that the calculated electrostatic force on the solid SWCNT of dielectric constant 10 is equal to that of the hollow cylinder whose dielectric constant is ~22.5. This modified value for the dielectric constant of SWCNTs is in excellent agreement with our results for FLG.

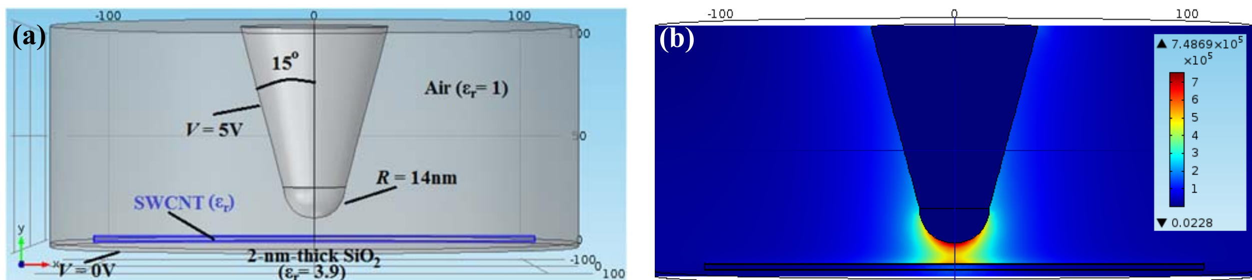

Figure A.1. (a) Geometric representation of the tip-SWCNT/SiO_2 system along with the parameters used in electrostatic 3D finite element calculations. (b) Cross-section of 3D finite element calculation of the electrostatic field distribution between the tip and the SWCNT/SiO_2 sample at z=8nm and V=5V.

APPENDIX B

Electrostatic Charge Distribution in FLG Systems

B1 Electrostatic Fringe Field Effects in Graphene Flake

B1.1 Circular graphene flake

Both experimental and theoretical studies have demonstrated that a strong charge accumulation takes place at the edges of the finite-size graphene flake due to the electrostatic fringe field effects [55, 63, 53]. Scanning gate microscope measurements of a monolayer graphene device on a SiO_2/Si substrate demonstrate that the charge accumulation at the edge of the graphene devices is significant, in particular in narrow devices such as graphene nanoribbons [53]. In addition, the charge distribution in a positively charged graphene sheet was studied using a charge/dipole molecular dynamics model and a strong charge accumulation was observed along the edges and at the corners of the rectangular graphene sheet [55, 63].

In order to figure out how the induced charge is distributed within the graphene sheet under an external electric field, we consider a circular graphene sheet of radius R placed at a distance of h above SiO_2 film and at a potential V_0 relative to the Si substrate. The corresponding induced charge density $q(r)$ can be calculated using the method of images. The charge density depends on the radial coordinate across the sheet, which varies in the range $0 < r < R$. Using the method of images, this problem is equivalent to two parallel circular sheets of radius R vertically separated by a distance $2h$ and placed at potentials V_0 (upper sheet) and $-V_0$ (lower sheet), such that the Si substrate plane ($z = 0$) is at zero potential. The center of the upper sheet is taken to be at $(0,0,h)$ and the center of the lower sheet at $(0,0,-h)$. Following the analytical solution developed by Felderhof [120], the electrostatic potential in the upper sheet can then be expressed by

$$V_0 = \int_0^r \frac{p(s)}{\sqrt{r^2 - s^2}} ds + \int_0^R W(r, 2h, s) p(s) ds \tag{B1}$$

where

$$W(r,z,s) = \mathrm{Re}\frac{1}{\sqrt{r^2+(z-is)^2}} \tag{B2}$$

satisfies Laplace's equation ($\nabla^2\varphi(r,z) = -4\pi q(r)\delta(z)$) everywhere, except on a disk of radius s centered at the origin in the $z=0$ plane, and the weight function $p(s)$ satisfies the Love equation

$$p(r) - \frac{1}{\pi}\int_0^1 \left[\frac{\kappa}{\kappa^2+(r-s)^2} + \frac{\kappa}{\kappa^2+(r+s)^2}\right] p(s)ds = \frac{2V_0}{\pi} \tag{B3}$$

where $\kappa = h/R$. We solved this integral equation numerically in MATHEMATICA using iteration with a suitable initial function. In order to evaluate the convergence of our numerical solution, we compared the "scaled" capacitance (multiplied by the factor $\pi/2$) of the sheet given by

$$C = \frac{1}{V_0}\int_0^R p(s)ds \tag{B4}$$

with that of Cooke [121]. We obtained the scaled capacitance of 1.8208 (For $\kappa = 1$) and 9.2328 (for $\kappa = 0.4$), which are in excellent agreement with those of Cooke [121] who reported the values of 1.8208 and 9.2330, respectively.

Finally, the induced charge density and the weight function are related by

$$q(r) = \frac{-1}{2\pi r}\frac{d}{dr}\left[\int_r^R \frac{sp(s)}{\sqrt{s^2-r^2}}ds\right] \tag{B5}$$

In **Figure B.1**, we show the normalized induced charge density profiles (from which the Fermi energy profiles shown in **Figure B.2** are extracted) for different values of h/R.

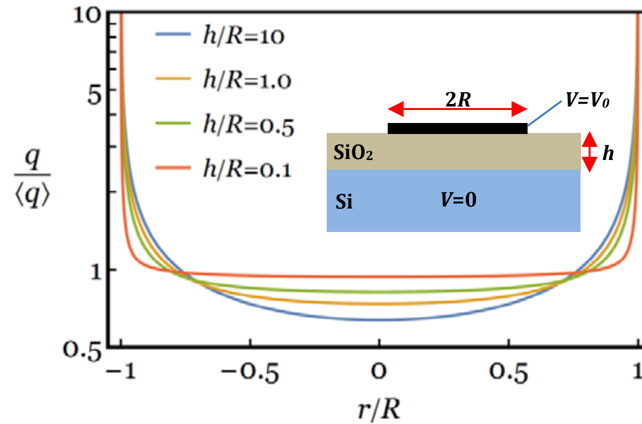

Figure B.1. Induced charge density profile of the sheet for different thickness-to-radius ratios.

In this work, for more practical applications, we set $\kappa = h/R$ to be 0.1 and thus the corresponding charge density profile can be given by

$$q(\mathbb{r}) = \frac{g(\mathbb{r})}{\sqrt{1-\mathbb{r}^2}} Q \tag{B6}$$

where $\mathbb{r}$ $(= r/R)$ is a dimensionless parameter, $g(\mathbb{r}) = 1.57 - 0.77\mathbb{r}^2 - 0.39\mathbb{r}^4 + \cdots$, and Q is the total charge density.

B1.2 Graphene nanoribbon

Similar to the charge distribution profile in the circular FLG, the charge distribution in a graphene nanoribbon of width w can be given by [122]

$$q_i(x, y, \alpha_i, Q_i) = \frac{f(x, y, \alpha_i)}{\langle f \rangle} Q_i \tag{B7}$$

where

$$f(x, y, \alpha_i) = \frac{\delta(y)}{\sqrt{(1+\alpha_i) - \left(\frac{x}{w}\right)^2}} \left[0.318 - 0.056 \left(\frac{w}{h}\right)^2 \left(\frac{2x^2}{w^2} - 1\right)\right] \tag{B8}$$

where $\delta(y)$ is the delta function and h is the dielectric thickness. The terms in the brackets are valid when the ribbon width is much smaller than the dielectric thickness ($w \ll h$). We refer the interested reader to the supplementary material of Ref. [123] for the charge distribution of the graphene nanoribbon with different ribbon width-dielectric thickness ratios w/h.

B1.3 Rectangular/square graphene flakes

Similar to the charge distribution profile in the circular FLG, the charge distribution in the rectangular graphene flakes with length l_x and width l_y can be given by

$$q_{ij} = \frac{f(\mathbb{x}, \mathbb{y})}{g(\alpha_{xi}, \alpha_{yi}) \sqrt{(1+\alpha_{xi}) - \mathbb{x}^2} \sqrt{(1+\alpha_{yi}) - \mathbb{y}^2}} \tag{B9}$$

where the charge distribution profile is normalized by

$$g(\alpha_{xi}, \alpha_{yi}) = \int_{\frac{-1}{2}}^{\frac{1}{2}} \int_{\frac{-1}{2}}^{\frac{1}{2}} \frac{f(\mathbb{x}, \mathbb{y})}{\sqrt{(1+\alpha_{xi}) - \mathbb{x}^2} \sqrt{(1+\alpha_{yi}) - \mathbb{y}^2}} d\mathbb{x}\, d\mathbb{y} \tag{B10}$$

where $\mathbb{x} = 2x/l_x$ and $\mathbb{y} = 2y/l_y$ are dimensionless parameters; x and y denotes, respectively, the x and y coordinates of atom j in the ith layer which carries the corresponding charge of q_{ij}; and $f(\mathbb{x}, \mathbb{y})$ is a polynomial function of $\mathbb{x}$ and $\mathbb{y}$ which only depends on the ratio of the graphene size to the dielectric thickness [123]. Also, α_{xi} and α_{yi} denote the amount of charge accumulation at the middle of the x and y edges relative to that at the center of the graphene flake, respectively. From **Eq. (B9)**, the amount of charge accumulation at the corner relative to that at the center of the rectangular graphene flake is obtained to be ~ $1/\sqrt{\alpha_{xi}\alpha_{yi}}$.

B2 Non-Uniform Fermi Energy Profile

Uniform charge density of ith layer is related to its corresponding constant Fermi energy $\mathbb{e}_{\text{F}i}$ by

$$\bar{Q}_i = \frac{e}{N}\int_0^{\mathbb{e}_{\text{F}i}} D_N(\mathbb{E})d\mathbb{E} = \frac{e}{\pi\gamma^2 N}\sum_{l=1}^{N_b}\sum_j (\mathbb{e}_{\text{F}i}^2 + 2\mathbb{e}_{\text{F}i}\gamma_1 \sin\theta) \qquad \text{(B11)}$$

Solving **Eq. (B11)** for $\mathbb{e}_{\text{F}i}$ yields

$$\mathbb{e}_{\text{F}i} = -\frac{\gamma_1}{N_b}\sum_{l=1}^{N_b}\sum_j \sin\theta + \sqrt{\frac{\pi\gamma^2 N}{N_b e}\bar{Q}_i + \left[\frac{\gamma_1}{N_b}\sum_{l=1}^{N_b}\sum_j \sin\theta\right]^2} \qquad \text{(B12)}$$

Similarly, the charge density profile can be related to the fermi energy profile as follows

$$\mathbb{E}_{\text{F}i}(\mathbb{r}, \alpha_i, \bar{Q}_i) = -\frac{\gamma_1}{N_b}\sum_{l=1}^{N_b}\sum_j \sin\theta + \sqrt{\frac{\pi\gamma^2 N}{N_b e}\bar{q}_i(\mathbb{r}, \alpha_i, \bar{Q}_i) + \left[\frac{\gamma_1}{N_b}\sum_{l=1}^{N_b}\sum_j \sin\theta\right]^2} \qquad \text{(B13)}$$

defining the charge density profile by

$$\bar{q}_i(\mathbb{r}, \alpha_i, \bar{Q}_i) = \frac{f(\mathbb{r}, \alpha_i)}{\langle f\rangle}\bar{Q}_i \qquad \text{(B14)}$$

and substituting **Eq. (B11)** into **Eq. (B14)** yield

$$\bar{q}_i(\mathbb{r}, \alpha_i, \mathbb{e}_{\text{F}i}) = \frac{f(\mathbb{r}, \alpha_i)}{\langle f\rangle} \times \frac{e}{\pi\gamma^2 N}\sum_{l=1}^{N_b}\sum_j (\mathbb{e}_{\text{F}i}^2 + 2\mathbb{e}_{\text{F}i}\gamma_1 \sin\theta) \qquad \text{(B15)}$$

Finally, substituting **Eq. (B15)** into **Eq. (B13)** leads to

$$\begin{aligned}\mathbb{E}_{\text{F}i}(\mathbb{r}, \alpha_i, \mathbb{e}_{\text{F}i}) = &-\frac{\gamma_1}{N_b}\sum_{l=1}^{N_b}\sum_j \sin\theta \\ &+ \sqrt{\frac{f(\mathbb{r}, \alpha_i)}{\langle f\rangle N_b}\sum_{l=1}^{N_b}\sum_j (\mathbb{e}_{\text{F}i}^2 + 2\mathbb{e}_{\text{F}i}\gamma_1 \sin\theta) + \left[\frac{\gamma_1}{N_b}\sum_{l=1}^{N_b}\sum_j \sin\theta\right]^2}\end{aligned} \qquad \text{(B16)}$$

B3 Fermi Level Profiles in *N*-Layer Graphene

Figure B.2(a) demonstrates the Fermi level profiles of a 5-LG system, while Fermi level profile of the innermost layer in an 8-LG system is shown in **Figure B.2(b)** for $Q_0 = 10^{13}\text{cm}^{-2}$. Far from the edge, we observe from **Figure B.2(b)** that sitting ~70% of the total induced charge in the innermost layer would cause a shift in the Fermi level from the ground state to the first excited state (as shown in brown solid curve in **Figure B.2(b)** and in brown dashed curve in the inset, which shows the energy band structure of the 8-LG system). However, our Fermi level analyses in the innermost layer of the bi-, tri-, tetra- and penta-LG systems do not exhibit any jump in the Fermi level of the region away from the edge when $Q_0 = 10^{13}\text{cm}^{-2}$. This can be attributed to the fact that the lowest energy of the first excitation band decreases for the *N*-LG system with a larger number of graphene layers. Following the evolution of Fermi level along the innermost layer in **Figure B.2(b)**, it is observed that a strong charge accumulation and thus sufficiently large shift in Fermi energy at the edge can give rise to a jump in the electronic band structures of FLG toward the second(0.4eV) and third(0.61eV) excitation energies, as shown in orange and green curves, respectively.

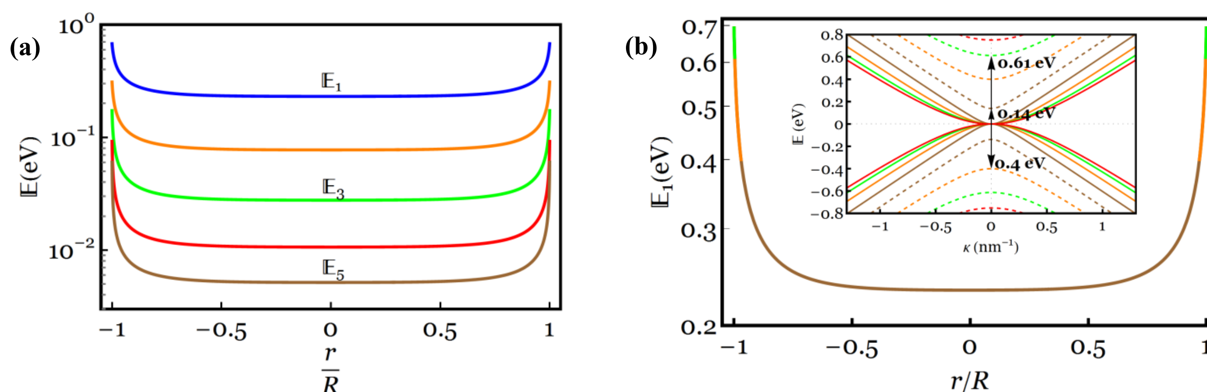

Figure B.2. **(a)** Fermi level profiles of a 5-LG system for $Q_0 = 10^{13}\text{cm}^{-2}$. **(b)** Fermi level profile of the innermost layer in an 8-LG system for $Q_0 = 10^{13}\text{cm}^{-2}$. Inset: low- and high-energy band structure of the 8-LG system. Brown, orange and green solid curves in the Fermi level profile and brown, orange and green dashed curves in the band structure represent the first (0.14 eV), second (0.40 eV) and third (0.61 eV) excitation energies, respectively.

B4 Local and Global Interlayer Charge Screening

Sui and Appenzeller [46] presented a systematic experimental study on charge and current distribution in FLG field-effect transistors and then proposed the following charge distribution in the FLG systems based on the Thomas-Fermi (TF) charge screening theory

$$\frac{Q_{i+1}}{Q_i} = \frac{h + d_i}{h + d_{i+1}} e^{\left(-\frac{d_{i+1}-d_i}{\lambda_{i,i+1}}\right)} \tag{B17}$$

$$Q_0 = \sum_{i=1}^{N} Q_i \tag{B18}$$

where the index i takes on values from 1 to N (N being the total number of graphene layers); Q_1 is the total induced charge in the closest layer to the SiO_2 substrate; Q_0 is the total induced charge in the graphene system; h (typically in the range of 50-300 nm) is the SiO_2 thickness; d_i is the distance from the bottom of the FLG system to the layer i (hence, $d_{i+1} - d_i = d = 0.335nm$ is the distance between adjacent graphene layers); and $\lambda_{i,i+1}$ is the local screening length between two consecutive layers. Considering that in many graphene-based electronic devices, the SiO_2 film is much thicker than the FLG, Eq. (S17) reduces to:

$$\frac{Q_{i+1}}{Q_i} = e^{\left(-\frac{d}{\lambda_{i,i+1}}\right)} \tag{B19}$$

We also define the global screening length λ between the innermost layer and the other layers by

$$\frac{Q_i}{Q_1} = e^{-\left[\frac{d(i-1)}{\lambda}\right]} \tag{B20}$$

Figure B.3(a) shows Q_i/Q_1 ratio as a function of the layer positions for a 5-LG system under three different gate densities of 10^{12}, 10^{13} and 10^{14}cm^{-2} and a similar plot for an 8-LG system for $Q_0 = 10^{12}$, 10^{13} and $5 \times 10^{13}\text{cm}^{-2}$ is presented in **Figure B.3(b)**. We observe from **Figure B.3** that our data can be well fitted by an exponential decay function when $Q_0 \leq 10^{13}\text{cm}^{-2}$.

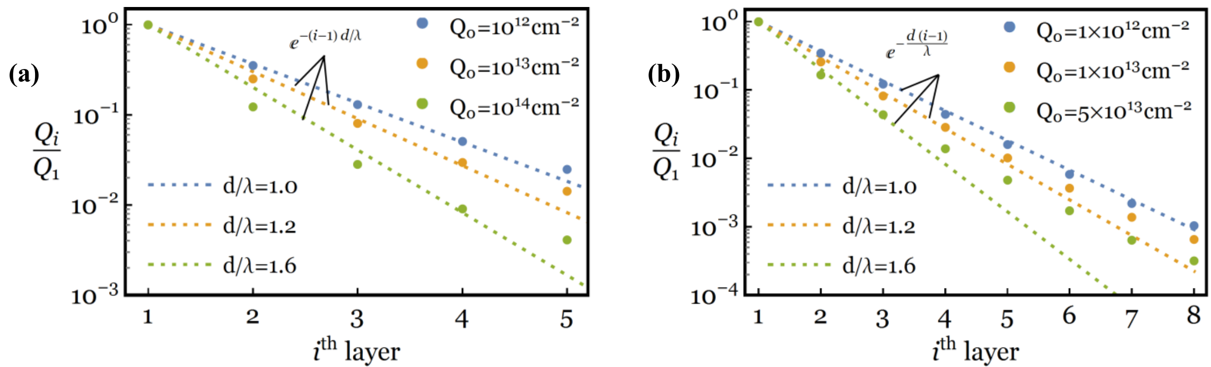

Figure B.3. Normalized average charge profiles across the layers of **(a)** a 5-LG system and **(b)** an 8-LG system for different values of Q_0. A decay length (d/λ) of 1.0, 1.2 and 1.6 is found by fitting the data with a function $e^{-(i-1)d/\lambda}$.

B5 Temperature-Dependent Discrete Model

In order to propose a mathematical discrete model that can be numerically solved at $T \neq 0$, we had to use a uniform charge distribution model, in which. **Eqs. (3.5)** and **(3.7)** in **Section 3.3** reduce to a constant charge density ($q_i = Q_i$) and a constant Fermi level ($\mathbb{E}_{\mathrm{F}i} = \mathbb{e}_{\mathrm{F}i}$), respectively. Therefore, the charge density of each layer can be expressed by

$$Q_i = \frac{e}{N} \int_0^\infty D_N(\mathbb{E}) f(\mathbb{E}) d\mathbb{E} \tag{B21}$$

where

$$f(\mathbb{E}) = \frac{1}{1 + \exp[(\mathbb{E} - \mathbb{e}_{\mathrm{F}i})/kT]} \tag{B22}$$

is the Fermi-Dirac distribution function, k the Boltzmann constant, T the absolute temperature, and $D_N(\mathbb{E})$ corresponds to **Eq. (3.4)** in **Section 3.3**. Also, the electrostatic energy U_e and band-filling energy U_b at temperature T can be given, respectively, by

$$U_e = \frac{d}{2\varepsilon_0} \sum_{i=1}^{N} \left(Q_0 - \sum_{j=1}^{i} Q_j \right)^2 \tag{B23}$$

and

$$U_b = \frac{1}{N} \sum_{i=1}^{N} \int_0^\infty \mathbb{E} D_N(\mathbb{E}) f(\mathbb{E}) d\mathbb{E} \tag{B24}$$

The charge distribution of *N*-LG is then determined by minimizing the total energy with respect to each $\mathbb{e}_{\mathrm{F}i}$ of the variational parameters. It is reasonably believed that the above mathematical simplification does not qualitatively and pretty much quantitatively change the results presented in **Figure (3.10)** of **Section 3.3.4** since our results for $T = 0$ obtained by the model given in this section and the one proposed in the main text are very close, if not identical, over the entire range of Q_0.

APPENDIX C

Atomistic Simulations in FLG Systems

C1 Atomistic Simulation Setup

To gain an in-depth understanding of underlying mechanisms associated with the normal and shear electrostatic exfoliation of 2D atomic layered materials, molecular dynamics (MD) simulations were performed with the LAMMPS software package. In order to mimic our exfoliation setup, the tapered silicon (001) layer was moved along the *x* direction with the rate of 1.5×10^{-2} Å/ps for the shear exfoliation case and was pulled away along the *z* direction with the rate of 1×10^{-2} Å/ps for the normal exfoliation case. Though the normal (pressing) load, humidity and exfoliation speed may contribute to the transfer printing of FLG, we do not investigate their possible effects in this study. In the case of normal exfoliation method, the contact pressure is not considered because FLG system is relaxed at room temperature for an adequate time to fully conform to the substrate surface.

C1.1 Description of intralayer carbon–carbon interactions

Reactive empirical bond order (REBO) potential function was adopted to model the intralayer carbon–carbon interactions within the same graphene layer. All the free graphene edges are passivated by hydrogen. To study the mechanical properties of carbon–based materials such as graphene, carbon nanotubes and diamond, the REBO potential has been shown to accurately capture the bond–bond interaction between carbon atoms as well as bond breaking and bond–reforming.

C1.2 Description of interlayer carbon-carbon interactions

In order to model interlayer carbon–carbon interactions between adjacent graphene flakes, interfacial adhesion energy of few–layer graphene/graphite provides a vital piece of information for characterizing the microscopic vdW interactions in FLG. Though many efforts

have been made to determine the interfacial adhesion energy of few–layer graphene and graphite using various experimental and theoretical approaches, the reported data are very diverse, ranging from $0.19 - 0.72\ \mathrm{Jm^{-2}}$ obtained by experimental measurements and from $0.03 - 0.51\ \mathrm{Jm^{-2}}$ predicted by theoretical models. For instance, in May 2015, a team at IBM Research–Zürich reported in *Science* a direct "accurate" mechanical measurement of the interfacial adhesion energy of incommensurate graphite ($0.227 \pm 0.005\ \mathrm{Jm^{-2}}$) using an atomic force microscopy setup under ambient conditions [124]. Surprisingly, three months later, researchers at University of Pennsylvania and Tsinghua University reported in *Nature Communications* the "first accurate" direct measurement of the interfacial adhesion energy of incommensurate graphite ($0.37 \pm 0.01\ \mathrm{Jm^{-2}}$) using a micro–force sensing probe based on the self–retraction phenomenon under ambient conditions and different temperatures [81]. We believe that a part of this large data scattering may be attributed to the graphene sample variations, different sample preparation processes, different measurement uncertainties associated with the different measurement techniques, and inherent poly–crystallinity of graphite both within and normal to the basal plane.

In order to gain atomistic insight into the exfoliation mechanism of graphitic systems, an empirical interlayer potential that can adequately model the interfacial adhesion energy between adjacent graphene layers is crucial. Though the widely–used Lennard–Jones (LJ) potential can reproduce the overall cohesion, equilibrium spacing and compressibility of graphite along the c–axis (z–axis), it considerably underestimates the corrugation in the interlayer interaction of graphene layers. Therefore, a registry–dependent (RD) interlayer potential that can accurately describe the corrugation was implemented in the LAMMPS code to model the carbon–carbon interaction between graphene flakes [67]. The RD model can predict the mean interfacial adhesion energy of $0.223\ \mathrm{Jm^{-2}}$ which is in excellent agreement with the recently reported accurate experimental value for the interfacial adhesion energy of the incommensurate graphite ($0.227 \pm 0.005\ \mathrm{Jm^{-2}}$) [124].

C1.3 LJ potential vs. RD potential for vdW interaction of FLG

Kolmogorov and Crespi [67] showed that the LJ potential fails to account for the variation of the corrugation energy surface of the graphite for different stacking modes (e.g., AB, AA, and ABC stackings). Such drawback leads to the interlayer shear modulus (C_{44}) of ~0.3 GPa

(using the LJ 12–6 potential with the well–depth energy of 2.84 meV and equilibrium distance of 0.339 nm), which is one order of magnitude smaller than the experimental value of 4.3–5.1 GPa in the graphite and FLG systems [125, 126, 127]. Shen and Wu [128] proposed changing the well–depth energy from 2.84 meV to 45.44 meV to achieve the interlayer shear modulus of 4.6 GPa; however this change leads to a drastic increase in the interlayer cohesive energy as well.

In order to provide a more accurate description of the vdW interaction between graphene flakes, the RD interlayer potential was proposed by which the interlayer potential between atom *i* on one flake and atom *j* on the adjacent flake can be expressed

$$\begin{gathered} V(\boldsymbol{r}_{ij}^{*}, \boldsymbol{n}_i, \boldsymbol{n}_j) = e^{-\alpha(r_{ij}^{*}-d)}\left[C_0 + f(\rho_{ij}) + f(\rho_{ji})\right] - A\left(\frac{r_{ij}^{*}}{d}\right)^{-6}, \\ \rho_{ij}^2 = r_{ij}^{*2} - (\boldsymbol{n}_i \boldsymbol{r}_{ij}^{*})^2, \quad \rho_{ji}^2 = r_{ij}^{*2} - (\boldsymbol{n}_j \boldsymbol{r}_{ij}^{*})^2, \\ f(\rho_{ij}) = e^{-(\rho_{ij}/\delta)^2}\left[C_1 + C_2\left(\frac{\rho_{ij}}{\delta_0}\right)^2 + C_3\left(\frac{\rho_{ij}}{\delta_0}\right)^4\right] \end{gathered} \tag{C1}$$

where r_{ij}^{*} and ρ_{ij} are the actual and lateral distances between two atoms, respectively; $\boldsymbol{n}_i(\boldsymbol{n}_j)$ is a vector normal to the sp^2 plane (which is formed by the three nearest bonded neighboring atoms) at the position of atom i (j); f is a function to compute a rapid decay in the interlayer potential energy. Following parameters are directly given from the original work [67]; $\alpha = 3.629$ Å^{-1}, $d = 3.34$ Å, $\delta_0 = 0.578$ Å, $A = 10.238$ meV, $C_0 = 3.030$ meV, $C_1 = 15.71$ meV, $C_2 = 12.29$ meV and $C_3 = 4.933$ meV. With this set–up, we obtained the in–plane carbon–carbon distance of 1.401 Å, the equilibrium separation of 3.365 Å for two planar graphene layers in AB stacking, the cohesion energy of 45.2 meV per atom with respect to one graphene layer (i.e., cleavage energy per atom), interlayer shear modulus of 5.01 GPa (C_{44}) and out–of–plane elastic modulus of 38.8 GPa (C_{33}), all in excellent agreement with their corresponding experimental values [129].

It is worth pointing out that during the normal and shear exfoliation process, we observed a slight interlayer rotation ($-2.5^{\circ} < \theta < 2.5^{\circ}$) of the FLG about the c–axis (z–axis) when using the RD potential, whereas modelling of the graphene–graphene interlayer binding by means of the standard LJ potential introduced a twist angle of $> \pm 20^{\circ}$ between the graphene flakes. This implies that the LJ potential fails to properly describe the corrugation potential of the FLG. In addition, for the same MD simulation but different interlayer potentials (LJ or RD potential), both the number and the orientation of printed flakes were completely different, indicating that the potential corrugation plays a crucial role in determining the intrinsic resistance to interlayer sliding and controlling the exfoliation behavior of the FLG under external electrostatic loads.

C1.4 Description of SiO_2 substrate

Tersoff potential developed by Munetoh et al. [130] was utilized for the Si–Si, Si–O and O–O covalent bonds. In spite of complete neglect of long–range Coulombic interaction, this potential is not only suitable for large–scale calculations but also capable of reproducing structural and dynamical properties of SiO_2 systems (e.g., the radial distribution function and phonon density of states of amorphous SiO_2), very well consistent with the experimental data. In order to ensure that the interfacial adhesion between the graphene and SiO_2 mainly depends on the vdW interaction rather than the long–range Coulombic interaction for the problem at hand, we used BKS potential [131], including long–range Coulombic interaction (which was modeled by the particle–particle particle–mesh method in LAMMPS), in few MD simulations and compared the results with those of Tersoff potential but observed no difference in the resulting number of exfoliated graphene flakes. Therefore, the Tersoff potential was chosen for the entire simulations due to its much lower computational cost. To obtain the amorphous bulk SiO_2, the crystalline SiO_2 substrate was constructed within a rectangular simulation domain of 110.2 × 108.8 × 32 $Å^3$ with period boundary conditions in all directions, annealed at T = 5000 K and 1 bar for 20 ps and slowly quenched to the room temperature at a rate of 2×10^{12} K/s. Then, the silica atoms in 10 Å of the simulation domain from the top were deleted to obtain the amorphous SiO_2 substrate with the final dimension of 110.2Å×108.8Å×22Å.

C1.5 Description of graphene/SiO_2 interface

A reasonable atomistic description of the interfacial adhesion between the FLG and SiO_2 substrate is essential for a better understanding of exfoliation mechanism underlying our electrostatic force–assisted methods. Koenig et al. [68] showed that the extreme flexibility of graphene allows it to follow the underlying morphology of SiO_2 substrate, making its interaction with the substrate more liquid–like than solid–like. Though few experimental efforts have been devoted to the determination of the graphene–SiO_2 interfacial binding, the measured monolayer graphene–SiO_2 adhesion energy ranges from 0.096 to 0.45 Jm^{-2} [68, 69, 132], which can potentially be attributed to the intrinsic ripples of graphene on SiO_2 substrate, and also to surface properties of SiO_2, such as surface roughness, different surface configurations (due to its amorphous nature), surface polarities, charge impurities, surface reactions with ambient humidity, and type of surface termination/defects (i.e., H–, Si– and O–terminated surfaces).

Unlike trapped charges (or charge impurities) in SiO_2 [68] and surface polar modes of SiO_2 [132], the surface reactions of SiO_2 with water could profoundly influence the graphene–SiO_2 interaction strength in such a way that the adhesion energy is reduced by surface hydroxylation and further reduced by adsorption of water molecules [70]. Also, the first-principles calculations show that the graphene–SiO_2 interfacial binding energy for H–, Si– and O–terminated surfaces can vary from 0.16 to 0.19 to 0.48 Jm^{-2}, respectively [133]. It is worth pointing out that the graphene–SiO_2 adhesion energy also depends on the number of graphene flakes and reduces consistently from 0.45±0.02 Jm^{-2} for monolayer graphene to 0.31±0.03 Jm^{-2} for FLG (2 to 5 layers) [68] based on the direct experimental measurements and from 0.5 Jm^{-2} for monolayer graphene to 0.295 Jm^{-2} for 8-LG based on an analytical solution [134].

Given that the graphene–SiO_2 interaction is physisorption in nature, it has been proposed that the short–range vdW interaction is the predominant mechanism at the graphene–SiO_2 interface rather than O–C and Si–C covalent bonds. As a result, we used a standard 12–6 LJ potential for describing Si–C and O–C interactions which can be expressed by

$$E(r^*) = 4\delta\varepsilon\left[\left(\frac{\sigma}{r^*}\right)^{12} - \left(\frac{\sigma}{r^*}\right)^{6}\right], \qquad r^* < r_c = 2.5\sigma \tag{C2}$$

where ε, σ, and r^* are the energy parameter, equilibrium distance and interatomic distance, respectively, and r_c is the cut–off distance (which is set to 2.5σ). Since there is no definitive value for the graphene–SiO_2 interfacial adhesion energy, the scaling factor δ is introduced to adjust the overall graphene–SiO_2 adhesion strength. Unless otherwise stated, the value of δ is set to be 1 for all simulations. According to the vdW interactions in the Universal Force Field (UFF) model and using the Lorentz–Berthelot mixing rules, the Si–C and O–C interaction parameters were calculated as follows: $(\varepsilon,\sigma)_{\mathrm{Si-C}} = (8.909\mathrm{meV}, 3.326\text{Å})$ and $(\varepsilon,\sigma)_{\mathrm{O-C}} = (3.442\mathrm{meV}, 3.001\text{Å})$.

From Eq. (C2), we computed the total vdW energy E_{vdW} stored between the innermost graphene flake with M atoms (=792) and the SiO_2 substrate with O atoms (=37800) as follows

$$E_{\mathrm{vdW}} = \sum_{i=1}^{M}\sum_{j=1}^{O} E(r_{ij}^*) = 4\delta\varepsilon\sum_{i=1}^{M}\sum_{j=1}^{O}\left[\left(\frac{\sigma}{r_{ij}^*}\right)^{12} - \left(\frac{\sigma}{r_{ij}^*}\right)^{6}\right] \qquad r_{ij}^* < r_c = 14\text{Å} \tag{C3}$$

Then the graphene–SiO_2 adhesion energy can readily be obtained by

$$\Upsilon = \frac{E_{\mathrm{vdW}}}{A} = \frac{E_{\mathrm{vdW}}}{MA_c} \tag{C4}$$

where A is the flake area ($= MA_c$); and A_c ($= 3\sqrt{3}a^2/4$, where $a = 1.42$ Å is the C–C bond length) is the area surrounding each carbon atom. Our MD calculations reveal that Υ is in the range of the measured monolayer graphene–SiO_2 adhesion energy (0.096–0.45 Jm^{-2}) when δ varies from 1 to 2. Results presented in **Figure C.1(a)** were averaged over the last 1000 time steps of the equilibrium procedure at T=300K and the error bars in the curves were obtained accordingly. As we discussed earlier, a wide range of values for the graphene/SiO_2 adhesion energy has been reported in the literature (ranging from 15 to 75 meV/atom). To investigate the effect of the graphene/SiO_2 interfacial adhesion strength on the exfoliation process of the uncharged FLG system, a series of simulations were performed at thirteen distinct vdW strength scaling factors δ over the interval from 1 to 2.2 (with 0.1 increments). The LJ interaction cutoff distance for the Si–C and O–C interactions was increased and set at 14 Å. **Figure C.1(b)** confirms that the graphene exfoliation in the absence of external electric filed requires the vdW strength scaling factor of over 1.3. Also, there was no observation of shear-exfoliated graphene for δ up to 2.2.

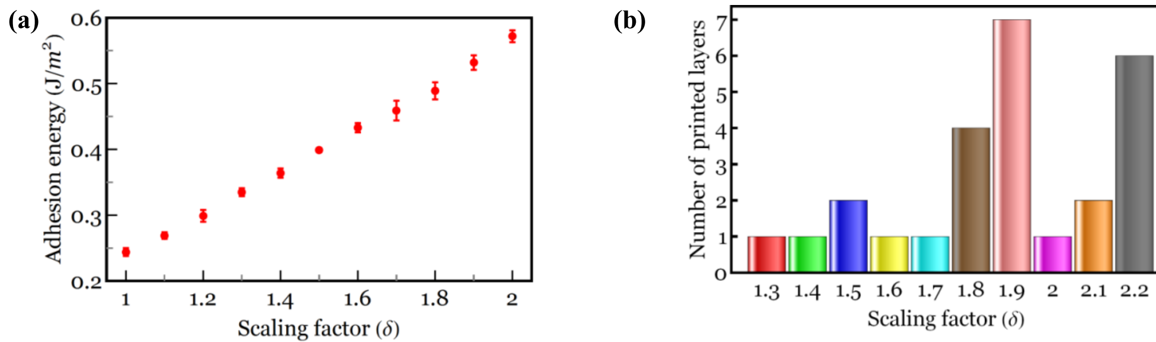

Figure C.1. (a) Graphene–SiO_2 adhesion energy as a function of the scaling factor. (b) Number of printed layers as a function of the scaling factor obtained by the normal exfoliation technique in the absence of the electrostatic forces.

C2 Charge Distribution and Fermi Profiles in a 8-LG System

C2.1 Charge density/Fermi level profiles of 8-LG

The induced excess charge density in the N–LG which is equal and opposite to the charge density on the silicon substrate, can be distributed over the ith layer. **Figure C.2** demonstrates the Fermi level profiles of the 8–LG system when $Q = 10^{13}\text{cm}^{-2}$. Furthermore, the corresponding charge density profile and the average charge density of the innermost layer are shown in **Figure C.3**.

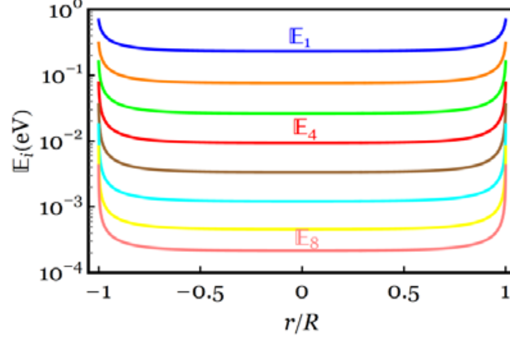

Figure C.2. Fermi level profiles of the 8–LG system for $Q = 10^{13}\text{cm}^{-2}$.

Our results in **Figure 4.2(a)** in the main text also suggest that the innermost layer plays the most important role in the electrostatic charge distribution of the N–LG systems. Hence, it is worth looking into its Fermi level and charge density profiles more in detail, as illustrated in **Figures C.3(a)** and **(b)**, respectively. Far from the edge, we observe that sitting ~70% of the total induced charge in the innermost layer would cause a shift in the Fermi level from the ground state to the first excited state (as shown in brown solid curve in **Figure C.3(a)** and in brown dashed curve in the inset, which shows the energy band structure of the 8–LG system). However, our Fermi level analyses in the innermost layer of the bi-, tri-, tetra- and penta–LG systems do not exhibit any jump in the Fermi level of the region away from the edge when $Q = 10^{13}\text{cm}^{-2}$. This can be attributed to the fact that the lowest energy of the first excitation band decreases for the *N*–LG system with a larger number of graphene layers. By following the evolution of the Fermi level along the innermost layer in **Figure C.3(a)**, it is observed that a strong charge accumulation and thus sufficiently large shift in the Fermi energy at the edge can give rise to a jump in the electronic band structures of FLG toward the second (0.4 eV) and third (0.61 eV) excitation energies, as shown in orange and green curves, respectively.

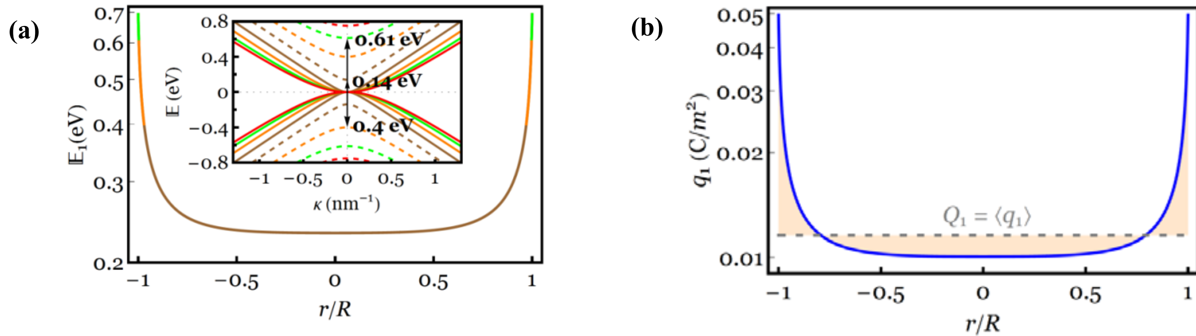

Figure C.3. (a) Fermi level profile of the innermost layer for $Q = 10^{13}\text{cm}^{-2}$. Inset: low–energy band structure of 8-LG. Brown, orange and green colors in the Fermi level profile and the band structure represent the first (0.14 eV), second (0.40 eV) and third (0.61 eV) excitation energies. (b) Corresponding charge density profile and the average charge density of the innermost layer.

C2.2 Layer-by-layer charge distribution in 8-LG

As shown in **Figure C.4(a)**, the charge density in the region very close to the edges is screened out an order of magnitude more weakly than that across the central region of the layer, which is mainly due to the presence of the strong fringe field along the edges. To quantitatively elucidate the correlation between the induced charge density and the average charge distribution through the 8–LG thickness, **Figure C.4(b)** clearly shows that almost 90% of the excess charge density resides in the two innermost layers, implying that the effective interlayer screening length can reliably be determined to be less than 0.7 nm (see **Figure C.5** for the calculation of the effective interlayer screening). The Inset to **Figure C.4(b)** further demonstrates that a larger value of Q_0 leads to a stronger charge screening normal to the layers.

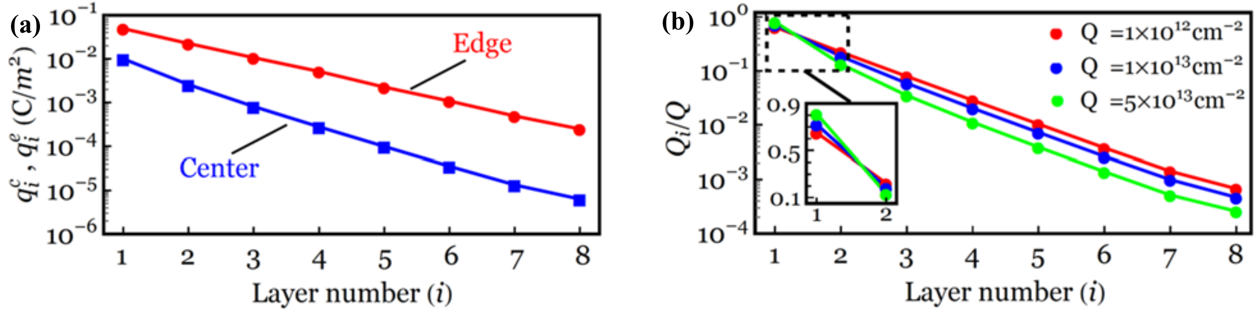

Figure C.4. (a) Charge density at the edge q_i^e and at the center q_i^c of the layer i. (b) Normalized average charge density across the layers of an 8–LG system for different gate charge densities. Inset: normalized average charge density in the two innermost layers to show the electrostatic charge screening effect. Zoom-in of a region in which the charge screening between the first and second layers is shown by a dashed black square.

C2.3 Effective interlayer screening:

We present in **Figure C.5(a)** the local screening length in the 8–LG system for three different values of Q_0. It is seen that the local screening length ranges from more than half the interlayer distance up to 2 layers. We also define the global screening length λ between the innermost layer and the other layers by

$$\frac{Q_i}{Q_1} = e^{-\left[\frac{d(i-1)}{\lambda}\right]} \quad \text{(C5)}$$

This new definition of the screening length allows us to explore how sharply the charges and thus the surface potentials drop across the FLG thickness and also provides us with a single value of the screening length to predict the charge distribution of all layers relative to that of the innermost layer. Keeping this definition in mind, we observed from **Figure C.5(b)** that our data

can be well fitted by the simple exponential decay function. Also, the charge screening for the larger induced charge is observed to be stronger.

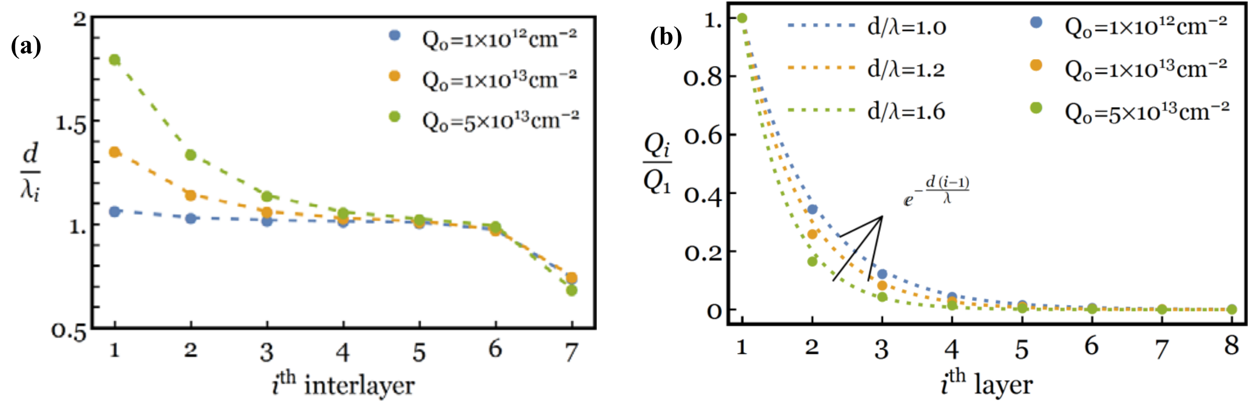

Figure C.5. (a) Local and (b) global charge screening lengths for different values of Q_0. A decay length (d/λ) of 1.0, 1.2 and 1.6 is found by fitting the data with a function $e^{-d/\lambda}$.

C2.4 Charge distribution in rectangular graphene flakes

The charge accumulation along the edge depends on the size and shape of the graphene flake, number of graphene layers, intensity of external electric field, graphene states (substrate-supported/suspended, defective/intact or functionalized/pristine graphene). To demonstrate how well our proposed spatial discrete model can predict the charge distribution within the graphene flake, in particular, along the edge, a comparison study between the present spatial discrete model, charge–dipole model [122] and analytical model is conducted to calculate the charge profile along the 4.92–nm–long zigzag edge of a 4.92nm×0.23nm rectangular monolayer graphene, as shown in **Figure C.6**.

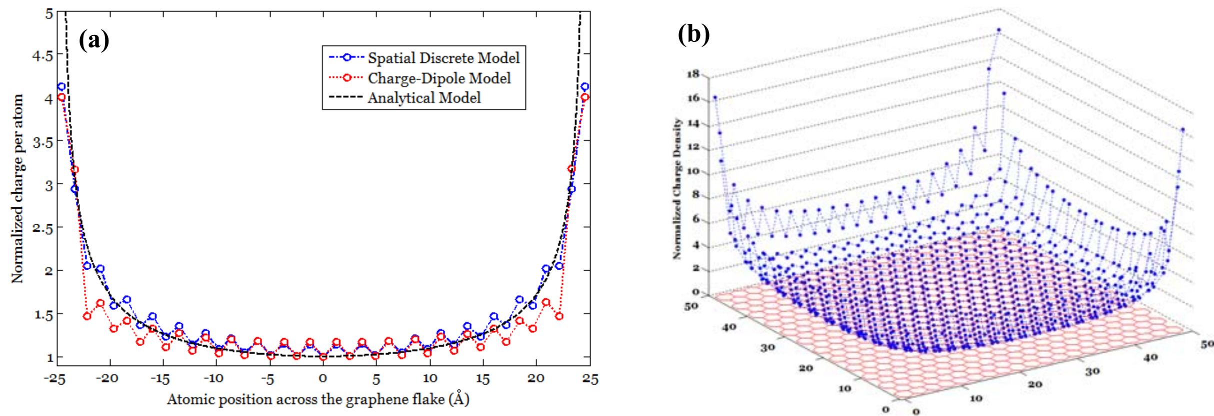

Figure C.6. (a) Comparison of the normalized charge profile along the zigzag edge of the graphene flake between the present spatial discrete model and the charge-dipole model. (b) Corresponding 3D charge distribution of the rectangular graphene sheet.

For comparison purposes, the charge of each atom is normalized to that located at the center of the zigzag edge and $Q = 3 \times 10^{12}/\mathrm{cm}^2$. **Figure C.6** reveals that unlike the analytical model, the spatial discrete model can successfully reflect the charge variations induced by the structure of the graphene edges and, therefore, yields results in better agreement with those obtained by the charge–dipole model. The interested reader can find more information on the spatial discrete model for rectangular flakes in the next section.

Similar to the charge distribution profile in the circular FLG, the charge distribution in the rectangular graphene flakes with length l_x and width l_y can be given by

$$q_{ij} = \frac{f(\mathbb{x}_{ij}, \mathbb{y}_{ij})}{g(\alpha_{xi}, \alpha_{yi})\sqrt{(1+\alpha_{xi}) - \mathbb{x}_{ij}^2}\sqrt{(1+\alpha_{yi}) - \mathbb{y}_{ij}^2}} \quad \text{(C6)}$$

where the charge distribution profile is normalized by

$$g(\alpha_{xi}, \alpha_{yi}) = \int_{\frac{-1}{2}}^{\frac{1}{2}}\int_{\frac{-1}{2}}^{\frac{1}{2}} \frac{f(\mathbb{x}, \mathbb{y})}{\sqrt{(1+\alpha_{xi}) - \mathbb{x}^2}\sqrt{(1+\alpha_{yi}) - \mathbb{y}^2}} d\mathbb{x}\, d\mathbb{y} \quad \text{(C7)}$$

where $\mathbb{x}_{ij} = 2x_{ij}/l_x$ and $\mathbb{y}_{ij} = 2y_{ij}/l_y$ are dimensionless parameters, x_{ij} and y_{ij} denotes, respectively, the *x* and *y* coordinates of atom *j* in the *i*th layer which carries the corresponding charge of q_{ij}. Also, α_{xi} and α_{yi} denote the amount of charge accumulation at the middle of the *x* and *y* edges relative to that at the center of the graphene flake, respectively. From Eq. (C6), the amount of charge accumulation at the corner relative to that at the center of the rectangular graphene flake is obtained to be ~ $1/\sqrt{\alpha_{xi}\alpha_{yi}}$.

C3 Configuration-Dependent Interlay Mechanical Properties of FLG

We have summarized the interlayer mechanical properties of FLG and graphite obtained from a wide range of experimental methods in **Table C1**, allowing more detailed conclusions to be made about the atomistic mechanisms governing the electrostatic exfoliation of the FLG. It can be deduced from **Table C1** that: (1) the stacking mode has only a slight impact on out-of-basal-plane elastic modulus C_{33}, whereas a small interlayer twist between two adjacent commensurate graphene flakes results in an order of magnitude decrease in the interlayer elastic modulus C_{44} and over two orders of magnitude decrease in the shear strength τ_s. Experimental results show average self-consistent values of C_{33}≈37.6±1.0 GPa and C_{44}≈4.7±0.5 GPa for

commensurate FLG and graphite and C_{33}≈36.6±1.1 GPa and C_{44}≈0.18–0.49 GPa for incommensurate counterparts; (2) attempts to measure the interlayer shear strength τ_s have yielded significant diversity in the reported values. For the case of incommensurate stacking state, τ_s and C_{44} have been reported to fall in the relatively narrow range of 0.12 to 3.1 GPa and 0.18 to 0.49 GPa, respectively. Contrary to our expectation that the measured values of τ_s would not significantly change for commensurate-stacked systems, experimental methods give values in the range of 5 MPa and 200 MPa. This unusual interlayer mechanical response in FLG and graphite can be hypothesized to primarily be the result of the strong dependence of τ_s and C_{44} on basal-plane dislocations, bulk-lattice imperfections, geometry of the structures and stacking misalignments. Given that the former two defects are much more prevalent in graphite than in commercially available defect-free FLG, we only focus on the latter effect on the interlayer shear behavior of graphitic systems.

Table C1. Interlayer elastic properties of FLG and graphite using experimental methods.

Method	Stack	C_{33} (GPa)	C_{44} (GPa)	σ_s (MPa)	τ_s (MPa)
Specific heat [135]	Canadian natural graphite	>18	2.3		
Static tests [80]	Polycrystalline graphite(Incommensurate)			10.3–20.7	
Uniaxial-shear stress [136]	Single-crystal graphite		4.5±0.6		0.25–0.75
Ultrasonic test [137]	Single-crystal graphite		4.0±0.4		
Ultrasonic/static tests [138]	Pyrolytic graphite(Incommensurate)	36.5±1	0.18–0.35		0.88–2.45
Neutron scattering [139]	High-quality pyrolytic graphite	37.1±0.5	4.6±0.2		
Ultrasonic test [140]	Pyrolytic graphite(Incommensurate)	36.6	0.281		
X-ray scattering [141]	Single-crystal graphite(Incommensurate)	36.6±1.2			
Brillouin scattering [142]	Graphite		5.05±0.35		
Partial dislocation motion [143]	HOPG				5–200
Friction force microscope [144]	HOPG(AB)				80–120*
X-ray scattering [126]	Single-crystal graphite(AB)	38.7±0.7	5.0±0.3		
Thermal noise excitation [145]	HOPG				2000–7000
Self-retraction motion [146]	HOPG(AB)				100±40
Self-folding conformation [147]	Multi-layer graphene(Incommensurate)		0.36–0.49		
Raman spectroscopy [127]	Multi-layer graphene(AB)		4.3		
Modulated nano-indentation [148]	HOPG	33±3			
	10-layer epitaxial graphene	36±3			
AFM-assisted mechanical shearing [124]	HOPG(Incommensurate)				0.5–3.1**
Self-retraction motion [81]	HOPG(Incommensurate)				0.12***

C3.1 MD simulations of interlayer mechanical properties of FLG

We carry out a set of MD simulations to investigate the effect of the stacking misalignments on both τ_s and C_{44}. To do so, stress-strain curves and elastic constants, such as, out-of-basal-plane elastic modulus C_{33} and interlayer shear modulus C_{44}, are calculated. The FLG substrate is modeled by four layers of graphene in AB stacking with the size of ~5nm ×

5nm where the bottom layer is fixed during the simulation. The moving graphene flake with the size of ~1.7nm × 1.7nm, is placed on the center of the substrate and periodic boundary conditions are applied to the substrate.

The interlayer force acting on the graphene flake with N atoms from the graphene substrate with M atoms can be expressed as

$$\boldsymbol{F} = F\left(F_x\hat{\boldsymbol{\imath}}, F_y\hat{\boldsymbol{\jmath}}, F_z\hat{\boldsymbol{k}}\right) = -\sum_{i=1}^{N}\sum_{j=1}^{M}\frac{\partial V\left(\boldsymbol{r}_{ij}^{*}, \boldsymbol{n}_i, \boldsymbol{n}_j\right)}{\partial \boldsymbol{r}_{ij}^{*}} \tag{C8}$$

where F_x, F_y and F_z are the force components acting on the flake along x, y and z directions, respectively. From Eqs. (C1) and (C8), one may, for example, write F_x as

$$\begin{aligned} F_x = \sum_{i=1}^{N}\sum_{j=1}^{M}\Bigg\{ & x_{ij}\left(\frac{\alpha}{r_{ij}^{*}}e^{-\alpha\left(r_{ij}^{*}-d\right)}\left[C_0 + f\left(\rho_{ij}\right) + f\left(\rho_{ji}\right)\right] - \frac{6A}{d^2}\left(\frac{r_{ij}^{*}}{d}\right)^{-8} \right. \\ & \left. - \frac{2}{\delta^2}e^{-\alpha\left(r_{ij}^{*}-d\right)}\sum_{l=ij,ji}\left[e^{-\frac{\rho_l^2}{\delta^2}}\left(C_2 + 2C_3\frac{\rho_l^2}{\delta^2}\right) - f(\rho_l)\right]\right) \\ & - \frac{2}{\delta^2}e^{-\alpha\left(r_{ij}^{*}-d\right)}\sum_{\substack{(l,m)=(ij,i),\\(l,m)=(ji,j)}} n_{mx}\left[e^{-\frac{\rho_l^2}{\delta^2}}\left(C_2 + 2C_3\frac{\rho_l^2}{\delta^2}\right) - f(\rho_l)\right]\left(\boldsymbol{n}_m\boldsymbol{r}_{ij}^{*}\right)\Bigg\} \end{aligned} \tag{C9}$$

where x_{ij} is the x component of the actual distance vector $\boldsymbol{r}_{ij}^{*}$ between two atoms i and j, and n_{mx} (m=i, j) is the x component of the unit vector $\boldsymbol{n}_m$.

The shear stress τ and normal stress σ induced by the lateral movement and vertical movement of the flake relative to the FLG substrate are then equal to $\tau = F_x/A = \rho F_x/N$ and $\tau = F_z/A = \rho F_z/N$, respectively, where A is the flake area and ρ denotes the planar atomic density (= 0.3818 Å^{-2}). The shear strain is defined as $\gamma = s_x/d$, where s_x and d are the average shear displacement of the graphene flake along the x direction and the interlayer distance, respectively. The interlayer shear modulus is then given by $C_{44} = \tau/\gamma$. Similarly, the normal strain is defined as $\varepsilon = s_z/h$, where s_z and h denote the average vertical displacement of the graphene flake along the z direction and the thickness of the FLG stack, respectively. The elastic modulus can be obtained by $C_{33} = \sigma/\varepsilon$.

From the simulated stress–strain curves in **Figure C.7**, the elastic moduli (C_{44} and C_{33}), strengths (τ_s and σ_s) and fracture strains (γ_f and ε_f) can be obtained: the elastic moduli are

calculated as the initial slope of the stress–strain curve; the strengths and fractures strain are defined at the point where the peak stress is reached. From **Figure C.7(a)**, it is seen that τ_s decreases by 30% within approximately $\pm 1^{\circ}$ and by 50% within approximately $\pm 2.5^{\circ}$ twist variation. It is observed from **Figure C.7(b)** that at the critical normal strain of ~0.07, the tensile strength reaches its peak with the value of ~1.7 GPa. Also, the interlayer rotation has no appreciable effect on σ_s. It should be noted that the cutoff was tuned in our exfoliation simulations to achieve ~20 MPa tensile strength, more consistent with the experiments.

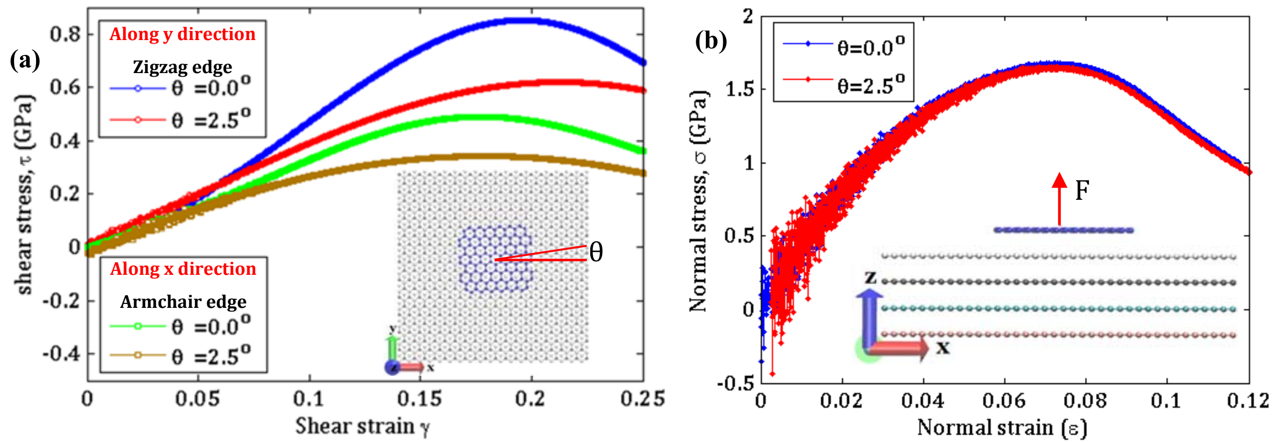

Figure C.7. (a) Shear stress-strain curves and (b) normal stress-strain curves for the graphene flake in the commensurate ($\theta = 0^{\circ}$) and incommensurate ($\theta = 2.5^{\circ}$) stacking.

APPENDIX D

Interfacial Adhesion Energy of 2D Materials and vdW Heterostructures

D1 Comparative Studies of Interfacial Adhesion Energy

In this section, we perform a comprehensive comparison study on the interfacial adhesion energy (IAE) of 2D crystals and 2D crystal/SiO_x heterostructures obtained from a wide range of experimental methods. While a vast majority of studies have been conducted on the interaction of G with G (**Section D1.1**) and SiO_x (**Section D1.2**) substrates with a wide range of reported IAE values, to the best of our knowledge, no IAE measurement at the hBN/hBN and hBN/SiO_x interfaces yet exists, and also there are a very limited number of reports on the interaction of MoS_2 with MoS_2 (**Section D1.1**) and SiO_x (**Section D1.2**) substrates. We also note that, to the best of our knowledge, there is no direct IAE measurement on the 2D crystal heterostructures.

D1.1 Comparison study on cohesion energy of 2D crystal homostructures

Although many attempts have been made over the last six decades to measure the cohesion energy of G crystal with the reported values ranging from 0.15–0.72 Jm^{-2} (**Table D1**), there are few direct measurements available for comparison. From the literature data, we found that our measurements for cohesion energy of G crystal are in excellent agreement with micro-force sensing probe measurements on 4 μm wide square mesas (0.37±0.01 Jm^{-2} [81]) and AFM-assisted shearing measurements on 3 μm wide square mesas (0.35 Jm^{-2} [149]), but inconsistent with the recent AFM-assisted shearing measurements on circular mesas of 100–600 nm in diameter (0.227±0.005 Jm^{-2} [124]). We revisited lateral stiffness calibration of all probes used in [124] by means of 3D finite element simulations. A typical optical microscope of probes (**Figure D.1(a)**), schematic of probe dimensions and lateral load (**Figure D.1(b)**) and their corresponding measured dimensions (**Figure D.1(c)**) were all given in the supplementary materials of [124]. We used the same Young's modulus of 169 GPa and shear modulus of 50.9 GPa as they did.

Table D1. Cohesion energy of carbon nanotubes, few-layer graphene, and graphite.				
Method	**Sample**	**Stack**	**Γ (J/m²)**	**Ref**
Heat of wetting	Graphite	N.A.	0.26±0.03	[150]
Radial deformation of MWCNT	Collapsed MWCNT	(Non–)AB*	0.15–0.31	[151]
Thermal desorption	HOPG	AB	0.37±0.03	[152]
MWCNT retraction	MWCNT	Non–AB	0.28–0.4	[153]
Deformation of thin sheets	HOPG	AB	0.19±0.01	[154]
AFM pull-off force measurements	HOPG	Non–AB	0.319±0.05	[155]
DWCNT inner-shell pull-out	DWCNT	Non–AB	0.436±0.074	[156]
SEM peeling of MWCNT	Collapsed MWCNT on 1-LG	(Non–)AB	0.40±0.18	[157]
	Flattened MWCNT on 1-LG		0.72±0.32	
AFM-assisted mechanical shearing	HOPG	Non–AB	0.227±0.005	[124]
Self-retraction motion	HOPG	AB	0.39±0.02	[81]
		Non–AB	0.37±0.01	
AFM-assisted mechanical shearing	HOPG	Non–AB	0.35	[149]
AFM nano-indentation	BLG/FLG onto FLG	Non–AB	0.307±0.041	[158]
Atomic intercalation of neon ion	1LG onto HOPG	Non–AB	0.221±0.095	[159]
Surface force balance	CVD-grown 1LG/1LG	Non–AB	0.230±0.008	[160]
	CVD-grown FLG/FLG	Non–AB	0.238±0.006	

* Intermediate between commensurate and incommensurate states

After carefully developing the 3D model of the probe in COMSOL based on the given optical image and dimensions (**Figure D.1(d)**), we first applied a lateral force of F_{tip}=10 nN to the tip apex and calculated the rotation of each probe φ about its long axis at a point right above the tip apex on the cantilever shank (with the same x and y coordinates as those of the tip apex) where the laser spot is normally positioned (**Figure D.1(e)**), followed by calculating the torsional stiffness $c_\varphi = k_\varphi / l_{tip}^2$ where $k_\varphi = (F_{tip} l_{tip} / \varphi)$. It is to be noted that l_{tip} should have been replaced by $l_{tip} + h$ (i.e., the vertical distance between the acting point of the force at the tip apex and the location of the laser spot) for the accurate calculation of c_φ and k_φ, however, for comparison purposes, we used the same equation as Koren et al. [124] did. We next applied a similar lateral force of 10 nN to the same point of laser incidence on the cantilever shank (**Figure D.1(f)**), followed by calculating the lateral stiffness $k_l = (F_{tip} / \Delta y)$ where Δy is the lateral deflection at the point of applied force. We finally calculated the effective lateral stiffness of the probe as follows $c_l = (1/k_l + 1/c_\varphi)^{-1}$. It is seen from **Table D2** that our 3D model predicts consistently stiffer (~1.5 times) probes than those described in the original work. We also noted that the normal spring constant of all probes k_n obtained by our simulations (with an average value of 3.04 N/m) is also more than twice the value of Koren et al. (1.40 N/m) [124], further indicating a systematic underestimation in their stiffness values. Using the modified lateral spring constant of 132 N/m yields a cohesion energy value of 0.340±0.008 Jm^{-2} at the G/G interface, which is more consistent with our measurements.

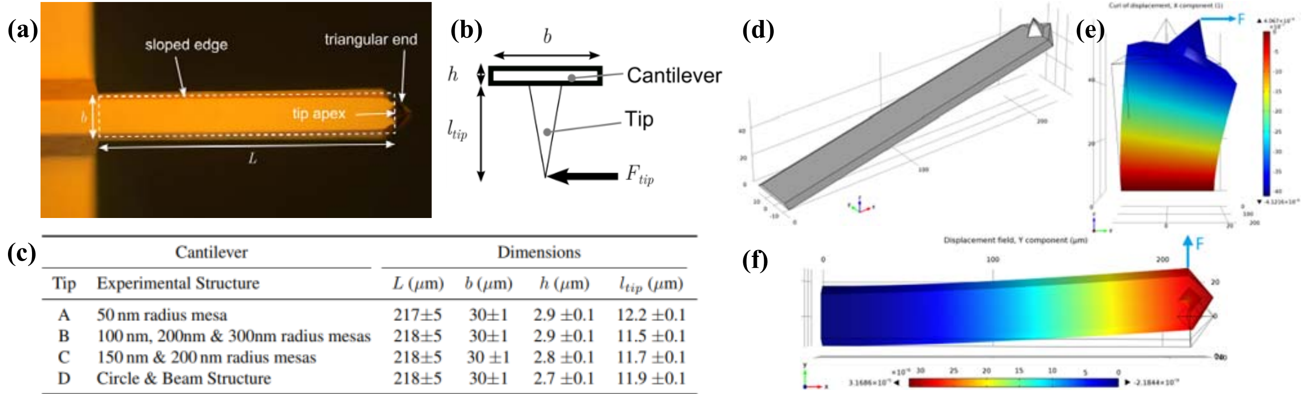

	Cantilever	Dimensions			
Tip	Experimental Structure	L (μm)	b (μm)	h (μm)	l_{tip} (μm)
A	50 nm radius mesa	217±5	30±1	2.9 ±0.1	12.2 ±0.1
B	100 nm, 200nm & 300nm radius mesas	218±5	30±1	2.9 ±0.1	11.5 ±0.1
C	150 nm & 200 nm radius mesas	218±5	30 ±1	2.8 ±0.1	11.7 ±0.1
D	Circle & Beam Structure	218±5	30±1	2.7 ±0.1	11.9 ±0.1

Figure D.1. (a) Typical optical microscope image of the AFM tip with an effective length and width of L and b, respectively. (b) Schematic drawing of probe dimensions and a lateral load applied to the apex. (c) Dimensions of the probes used. (a)-(c) are directly used from [124]. (d) Corresponding 3D model of the AFM probe. (e) Rotation of the probe A about its long axis x when a lateral force of 10 nN is applied to the tip apex in the positive y direction, yielding a torsional stiffness value of c_φ=222.74 N/m. (e) Lateral deflection of the probe A when a force of 10 nN in the positive y direction is applied to a point on the cantilever shank with the same x distance from the cantilever root as the x distance of the tip apex, yielding a lateral bending stiffness value of k_l=344.59 N/m.

Using the similar finite element technique, we also calculated the effective lateral stiffness of our probe to be 83.8 N/m, which is an order of magnitude larger than the axial spring constant of the probe (8.60±0.40 N/m), confirming that the accuracy of shear force measurements using the conventional lateral shear force microscopy technique is highly limited by the large spring constant of the probe.

We also note that to the best of our knowledge no cohesion energy measurement on the hBN homointerface yet exists, while there is only one measured cohesion energy value of 0.22 Jm^{-2} at the MoS_2 homointerface using a nanomechanical cleavage technique [161], which is lower than half the value observed in our experiment. We believe that in their calculations, a very low bending stiffness value of 0.92 eV has been used for the monolayer MoS_2 which is even lower than that of monolayer G (1.49 eV) and monolayer hBN (1.34 eV) whose thicknesses are almost half the thickness of MoS_2, resulting in such a low cohesion energy value in their MoS_2 homostructure (see **Section D4**).

Table D2. Comparisons between calibrated stiffness of probes reported by Koren et al. [124] and the present work.

Type	$k_n(N/m)$		$c_\varphi(N/m)$		$k_l(N/m)$		$c_l(N/m)$		**Ratio**
	Koren	Present	Koren	Present	Koren	Present	Koren	Present	
A	1.19	3.31	218	223	183	343	99	135	1.36
B	1.40	3.26	202	248	150	338	86	143	1.66
C	1.71	2.94	168	217	137	327	75	130	1.73
D	1.30	2.63	176	189	160	315	84	118	1.40
Avg.	**1.40**	**3.04**	**191**	**219**	**158**	**331**	**86**	**132**	**1.53**

D1.2 Comparison study on interfacial adhesion energy of 2D crystal/SiO_x

Despite many experimental studies devoted to the IAE determination of 2D crystals/SiO_x heterostructures, no experimental data are available on the interaction of hBN/SiO_x, whereas the reported IAE data on the interaction of G and MoS_2 with SiO_x are very diverse, ranging from 0.09–0.90 Jm^{-2} at the G/SiO_x interface (**Table D3**) and 0.08–0.48 Jm^{-2} at the MoS_2/SiO_x interface (**Table D4**). We believe that a part of this large data scattering can be attributed to different surface properties of SiO_x during sample preparation, leading to different surface roughness, surface configurations (due to its amorphous nature), surface polarities, charge impurities, surface reactions with ambient humidity, and type of surface termination/defects (i.e., H–, Si– and O–terminated surfaces).

Table D3. Interlayer adhesion energy of carbon nanotubes, few-layer graphene, and graphite on SiO_x.

Method	Sample	Γ (J/m²)	Ref
AFM nano-indentation	BLG/FLG	0.270±0.020	[158]
Pressurized blister	1LG	0.45±0.02	[68]
	2-5LG	0.31±0.03	
Pressurized blister	1LG	0.24	[69]
Pressurized blister	1LG	0.140±0.040	[162]
	5LG	0.160±0.060	
AFM with a microsphere tip	1LG	0.46±0.02	[163]
Intercalation of nanoparticles	5LG	0.302±0.056*	[164]
Infrared crack opening Interferometry	1LG	0.357±0.016	[165]
Nanoparticle-loaded blister	1LG	0.453±0.006	[70]
	3-5LG	0.317±0.003	
	10-15LG	0.276±0.002	
Intercalation of nanoparticles	FLG	0.567	[166]
Colorimetry technique	2LG	0.9	[167]
Interfacial nanoblisters	1LG	0.093±0.001	[168]

* After making a correction in *E* from 0.5 to 1 TPa.

Table D4. Interlayer adhesion energy of MoS_2 on SiO_x.

Method	Sample	Γ (J/m²)	Ref
Intercalation of nanoparticles	FL	0.482	[166]
Pressurized blister	1L	0.212±0.037	[169]
	2L	0.166±0.004	
	3L	0.237±0.016	
	1L CVD	0.236±0.021	
Wrinkle	FL	0.170±0.033	[170]
Interfacial nanoblisters	1L	0.082±0.001	[168]

D2 Effect of Tilt Angle on Interfacial Adhesion Energy Measurements

Flat tips can result in direct and accurate acquisition of the interfacial adhesion energy, provided they are carefully aligned with respect to the sample surface. In this study, an in-situ flattened tip was used as a means to minimize the effect of the tilt angle of the substrate on the

IAE measurements. Nevertheless, to investigate the dependence of the IAE on the misalignment of the sample, we used a home-made setup consisting of a variable tilt mount with an angle resolution of 0.5° to measure the IAE of G tip on the G substrate at a contact pressure of 1 MPa and 10 MPa. The G substrate was first rotated about the axis perpendicular to the probe length to achieve the maximum pull-off force, followed by the rotation of the substrate about the axis parallel to the probe length with an increment of 0.5° for the subsequent IAE measurements at the G/G interface. Ten IAE measurements were taken from different locations of the G sample for each tilt angle. Given that the maximum IAE value is presumed for the fully aligned tip-sample system, we set the corresponding tilt angle to be zero and accordingly the IAE values are reported for tilt angles ranging from -3° to 3°, as shown in **Figure D.2(a)**.

It is seen that the IAE of G/G is almost independent of the contact pressure within the studied tilt angle range. It is also observed that the IAE exhibits a very weak dependence on the tilt angle of less than 1.5° (within our experimental errors) and only ~30% reduction at the tilt angle of 3°. This result is interesting because in the literature a larger adhesion force reduction of ~30% and 60% was reported at a tilt angle of 1° and 3°, respectively, for a flat silicon tip (nominal spring constant: 48 N/m) with a 2 μm diameter contact area over a 2 nm thick SiO_x substrate [171]. More than an order of magnitude smaller contact area in the present study (i.e., 60 nm versus 2 μm diameter flat tip apex) motivates us to investigate to what extent the misalignment effect on the interfacial adhesion force is controlled by the size of the contact area.

To do so, we perform a set of classical MD simulations to calculate the pull-off force between the SiO_x substrate and the square flakes of graphene with both small (2nm×2nm) and large (10nm×10nm) flake sizes. The SiO_x substrate was tilted clockwise in the range of 0° to 3° and the pull-off force was obtained as the tapered silicon layer was moved away from the sample surface. For comparison purposes, pull-off force was normalized with respect to maximum pull-off force at a tilt angle of 0°. It is evident from **Figure D.2(b)** that pull-off force in the larger flakes exhibits a significantly stronger dependence on the tilt angle compared to that in smaller flakes, further supporting our experimental observations that the smaller flat tip apex provides more reliable IAE values on tilted substrates.

We also note that over an order of magnitude smaller torsional stiffness of our probe compared to that in [171] can play a role in the formation of conformal contact at the tilted G/G interface, leading to the lower sensitivity of our IAE measurements toward the tilt angle

(according to the Euler-Bernoulli equation, the torsional stiffness k_φ is proportional to the normal stiffness k_n of the probe of length L and can be given by: $k_\varphi=4k_nGL^2/(3E)$ where E and G are the Young's and shear moduli of silicon, respectively).

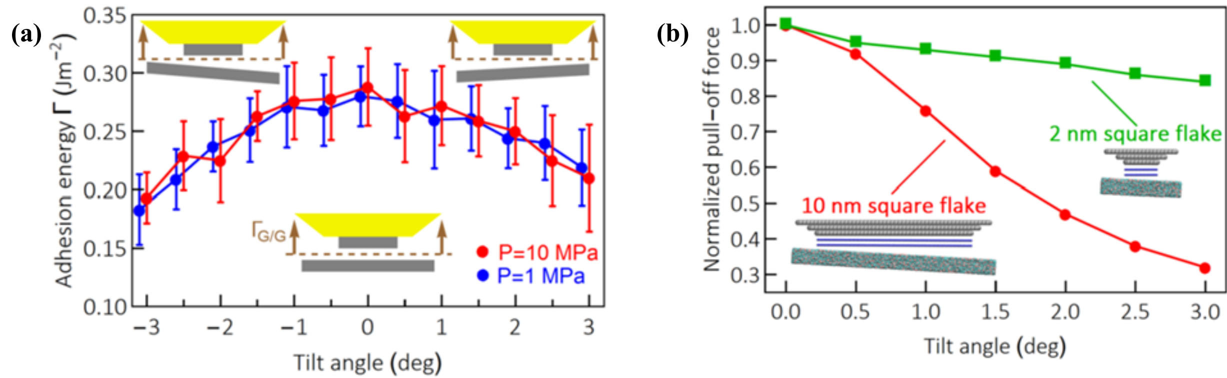

Figure D.2. (a) Interfacial adhesion energy measurements of G/G as a function of tilt angle. **(b)** MD calculations of normalized pull-off force versus the tilt angle of the SiO_x substrate at the interface of SiO_x and the small (2nm×2nm) and large (10nm×10nm) graphene flakes.

D3 Static Spring Constant Calibration

The main source of uncertainty in our AFM measurements lies in the determination of spring constant k of the AFM probe subjected to the normal or shear force at the apex. A large number of studies have addressed this issue in the past, and have suggested different techniques producing more or less uncertainty in the calculation of this parameter. The method that is most viable for in-situ characterization is the thermal method (independent of material properties of the AFM cantilever), requiring knowledge of instrument parameters and the mean-square amplitude vibrations of the cantilever as a function of frequency only, which can be efficiently and quickly measured before each experiment.

We measure thermal fluctuations of the free end of the cantilever to determine its spring constant, which, according to the equipartition theorem, is $= k_B T/\langle z^2(f)\rangle$, where T is the room temperature, k_B is Boltzmann's constant, and $\langle z^2(f)\rangle$ is the mean square of the cantilever thermal fluctuation amplitude. Because the thermal noise method relies on the measurement of cantilever fluctuations, some corrections are required to achieve an accurate determination of the spring constant.

D3.1 Spring constant calibration under a normal load at the apex

(a) *Contribution of fundamental natural frequency*: Basically, $\langle z^2(f) \rangle$ is obtained by integrating the amplitude power spectrum of the cantilever (which is modeled by a simple harmonic thermally-driven oscillator) over the whole frequency range. However, in practice, the dominant contributions of the thermally driven fluctuations is at and around the fundamental natural frequency, f_1, and, as a result, the amplitude spectral density is recorded and integrated over a few *k*Hz band of frequencies centered at the fundamental natural frequency. Hence, the expression for the spring constant needs to be modified by

$$k = \frac{12}{\alpha_1^4} \frac{Q}{\pi} \frac{k_B T}{\langle z^2(f_1) \rangle} \frac{\Delta f}{f_1} \tag{D1}$$

where $\alpha_1 = 1.8751$ is the parameter quantifying the amount of energy stored in the fundamental vibration mode, Q and $\langle z^2(f_1) \rangle$ denote the quality factor and the mean square cantilever displacement in the fundamental mode, respectively, and Δf is the frequency resolution. An accurate measurement of the mean square displacement in a region around the fundamental natural frequency is challenging for the AFM probes and the following effects must be taken into account.

(b) *Conversion of virtual to actual deflection*: The AFM measures the angular changes (virtual deflection, $\hat{z}$) rather than the actual deflection, z, so it is necessary to correct the mean-square amplitude of the cantilever vibration to account for these angular changes. The actual deflection z for the fundamental mode can be related to the virtual deflection $\hat{z}$ through the following expression [172]

$$\langle z^2(f_1) \rangle = \left(\frac{3}{2} \frac{\sin \alpha_1 + \sinh \alpha_1}{\alpha_1 \sin \alpha_1 \sinh \alpha_1} \right)^2 \langle \hat{z}^2(f_1) \rangle \tag{D2}$$

(c) *Effect of the protruding tip*: In the contact mode, the adhesion force is applied to the tip apex not to the free end of the cantilever. Hence, we need to take the offset end load into consideration. As schematically illustrated in **Figure D.3**, a tip protruded from the free end of a cantilever tilted by an angle θ with respect to a horizontal surface increases the effective lever of the force from $L \cos \theta - x$ to $L \cos \theta + D \sin \beta - x$, where the effective tip height D is measured from the tip apex to the midpoint of the cantilever thickness.

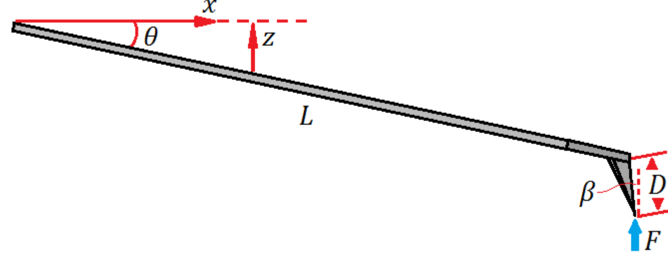

Figure D.3. Schematic drawing of a cantilever tilted by an angle θ with respect to a horizontal surface subjected to a normal force along the positive *z* axis.

Following the work of Hutter [173], the bending moment-curvature relation in the cantilever can be expressed by the following differential equation

$$EI\cos^3\theta\frac{d^2z}{dx^2} = F(L\cos\theta + D\sin\beta - x) \tag{D3}$$

After integrating and applying the boundary condition $dz/dx\,(x=0) = -\tan\theta$, we can find the inclination at the free end about the equilibrium slope as follows

$$\Delta\hat{z} = \frac{dz}{dx} = \frac{FL}{2EI\cos^2\theta}(L\cos\theta + 2D\sin\beta) \tag{D4}$$

Further integration of Eq. (D3) and using the boundary condition $z(x=0) = 0$ lead to the deflection at the free end of the cantilever as follows

$$\Delta z = \frac{FL^2}{3EI}\left(L\cos\theta + \frac{3}{2}D\sin\beta\right)\cos\theta \tag{D5}$$

By inspection of Eqs. (D4) and (D5), the relation between the actual and virtual deflections in Eq. (D2) is further modified to

$$\langle z^2(f_1)\rangle = \left(\frac{3}{2}\frac{\sin\alpha_1 + \sinh\alpha_1}{\alpha_1\sin\alpha_1\sinh\alpha_1}\right)^2\left(\frac{2L\cos\theta + 4D\sin\beta}{2L\cos\theta + 3D\sin\beta}\right)^2\langle\hat{z}^2(f_1)\rangle \tag{D6}$$

(d) *Effect of size and position of the laser spot*: The laser spot size is primarily defined by the laser wavelength and microscope objective being used. While the minimum achievable spot size is diffraction limited, according to the laws of physics and optics, the laser spot diameter D_s is equal to 1.22 λ / N.A., where λ is the wavelength of the laser, and N.A. is the numerical aperture of the microscope objective being used. In our AFM setup with an 830 nm laser and a 0.28/10x objective, the theoretical spot diameter is 3.62 μm. Such a small optical spot (compared to the long length of the probe, i.e., D_s/L_{eff} = 3.62μm/(231.4μm×cos12°) = 0.016) which is placed at the

very end of the cantilever has a negligible effect on correction factor considered in Eq. (D2) [174].

(e) *Effect of the angle of repose*: The optical lever sensitivity, S, defined by the ratio of the displacement of the piezo-scanner Δz_0 and the position-sensitive photo-detector (PSPD) voltage ΔV_0, is the factor that allows us to convert the cantilever deflection from volts to nanometers. Basically, the optical lever sensitivity is the slope of a force curve obtained by placing the probe in contact with an infinitely stiff surface and ramping the scanner position. However, the value of S ($=\Delta z_0/\Delta V_0$) is obtained in the scanner's reference frame while the contact force acts in the cantilever's reference frame, which is tilted at a repose angle of θ with respect to the sample. Hence, we need to divide S by $\cos\theta$, leading to

$$\langle z^2(f_1)\rangle = \left(\frac{3}{2}\frac{\sin\alpha_1 + \sinh\alpha_1}{\alpha_1 \sin\alpha_1 \sinh\alpha_1}\right)^2 \left(\frac{2L\cos\theta + 4D\sin\beta}{2L\cos\theta + 3D\sin\beta}\right)^2 \left(\frac{S}{\cos\theta}\right)^2 \langle \Delta V^2(f_1)\rangle \quad \text{(D7)}$$

where $\langle \Delta V^2(f_1)\rangle$ is the mean square voltage at the fundamental natural frequency.

Substituting Eq. (D7) into (D1), we end up with a full expression for the spring constant of the probe as follows

$$k = \frac{16}{3\alpha_1^2}\left(\frac{\sin\alpha_1 \sinh\alpha_1}{\sin\alpha_1 + \sinh\alpha_1}\right)^2 \left(\frac{2L\cos\theta + 3D\sin\beta}{2L\cos\theta + 4D\sin\beta}\right)^2 (\cos^2\theta)\frac{Qk_BT}{\pi S^2\langle \Delta V^2(f_1)\rangle}\frac{\Delta f}{f_1} \quad \text{(D8)}$$

By setting $\alpha_1 = 1.8751$, Eq. (D8) can be further simplified to

$$k = 0.8174\left(\frac{2L\cos\theta + 3D\sin\beta}{2L\cos\theta + 4D\sin\beta}\right)^2 (\cos^2\theta)\frac{Qk_BT}{\pi S^2\langle \Delta V^2(f_1)\rangle}\frac{\Delta f}{f_1} \quad \text{(D9)}$$

Our XE-70 AFM head provides a tilt angle of $\theta = 12°$. From the SEM measurements of the probe geometry, the following parameters were determined: $\beta = 10.5°$, $L = 231.4\mu m$, $D = 20.7\mu m$. All measurements were performed in the ambient conditions at $T = 295\,K$. Three parameters Q, f_1, and $\langle \Delta V^2(f_1)\rangle$ are determined by acquiring the thermal noise power spectrum using the SR760 FFT Spectrum Analyzer with the frequency resolution of $\Delta f = 15.625$ Hz. The optical lever sensitivity, S, on the sapphire sample was 14.32 nm/V.

Figure D.4(a) shows the typical measurement of the mean square voltage amplitude by connecting the spectrum analyzer to the output of the preamplifier of the PSPD of the AFM controller. The spectrum analyzer measures the mean square voltage amplitude for the fundamental cantilever oscillation mode, which can be represented as

$$\langle \Delta V^2(f) \rangle = \frac{A}{f} + B + \frac{\langle \Delta V^2(f_1) \rangle}{Q^2} \frac{1}{[1-(f/f_1)^2]^2 + (f/Qf_1)^2} \quad \text{(D10)}$$

where the first two terms are used to account for a 1/f noise background and a white-noise floor, respectively. Once Eq. (D10) is fitted to the data by five fit parameters A, B, Q, f_1, and $\langle \Delta V^2(f_1) \rangle$, the last three ones are used for the calculation of the spring constant from Eq. (D9) which is obtained to be 3.05 N/m. In a second approach, we employed the Sader method [175] with the input parameters of $(L, w, f_1, Q) = (230.8\mu\text{m}, 36.4\mu\text{m}, 73.375\text{kHz}, 225.1)$, yielding a static spring constant of 3.29 N/m. This is slightly higher than the value predicted by Eq. (D9) because the effects of the protruding tip and the angle of repose were not taken into account. After considering these effects, the spring constant becomes 3.10 N/m, more consistent with that of thermal noise method. Note that the effective length in the Sader method was modified to account for the triangular end of the cantilever such that the new rectangular cantilever exhibits the exact same deflection response as the original cantilever.

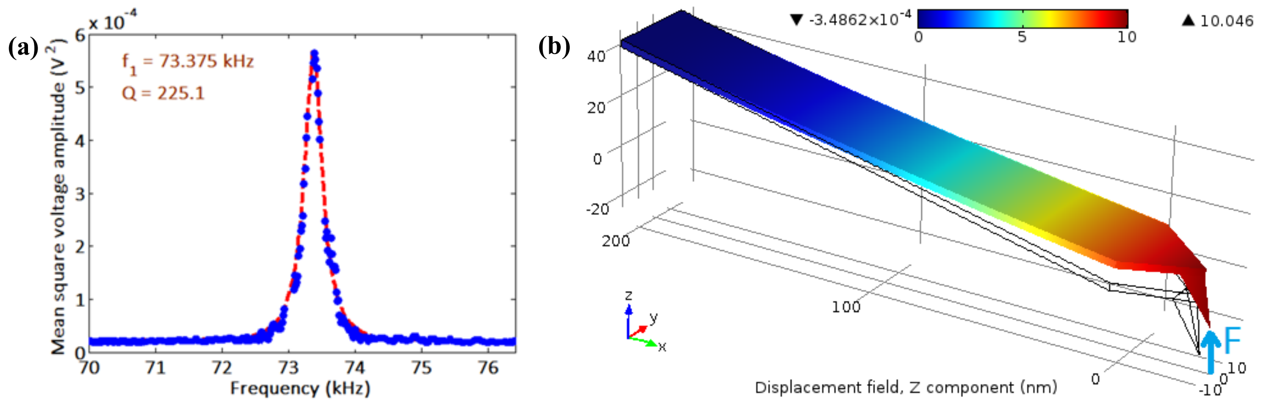

Figure D.4. (a) Mean square fluctuations in amplitude as a function of frequency for the probe with the protruded tip in air. The blue curve is the original data while the dash curve is the fit to the data using Eq. (12). (b) Deflection of the probe when a contact force of 30 nN is applied to the apex in the positive *z* direction, yielding a spring constant of 2.99 N/m.

In a third approach, we estimated the spring constant of the probe by performing a finite element method simulation using COMSOL™. The effective dimensions of the probe were measured using SEM images to an accuracy of ±0.5μm and ±2μm for the width and length, respectively, and ±100nm for the thickness. Assuming that the probes are typically fabricated from a [100] wafer with their long axis aligned with a <110> direction, we considered the elastic modulus of silicon to be E_{110}=169 GPa. After tilting the probe by 12° about the *x* axis, we applied a 30 nN force in the positive z direction to the tip apex while the root of the cantilever

was fixed (**Figure D.4(b)**). From the computed deflection, the stiffness of the probe was calculated to be 2.99 N/m, in excellent agreement with the static spring constant obtained from thermal noise and Sader methods. For the purpose of this experiment, the mean value of the three methods (3.05±0.05 N/m) was taken as the static normal spring constant, enabling us to obtain the adhesion force by $F = kS\Delta V$, where ΔV is the measured PSPD voltage signal.

D3.2 Spring constant calibration under an axial load at the apex

In this study, we moved 2D crystal substrates along the long axis of the cantilever tip rather than perpendicular to its long axis to obtain more accurate shear force measurements. In order to demonstrate the higher force resolution in the present axial shear force microscopy technique compared to that in the conventional lateral shear force microscopy technique, we determine the spring constant of the probe for each case.

The spring constant of the probe under the axial load can be related to the previously calibrated spring constant under the normal load by calculating the deflection ratio of the free end of the cantilever under normal and axial loading conditions. In the contact mode, the axial force directed to the long axis of the cantilever is applied to the tip apex, as shown in **Figure D.5(a)**. The bending moment-curvature relation in the cantilever can be expressed by the following differential equation

$$EI\cos^3\theta\frac{d^2z}{dx^2} = F(L\cos\theta - x)\tan\theta + FD\cos\beta \qquad \text{(D11)}$$

After integrating Eq. (D11) twice with respect to *x* and applying the relevant boundary conditions, we can find the deflection at the free end of the cantilever as follows

$$\Delta z = \frac{FL^2}{3EI}\left(L\sin\theta + \frac{3}{2}D\cos\beta\right)\cos\theta \qquad \text{(D12)}$$

By inspection of Eqs. (D5) and (D12), one can analytically determine the deflection ratio for the axial and normal loads as follows

$$\frac{\Delta z_{\text{axial}}}{\Delta z_{\text{normal}}} = \frac{2L\sin\theta + 3D\cos\beta}{2L\cos\theta + 3D\sin\beta} = 0.339 \qquad \text{(D13)}$$

Because the spring constant is inversely proportional to the tip deflection, the spring constant of the probe under the axial load can be determined by (3.05N/m)/0.339 = 9.00N/m. In a second approach, we carried out a similar finite element method simulation with the axial load of 30 nN applied to the positive *x* direction (**Figure D.5(b)**). From the computed deflection, the spring

constant of the probe was calculated to be 8.20 N/m. For the purpose of this experiment, the mean value of the two methods (8.60±0.40 N/m) was taken as the static spring constant under the axial load. This value is an order of magnitude smaller than the lateral spring constant of the probe (i.e., 83.8 N/m when the shear force acts perpendicular to the long axis of the cantilever), indicating much more accurate shear force measurements in the present shear force microscopy technique. This is also confirmed by our shear force measurements with atomic-level resolution (**Figure 5.9(b)**).

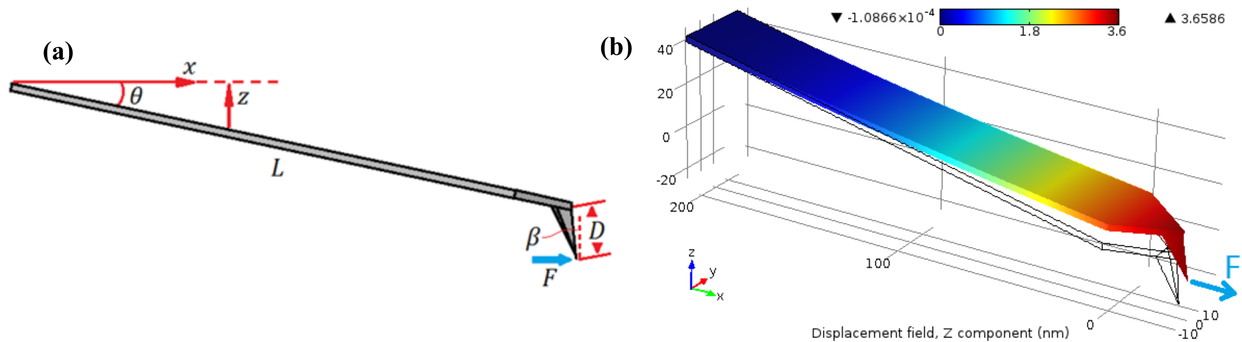

Figure D.5. (a) Schematic drawing of a cantilever tilted by an angle θ with respect to a horizontal surface subjected to a axial force directed to the long axis of the cantilever along the positive *x* axis. (b) Deflection of the probe when a contact force of 30 nN is applied to the apex in the positive *x* direction, yielding a spring constant of 8.20 N/m.

D4 Calculation of Bending Stiffness in 2D Crystals

A direct measurement of in-plane elastic modulus of monolayer G (342±8 Nm^{-1} [2]), bilayer G (645±16 Nm^{-1} [2]), monolayer hBN (289±24 Nm^{-1} [2]) and monolayer MoS_2 (180±60 Nm^{-1} [3], 120±30 Nm^{-1} [176]) was reported by AFM nanoindentation of suspended 2D crystal membranes. Also, the bending stiffness of monolayer G (1.49eV) [177], monolayer hBN (1.34eV) [177] and monolayer MoS_2 (11.7eV) [176] is obtained by first principles calculations, whose in-plane elastic modulus of monolayer 2D crystals is consistent with the aforementioned experimental values. In addition, the bending stiffness of bilayer G (35.5 eV) was calculated by measuring the critical voltage for snap-through of pre-buckled graphene membranes [178].

D5 Molecular Dynamics Simulations of G/SiOx Heterostructure

To gain an in-depth understanding of underlying mechanisms associated with the interaction of G crystal and the SiO_x substrate, we performed classical MD simulations using the LAMMPS simulator at room temperature. Four 98.2Å×102.1Å G layers with AB stacking were

placed at a distance of 3.0 Å above an amorphous SiO_x substrate (143.3×146.5×21.3Å^3) while the flattened tip was modeled by a tapered silicon (001) layer. To hold the system in space, 2 Å of the SiO_x substrate from the bottom was treated as rigid throughout the simulation. We adopted reactive empirical bond order potential function to model the intralayer carbon–carbon interactions within the same G layer while the free G edges were passivated by hydrogen. A registry–dependent interlayer potential that can accurately describe the overall cohesion, corrugation, equilibrium spacing and compressibility of few-layer G was implemented in the LAMMPS code to model the carbon–carbon interaction between G flakes. Tersoff potential and Stillinger-Weber potential were utilized for the modelling of SiO_x substrate and silicon (001) layer, respectively. We used a standard 12–6 Lennard-Jones potential for describing Si–C and O–C long-range vdW interactions according to the Universal Force Field model and the Lorentz–Berthelot mixing rules, whereas O–C and Si–C covalent bonds at the G/SiO_x interface were modeled by the Tersoff potential. The glue between the tip and the few-layer G nanomesa was simply modeled by applying the Lennard-Jones potential between the silicon layer and the topmost G layer using a larger Si–C interaction energy. The calculations were conducted in the NVT ensemble using the Nosé-Hoover thermostat and Newton's equations of motion were integrated using the velocity Verlet algorithm with a time step of 1 fs. The total interfacial force (i.e., vdW and non-vdW forces) and relative displacement between the innermost G layer and the SiO_x substrate were simultaneously monitored as the tapered silicon (001) layer was pulled in the normal direction with a constant speed of 10^{-2} Å/ps.

BIBLIOGRAPHY

[1] R. Lv, J. A. Robinson, R. E. Schaak, D. Sun, Y. Sun, T. E. Mallouk and M. Terrones, "Transition Metal Dichalcogenides and Beyond: Synthesis, Properties, and Applications of Single- and Few-Layer Nanosheets," *Accounts of Chemical Research,* vol. 48, no. 1, p. 56–64, 2015.

[2] A. Falin, Q. Cai, E. J. G. Santos, D. Scullion, D. Qian, R. Zhang, Z. Yang, K. Huang and et al., "Mechanical properties of atomically thin boron nitride and the role of interlayer interactions," *Nature Communications,* vol. 8, p. 15815, 2017.

[3] S. Bertolazzi, J. Brivio and A. Kis, "Stretching and Breaking of Ultrathin MoS2," *ACS Nano,* vol. 5, no. 12, p. 9703–9709, 2011.

[4] B. Radisavljevic, A. Radenovic, J. Brivio, V. Giacometti and A. Kis, "Single-Layer MoS2 Transistors," *Nature nanotechnology,* vol. 6, pp. 147-150, 2011.

[5] H. Rokni and W. Lu, "Nanoscale probing of interaction in atomically thin layered materials," *ACS Central Science,* pp. 288-297, 2018.

[6] M. Chen, H. Rokni, W. Lu and X. Liang, "Scaling behavior of nanoimprint and nanoprinting lithography for producing nanostructures of molybdenum disulfide," *Microsystems & Nanoengineering,* vol. 3, p. 17053, 2017.

[7] M. Chen, H. Nam, H. Rokni, S. Wi, J. S. Yoon, P. Chen, K. Kurabayashi, W. Lu and X. Liang, "Nanoimprint-assisted shear exfoliation (NASE) for producing multilayer MoS2 structures as field-effect transistor channel arrays," *ACS Nano,* vol. 9, no. 9, pp. 8773-8785, 2015.

[8] F. Pizzocchero, L. Gammelgaard, B. S. Jessen, J. M. Caridad, L. Wang, J. J. Hone, P. Bøggild and T. J. Booth, "The hot pick-up technique for batch assembly of van der Waals heterostructures," *Nature Communications,* vol. 7, p. 11894, 2016.

[9] K. S. Novoselov, A. Mishchenko, A. Carvalho and A. H. Castro Neto, "2D materials and van der Waals heterostructures," *Science,* vol. 353, no. 6298, p. 9439, 2016.

[10] L. Britnell, R. Gorbachev, R. Jalil, B. Belle, F. Schedin, A. Mishchenko, T. Georgiou, M. Katsnelson, L. Eaves and S. Morozov, "Field-effect tunneling transistor based on vertical graphene heterostructures," *Science ,* vol. 335 , no. 6071, pp. 947-950, 2012.

[11] T. Georgiou, R. Jalil, B. D. Belle, L. Britnell, R. V. Gorbachev, S. V. Morozov, Y.-J. Kim, A. Gholinia, S. J. Haigh and O. Makarovsky, "Vertical field-effect transistor based on

graphene–WS2 heterostructures for flexible and transparent electronics," *Nature Nanotechnology,* vol. 8, no. 2, p. 100, 2013.

[12] L. Britnell, R. M. Ribeiro, A. Eckmann, R. Jalil, B. D. Belle, A. Mishchenko, Y. J. Kim, R. V. Gorbachev, T. Georgiou, S. V. Morozov, A. N. Grigorenko, A. K. Geim, C. Casiraghi, A. H. Castro Neto and K. S. Novoselov, "Strong Light-Matter Interactions in Heterostructures of Atomically Thin Films," *Science,* vol. 340, no. 6138, pp. 1311-1314, 2013.

[13] J. H. Garcia, A. W. Cummings and S. Roche, "Spin Hall Effect and Weak Antilocalization in Graphene/Transition Metal Dichalcogenide Heterostructures," *Nano Letters,* vol. 17, no. 8, p. 5078–5083, 2017.

[14] D. K. Bediako, M. Rezaee, H. Yoo, D. T. Larson, S. Y. F. Zhao, T. Taniguchi, K. Watanabe, T. L. B. Thomas, E. Kaxiras and P. Kim, "Heterointerface effects in the electrointercalation of van der Waals heterostructures," *Nature,* vol. 558, p. 425–429, 2018.

[15] M. Velický and P. S. Toth, "From two-dimensional materials to their heterostructures: An electrochemist's perspective," *Applied Materialstoday,* vol. 8, pp. 68-103, 2017.

[16] M. A. Khan, S. Rathi, C. Lee, D. Lim, Y. Kim, S. J. Yun, D. H. Youn and G. H. Kim, "Tunable Electron and Hole Injection Enabled by Atomically Thin Tunneling Layer for Improved Contact Resistance and Dual Channel Transport in MoS2/WSe2 van der Waals Heterostructure," *ACS Applied Materials & Interfaces,* vol. 10, pp. 23961-23967, 2018.

[17] S. Deng and V. Berry, "Wrinkled, rippled and crumpled graphene: an overview of formation mechanism, electronic properties, and applications," *Materialstoday,* vol. 19, no. 4, pp. 197-212, 2016.

[18] R. Roldán, J. A. S. Guillén, M. P. L. Sancho, F. Guinea, E. Cappelluti and P. Ordejón, "Electronic properties of single-layer and multilayer transition metal dichalcogenides MX2 (M = Mo, W and X = S, Se)," *Annalen der Physik,* vol. 526, no. 9-10, pp. 347-355, 2014.

[19] J. Chen, J. H. Walther and P. Koumoutsakos, "Strain Engineering of Kapitza Resistance in Few-Layer Graphene," *Nano Letters,* vol. 14, no. 2, p. 819–825, 2014.

[20] J. H. Wong, B. R. Wu and M. F. Lin, "Strain Effect on the Electronic Properties of Single Layer and Bilayer Graphene," *Journal of Physical Chemistry C,* vol. 116, no. 14, p. 8271–8277, 2012.

[21] H.-Y. Chang, S. Yang, J. Lee, L. Tao, W.-S. Hwang, D. Jena, N. Lu and D. Akinwande, "High-Performance, Highly Bendable MoS2 Transistors with High-K Dielectrics for Flexible Low-Power Systems," *ACS Nano,* vol. 7, pp. 5446-5452, 2013.

[22] Q. He, Z. Zeng, Z. Yin, H. Li, S. Wu, X. Huang and H. Zhang, "Fabrication of Flexible MoS2 Thin-Film Transistor Arrays for Practical Gas-Sensing Applications," *Small,* vol. 8, pp. 2994-2999, 2012.

[23] Z. Yin, H. Li, H. Li, L. Jiang, Y. Shi, Y. Sun, G. Lu, Q. Zhang, X. Chen and H. Zhang,

"Single-Layer MoS2 Phototransistors," *ACS nano,* vol. 6, pp. 74-80, 2011.

[24] M. Chen, H. Nam, S. Wi, G. Priessnitz, I. M. Gunawan and X. Liang, "Multibit Data Storage States Formed in Plasma-Treated MoS2 Transistors," *ACS Nano,* vol. 8, pp. 4023-4032, 2014.

[25] S. Wi, H. Kim, M. Chen, H. Nam, L. J. Guo, E. Meyhofer and X. Liang, "Enhancement of Photovoltaic Response in Multilayer MoS2 Induced by Plasma Doping," *ACS nano,* vol. 8, pp. 5270-5281, 2014.

[26] K. F. Mak, C. Lee, J. Hone, J. Shan and T. F. Heinz, "Atomically Thin MoS2: A New Direct Gap Semiconductor. , ,," *Physical Review Letters,* vol. 105, p. 136805, 2010.

[27] D. Xiao, G.-B. Liu, W. Feng, X. Xu and W. Yao, "Coupled Spin and Valley Physics in Monolayers of MoS2 and Other Group-VI Dichalcogenides," *Physical Review Letters,* vol. 108, p. 196802, 2012.

[28] L. Wang, Y. Wang, J. I. Wong, T. Palacios, J. Kong and H. Y. Yang, " Functionalized MoS2 Nanosheet-Based Field-Effect Biosensor for Label-Free Sensitive Detection of Cancer Marker Proteins in Solution," *Small,* vol. 10, pp. 1101-1105, 2014.

[29] M. Shanmugam, C. A. Durcan and B. Yu, "Layered Semiconductor Molybdenum Disulfide Nanomembrane Based Schottky-Barrier Solar Cells," *Nanoscale ,* vol. 4, pp. 7399-7405, 2012.

[30] S. Kim, A. Konar, W.-S. Hwang, J. H. Lee, J. Lee, J. Yang, C. Jung, H. Kim, J.-B. Yoo, J.-Y. Choi, Y. W. Jin, S. Y. Lee, D. Jena, W. Choi and K. Kim, "High-Mobility and Low-PowerThin-Film Transistors Based on Multilayer MoS2 Crystals," *Nature Communications,* vol. 3, p. 1011, 2012.

[31] S. Das, H.-Y. Chen, A. V. Penumatcha and J. Appenzeller, "High Performance MultilayerMoS2 Transistors with Scandium Contacts," *Nano Letters ,* vol. 13, pp. 100-105, 2013.

[32] Y. Liu, H. Nan, X. Wu, W. Pan, W. Wang, J. Bai, W. Zhao, L. Sun, X. Wang and Z. Ni, "Layer-by-Layer Thinning of MoS2 by Plasma," *ACS Nano,* vol. 7, pp. 4202-4209, 2013.

[33] K. S. Novoselov, "Two-dimensional atomic crystals," *PNAS,* vol. 102, pp. 10451-10453, 2005.

[34] W. Lu, D. Wang and L. Chen, "Near-static dielectric polarization of individual carbon nanotubes," *Nano Letters,* vol. 7, no. 9, pp. 2729-2733, 2007.

[35] J. P. Reed, B. Uchoa and e. al., "The effective fine-structure constant of freestanding graphene measured in graphite," *Science ,* vol. 330, pp. 805-808, 2010.

[36] Y. Gan, G. A. de la Pena, A. Kogar and e. al., "Reexamination of the effective fine structure constant of graphene as measured in graphite," *Physical Review B,* vol. 93, p. 19515, 2016.

[37] D. C. Elias, R. V. Gorbachev, A. S. Mayorov and e. al., " Dirac cones reshaped by

interaction effects in suspended graphene," *Nature Physics,* vol. 7, pp. 701-704, 2011.

[38] A. Bostwick and e. al., "Observation of plasmons in quasi-freestanding doped graphene," *Science ,* vol. 328, pp. 999-1002, 2010.

[39] D. A. Siegel, C. H. Park and e. al., "Many-body interactions in quasi-freestanding graphene.," *PNAS ,* vol. 108, no. 28, pp. 11365-11369, 2011.

[40] Y. Wang, V. W. Brar, A. V. Shytov and et al, "Mapping dirac quasiparticles near a single Coulomb impurity on graphene," *Nature Physics,* vol. 8, pp. 653-657, 2012.

[41] T. Ohta, A. Bostwick, J. McChesney, T. Seyller, K. Horn and E. Rotenberg, "Interlayer interaction and electronic screening in multilayer graphene investigated with angle-resolved photoemission spectroscopy," *Phys. Rev. Lett.,* vol. 98, p. 206802 , 2007.

[42] D. Sun and e. al., "Spectroscopic Measurement of Interlayer Screening in Multilayer Epitaxial Graphene," *Physical Review Letters,* vol. 104, p. 136802 , 2010.

[43] D. Ziegler, P. Gava, J. Güttinger, F. Molitor, L. Wirtz, M. Lazzeri, A. M. Saitta, A. Stemmer, F. Mauri and C. Stampfer, "Variations in the work function of doped single- and few-layer graphene assessed by Kelvin probe force microscopy and density functional theory," *Phys. Rev. B,* vol. 83, p. 235434 , 2011.

[44] X. Wang, J. Xu, W. Xie and J. Du, "Quantitative Analysis of Graphene Doping by Organic Molecular Charge Transfer," *J. Phys. Chem. C.,* vol. 115, pp. 7596-7602, 2011.

[45] A. Ballestar, P. Esquinazi, J. Barzola-Quiquia, S. Dusari, F. Bern, R. R. da Silva and Y. Kopelevich, "Possible superconductivity in multi-layer-graphene by application of a gate voltage," *Carbon,* vol. 72, pp. 312-320, 2014.

[46] Y. Sui and J. Appenzeller, "Screening and Interlayer Coupling in Multilayer Graphene Field-Effect Transistors," *Nano Lett,* vol. 9, no. 8, p. 2973–2977, 2009.

[47] H. Miyazaki, S. Odaka, T. Sato, S. Tanaka, H. Goto, A. Kanda and e. al., "Interlayer screening length to electric field in thin graphite film," *Appl. Phys. Express,* vol. 1, p. 034007, 2008.

[48] H. Chen, "Measurement of interlayer screening length of layered graphene by plasmonic nanostructure resonances," *J. Phys. Chem. C. ,* vol. 117, pp. 22211-22217, 2013.

[49] P. Visscher and L. Falicov, "Dielectric screening in a layered electron gas," *Phys Rev B,* vol. 3, p. 2541–2547, 1971.

[50] F. Guinea, "Charge distribution and screening in layered graphene systems," *Phys Rev B,* vol. 75, p. 235433 , 2007.

[51] M. Kuroda, J. Tersoff and G. Martyna, "Nonlinear screening in multilayer graphene systems," *Phys Rev Lett,* vol. 106, p. 116804 , 2011.

[52] H. Goto, E. Uesugi, E. R., F. A. and Y. Kubozono, "Edge-dependent transport properties in graphene," *Nano Lett.,* vol. 13, p. 1126–1130, 2013.

[53] J. Chae and et al., "Enhanced Carrier Transport along Edges of Graphene Devices," *Nano*

Lett. , vol. 12, no. 4, pp. 1839-1844, 2012.

[54] C. Barraud, C. T., B. P., S. I., T. T., W. K., I. T. and E. K., "Field Effect in the Quantum Hall Regime of a High Mobility Graphene Wire," *J Appl Phys.* , vol. 073705 , p. 116, 2014.

[55] Z. Wang and R. Scharstein, " Electrostatics of Graphene: Charge Distribution and Capacitance," *Chem Phys Lett.,* vol. 489, pp. 229-236, 2010.

[56] T. Andrijauskas, A. Shylau and I. Zozoulenko, " Thomas–Fermi and Poisson Modeling of Gate Electrostatics in Graphene Nanoribbon. Lithuanian," *Journal of Physics,* vol. 52, no. 1, pp. 63-69, 2012.

[57] C. Ltd, Silica and silicon dioxide-properties.

[58] L. Fumagalli, G. Ferrari, M. Sampietro and G. Gomila, "Dielectric-constant measurement of thin insulating films at low frequency by nanoscale capacitance microscopy," *2007,* vol. 91, p. 243110, Appl. Phys. Lett..

[59] G. Gramse, I. Casuso, T. J., L. Fumagalli and G. Gomila, "Quantitative dielectric constant measurement of thin films by DC electrostatic force microscopy," *Nanotech,* vol. 20, p. 395702, 2009.

[60] W. Lu, D. Wang and L. Chen, "Near-static dielectric polarization of individual carbon nanotubes," *Nano Lett.* , vol. 7, no. 9, pp. 2729-2733, 2007.

[61] S. Berciaud, M. Potemski and C. Faugeras, "Probing Electronic Excitations in Mono- to Pentalayer Graphene by Micro Magneto-Raman Spectroscopy," *Nano Lett.,* vol. 14, p. 4548–4553, 2014.

[62] I. J. Vera-Marun and e. al., "Quantum Hall transport as a probe of capacitance profile at graphene edges," *Appl Phys Lett.,* vol. 102, p. 013106 , 2013.

[63] A. Wilmes and S. Pinho, "A Coupled Mechanical-Charge/Dipole Molecular Dynamics Finite Element Method, with Multi-Scale Applications to the Design of Graphene Nano-Devices," *Int. J. Numer. Meth. Eng.,* vol. 100, pp. 243-276, 2014.

[64] J. Yang and L. Liu, "Effects of Interlayer Screening and Temperature on Dielectric Functions of Graphene by First-Principles," *J Appl Phys.,* vol. 120, p. 034305 , 2016.

[65] H. Rokni and W. Lu, "Layer-by-layer insight into electrostatic charge distribution of few-layer graphene," vol. 7, p. 42821, 2017.

[66] D. W. Brenner, O. A. Shenderova, J. A. Harrison, S. J. Stuart, B. Ni and S. B. Sinnott, "A second–generation reactive empirical bond order (REBO) potential energy expression for hydrocarbons," *J. Phys. Condens. Matter* , vol. 14, p. 783–802, 2002.

[67] A. Kolmogorov and V. Crespi, "Registry–dependent interlayer potential for graphitic systems," *Phys. Rev. B,* vol. 71, p. 235415, 2005.

[68] S. P. Koenig, N. G. Boddeti, M. L. Dunn and J. S. Bunch, "Ultrastrong adhesion of graphene membranes," *Nature Nanotechnology,* vol. 6, pp. 543-546, 2011.

[69] i. N. G. Boddet, S. P. Koenig, R. Long, J. L. Xiao, J. S. Bunch and M. L. Dunn, "Mechanics of adhered, pressurized graphene blisters," *Journal of Applied Mechanics,* vol. 80, p. 040909, 2013.

[70] X. Gao, X. Yu, B. Li, S. Fan and C. Li, "Measuring graphene adhesion on silicon substrate by single and dual nanoparticle-loaded blister," *Advanced Materials Interfaces,* vol. 4, no. 9, p. 1601023, 2017.

[71] W. Bao, K. Myhro, Z. Zhao and e. al., "In situ observation of electrostatic and thermal manipulation of Suspended Graphene Membranes," *Nano Lett.,* vol. 12, p. 5470−5474, 2012.

[72] M. Dequesnes, S. Rotkin and N. R. Aluru, "Calculation of pull–in voltages for carbon–nanotube–based nanoelectromechanical switches," *Nanotechnol,* vol. 13, p. 120−131, 2002.

[73] M. Dequesnes, Z. Tang and N. R. Aluru, "Static and dynamic analysis of carbon nanotube–based switches," *J. Eng. Mater. Technol. ,* vol. 126, p. 230–237, 2014.

[74] X. Liang, A. S. P. Chang, Y. Zhang, B. D. Harteneck, H. Choo, D. L. Olynick and S. Cabrini, "Electrostatic Force Assisted Exfoliation of Prepatterned Few-Layer Graphenes into Device Sites," *Nano Lett,* vol. 9, p. 467–472, 2009.

[75] X. G. Liang, V. Giacometti, A. Ismach, B. D. Harteneck, D. L. Olynick and S. Cabrini, "Roller-Style Electrostatic Printing of Prepatterned Few-Layer-Graphenes," *Appl. Phys. Lett. ,* vol. 96, p. 013109, 2010.

[76] C. Wang, K. J. Morton, Z. Fu, L. W. D. and S. Y. Chou, "Printing of sub-20 nm wide graphene ribbon arrays using nanoimprinted graphite stamps and electrostatic force assisted bonding," *Nanotech,* vol. 22, p. 445301, 2011.

[77] Z. Liu, S. M. Zhang, J. R. Yang, J. Z. Liu, Y. L. Yang and Q. S. Zheng, "Interlayer shear strength of single crystalline graphite," *Acta Mech. Sinica,* vol. 28, p. 978–982, 2012.

[78] M. Dienwiebel, N. Pradeep, G. S. Verhoeven, H. W. Zandbergen and J. W. M. Frenken, "Model experiments of superlubricity of graphite," *Surf. Sci.,* vol. 576, no. 1–3, p. 197–211, 2005.

[79] H. Zhang, Z. Guo, H. Gao and T. Chang, "Stiffness–dependent interlayer friction of graphene," *Carbon ,* vol. 94, p. 60–66, 2015.

[80] E. J. Seldin, "Stress–strain properties of polycrystalline graphites in tension and compression at room temperature," *Carbon ,* vol. 4, p. 177–191, 1966.

[81] W. Wang, S. Dai, X. Li, J. Yang, D. J. Srolovitz and Q. Zheng, "Measurement of the cleavage energy of graphite," *Nature Communications,* vol. 6, p. 7853, 2015.

[82] E. Thormann, A. C. Simonsen, P. L. Hansen and O. G. Mouritsen, "Force trace hysteresis and temperature dependence of bridging nanobubble induced forces between hydrophobic surfaces," *ACS Nano,* vol. 2, no. 9, pp. 1817-1824, 2008.

[83] R. Jones, H. M. Pollock, J. A. S. Cleaver and C. S. Hodges, "Adhesion Forces between Glass and Silicon Surfaces in Air Studied by AFM: Effects of Relative Humidity, Particle Size, Roughness, and Surface Treatment," *Langmuir,* vol. 18, no. 21, pp. 8045-8055, 2002.

[84] A. Çolak, H. Wormeester, H. J. W. Zandvliet and B. Poelsema, "The influence of instrumental parameters on the adhesion force in a flat-on-rough contact geometry," *Applied Surface Science,* vol. 353, pp. 1285-1290, 2015.

[85] H. Kasai, K. Tolborg, M. Sist, J. Zhang, V. R. Hathwar, M. Ø. Filsø, S. Cenedese, K. Sugimoto, J. Overgaard, E. Nishibori and B. B. Iversen, "X-ray electron density investigation of chemical bonding in van der Waals materials," *Nature Materials,* vol. 17, pp. 249-252, 2018.

[86] Z. Li, A. Kozbial, N. Nioradze, D. Parobek, G. J. Shenoy, M. Salim, S. Amemiya, L. Li and H. Liu, "Water Protects Graphitic Surface from Airborne Hydrocarbon Contamination," *ACS Nano,* vol. 10, no. 1, p. 349–359, 2016.

[87] Z. Li, Y. Wang, A. Kozbial, G. Shenoy, F. Zhou, R. McGinley, P. Ireland, B. Morganstein, A. Kunkel, S. P. Surwade, L. Li and H. Liu, "Effect of Airborne Contaminants on the Wettability of Supported Graphene and Graphite," *Nature Materials,* vol. 12, pp. 925-931, 2013.

[88] X. Li, H. Qiu, X. Liu, J. Yin and W. Guo, "Wettability of supported monolayer hexagonal boron nitride in air," *Advanced Functional Materials,* vol. 27, p. 1603181, 2017.

[89] A. Kozbial, X. Gong, H. Liu and L. Li, "Understanding the Intrinsic Water Wettability of Molybdenum Disulfide (MoS2)," *Langmuir,* vol. 31, no. 30, p. 8429–8435, 2015.

[90] M. E. Schrader, "Ultrahigh-Vacuum Techniques in the Measurement of Contact Angles. 5. LEED Study of the Effect of Structure on the Wettability of Graphite," *Journal of Physical Chemistry,* vol. 84, p. 2774−2779, 1980.

[91] A. Kozbial, Z. Li, J. Sun, X. Gong, F. Zhou, Y. Wang, H. Xu, H. Liu and L. Li, "Understanding the Intrinsic Water Wettability of Graphite," *Carbon,* vol. 74, p. 218−225, 2014.

[92] A. Kozbial, C. Trouba, H. Liu and L. Li, "Characterization of the Intrinsic Water Wettability of Graphite Using Contact Angle Measurements: Effect of Defects on Static and Dynamic Contact Angles," *Langmuir,* vol. 33, p. 959−967, 2017.

[93] C. A. Amadei, C. Y. Lai, D. Heskes and M. Chiesa, "Time Dependent Wettability of Graphite Upon Ambient Exposure: The Role of Water Adsorption," *Journal of Chemical Physics,* vol. 141, p. 084709, 2014.

[94] Y. Wei and C. Q. Jia, "Intrinsic Wettability of Graphitic Carbon," *Carbon ,* vol. 87, p. 10−17, 2015.

[95] A. Ashraf, Y. Wu, M. C. Wang, N. R. Aluru, S. A. Dastgheib and S. Nam, "Spectroscopic Investigation of the Wettability of Multilayer Graphene Using Highly Ordered Pyrolytic Graphite as a Model Material," *Langmuir,* vol. 30, p. 12827−12836, 2014.

[96] J. Gao, B. Li, J. Tan, P. Chow, T. M. Lu and N. Koratkar, "Aging of Transition Metal Dichalcogenide Monolayers," *ACS Nano,* vol. 10, no. 2, p. 2628–2635, 2016.

[97] B. C. Windom, W. G. Sawyer and D. W. Hahn, "A Raman spectroscopic study of MoS2 and MoO3: applications to tribological systems," *Tribology Letters,* vol. 42, p. 301, 2011.

[98] Z. Peng, R. Yang, M. A. Kim, L. Li and H. Liu, "Influence of O2, H2O and airborne hydrocarbons on the properties of selected 2D materials," *RSC Advances,* vol. 7, p. 27048, 2017.

[99] M. F. Khan, G. Nazir, V. M. Lermolenko and J. Eom, "Electrical and photo-electrical properties of MoS2 nanosheets with and without an Al2O3 capping layer under various environmental conditions," *Science Technology Advanced Materials,* vol. 17, no. 1, p. 166–176, 2016.

[100] A. V. Kretinin, Y. Cao, J. S. Tu, G. L. Yu and et al., "Electronic properties of graphene encapsulated with different two-dimensional atomic crystals," *Nano Letters,* vol. 14, p. 3270–3276, 2014.

[101] Y. Ryu, W. Kim, S. Koo, H. Kang, W. K, T. Taniguchi and S. Ryu, "Interface-Confined Doubly Anisotropic Oxidation of Two-Dimensional MoS2," *Nano Letters,* vol. 17, no. 12, p. 7267–7273, 2017.

[102] K. S. Vasu, E. Prestat, J. Abraham, J. Dix, R. J. Kashtiban, J. Beheshtian, J. Sloan, P. Carbone, M. Neek-Amal, S. J. Haigh, A. K. Geim and R. R. Nair, "Van der Waals pressure and its effect on trapped interlayer molecules," *Nature Communications,* vol. 7, p. 12168, 2016.

[103] A. Verdaguer, C. Weis, G. Oncins, G. Ketteler, H. Bluhm and M. Salmeron, "Growth and Structure of Water on SiO2 Films on Si Investigated by Kelvin Probe Microscopy and in Situ X-ray Spectroscopies," *Langmuir,* vol. 23, no. 19, p. 9699–9703, 2007.

[104] T. Uwanno, Y. Hattori, T. Taniguchi, K. Watanabe and K. Nagashio, "Fully dry PMMA transfer of graphene on h-BN using a heating/cooling system," *2D Materials,* vol. 2, p. 41002, 2015.

[105] X. Zhang, F. Jia, B. Yang and S. Song, "Oxidation of Molybdenum Disulfide Sheet in Water under in Situ Atomic Force Microscopy Observation," *Journal of Physical Chemistry C,* vol. 121, no. 18, p. 9938–9943, 2017.

[106] J. D. Wood, C. M. Harvey and S. Wang, "Adhesion toughness of multilayer graphene films," *Nature Communications,* vol. 8, p. 1952, 2017.

[107] Y. Zhang, V. W. Brar, C. Girit, A. Zettl and M. F. Crommie, "Origin of Spatial Charge Inhomogeneity in Graphene," *Nature Physics,* vol. 5, p. 722–726, 2009.

[108] M. Yamamoto, T. L. Einstein, M. S. Fuhrer and W. G. Cullen, "Charge Inhomogeneity Determines Oxidative Reactivity of Graphene on Substrates," *ACS Nano,* vol. 6, no. 9, p. 8335–8341, 2012.

[109] D. W. Boukhvalov and M. I. Katsnelson, "Enhancement of Chemical Activity in

Corrugated Graphene," *Journal of Physical Chemistry C,* vol. 113, no. 32, p. 14176–14178, 2009.

[110] X. Fan, R. Nouchi and K. Tanigaki, "Effect of Charge Puddles and Ripples on the Chemical Reactivity of Single Layer Graphene Supported by SiO2/Si Substrate J. Phys. Chem. C. , 115,," *Journal of Physical Chemistry C,* vol. 115, p. 12960–12964, 2011.

[111] D. C. Elias, R. R. Nair, T. M. G. Mohiuddin, S. V. Morozov, P. Blake, M. P. Halsall, A. C. Ferrari, D. W. Boukhvalov, M. I. Katsnelson, A. K. Geim and K. S. Novoselov, "Control of Graphene's Properties by Reversible Hydrogenation: Evidence for Graphane," *Science,* vol. 323, no. 5914, pp. 610-613, 2009.

[112] S. Park, H. Kim, D. Seol, T. Park, M. Leem, H. Ha, H. An, H. Y. Kim, S. J. Jeong, S. Park, H. Kim and Y. Kim, "Evenly transferred single-layered graphene membrane assisted by strong substrate adhesion," *Nanotechnology,* vol. 28, p. 145706, 2017.

[113] S. Kumar, D. Parks and K. Kamrin, "Mechanistic Origin of the Ultrastrong Adhesion between Graphene and a-SiO2: Beyond van der Waals," *ACS Nano,* vol. 10, no. 7, p. 6552–6562, 2016.

[114] G. D. C. Rodrigues, P. Zelenovskiy, K. Romanyuk, S. Luchkin, Y. Kopelevich and A. Kholkin, "Strong piezoelectricity in single-layer graphene deposited on SiO2 grating substrates," *Nature Communications,* vol. 6, p. 7572, 2015.

[115] S. Das, D. Lahiri, A. Agarwal and W. Choi, "Interfacial bonding characteristics between graphene and dielectric substrates," *Nanotechnology,* vol. 25, p. 045707, 2014.

[116] P. Shemellaa and S. K. Nayak, "Electronic structure and band-gap modulation of graphene via substrate surface chemistry," *Applied Physics Letters,* vol. 94, p. 032101, 2009.

[117] D. Li, S. Wi, M. Chen, B. Ryu and X. Liang, "Nanoimprint-assisted shear exfoliation plus transfer printing for producing transition metal dichalcogenide heterostructures," *Journal of Vacuum Science & Technology B,* vol. 34, p. 06KA01, 2016.

[118] W. G. Cullen, M. Yamamoto, K. M. Burson, J. H. Chen, C. Jang, L. Li, M. S. Fuhrer and E. D. Williams, "High-Fidelity Conformation of Graphene to SiO2 Topographic Features," *Physical Review Letters ,* vol. 105, p. 215504, 2010.

[119] C. H. Lui, L. Liu, K. F. Mak, G. W. Flynn and T. F. Heinz, "Ultraflat graphene," *Nature,* vol. 462, p. 339–341, 2009.

[120] B. Felderhof, "Derivation of the love equation for the charge density of a circular plate condenser," *arXiv:1309.3662v1,* 2013.

[121] Cooke and J.C., "The Coaxial circular disc problem," *Zeitschrift fur Angewandte Mathematik und Mechanik,* vol. 38, pp. 349-356, 1958.

[122] P. Silvestrov and K. Efetov, "Charge accumulation at the boundaries of a graphene strip induced by a gate voltage: Electrostatic approach," *Phys. Rev. B,* vol. 77, p. 155436 , 2008.

[123] S. Thongrattanasiri, S. I and F. de Abajo, "Plasmons in electrostatically doped graphene,"

Appl. Phys. Lett., vol. 100, p. 201105 , 2012.

[124] E. Koren, E. Lörtscher, C. Rawlings, A. W. Knoll and U. Duerig, "Adhesion and friction in mesoscopic graphite contacts," *Science,* vol. 348, no. 6235, pp. 679-683, 2015.

[125] M. Grimsditch, "Shear elastic modulus of graphite," *J. Phys. C,* vol. 16, p. 143, 1983.

[126] A. Bosak and M. Krisch, "Elasticity of single–crystalline graphite: Inelastic X–ray scattering study," *Phys. Rev. B,* vol. 75, p. 153408, 2007.

[127] P. H. Tan, W. P. Han and e. al., "The shear mode of multilayer graphene," *Nat. Materials,* vol. 11, p. 294–300, 2012.

[128] Y. K. Shen and H. A. Wu, "Interlayer shear effect on multilayer graphene subjected to bending," *Appl. Phys. Lett. ,* vol. 100, p. 101909, 2012.

[129] M. Reguzzoni, A. Fasolino, E. Molinari and M. C. Righi, "Friction by Shear Deformations in Multilayer Graphene," *J. Phys. Chem. C,* vol. 116, p. 21104−21108, 2012.

[130] S. Munetoh, T. Motooka, M. K. and A. Shintani, "Interatomic potential for Si–O systems using Tersoff parameterization," *Comput. Mater. Sci.,* vol. 39, p. 334, 2007.

[131] V. B. W. H. Beest, G. J. Kramer and R. van Santen, "Force fields for silicas and aluminophosphates based on ab initio calculations," *Phys. Rev. Lett. ,* vol. 64, p. 1955, 1990.

[132] J. Sabio, C. Seoanez, S. Fratini, F. Guinea, A. H. Castro and F. Sols, "Electrostatic interactions between graphene layers and their environment," *Phys. Rev. B,* vol. 77, p. 195409, 2008.

[133] A. N. Rudenko, F. J. Keil, M. I. Katsnelson and A. I. Lichtenstein, "Interface interactions between local defects in amorphous SiO2 and supported graphene," *Phys. Rev. B ,* vol. 84, p. 085438, 2011.

[134] Y. He and W. O. G. Yu, " Interface adhesion properties of graphene membranes: thickness and temperature effect," *J. Phys. Chem. C,* vol. 119, pp. 5420-5425, 2015.

[135] J. C. Bowman and J. A. Krumhansl, "The low-temperature specific heat of graphite," *J. Phys. Chem. Solids,* vol. 6, p. 367, 1958.

[136] D. E. Soule and C. W. Nezbeda, "Direct Basal-Plane Shear in Single-Crystal Graphite," *J. Appl. Phys,* vol. 39 , p. 5122, 1968.

[137] E. J. Seldin, " Defense Ceramic Information Center," in *Ninth Biennial Conference on Carbon, Chestnut Hill, Massachusetts*, Columbus, Ohio, 1969.

[138] O. L. Blakslee, D. G. Proctor, E. J. Seldin, G. B. Spence and T. Weng, "Elastic constants of compression-annealed pyrolytic graphite," *J. Appl. Phys.,* vol. 41, p. 3373, 1970.

[139] R. Nicklow, N. Wakabayashi and H. G. Smith, "Lattice Dynamics of Pyrolytic Graphite," *Phys. Rev. B,* vol. 5, p. 4951, 1972.

[140] W. B. Gauster and I. J. Fritz, "Pressure and temperature dependences of the elastic constants of compression–annealed pyrolytic graphite," *J. Appl. Phys.,* vol. 45, p. 3309,

1974.

[141] N. Wada, R. Clarke and S. A. Solin, "X–ray compressibility measurements of the graphite intercalates KC8 and KC24," *Solid State Commun.* , vol. 35, p. 675, 1980.

[142] M. Grimsditch, "Shear elastic modulus of graphite," *J. Phys. C,* vol. 16, p. 143, 1983.

[143] S. R. Snyder, W. W. Gerberich and H. S. White, "Scanning tunneling-microscopy study of tip-induced transitions of dislocation-network structures on the surface of highly oriented pyrolytic graphite," *Phys. Rev. B,* vol. 47, p. 10823, 1993.

[144] G. S. Verhoeven, M. Dienwiebel and J. W. M. Frenken, " Model calculations of superlubricity of graphite," *Phys. Rev. B,* vol. 70, p. 165418, 2004.

[145] X. D. Ding, Y. Z. Wang, X. M. Xiong and e. al., " Measurement of shear strength for HOPG with scanning tunneling microscopy by thermal excitation method," *Ultramicroscopy* , vol. 115, p. 1–6, 2011.

[146] Z. Liu, J. Yang, F. Grey, J. Z. Liu and e. al., "Observation of microscale superlubricity in graphite," *Phys. Rev. Lett.* , vol. 108, p. 205503, 2012.

[147] X. Chen, Y. C. and C. Ke, "Bending stiffness and interlayer shear modulus of few-layer graphene," *Appl. Phys. Lett.* , vol. 106, p. 101907, 2015.

[148] Y. Gao, A. Kim, S. Zhou, H. C. Chiu, D. Nelias, C. Berger and e. al., "Elastic Coupling between layers in two-dimensional materials," *Nat. Mater.,* vol. 14, pp. 714-720, 2015.

[149] C. C. Vu, S. Zhang, M. Urbakh, Q. Li, Q. C. He and Q. Zheng, "Observation of normal-force-independent superlubricity in mesoscopic graphite contacts," *Physical Review B,* vol. 94, p. 081405, 2016.

[150] L. A. Girifalco and R. A. Lad, "Energy of cohesion, compressibility, and the potential energy functions of the graphite system," *Journal of Chemical Physics,* vol. 25, pp. 693-697, 1956.

[151] L. X. Benedict, N. G. Chopra, M. L. Cohen, A. Zettl, S. G. Louie and V. H. Crespi, "Microscopic determination of the interlayer binding energy in graphite," *Chemical Physics Letters,* vol. 286, no. 5-6, pp. 490-496, 1998.

[152] R. Zacharia, H. Ulbricht and T. Hertel, "Interlayer cohesive energy of graphite from thermal desorption of polyaromatic hydrocarbons," *Physical Review B,* vol. 69, p. 155406, 2004.

[153] A. Kis, K. Jensen, S. Aloni, W. Mickelson and A. Zettl, "Interlayer Forces and Ultralow Sliding Friction in Multiwalled Carbon Nanotubes," *Physical Review Letters,* vol. 97, no. 2, p. 025501, 2006.

[154] Z. Liu, J. Z. Liu, Y. Cheng, Z. Li, L. Wang and Q. Zheng, "Interlayer binding energy of graphite: A mesoscopic determination from deformation," *Physical Review B,* vol. 85, p. 205418, 2012.

[155] Z. Deng, A. Smolyanitsky, Q. Li, X. Q. Feng and R. J. Cannara, "Adhesion-dependent

negative friction coefficient on chemically-modified graphite at the nanoscale," *Nature Materials,* vol. 14, pp. 714-720, 2012.

[156] R. Zhang, Z. Ning, Y. Zhang, Q. Zheng, Q. Chen, H. Xie, Q. Zhang, W. Qian and F. Wei, "Superlubricity in centimeters-long double-walled carbon nanotubes under ambient conditions," *Nature Nanotechnology,* vol. 8, pp. 912-916, 2013.

[157] M. R. Roenbeck, X. Wei, A. M. Beese, M. Naraghi, A. Furmanchuk, J. T. Paci, G. C. Schatz and H. D. Espinosa, "In Situ Scanning Electron Microscope Peeling To Quantify Surface Energy between Multiwalled Carbon Nanotubes and Graphene," *Acs Nano,* vol. 8, no. 1, pp. 124-138, 2014.

[158] P. Li, Z. You and T. Cui, "Adhesion energy of few layer graphene characterized by atomic force microscope," *Sensors and Actuators A: Physical,* vol. 217, pp. 56-61, 2014.

[159] J. Wang, D. C. Sorescu, S. Jeon, A. Belianinov, S. V. Kalinin, A. P. Baddorf and P. Maksymovych, "Atomic intercalation to measure adhesion of graphene on graphite," *Nature Communications,* vol. 7, p. 13263, 2016.

[160] C. D. V. Engers, N. E. A. Cousens, V. Babenko, J. Britton, B. Zappone, N. Grobert and S. Perkin, "Direct measurement of the surface energy of graphene," *Nano Letters,* vol. 17, pp. 3815-3821, 2017.

[161] D. M. Tang, D. G. Kvashnin, S. Najmaei, Y. Bando, K. Kimoto, P. Koskinen, P. M. Ajayan, B. I. Yakobson, P. B. Sorokin, J. Lou and D. Golberg, "Nanomechanical cleavage of molybdenum disulphide atomic layers," *Nature Communications,* vol. 5, p. 3631, 2014.

[162] N. G. Boddeti, X. Liu, R. Long, J. L. Xiao, J. S. Bunch and M. L. Dunn, "Graphene blisters with switchable shapes controlled by pressure and adhesion," *Nano Letters,* vol. 13, no. 12, pp. 6216-6221, 2013.

[163] T. Jiang and Y. Zhu, "Measuring graphene adhesion using atomic force microscopy with a microsphere tip," *Nanoscale,* vol. 7, p. 10760, 2015.

[164] Z. Zhong, C. L. Chen, M. R. Dokmeci and K. T. Wan, "Direct measurement of graphene adhesion on silicon surface by intercalation of nanoparticles," *Journal of Applied Physics,* vol. 107, p. 026104, 2010.

[165] S. R. Na, J. W. Suk, R. S. Ruoff, R. Huang and K. M. Liechti, "Ultra long-range interactions between large area graphene and silicon," *ACS Nano,* vol. 8, no. 11, pp. 11234-11242, 2014.

[166] J. Torres, Y. Zhu, P. Liu, S. C. Lim and M. Yun, "Adhesion energies of 2D graphene and MoS2 to silicon and metal substrates," *Physica Status Solidi A,* vol. 215, no. 1, p. 1700512, 2018.

[167] S. J. Cartamil-Bueno, A. Centeno, A. Zurutuza, P. G. Steeneken, H. S. J. van der Zanta and S. Houri, "Very large scale characterization of graphene mechanical devices using a colorimetry technique," *Nanoscale,* vol. 9, p. 7559, 2017.

[168] D. A. Sanchez, Z. Dai, P. Wang, A. Cantu-Chavez, C. J. Brennan, R. Huang and N. Lu,

"Mechanics of spontaneously formed nanoblisters trapped by transferred 2D crystals," *PNAS,* vol. 115, no. 31, pp. 7884-7889, 2018.

[169] D. Lloyd, X. Liu, N. Boddeti, L. Cantley, R. Long, M. L. Dunn and J. S. Bunch, "Adhesion, Stiffness, and Instability in Atomically Thin MoS2 Bubbles," *Nano Letters,* vol. 17, no. 9, pp. 5329-5334, 2017.

[170] S. Deng, E. Gao, Z. Xu and V. Berry, "Adhesion energy of MoS2 thin films on silicon-based substrates determined via the attributes of a single wrinkle," *ACS Applied Materials Interfaces,* vol. 9, no. 8, pp. 7812-7818, 2017.

[171] A. Çolak, H. Wormeester, H. J. W. Zandvliet and B. Poelsema, "Surface adhesion and its dependence on surface roughness and humidity measured with a flat tip," *Applied Surface Science,* vol. 258, no. 18, pp. 6938-6942, 2012.

[172] G. A. Matei, E. J. Thoreson, J. R. Pratt and et al., "Precision and accuracy of thermal calibration of atomic force microscopy cantilevers," *Review of Scientific Instruments,* vol. 77, p. 083703, 2006.

[173] J. Hutter, "Comment on Tilt of Atomic Force Microscope Cantilevers: Effect on Spring Constant and Adhesion Measurements," *Langmuir,* vol. 21, p. 2630, 2005.

[174] R. Proksch, T. E. Schäffer, J. P. Cleveland, R. C. Callahan and M. B. Viani, "Finite optical spot size and position corrections in thermal spring constant calibration," *Nanotechnology,* vol. 15, pp. 1344-1350, 2004.

[175] J. E. Sader, J. W. M. Chon and P. Mulvaney, "Calibration of rectangular atomic force microscope cantilevers," *Review of Scientific Instruments,* vol. 70, p. 3967, 1999.

[176] R. C. Cooper, C. Lee, C. A. Marianetti, X. Wei, J. Hone and J. W. Kysar, "Nonlinear elastic behavior of two-dimensional molybdenum disulfide," *Physical Review B,* vol. 87, p. 035423, 2013.

[177] K. N. Kudin and G. E. Scuseria, "C2F, BN, and C nanoshell elasticity from ab initio computations," *Physical Review B,* vol. 64, p. 235406, 2001.

[178] N. Lindah, D. Midtvedt, J. Svensson, O. A. Nerushev, N. Lindvall, A. Isacsson and E. E. B. Campbell, "Determination of the Bending Rigidity of Graphene via Electrostatic Actuation of Buckled Membranes," *Nano Letters,* vol. 12, no. 7, p. 3526–3531, 2012.